Author:
Typos, Stavros

Title:
Propagation modelling for next generation wireless high-speed communication systems

Propagation Modelling for Next Generation Wireless High-Speed Communication Systems

By

STAVROS TYPOS

Department of Electrical and Electronics Engineering
UNIVERSITY OF BRISTOL

A dissertation submitted to the University of Bristol in accordance with the requirements of the degree of DOCTOR OF PHILOSOPHY in the Faculty of Engineering.

MARCH 2021

Word count: 47928

Abstract

Improved coverage, high data rates and Quality of Service (QoS) constitute essential features of 5G networks. The adoption of massive MIMO and millimeter-Wave (mmWave) technologies did not only improve these features but also resolved the spectrum limitations faced in 4G. Among the many resulting emerging vertical industries, Connected Autonomous Vehicles (CAVs) along with vehicle-to-everything (V2X) communications are deemed to transform the transportation landscape with numerous far-reaching societal and economic benefits. However, high mobility scenarios pose additional challenges in vehicular communications due to the rapid change in the environment, and specifically the channel coefficients. Thus, with the growing demand for such communication systems, wireless concepts for data exchange in time-variant networks become increasingly interesting.

In this work, the enabling technologies, major challenges and significant opportunities mmWave frequencies can introduce to vehicle-to-infrastructure (V2I) communications are discussed. Using a ray-tracing approach, the effects of the propagation channel on high mobility mmWave applications are studied. A spatiotemporal characterisation of the environment is performed, and the antenna design parameters' effects are explored. Physical radiowave propagation models for mmWave are also used to assess as well as improve the achievable throughput, coverage and Signal-to-Noise-Ratio (SNR) in High-Speed Train (HST) and urban environments using reduced resolution, non-uniform codebook schemes.

The proposed designs operate on the premise that line-of-sight (LOS) rays dominate the mmWave links, and the sectors with the highest antenna gain are the ones around the LOS ray direction, aiming to find the sectors which cover the LOS ray in fewer search steps. Codebook solutions are shown to provide the best performance compromise between data rates, outage percentage and AP separation, allowing constant connectivity between terminals though with an increased variability of throughput. Beamforming setup time is also shown to be reduced significantly while at the same time keeping throughput stable. Finally dynamic sector design in conjunction with multi-stage BF processeses is applied in urban vehicular architectures and is shown to significantly reduce time to setup and subsequently the effects of channel aging in mmWave environments.

DEDICATIONS

To my dear parents, Georgios and Thomai.

Acknowledgements

First and foremost I am extremely grateful to my supervisors, Dr. Simon Armour and Prof. Angela Doufexi for their invaluable advice, continuous support and assistance at every stage of my PhD degree. I also appreciate both of them spending a great amount of their time and effort on providing me constructive feedback on every piece of my written work including this manuscript.

I would also like to thank Prof. Mark Beach for his continuous support and constant encouragement to participate in various training courses and many research activities as well as his immaculate job as an internal assessor for my project.

My sincere thanks also go to Dr. Angelos Goulianos, Dr. Vaia Kalokidou, Dr. Di Kong and Dr. Alberto Loaiza Freire for all the technical support in the early stages of this work.

I would also like to thank Dr. Ian Hindmarch and Mr. Paul Thomas from GCHQ for their constant support with the ray-tracer updates and integrations.

Last but not least I would like to acknowledge Mr. Eleftherios Mallios for his help and exemplary reviews of the mathematical analyses performed throughout this thesis.

This work was supported by the Engineering and Physical Sciences Research Council and the University of Bristol

Author's declaration

I declare that the work in this dissertation was carried out in accordance with the requirements of the University's Regulations and Code of Practice for Research Degree Programmes and that it has not been submitted for any other academic award. Except where indicated by specific reference in the text, the work is the candidate's own work. Work done in collaboration with, or with the assistance of, others, is indicated as such. Any views expressed in the dissertation are those of the author.

SIGNED: Stavros Typos DATE: 29/03/2021

Table of Contents

Page

List of Tables

Table **Page**

List of Figures

Figure **Page**

Chapter 1

Introduction

Over the past two decades an unprecedented growth in wireless services and supporting technologies has been observed. Technology upgrades ranging from wireless access systems and cellular phones to machine-to-machine (M2M) and sensoring devices, have resulted into a rapid increase in the demand for different types of mobile communications services. According to CISCO, at the end of 2020 mobile data traffic was observed to almost double in the span of only one year. By 2023, more than 30 billions of devices are predicted to circulate in 5G networks while M2M communications would grow to a 50 percent (14.7 billion M2M connections) of the total connected devices by 2023 [2].

However to reach today's truly broadband-ready 5G networks, technology evolved from primitive analogue-based methods to digital, efficient and sophisticated ones that provide good Quality of Service to a large number of users. An overview of the path from the first generation of mobile systems to the most recent IP-based data centric solutions is quickly presented in Table 1.1 below.

In fifth-generation networks (5G), the concept of multiple networks convergence becomes increasingly important. 5G's research vision was to provide seamless connectivity between many different types of services to an increasing amount of devices. Even though the concept of monitoring and controlling of different devices operating on one or multiple networks has been promoted for some time, several market trends have sped up the process. As a result there is an increased need for universal propagation models that could be used to optimise and plan those networks that could contain thousands of devices operating together. The increase of the number of such devices can be seen in Figure 1.1.

With 5G communication networks rapidly rolling out globally, it is time to ask how 5G - and by extension 6G - will help revolutionize vehicular communications. Among many emerging

TABLE 1.1. Different generations in wireless communication (Figure reproduced from [3])

The generation	Access protocols	Key features	Level of evolution
1G	FDMA	Analog, primarily voice, less secure, support for low bit rate data	Access to and roaming across single type of analog wireless networks
2G&2.5G	TDMA,CDMA	Digital, more secure, voice and data	Access to and roaming across single type of digital wireless networks and access to 1G
3G&3.5G	CDMA 2000,W-CDMA,HSDPA,TD-SCDMA	Digital, multimedia, global roaming across a single type of wireless network(for example, cellular), limited IP interoperability, 2Mbps to several 2Mbps	Access to and roaming across digital multimedia wireless networks and access to 2G and 1G
4G	OFDM	Global roaming across multiple wireless networks, 10Mbps-100Mbps, IP interoperability for seamless mobile internet	Access to and roaming across diverse and heterogeneous mobile and wireless Broadband networks and access to 3G,2G and 1G
5G	OFDM, SCMA, NOMA, BDMA (mmWave)	Massive MIMO and mmWave spatial separability, M2M and IoT	Access to and roaming across hetNets and seamless integration of multiple access technologies. Access to 4G, 3G,2G and 1G.

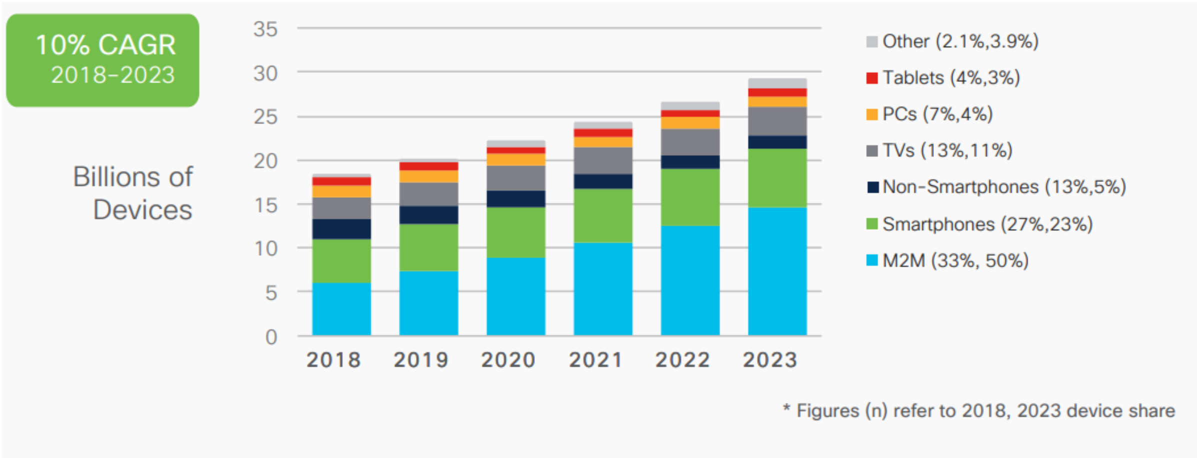

FIGURE 1.1. Mobile traffic trends 2018-2023 [2]

vertical industries, connected autonomous vehicles (CAVs) are deemed to transform our travel experience with numerous far-reaching societal and economic benefits. CAV technologies would allow the vehicle to be able to communicate with its environment in addition to other vehicles in the proximity. Such technologies would provide an unprecedented opportunity to utilise road infrastructure more efficiently, reduce the risk of accidents and vehicular emissions. Generally, the technologies being developed to support CAVs include:

1. Vehicle to Vehicle (V2V) technology allowing relay of traffic information and conditions
2. Vehicle to Infrastructure (V2I) technology allowing guidance and signal phasing to reduce physical clutter in cities.
3. Vehicle to Everything (V2X) technology that describes connectivity between the vehicle and all appropriate technologies

Future vehicles would almost definitely include a combination of different wireless connectivity systems that would introduce the above-mentioned solutions. Wi-Fi, LTE, mmWave and Bluetooth (IEEE 802.15.4) are some of the contender enabling technologies.

Even though this work focuses in providing analyses and considerations for mmWave communication systems, we discuss existing cellular and LAN wireless technologies as they already introduced techniques and technologies that are the basis of 5G systems. Features such as the ones listed below were paramount in the development of today's 5G leading technologies and specifically of mmWave infrastructure to increase the overall robustness of the system but also support higher data rates and realise directional communications.

4G wireless mobile networks can provide a mostly uninterrupted connection to cover the "always-on" requirements of specific applications. At the same time, Wi-Fi technologies achieve relatable speeds and coverage but on a much smaller (local) scale. One of the most important features of those sub-6GHz networks is the very high-speed IP packet transmission achievable even in mobility scenarios due to the inherent lower delay of those systems. The 100Mbps speeds were found to be achievable even in high mobility scenarios (trains, cars) while speeds as high as 1 Gbps were observed in a non-moving receiver [4]. Technologies operating at the sub-6 GHz range became quite popular due to the wave properties at this radio spectrum range as radio waves have the ability to penetrate a wide variety of material types and thickness (e.g. concrete, glass and other materials used in buildings).

Since Wi-Fi technologies were introduced at the late 1990's, supported technologies have evolved from a simple positioning system to becoming the basis of most indoor and outdoor applications. **Wireless LANs** can be regarded as a mature technology, thus most of the connectivity issues have been resolved and current WLAN research revolves around seamless connectivity and better spectrum utilisation. However, what is important on the context of this research is the introduction of **beamforming** concepts. In such systems, the location of the connected devices would be identified and the signal would be directed towards the device, hence increasing spatial separability, reducing interference and user experience through an increase in the connection speed.

Regarding the fourth generation of cellular networks that was presented earlier, the leading and enabling technology (LTE) was the most vital addition. **Long Term Evolution (LTE)** is based on redesigned interfaces and networks and supports a variety of frequencies (700 MHz to 3.8 GHz) and bandwidths (1.4 MHz - 20 MHz) [5]. Due to the low frequencies employed in the system, cell sizes can reach up to a range of 100km and allow for high mobility scenarios. The most important features of LTE though, relate to the introduction of **Multiple-Input/Multiple-Output (MIMO)** antennas that can be supported in both uplink and downlink allowing a theoretical speed of 300Mbps along with beamforming techniques to direct the beams. These characteristics make LTE a very important, not only as a stand-alone technology but also as a keystone for 5G and beyond systems.

With sub-6GHz frequencies becoming even more crowded as data consumption increases alongside with the number of connected devices to the network - from wireless connected devices, home appliances and even satellite applications - study on more efficient utilisation or investigation on less crowded frequencies was required. Considering sub-6GHz frequencies, even though the spectrum at 5GHz is less crowded, it still fails to completely cover the needs for "always-on" connectivity [2].

Massive MIMO and mmWave were the two key technologies that were introduced in 5G to allowed for better utilisation of the spectrum, to offload current systems and decongest the lower frequencies of the spectrum. Carriers have been investigating a number of even higher frequency bands that can be added to 5G infrastructure as currently there is an enormous amount of unused and unlicensed spectrum. The integration of mmWave could provide a huge boost in communication capacity due to the increased spatial separation (due to short coverage ranges) and spectral availability [6]. mmWave was initially proposed as one of the driving forces of 5G. However, as 5G has gone near term and focused in improving technologies at sub-6GHz, vehicular mmWave technologies have been pushed as a candidate for 6G communications especially for wider scale deployments. This research was performed within the 5G framework but the derived solutions will also be applicable and more suitable to 6G vehicular telecommunications.

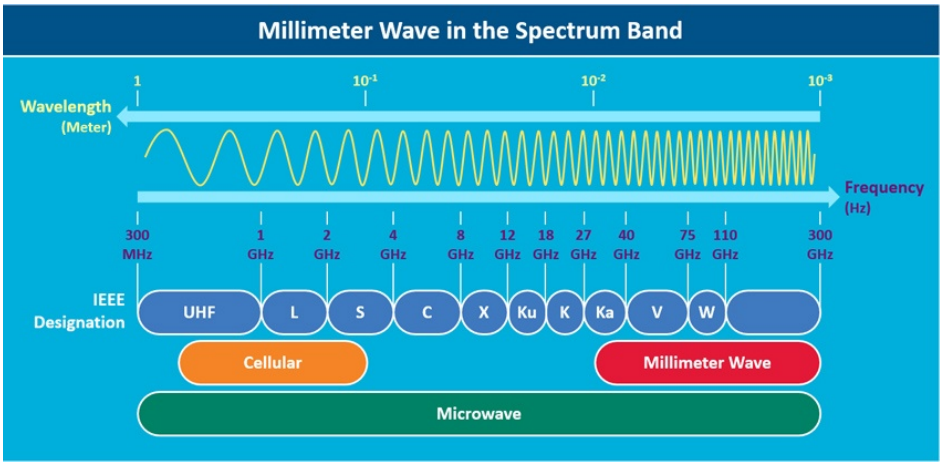

FIGURE 1.2. Graphical representation of microwave and mmWave bands

Even though mmWave seems to be able to solve the network congestion problem, several challenges introduced by the radiowave propagation characteristics need careful consideration. Novel circuit design, interference mitigation and anti-blockage techniques, as well as system control and spatial reuse features need to be investigated in order such systems to be deployed.

Frequencies at the higher side of the spectrum operate in a fundamentally different way compared to sub-6GHz ones. Such frequencies are characterised by an exponentially increased path loss and as such resulting in confined coverage in networks. Rappaport in [3] confirms the frequency dependence of this propagation parameter as the path loss seems to exponentially increase with distance as the frequency increases. Moreover, sensitivity to blockage and directivity are some of the other major differences that inherently exist in mmWave frequencies.

The technology that has the most potential of overcoming these challenges concentrates on directional transmission and smart/adaptive antenna arrays. High-gain steerable antennas are considered by many lead researchers to be the most promising technology to mitigate the channel effects. A large part of the research concentrates on developing algorithms that would be used for beam steering and tracking, i.e. beamforming. Adaptive and dynamic beamforming is essential as it would be used to direct the energy of the antenna towards the optimal direction to account for the rapid variations in the channel especially with increased mobility applications. Thus, a user would be able to experience the gigabit connectivity promised in those frequencies.

Although the majority of the literature was focused in generating well-defined models that can characterise mmWave systems there are some not as well defined parameters and approximations regarding the propagating channel and environment. Extensive reports regarding beam codebook design is provided in 802.15.3c [7]. However, it only covers 2-D arrays with uniform spacing of half-wavelength that at the same time do not consider amplitude adjustments. There is also an increased interest in ensuring spherical coverage requirements around the transmitting and receiving antenna [3, 5, 8] which at times creates redundancies and slows the beamforming process, especially in high mobility scenarios.

There are many reports in literature that cover management and optimisation of the antenna's beam parameters through machine learning [9–11] but such methods normally tend to over-simplify and use considerable assumptions regarding the channel and environment to ensure reasonable algorithm training time. Hence, the effects that small objects, clutter or other vehicles have in the received power and angular distribution around the transmitting and receiving antenna is significant in mmWave architectures and not considered in such studies. Hence suboptimal view of the environment is achieved reducing the accuracy of the model. Moreover, most of the literature assumes ideal omni-directional antenna elements and patterns, ignoring realistic antenna patterns and the impact of terminal housing. In [8] a detailed approach in beam generation is described and the terminal housing issues are addressed but issues regarding speed and all the steming concerns such as channel aging or high capacity are not discussed at all.

1.1 Aims and Key Objectives

The ultimate aim of this thesis is to develop and demonstrate a set of useful tools and methodologies to tackle the issues in high-mobility and high-frequency future networks. Important research questions such as how the antenna's properties affect the propagating channel, how the physical structure and infrastructure of urban environments can inspire cost effective design of mmWave networks, and how non-uniform pattern design can considerably affect the performance of those networks need to be addressed.

Work undertaken in this PhD builds upon peer-reviewed work of multiple researchers in the Communications Systems and Networks group in the University of Bristol. Propagation modelling, antenna design, system-level simulators and analysis techniques have been separately developed as well as thoroughly tested and applied for a variety of applications. The personal contribution of the author of this thesis focused on the comprehensive integration of measured and modelled antenna characteristics, state-of-the art propagation modelling for outdoor environments, and sophisticated physical (PHY) layer simulators to allow suitable integration into a complete model suitable for high-frequency mmWave vehicular applications. The functionality of the ray-tracer, antenna modelling techniques and simulator were expanded throughout this work to allow for the modelling of uniform and non-uniform codebook solutions and measure the effects these methods have in system performance assuming high-mobility.

The method takes as inputs the measured or simulated electric field response data of a single element antenna and generates the desired codebook according to the requirements on the codebook size, spherical coverage or any relevant parameter to the use case. The method can be applied in a straightforward manner to different antenna type, antenna array configuration, placement and terminal housing design.

The design process is completely modular so antenna/codebook parameters can be modified at any stage of the simulation for any relevant use case consideration. Specifically, the modularity of the ray-tracer allows us to even create test environments and study the communications channel analytically even for planning purposes. This streamlined process is used to propose and benchmark static or dynamic resolution codebooks against ideal beamformers to test performance within multiple vehicular use cases in terms of throughput, coverage and cost.

The key contributions of this thesis are summarised as follows:

1. A detailed analysis of the physical channel characteristics and parameters of vehicular environments in comparison to already defined stochastic models. Results from the analysis (presented in Chapter 4) were used in 3GPP release 15 update meetings regarding channel modelling parameters in urban architectures.

2. A study on the positioning of APs in urban and train environments to maximise the ratio of LoS links within a set route to significantly improve the performance and viability of a mmWave for high-speed wireless applications (Chapter 4)

3. A mathematical analysis taking into consideration common infrastructure design practices and approximations to provide angular analytics and simplify the design of a phased antenna array and the relevant codebooks to three main parameters (Chapter 5)

4. A codebook-based beamforming model, which can be integrated with a physical propagation model in order to generate a channel model suitable for system-level simulations, is introduced (Chapter 5). The model can support any antenna radiation pattern orientation and arbitrary MIMO array configuration in the 3D space.

5. Non-uniform codebook designs for High-Speed-Train (HST) and urban vehicular use cases, considering surrounding infrastructure and train track/urban area design(Chapters 5,6).

6. The impact of uniform and non-uniform codebook design on system performance, beamforming setup time and channel aging (Chapter 6).

This work focuses on mmWave implementations in high speed V2I environments with mentions to V2V and Infrastructure-to-Infrastructure applications.

1.2 List of Publications

1. V. Kalokidou, S. Typos, E. Mellios, A. Doufexi and A. Nix, "Performance Evaluation of mmWave in 5G Train Communications," 2018 IEEE 29th Annual International Symposium on Personal, Indoor and Mobile Radio Communications (PIMRC), 2018, pp. 391-395.

2. S. Typos, V. Kalokidou, S. Armour, A. Doufexi, E. Mellios and A. Nix, "Codebook Performance Evaluation of mmWave in Train Communications," 2020 IEEE 91st Vehicular Technology Conference (VTC2020-Spring), 2020, pp. 1-6.

3. S. Typos, S. Armour and A. Doufexi, "Non-Uniform Codebook Configurations for High-Speed Rail Communications," 2021 IEEE 93rd Vehicular Technology Conference (VTC2021-Spring), 2021, pp. 1-7.

1.3 Thesis Outline

The rest of this thesis is organized as follows. Chapter 2 introduces the basic principles of antennas and propagation, which will be useful for the comprehensive understanding of the rest of the thesis. An overview of the most common wireless channel modelling techniques and their main advantages and limitations is presented as well. A short discussion on well established channel models that will be used throughout the thesis for comparison is provided as well.

Chapter 3 presents a description of a 3D ray-based wireless channel modelling methodology that allows any multi-element antenna array, orientated as required, to be integrated with a physical radiowave propagation model. A discussion on the database formulation in terms of the accuracy of the environment is provided. The accuracy of the propagating mechanisms and models used for each are also presented in the context of mmWave communications. A method for system-level simulations following the combination of the generated antenna arrays and propagation models is also discussed. Finally, beamforming techniques based on two well established standards are presented.

Chapter 4 follows the aforementioned channel modelling technique in order to investigate and highlight the impact of antennas and propagation on the channel and system-level performance of a digital wireless communication system. Two case studies considering high-speed applications (HST and urban vehicular) are introduced to quantify the effects of the environment and beamforming in mmWave communications. A system-level performance evaluation is performed in the train scenario to discuss the effects of frequency, beamforming and access point spacing in throughput and coverage.

Chapter 5 studies the effects of codebooks in the design of high-speed environments. Uniform configurations are discussed according to their resolution for HST scenarios. A method to enhance the mmWave beamforming design is presented using non-uniform codebooks to take advantage of the simplified geometries in rail scenarios in order to reduce beamforming time without any performance loss.

Chapter 6 discussed the concepts presented in Chapter 5 in the setting of a more complex urban environment. Junction cases such as roundabouts and corssings are studied in terms of their physical design parameters and the optimal placement of APs is discussed in that context. Multi-step codebook solutions are modelled and their performance is discussed in terms of the system. Finally the effect of those parameters in beamforming setup time and channel aging are discussed considering a single user traversing throughout the environment.

Finally, Chapter 7 draws conclusions of the thesis and discusses ideas for future work inspired by its outcomes.

CHAPTER 2

Wireless Propagation, Antenna Theory and Channel Modelling

Investigation into channel characterisation is essential to ensure that progress can be made to meet the ever-growing demand for data. In order to design, develop and deploy efficient mmWave systems, it is vital to know the properties of the propagating antenna (or antennas) and channel. Antennas on mobile and access point terminals play a pivotal role in a wireless communications system as they ultimately determine the system's performance along with the propagating medium between them. Thus it becomes a really important task to accurately evaluate these devices as their performance could greatly influence the propagation channel model. Specifically, great attention needs to be given in understanding the properties of the propagating channel as well as antenna design properties due to the inherent frequency dependence of the propagation constants.

2.1 Introduction

As the number of connected devices and data demand increases [2], sub-6GHz frequency bands are becoming more and more crowded. For this and a variety of other reasons such as spatial separation and security, millimeter wave (mmWave) frequency solutions have become even more attractive. mmWave networks do not only provide an overall improvement in throughput as an immediate result of the increased bandwidth, but also natively facilitate dense spatial reuse of spectrum. Due to the high attenuation encountered at these frequencies and hence the reduced range compared to sub-6GHz systems, a more efficient spectrum usage can be achieved even in more confined networks.

However, those high attenuation properties encountered at mmWave frequencies [3] require appropriate characterisation and consideration to achieve optimal performance, especially in time varying channels. Adaptive beamforming (BF), antenna directivity and spatial reuse features are some of the areas that need to be investigated to deploy mmWave systems. An overview of propagation and signal processing techniques for 5G and especially for mmWave can be found in [12, 13].

Knowing the characteristics of the propagating channel is essential for propagation modelling. In a wireless medium, different paths can be observed at each link due to obstructions and blockages in the environment. Each of those paths has its own electrical length and hence a unique time of flight thus leading to a different received signal strength (and attenuation), time delay, phase and arrival angle for each of those paths, giving rise to a complex time-varying propagation channel. The effect of the channel to those parameters will be analysed below.

In addition to the independent properties of those entities, it is quite critical to investigate how the integration of the propagating channel and the antenna model would affect the system. There is a critical need to have both theoretical and practical research in antenna design as well as antenna and radio channel modelling as both of these are vital in the design and optimization of communication systems. An accurate channel model would help in the design, behaviour and performance optimisation of the constituents of a communication system and would be ultimately able to provide analytical or simulation-based investigations of its performance. Therefore, by optimising the placement of the transmitting or receiving antenna, a great performance gain could be achieved leveraging detailed modelling techniques.

The aim of this chapter is to introduce the basic principles of antennas and radiowave propagation that will be useful for the comprehensive understanding of the rest of the thesis. The antennas and the propagation environment essentially constitute the fundamental elements of the wireless channel. The main characteristics that need to be accurately defined when an communications system is designed, evaluated or optimised will be presented along with an introduction to some of the most wiedespread channel models that will be used to benchmark the proposed schemes throughout this work. Propagation mechanisms and specifically their dependencies in the surrounding environment, operating frequency, bandwidth of operation, physical separation and mobility are discussed in detail. Antenna parameters regarding to normal antenna operation and specifically related to beamforming, adaptive antenna schemes and polarisation are presented as well considerations for mmWave systems deployments. The rest of the chapter is organised as follows. Section 2.2 will introduce the characteristics of the propagation channel. The properties of antennas in relation to their design and propagation environment are presented in Section 2.3. Section 2.4 will provide a brief introduction into wireless channel modelling techniques while in 2.5 we will be discuss and compare some of those models in regard to the proposed channel characteristics. Finally, Section 2.6 will conlude the chapter. Sections 2.2 up to 2.4 ultimately include all of the background information needed for the understanding of this thesis, while Section 2.5 includes the state-of-the-art in propagation modelling.

2.2 Wireless Propagation Channel Characteristics

2.2.1 Path Loss

Line-of-Sight (LoS) transmission refers to the simplest propagation scenario that could appear in a wireless network. It takes place when the transmitted radio wave travels throughout the channel to the receiver without encountering any obstruction that could divert or even completely block its path. The factor that determines the power loss (in dB scale) in this specific case, is referred to as free-space path loss and is expressed by the equation below,

$$PL = 10\log\left(\frac{4\pi d}{\lambda}\right)^2 \tag{2.1}$$

where PL denotes the path loss, d is the separation distance between the transmitter and the receiver, and λ is the carrier wavelength.

Equation 2.1 shows the frequency dependence of this propagation parameter as the path loss seems to exponentially increase with distance as the frequency increases, which is also confirmed by Figure 2.1. Additional factors such as oxygen and moisture absorption or rain attenuation for frequencies above 60GHz have not been included. Excluding those factors, the received power at the terminal is given by the equation below

$$P_R = P_T + G_T + G_R - PL \tag{2.2}$$

where P_R and G_R are the received power and antenna gain and P_T and G_T the analogous transmitter coefficients in dB.

However, in reality wireless propagation is not only contained into the LoS scenario. Hence, the path loss equation needs to be able to apply to every possible scenario and not only to the LoS one or scenarios with a very strong dominant LoS multipath component (e.g. point to point microwave link). To account for more complex environments the above equation is modified to facilitate those cases by modelling path loss to be proportional with distance the same way but replacing the square law with a n^{th} law.

$$PL = 10\log\left(\left(\frac{4\pi}{\lambda}\right)^2 d^n\right) \tag{2.3}$$

To model the path loss in more complex environments, the n exponent of the equation increases along with the complexity of the environment leading to larger values of n for more complex (e.g. dense urban) scenarios reaching up to even a value of 6.5. On the other side,

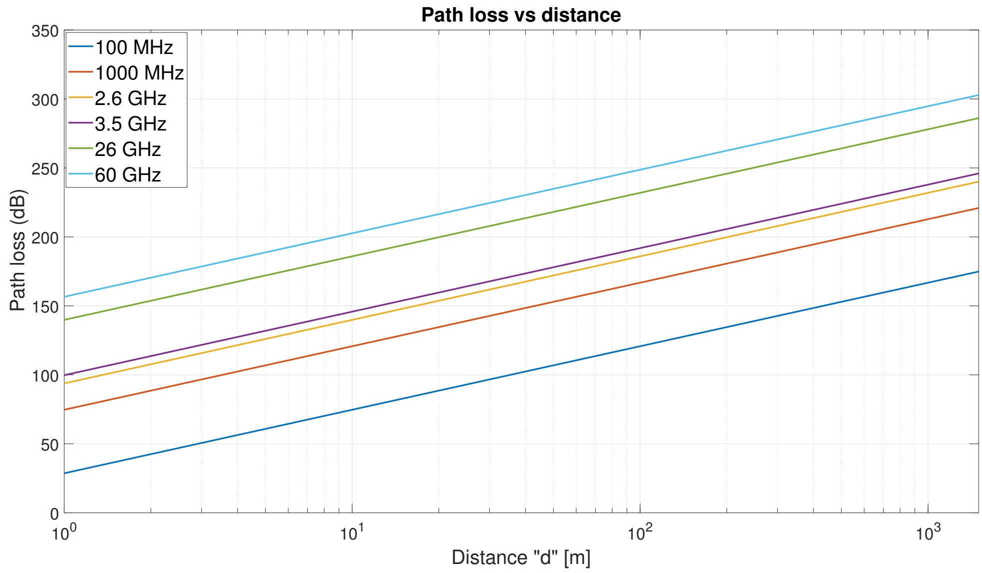

FIGURE 2.1. Free-space PL as a function of distance for different frequencies

waveguide environments might achieve values of n smaller than 2 as propagation is benefited in these specific scenarios. The effect of different values of n in received power can be seen in Figure 2.2.

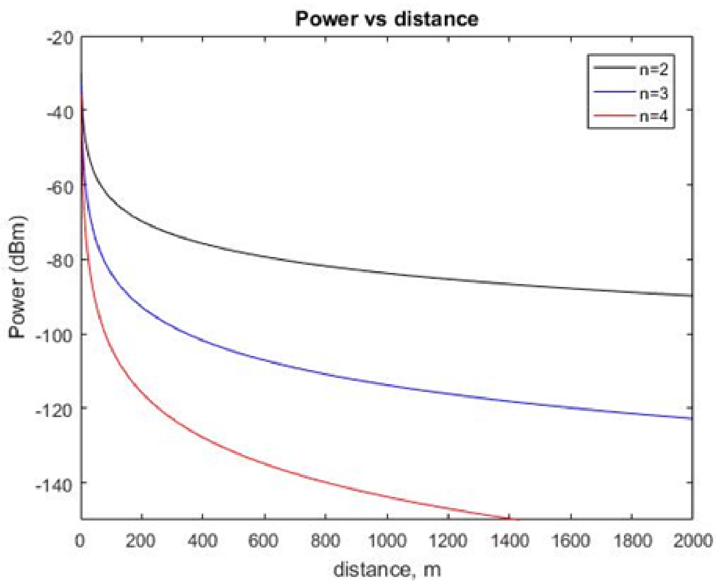

FIGURE 2.2. Effects of n-value in received power

Some complex empirical models have been developed as well to model path loss such as the

Okumura, Hata, COST 231 and the modified Hata models [14–16]. Even though these models and especially the Okumura model are ideal for low-rise urban environments, the fact that they were developed for lower frequencies (150-1920 MHz), increased base station heights and link distances on the range of 1 km to 100 km, renders them inaccurate for the target frequencies and applications in the scope of this thesis.

2.2.2 Narrowband Characterisation

For a signal in a propagation channel, the channel can be classed as either narrowband or wideband. It is considered narrowband if all the frequency components of the signal are affected in a similar manner within the channel i.e. the signal bandwidth is far less than the coherent bandwidth. Specifically, the channel coherence bandwidth is defined as the bandwidth within which all the frequency components of a signal are affected in a similar manner [17]. For a wideband channel on the other hand, the signal bandwidth is much greater than that over which the frequency components are affected similarly within the channel. As such the channel characteristics are a function of frequency for a wideband channel.

2.2.2.1 Shadow Fading

As a user is moving through the environment, large obstacles attenuate the received signal strength. This phenomenon is called shadow fading, which is also known as slow fading because its rate of change is generally low. Shadow fading is mainly caused in cases where a large object would obstruct the transmission path (usually buildings, foliage and urban clutter) and create radio shadows. Slow fading exhibits itself in terms of slow signal power and phase variation as the receiver moves around the environment. An example of shadow fading caused by a building blocking the path in different instances of time can be seen in Figure 2.3 below.

The describe the above mentioned modification the distance exponent is added into the path loss equation to account for those effects (F_{SF}), modelled as a Gaussian random variable with zero mean.

$$PL = 10\log\left(\left(\frac{4\pi}{\lambda}\right)^2 d^n\right) + F_{SF} \tag{2.4}$$

However, it has to be mentioned that this increase that accounts for heavily built-up urban centres and low mounted base-station antennas is not based on any physical knowledge but instead a pragmatic way to account for the shadowing losses sometimes varying up to 20 dB from a city block to another.

2.2.2.2 Fast Fading

Although shadowing effects could reach a severe level of attenuation that could cause even signal loss, its degree of variation is pretty slow (thus the name). In a wireless communications system,

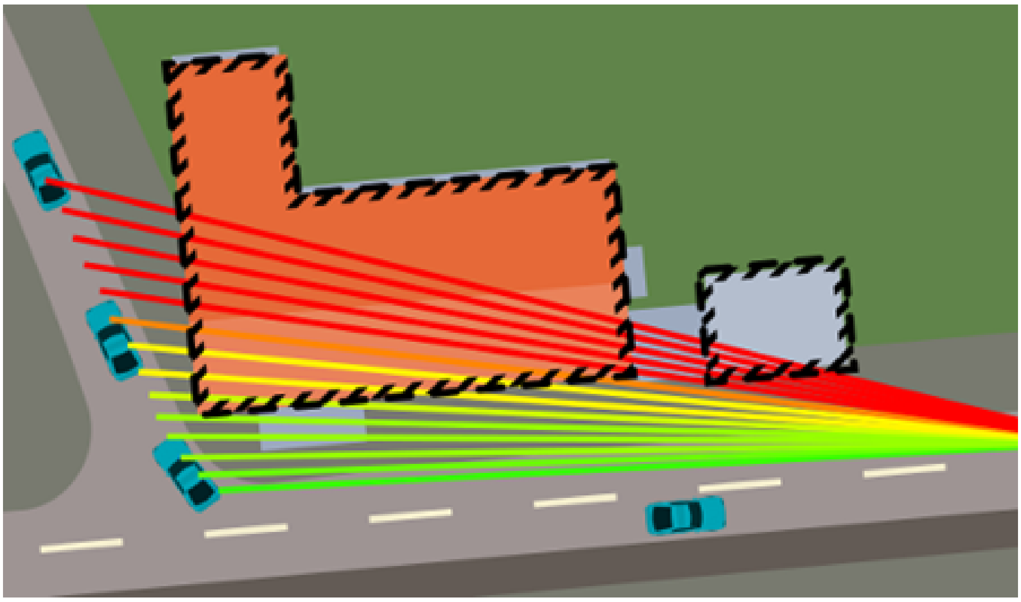

FIGURE 2.3. Building Blockage

there is another form of fading that can be observed and accredited to the multipath nature of the propagation; fast fading. Each multipath component arrive at the receiver following a unique path thus having different arrival time, angle and power. This results into constructive or destructive interference that is the effect of phasor addition at the receiver. Due to the quickly varying nature of the phase and amplitude imposed by the propagating channel have a high degree of variation thus leading to multiple fades in the channel.

Specifically, within the propagation environment we can observe two distinct models of fading:

1. Rician fading: for the case where there is a dominant stationary signal component present (such as LOS) and
2. Rayleigh fading: for the case where there is no predominant LoS component between the transmitter and receiver.

2.2.3 Wideband Characterisation

In contrast to the narrowband characteristics examined in the preceding section, the wideband characteristics of a channel relate to the response of the channel to broadband signals i.e. signals whose bandwidths are larger than the channel coherence bandwidth.

2.2.3.1 Delay Spread

As mentioned above, the physical environment causes the signal to reach the receiver with unique power and delay for each component. The effects of delay (or time-of-arrival) can be represented by the power delay profile (PDP) which is obtained by measuring the received power of each multipath and plotting it over its time of flight. In other words, delay spread measure of the multipath richness of a communications channel. The RMS delay spread is the acquired by normalising the time axis and plot using the delay from the first received multipath. To avoid the effects that might be caused in the case of a multipath component arriving with a very large delay, a maximum excess delay time is defined to annotate the maximum resolvable delay. This restriction is placed along with a dynamic power range in order to avoid ambiguous analysis and ensure Inter Symbol Interference free (ISI-free) channels.

2.2.3.2 Angular Spreads

Apart from the delay, the angle of departure (AoD) and arrival (AoA) differs for each ray that leaves the transmitter and reaches through various propagation mechanisms the receiver terminal. The angular profile can be interpreted as the spread between the angle values of each multipath component by plotting the power against the elevation or the azimuth of the AoD or AoA. The angular spread is then derived by normalising to the strongest ray.

2.2.3.3 Doppler Spread

The Doppler spread metric is used to account for mobility scenarios. To exhibit this, the simplest use case scenario is studied where a receiver is mounted on top of a moving vehicle. It can easily be seen by simple geometry (in the azimuth plane) that the phase of the arriving multipath component will change over time as the vehicle is not static. Following that, it is trivial to prove that this will result in a change in the frequency of each ray component.

The Doppler frequency shift f_l of the l^{th} MPC is defined by equation

$$f_l = \frac{|v| \cos\left(\omega_{AoA,l} - \omega_v\right) \cos\left(\zeta_{AoA,l} - \zeta_v\right)}{\lambda} \tag{2.5}$$

Ultimately, Doppler spread is dependent on the direction of the movement, as if the receiver moves towards the transmitter the Doppler shift would be positive and vice versa. Moreover, the Doppler shift refers to one single multipath component each time thus the absolute difference between the smallest and the largest shift during the movement is referred to as Doppler spread.

2.2.4 K-factor

The wireless medium is mainly composed by constantly time-varying channels, hence to distinguish between slow and fast varying channels, the K-factor is defined. The K-factor is used as a measure to determine the amount of variation in a channel and is equal to the ratio of the highest received power multipath component over the power achieved in all of the rest of the paths. A large K-factor associates to a dominant and possibly even a LoS component (up to even

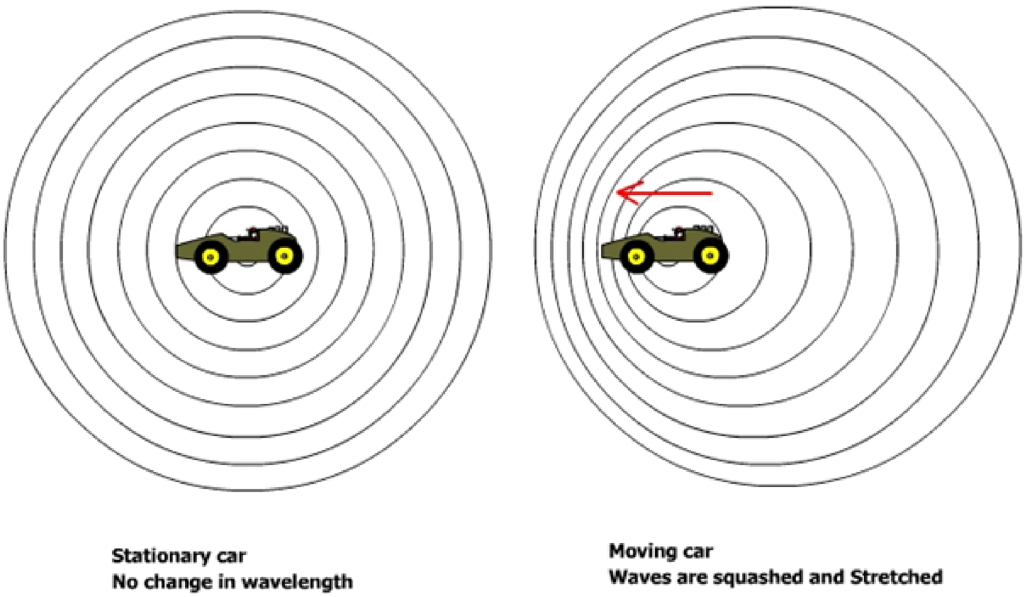

FIGURE 2.4. Doppler Frequency Shift

20 dB), thus meaning reduced channel variation. In contrast, a low K-factor equates to high signal variations in the channel, meaning most of the multipath components arrive with the same power at the receiver. In such cases, K-factor can reach values as low as -10.

2.3 Antennas

Antenna properties are quite important in determining the system's performance as the propagation properties in the channel and the achievable cell capacity are ultimately affected by the antenna radiating patterns [18]. Moreover, antenna operating frequency, gain, efficiency and directivity patterns have been proven to influence the electromagnetic properties that govern propagation in the channel to a large degree. Sections below briefly explain how antennas operate and the properties above are explained in more detail.

2.3.1 Antenna Radiation

Antennas are the most essential components for all wireless and radio applications. Depending on their design, antennas as a structure, radiate energy into the free-space due to either time varying current or electric field. The radiated radio wave propagates to the environment in a fashion that is defined by the antenna type. An omnidirectional antenna would radiate in all directions equally, while a directional (or high gain) antenna would focus the beam to a specific direction. In both antenna types, the field produced propagates with a spherical wavefront. As the distance from the antenna (or the array for MIMO deployments) increases the curvature of the propagating sphere decreases.

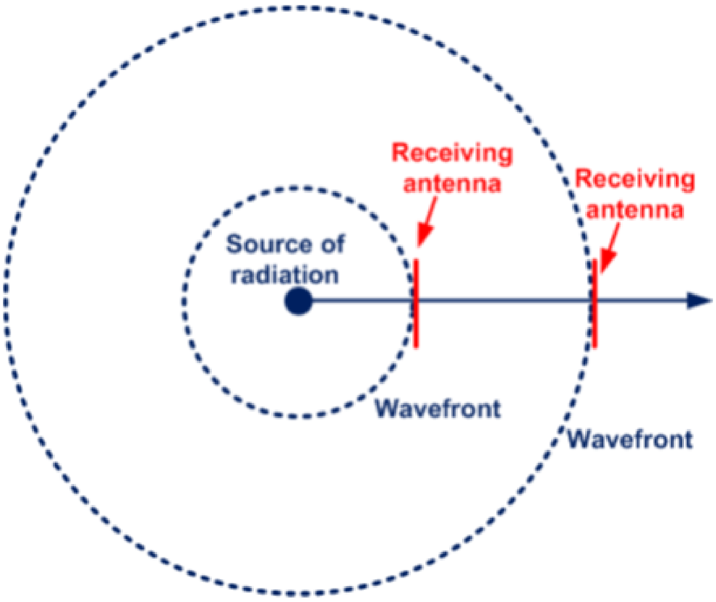

FIGURE 2.5. Near and Far Field Radiation

At some point as the distance from the antenna increases, the curvature of the wavefront will be so low that the propagating wavefront is no longer perceived as spherical at the receiver. At that point, the wavefront can be approximated as planar to allow easier analysis [19]. The distance d from the transmitter that this effect is observed can be calculated by the following equation.

$$d > \frac{2L^2}{\lambda} \tag{2.6}$$

Where L is the physical dimension of the antenna or array and λ is the wavelength.

The region beyond this distance is called far-field while distances between d and the antenna are the near-field regions. One very important feature of the antenna that describes the direction of the field is the polarisation. Moreover polarisation is quite important when evaluating the reflection or a diffraction of a ray and most importantly could greatly affect the system performance. Polarisation could either be linear, circular and elliptic with the first two being special cases of the latter.

However, larger antenna systems will include MSs and scatterers inside the near-field. This will have a large effect in the perceived signal as the wavefront would no longer be planar. To put it simply, the Rayleigh distance Z becomes large as the array aperture d increases, and as a result $d < Z$ or $d \approx Z$. When analysing and modelling massive MIMO the effects of near field propagation must be taken into consideration, i.e. spherical wavefronts over large arrays. In [20] an analysis on the necessity of spherical modelling is presented.

Analytical research on determining the optimal distance (R_g) according to array size within which the channel should be modelled using a spherical wave model. The level of accuracy, separation between the antennas, wavelength, and the orientation of the arrays play an important role in modelling such effects. However, in mmWave MIMO antennas due to the increased packing density, the antenna aperture is considerably smaller hence such effects even though important for sub-6GHz systems will not be considered for mmWave architectures.

The last parameter that is important in terms of radiation is the **polarisation** of a terminal. The polarisation of an antenna specifies the direction of the electric field and can be linear, circular or elliptical. In linear polarisation, the electric field varies along a constant line as the radiowave propagatesand is usually classified as vertical and horizontal, with E^{θ} or E^{ϕ} corresponding to the vertical or the horizontal electric field component. In this work specifically, only linearly polarised antennas are considered.

2.3.2 Directivity and Gain

Directivity is a quite important measure for antennas, especially for emerging mmWave technologies that need to concentrate the antenna signal to a specific direction. Directivity can measure the ratio of signal radiated to a specific direction over the average value to every other possible direction. An example is presented on Figure 2.6, where an isotropic (same intensity of radiation in all directions) and a highly directional antenna are being shown.

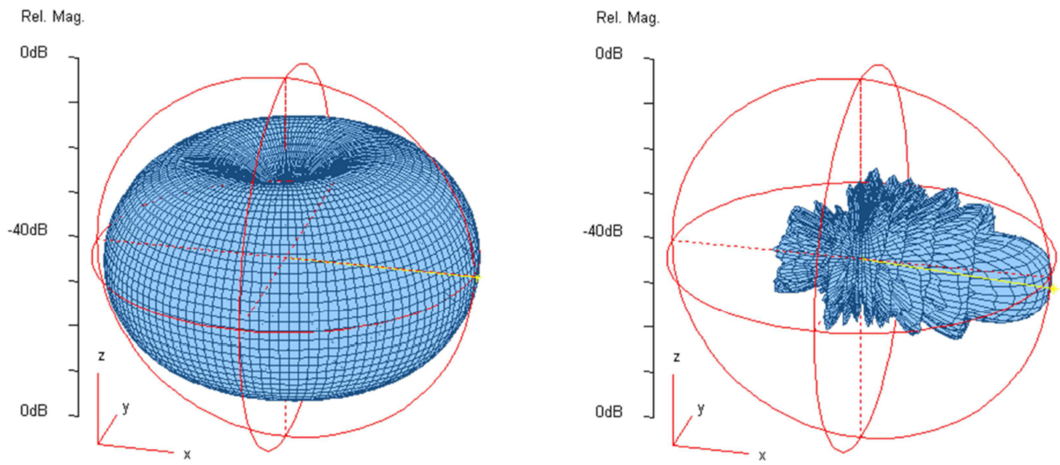

FIGURE 2.6. Directivity And Gain

Directional antennas that mostly use beamforming to focus the beam at specific directions tend to exhibit higher signal density - and thus high directivity - at the desired direction compared to isotropic sources that have a directivity value of 1 everywhere. Directivity is commonly expressed in dBi.

The antenna gain is a key performance measure for antennas that is the product of its directivity and efficiency. It is an important measure as it specifies the efficiency of the antenna to a specific direction. The antenna efficiency is defined as the percentage of the physical aperture area which actually captures radio frequency (RF) energy [19] and hence it's a measure of the amount of the non-radiated energy that is fed to the antenna port. It is important to be noted that directivity and thus antenna gain are frequency and angle dependent.

2.3.3 Antenna Pattern

An antenna or radiation pattern is one of the most basic structures that will be discussed throughout this thesis, as they graphically represent the radiation properties of any antenna or antenna array as a function of space; i.e. they describe how the antenna radiates of receives in space. As gain is not an infinite value, it is clear that antennas radiate energy in all directions in the 3D space up to some extent, thus two principal planes are introduced in order to describe the antenna properties.

Antennas with well-behaved patterns are usually characterised using two principal plane to retain as many information as possible when described. Two terms are normally used for such characterisation; **azimuth** and **elevation**. The azimuth plane pattern is used to refer to the "horizontal", whereas the elevation plane pattern to the "vertical" direction. When an antenna is being discussed, the assumption is that the antenna is mounted (or measured) in the orientation in which it will be used [1]. The coordinate system is shown in Figure 2.7. As presented, the x-y plane (theta = 90 deg) is the azimuth plane, while the orthogonal y-z plane (phi) = 90 deg) is the elevation plane.

The elevation plane pattern is made traversing the entire y-z plane around the antenna under test [1].

The antenna patterns in both of these principal directions are normally plotted using polar coordinates to help with visualisation of the pattern as plotting in such a way explicitly shows the pattern as if the antenna is mounted and radiating. However, in cases where the multiple beams have to be plotted and the power level of each is important, Cartesian coordinates can be used to describe the lobes in either 2D or 3D plots. This important especially when describing codebook patterns or antennas in which side and back lobe parameters are important.

2.3.4 Properties of Antenna Patterns

In every antenna pattern we can observe portions of that pattern that contain large part of the radiation. Those structures are called **lobes** and can be categorised as **main**, **side** or **back** lobes depending on the position compared to the orientation of the antenna that they appear. These areas are labeled in Figure 2.8.

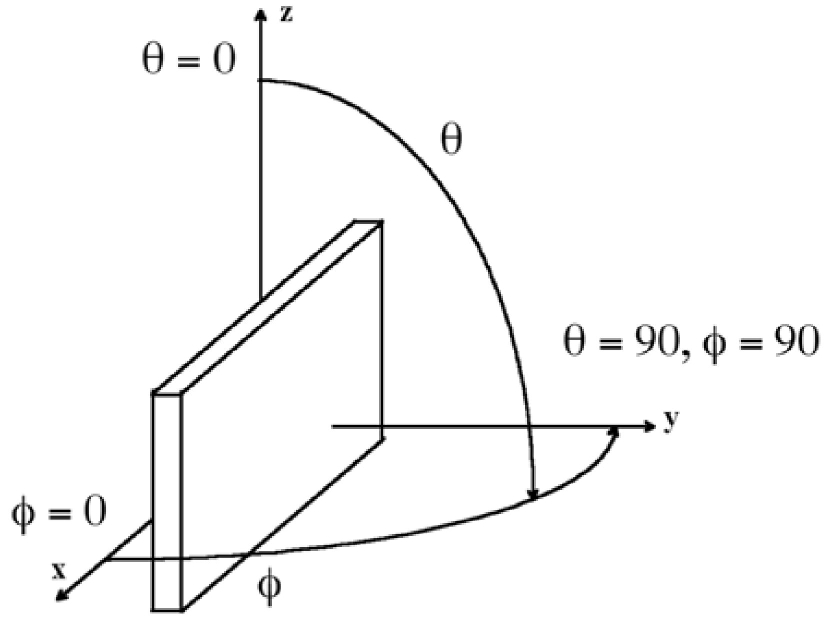

FIGURE 2.7. Antenna Measurement Coordinate System

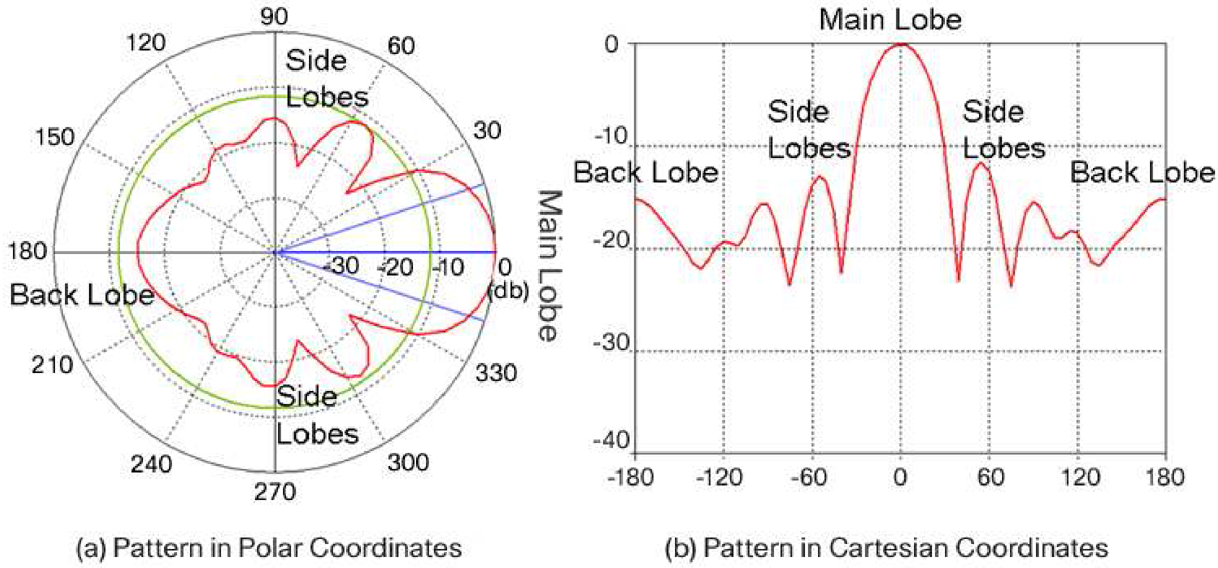

FIGURE 2.8. Radiation Patterns in Polar and Cartesian Coordinates Showing Various Types of Lobes [1]

Lobes are normally surrounded by regions that the radiation is relatively weaker or even close to non-existent. These areas are called **nulls**. Nulls can be present in both the azimuth and elevation plane. This has an effect on the surrounding environment as areas around the antenna with little radiation are formed. These low signal areas should be avoided for transmission and antenna beam vectors should be designed to minimise such effects. A schematic of the coverage gaps due to this antenna property can be seen in Figure 2.9.

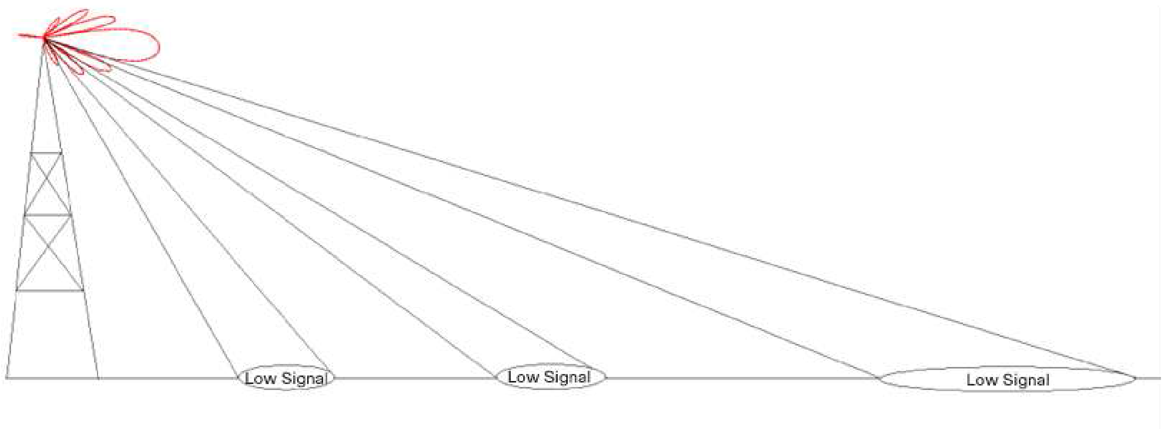

FIGURE 2.9. Coverage Gaps from Elevation Plane Nulls

The 3dB point is a common metric that is used in amplifiers filters and antennas and is typically defined as the point where the power of the beam has dropped by half (i.e. half-power beamwidth). In antennas the **half-power beamwidth (HPBW)** it is a metric of space; i.e. the angle off boresight of which the power of the lobe falls to half of the maximum gain of that same lobe. The HPBW is normally defined for each of the principal planes and highly depends on the element design and properties, or the combination of elements in an antenna array. This is illustrated in Figure 2.8. This metric will be used in this thesis to describe the width the beams that are being discussed along with the corresponding gain as beamwidth is directly linked to antenna gain.

Polarisation is another important mechanism that affects performance in antennas. In the case of linearly polarised antennas specifically we can observe co- and cross-polarisation effects. The power received by an antenna is directly proportional to the cosine of θ ($cos(\theta)$), where θ is the angle between the E-vectors of the received wave and the one of the orientation of the receiving antenna. This shows that θ is dependent on its initial placement and rotation within the environment. Thus we can infer that the maximum received power is when $\theta = 180°$ or else when cross polarisation is equal to 0. Subsequently, minimum power is observed when cross-polarisation reaches its maximum or else when $\theta = 90°$. In circularly polarised antennas, these effects are not observed and thus, the same power is received irrespective of θ.

2.3.5 Phased Antenna Arrays

2.3.5.1 Basic Principles and Possible Arrangements

Phased array antenna architectures were originally developed as more flexible and cost effective solutions for rapidly switching radar architectures in ground-controlled approach systems for aircrafts. In these arrays, every single antenna element (or radiator) is fed with a discrete phase shift compared to the reference element, such that the resulting antenna can be steered in the 3D domain electronically.

Phased antenna arrays are built based on the principles of phase-dependent superposition of adjacent radiating sources. When two or more antenna elements are placed next to each other amplification or attenuation effects are observed if their signals are in or out of phase respectively due to interference. To put it simply, when the same phase shift is used in two or more neighbouring elements, superposition is achieved and the resulting signal is amplified in the main direction and attenuated in the secondary ones.

To control the direction of this amplified beam, a phase-regulating module can be used. This electronic control of the direction of radiation allows steering of the beam to the appropriate directions. There are some limitations, however, to the angles that the beam can be rotated. Extreme tilting in one of the principle directions, can have detrimental effects to the achievable patterns as the antenna aperture is significantly reduced. This leads to an increased number and size of side lobes as well as reduction in the beamwidth of the main lobe. This however has diminishing effects with increased frequency and directivity, as the size of the antenna gets considerably smaller due to higher packing density the higher we move in the spectrum.

To achieve higher directivity, the number of radiators in the array configuration can be increased. One important property is that radiators are not restricted in the type of antenna to be used as an element of the array. Those elements can be combined in an analog way using a single RF chain, or use multiple chains to control each element (digital beamforming). These beamforming methods will be discussed in more detail in chapter 3.

There are some considerable advantages that phased array systems inherently exhibit. With such configurations, we can acheve high antenna gain while reducing the size and width of the side-lobes. Moreover, the much faster switching that can be achieved compared to physical methods, allow the simultaneous generation of multiple beam pattern. In the paragraphs below, examples of widely used array configurations are presented.

The most widely researched and used configuration is a Linear Array or a Uniform Linear Array (ULA). These architectures usually employ a single phase shifter that controls multiple lines of the array to allow rotation of the angle of the radiation pattern. ULAs are the most simple arrangements applied in modern communication systems, but can only achieve beam steering in only one of the principle directions.

Planar Arrays or Uniform Planar Arrays (UPAs) on the other side employ a phase shifter and power control unit per element to control amplitude and phase in the radiator level. The elements are arranged like a matrix, the flat arrangement of all elements forms the entire antenna. This significantly increases the complexity and thus the cost of the system, but enables advanced control over the steering of the beam. With such configurations beam deflection and steering is now possible in both the elevation and azimuth planes. An example planar array architecture is displayed in Figure 2.10

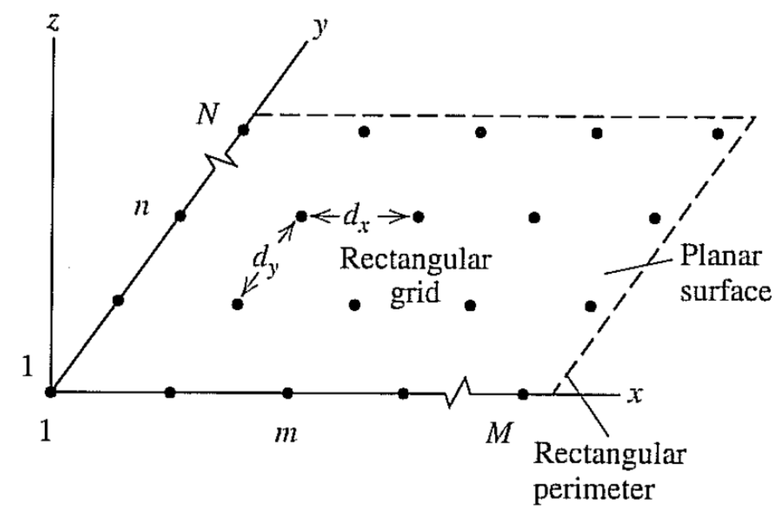

FIGURE 2.10. Planar Array Configuration

Having described the architecture, it is imperative to calculate the phase shift $x = \Delta\phi$ between two adjacent radiators to achieve the desired deflection angle. For this calculation a simplistic linear array of single radiators is considered.

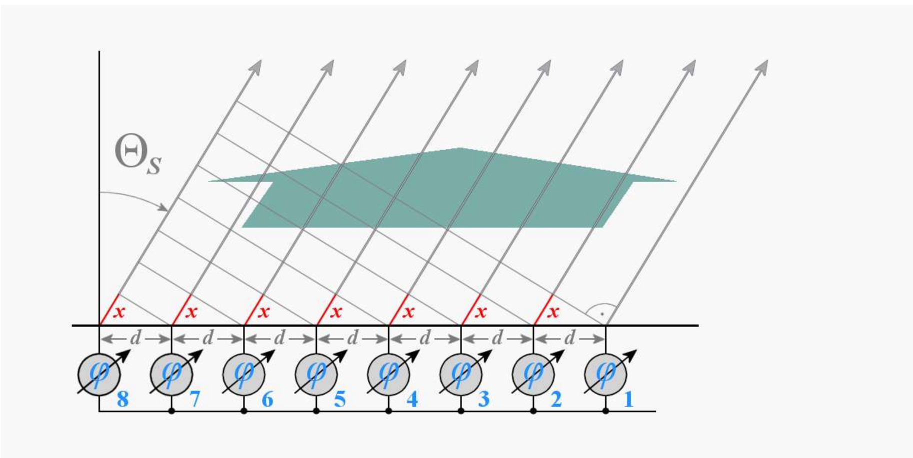

FIGURE 2.11. Graphic Derivation of Phase Shift Formula

A set of right-angled triangles can be defined between two radiators and the auxiliary line perpendicular to the wavefront with the hypotenuse (d) describing the distance between two radiators [21] as seen in Figure 2.11 .

$$x = d \cdot \sin \Theta_S \tag{2.7}$$

If we describe this distance x in terms of the wavelength we get:

$$\frac{360°}{\Delta\varphi} = \frac{\lambda}{x} \tag{2.8}$$

Where $\Delta\varphi$ is the phase shift between two successive elements, d the distance between the radiating elements and Θ_S the beam steering angle Applying both equations together we get the complete solution:

$$\Delta\varphi = \frac{360° \cdot d \cdot \sin \Theta_S}{\lambda} \tag{2.9}$$

2.4 Approaches to Propagation Modelling

2.4.1 Wireless Channel Modelling

Wireless environment modelling is an old but definitely a not outdated establishment. Nowadays, an all the more increasing need for wireless services, triggered by both the growth in the connected devices numbers and ever-increasing data traffic applications and services. This explosive growth of traffic will result in an analogous increase in the future systems challenges that appear to be far beyond even from what the International Telecommunication Union (ITU) initially established. With all this growing demand for access to the wireless medium that was described above, wireless models for the data exchange in time variant networks become more and more interesting. To describe and thus assess the mobile radio channels in such networks, a number of different channel prediction models have to be used.

Channel models are thus crucial and indispensable tools in the design and optimisation of communication systems. Stochastic channel models (SCMs) are currently widely deployed due to their intrinsic low complexity. Even though SCMs only require low computational resources, only a part of the channel features is retained, a high variability between results is observed and the analysis in a 3D domain is quite restricted.

Deterministic techniques such as ray-tracing based radio wave propagation prediction models manage to reduce this variability and include a greater amount of the channel features with only a slight increase in the computational load. Ray-tracing as a method is considerably flexible due to its ability to model both indoor and outdoor scenarios.

For outdoor networks, the CSN's ProPhecy ray-tracing tool represents a benchmark in urban and rural propagation modelling. ProPhecy allows antennas and RF propagation to be studied cost effectively and in tremendous detail in all types of 3D virtual environments. The tool uses a unique Radar Cross Section (RCS) algorithm that was developed in-house over a 15-year period [22–30].

Ray tracer capabilities, however, are not quite in line with the needs of future systems as modelling for higher frequencies or large antenna arrays is quite limited. Several physical propagation effects or geographical environment aspects are omitted or not captured by current ray tracing techniques. The use of those tools need to be extended to accommodate a number of challenges endemic to 5G and beyond technologies.

All the physical propagation mechanisms and antenna patterns previously presented provide crucial information about how the network can be planned. In order to acquire or predict the channel characteristics (e.g. received power, AoA, time dispersion) channel models are used. Channel modelling has always been an indispensable tool in the design and optimisation of communication systems by supporting multiple network styles.

Channel models need two main elements in order to be formulated; the antenna and the propagation model. The physical propagation model can be defined following a number of models that are either deterministic (e.g. ray tracing), stochastic (either geometric or non-geometric) or even analytical (e.g. the Okumura-Hata model). The two models are then combined in order to devise the complete MIMO channel matrix that would be ready to be fed in system-level simulators by using either a ray-based double-directional or a correlation-based method. Figure 2.12 demonstrates this progress.

The following sections would mainly concentrate in physical radiowave propagation models and the reasoning behind using a ray tracing model will be presented at the end of the chapter.

Propagation models can further be classified on the basis of the underlying modelling technique adopted. Under this approach, models can be classified as empirical, deterministic (or physical), semi-deterministic and theoretical.

2.4.1.1 Empirical

Empirical, or otherwise known as analytical models are simply a set of site specific measurement based models that are used to provide a set of equations. This set is based on measurements that ultimately relate the received signal strength, height of the transmitter and receiver, frequency and most importantly, distance and separation between the receiving terminal and the basestation (BS).

To acquire those parameters however, it is essential that detailed measurement equipment is used and in addition multiple time consuming experiments be performed. The results from those signal strength measurements are then statistically fitted into the equations described above. In those models, there is no mention of electromagnetic propagation aspect or any interaction

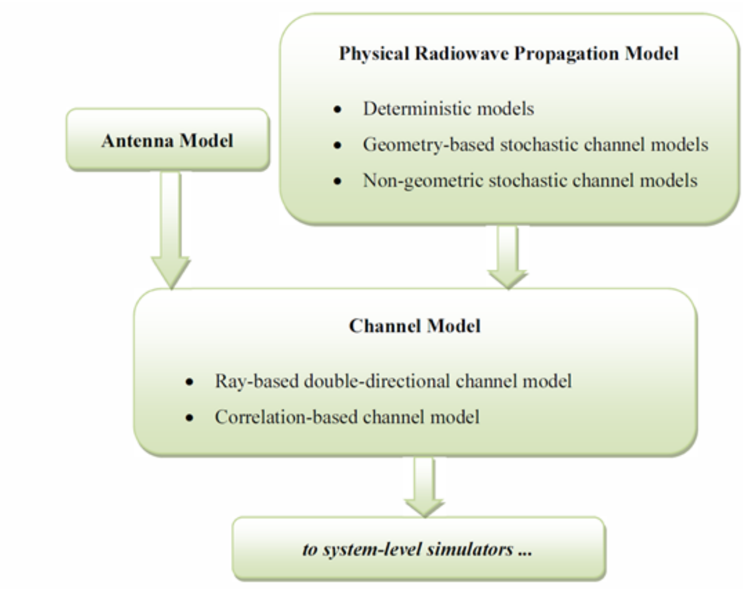

FIGURE 2.12. Schematic representation of modelling the wireless radio channel

with the physical environment described in the model; only signal strength values. Thus they are simply described as narrowband models.

The most significant limitation of these types of models is that they are completely site specific and cannot be translated in any other environment. Measurements are completely dependent on the original environment and as no other information is given in the model such models fail to even predict time, angular spread or even frequency. Examples of empirical models include the FCC, the CCIR model and the previously mentioned Okumura-Hata model.

2.4.1.2 Deterministic

Deterministic models may be characterised as the complete opposite of non-geometric stochastic models. Such models are completely based on the physical laws that dominate the interaction of waves and their surrounding environment. To put it simply, geometrical optics and electromagnetic laws derived directly from Maxwell equations are used to describe the propagation of electromagnetic waves in any type of environment. Thus, as physical laws remain constant and the environment does not change, the variation of replicate measurements of the propagation parameters would be zero.

Deterministic models can be categorised in three main categories either according to the resolvable dimensions (2D or 3D), or according to bandwidth applications (narrowband or wideband) or depending on the size of the cell to be studied.

To follow the deterministic approach for modelling, there is a need of a detailed database that would be used to digitally recreate the propagation environment using simple approximations and detail relative to the scale of the model is to be used. However, the multiple databases needed to construct the model could mean a huge need of a large amount of computational resources if all of the environment resources were to be modelled in detail. Thus, simple approximations (e.g. rasterization techniques or approximation of hills or buildings by simple shapes) are sometimes being considered in the models to reduce computational time and requirements [22]. One further negative aspect of such models is the need for a constant update of those databases as in modern age our surroundings continuously change in a rapid fashion.

2.4.1.3 Semi-Deterministic

Stochastic channel models (SCM) provide another way to model the propagation environment while retaining the physical propagation characteristics. SCMs are crucial and indispensable tools in the design and optimisation of communication systems and are currently widely deployed due to their intrinsic low complexity. SCMs and generally physical models are for those reasons more fitting to simulate real life physical environments, thus the most recent channel models developed for ad-hoc networks being mostly such models. Compared to empirical models that are completely site specific, stochastic models are universal as in such models the ray scatterers are being placed between the transmitter and receiver in either a completely stochastic way (non-geometric) or by using some simple geometric considerations.

Geometric stochastic channel modelling (GSCM) is the most widely deployed technique in terms of stochastic modelling. The geometry based approach is able to easily capture the essential characteristics of the propagation channel and can then be applied to a diverse amount of different propagation scenarios by using arbitrary geometries. There are multiple standardised GSCMs such as the TGn channel models , the 3GPP Spatial Channel Model (SCM) and SCM-Extended (SCME), the 802.16m channel model, and the WINNER I, WINNER II and WINNER+ each of which can be found in more depth in [31–36] respectively. The most significant disadvantage with GSCMs is the non-existent - or in the best case - limited detail in modelling elevation. With analysis being detailed only in the azimuth plane those models lack accuracy, thus making them unfit for detailed environment analysis if the intrinsic high variability of the model is taken into consideration as well.

GSCMs formulate the propagation scenario in a statistical way according to some initial deterministic information about the geometry of the environment. Most of the models in this category contain a number of different scenarios that is used to describe the best fit in each specific experimental case. An example of this would be the WINNER II model which includes a database of 18 propagation environments. Moreover, the WINNER model (as most of the above mentioned standardised GSCM) use a multipath clustering technique to group rays with similar propagation properties. Figure 2.13 shows the cluster grouping of multiple MPCs for the COST 2100 MIMO channel model [37].

As mentioned previously, GSCM contain both a deterministic and a stochastic process in

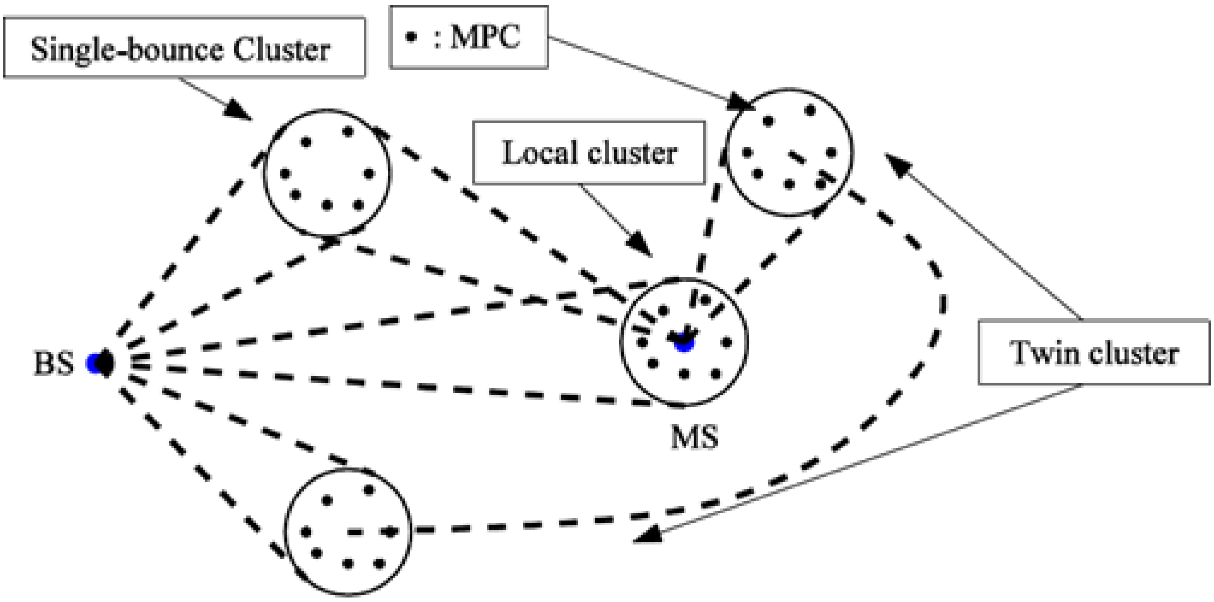

FIGURE 2.13. Clustered channel model topology

modelling the system. The propagation environment choice and the following clustering comprise the deterministic part of the process while the stochastic randomness is introduced by choosing the propagation parameters as correlated variables from probability density functions (PDFs). The most important function of GSCMs is that they follow a double-directional channel modelling procedure. According to this technique the antennas and the physical environment are separated and thus each antenna location, radiation pattern and orientation is able to be chosen independently.

The **non-geometric** approach in stochastic channel modelling can be related to the geometric approach but instead it removes the deterministic nature contained in the choice of the propagation scenario completely. Clustering techniques are still used to group rays and ease the analysis of the various multipath components. Poisson processes with a fixed rates of Λ and λ are used to model the cluster and ray arrival times respectively. The most important model in this category is the Saleh-Valenzuela model which can be seen in more detail in [38].

2.4.1.4 Theoretical

Theoretical models are based purely on theoretical assumptions about propagation in the radio environment but without using any specific physical information about the environment. They are not applicable to any real propagation environment and are aimed mainly at allowing theoretical studies of the radio channel. Examples of theoretical models include the models by Bello ([33]), Clarke ([34]), and Ossana ([35]) amongst others. Such models have enabled channel behaviour (such as envelope fading statistics) to be studied and statistical distributions of signal envelope, arrival angles and phase variation to be developed. Because they cannot be applied to any realistic environments, such models are not used in network planning.

2.5 Channel Models for mmWave Communications with Focus in non-Static Environments and State of the Art

Since the early 1990's there has been an increased interest about how electromagnetic waves propagate above 6 GHz frequencies due to at higher frequencies there is more spectrum available that could be exploited. Many measurement campaigns have been performed especially in the K-band (18 -27 GHz), Ka-band (27 - 40 GHz), and V-band (40 -75 GHz). It is of great interest that there exist a band for global harmonisation, and EU and UK are actively promoting to establish the "pioneer" band (26 GHz: 24.25 - 27.5 GHz) as the priority millimeter wave band [39]. On the other hand USA has enabled licenses for 28 GHz and 38 GHz to aid development and deployment of 5G technologies as stated by the Federal Communications Commission [40]. Moreover, Japan is considering the adoption of similar frequencies as USA, and China coincides with EU [41].

This section presents a literature survey of published channel models and summarise the main characteristics of the channel especially at 28 GHz, based on recent studies and reports published by major standard bodies such as 3rd Generation Partnership Project (3GPP), 5G Public-Private Partnership (5GPPP), as well as the University of New York (NYU), METIS 2020, and software implementations such as MiWEBA, and QuaDRIga.

It is important to properly understand the behavior of the channel in order to develop accurate models that can emulate the dynamics of the wireless channel at high frequencies to test the performance of upcoming mmWave wireless devices whose design will have to shift from an omnidirectional operation to spatial focusing which will be characterised for having high-gain, highly directional antenna arrays, capable of electronically steer the beam with specific algorithms to acquire and track the signal to guaranty a reliable communication. To establish a communication link between transmitter and receiver the steerable antennas must point along the LOS path or a strong reflected path.

A brief description of each channel model is given and Large-Scale Parameters (LSP) such as path loss, delay spread, number of clusters, angles of departure and arrival among others will be described for each model. Target frequency focused is 28 GHz. Common propagation scenarios described in literature are Rural Macrocell (RMa); Urban Macro-cellular (UMa), Urban Micro-cellular (UMi), Indoor, and Outdoor to Indoor (O2I) environments, being these of higher priority, and scenarios such as device to device (D2D), vehicle to vehicle (V2V) among others are also being researched.

An UMi scenario is considered an open area in the order of 50 to 100 meters, where a transmitter is placed between 3 to 20 m height and the receiver may vary between 1.5 to 2.5 m in height. The expected distance between cells are between 100 to 200 meters. In an UMa scenario the base stations (BS) are mounted at 25 to 35 m and the expected coverage area is between 200 and 500 meters. Mobility in the horizontal plane is 3km/h for all scenarios [42, 43].

2.5.1 Channel Models Overview

2.5.1.1 3GPP TR 38.901

The technical report 38.901 published by the 3GPP covers the modelling of the physical layer of both the user terminal (UT) and access network of 3GPP systems, and captures the channel models for frequencies from 0.5 GHz up to 100 GHz. It is based on the 3D SCM for LTE model (3GPP TR 36.873). Supported scenarios are UMi street canyon, UMa, Indoor and RMa. The maximum bandwidth supported is up to 10% of the center frequency but no larger than 2GHz [42].

2.5.1.2 mmMagic

5GPP has recently released the "Measurement Result and Final mmMAGIC Channel Models", after conducting extensive multi-frequency channel measurements and simulations campaigns, covering various 5G propagation scenarios, some of them were contributions to the models being developed by 3GPP and ITU and QuaDRIga. The channel model is a Geometry Based Stochastic Model (GSCM) whose base line is the latest 3GPP channel model with additional features which covers a frequency range from 6 to 100 GHz and it is focused on the modelling of frequency-dependent large scale parameters, ground reflection effects, cluster and sub-paths, small-scale fading, blockage, building penetration among others extensively detailed in [44].

2.5.1.3 NYU Wireless

The University of New York NYU has developed a statistical spatial channel model (SSCM) developed using time clusters (TC) and spatial lobes (SL) to generate multipath parameters for omnidirectional and directional channel impulse responses (CIR) and their corresponding power angle spectra (PAS) based on real measurements at multiple frequencies from 28 to 73 GHz. Supported scenarios are UMi, Uma, and RMa, and these are applicable for a wide range of frequencies from 0.5 to 100 GHz [45]. With the data collected from the measurement campaigns they were able to develop a statistical channel model fully detailed in [46].

2.5.1.4 METIS

METIS (Mobile and wireless communications Enablers for the Twenty-twenty Information Society) consists of three channel models, map-based (ray tracing), stochastic, and a hybrid model. The models were derived from measurements and simulations. Supported frequencies in the models are from 0.45 GHZ to 70 GHz. The stochastic model is specified in separated frequency bands. The supported bandwidth for the stochastic model for frequencies below 6GHz is up to 100

MHz and 1GHz specifically for 60 GHz, and 10% of the center frequency for the map-based model. Depending on the model used certain propagation scenarios are supported. The map-based model is suitable for evaluating massive MIMO/ advances beamforming and for pathloss modelling for D2D and V2V. The stochastic model is a geometry based stochastic channel model (GSCM) further development from WINNER/3GPPP that provides multi-dimensional shadowing maps, millimetre-wave parameters, direct sampling of the power angular spectrum (PAS) and frequency dependent pathloss. The channel models are antenna independent. The particularity of this channel model is that instead of proposing a unique value for each parameter, it is proposed a range from a minimum and maximum values [47].

2.5.1.5 MiWEBA

Millimeter-Wave Evolution for Backhaul and Access (MiWEBA) project developed a quasi-deterministic (Q-D) channel model, which combines a geometry-based approach for a limited number of multipath components and a stochastic approach. The scenarios considered in the channel model are classified in access (open area, street canyon and Indoor), backhaul/front haul (above roof top, street canyon), and D2D (open area, street canyon and Indoor), among others. It is stated that mmWave channel impulse response (CIR) is comprised of a few Q-D strong rays (D-rays), a number of relatively weak random rays (R-rays), and flashing rays (F-rays). The model is limited for 60 GHz [48].

2.5.1.6 QuaDRIga

Quasi deterministic radio channel generator (QuaDRIGa) channel model is based from the Wireless World Initiative for New Radio (WINNER+) channel model and the 3GPP-3D channel model. It is a geometry-based stochastic channel modelling. The channel parameters are determined stochastically, based on statistical distributions obtained from measurements. The frequency range supported is from 2 to 6 GHz, with a maximum bandwidth of 100 MHz. In Quadriga each scattering cluster is approximated by 20 individual scatters. Depending on the angular spread and amount of diffuse scattering the typical number of clusters for LOS scenarios are around 10 and for NLOS are around 20.

2.5.2 Path loss (PL) Modelling

Data shown in this section have been extracted directly from the publicly available literature and the main comparison was done for 28 GHz frequency, Urban Microcell (UMi) environment in LOS and NLOS scenarios, where it was possible to observe that some parameters are similar among some models and others have large differences. In all channel models, it has been pointed out that simulations and measurements agree with each other, which helped them validate their data, but is clear that certain assumptions where considered and some unique definitions were done, therefore results between models may be different.

Among all different channel models found in literature mainly three path loss models are considered. 3GPP models and the ones based on it use the Alpha-Beta-Gamma (ABG) model with an additional dependency on base station and terminal heights, and with a Line of Sight (LOS) breakpoint, whereas the University of New York has considered the Close-In (CI) free space reference distance PL model with a 1 m reference distance and an extra attenuation term to account on atmospheric conditions, and the Close-In free space reference distance model with frequency-dependent path loss exponent (CIF) [43, 45]. For UMi scenarios it has been found out that the path loss in line of sight conditions follow Friss's free space path loss model very closely. Shadow fading seems to be similar to sub 6 GHz frequencies [44].

The CI model is given by

$$PL^{CI}(f,d)[dB] = FSPL(f,1m)[dB] + 10n\log_{10}(d) + AT[dB] + X_{\sigma}^{CI} \tag{2.10}$$

Where d is the 3D distance between transmitter (Tx) and receiver (Rx) and n is the path loss exponent (PLE), AT is the attenuation term induced by atmosphere, $FSPL$ denotes the free space path loss and X_{σ}^{CI} is a zero-mean Gaussian random variable with standard σ deviation in dB. The ABG model is given by

$$PL^{ABG}(f,d)[dB] = 10\alpha\log_{10}(d) + \beta + 10\gamma\log_{10}(f) + X_{\sigma}^{ABG} \tag{2.11}$$

where α captures how the PL increase as the T-R in distance (m) increases, β is a floating offset value in dB, γ captures the PL variation over the frequency f in GHz, and X_{σ}^{ABG} is the Shadow Fading (SF) deviation term in dB.

The CIF model is an extension of the CI model, and uses a frequency-dependent path loss exponent given by:

$$PL^{CIF}(f,d)[dB] = FSPL(f,1m) + 10n\left(1 + b\left(\frac{f-f_0}{f_0}\right)\right)\log_{10}\left(\frac{d}{1m}\right) + X_{\sigma}^{CIF} \tag{2.12}$$

where n is the PLE, b is an optimization parameter that captures the slope, or linear frequency dependency of the path loss exponent that balances at the centroid of the frequencies being modelled, f_o is a fixed reference frequency, the centroid of all frequencies represented by the path loss model [43].

A comparison of PL in these models is plotted in Figure 2.14.

2.5.3 Channel parameters

Large-scale parameters (LSP) are a collection of parameters that in an outdoor environment are supposed to be constant over a large area (area of several wavelengths)[49]. LSP denote

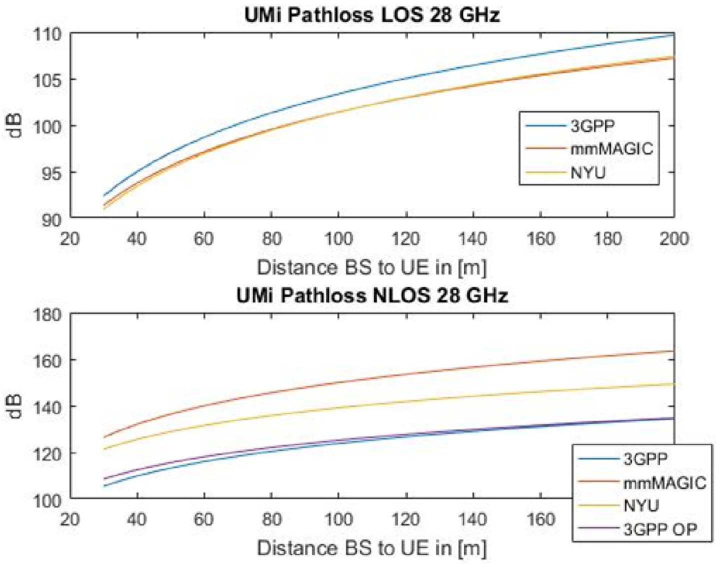

FIGURE 2.14. Comparison of Path Loss in models

the omini-directional RMS Delay Spread (DS), the azimuth spread (AS), the shadow fading, and K-factor for LOS scenarios, which exhibit significant correlation for a given transmitter to receiver link [50].

Each channel model has a different approach of how the multipaths are distributed and grouped depending on the scenarios. A cluster is usually defined as a group of multipaths or rays closely spaced to each other in the time and angular domains due to structure of the reflecting surfaces [48]. 3GPP channel model's cluster distribution for scenarios of UMi is summarized in Table 2.1

TABLE 2.1. Summary of number of clusters and its distribution for UMi and Indoor scenarios

3GPP	UMi LOS	UMi NLOS
Number of Clusters N	12	19
Number of rays per cluster M	20	20
Cluster DS [ns]	5	11
Cluster ASD [deg]	3	10
Cluster ASA [deg]	17	22
Cluster ZSA [deg]	7	7
Per cluster SF std [dB]	3	3

Within the mmMAGIC model, to determine the number of clusters, ray tracing and measurements were used. To group the subpaths in clusters a Kmeans++ algorithm [51] is used and the Euclidean distance is used as metric, which takes into account the delays, powers and angles of arrival (AoA), therefore it mostly considers the clustering from the UE's perspective [52]. The cluster's distribution parameters are summarized in Table 2.2.

TABLE 2.2. Summary of LSP parameters from mmMAGIC Channel model

mmMAGIC	UMi LOS	UMi NLOS
Number of Clusters N	2	3
Number of rays per cluster M	20	26
Cluster DS [ns]	16	23.5
Cluster ASD [deg]	3	10
Cluster ASA [deg]	15	22.1
Cluster ZSA [deg]	7.1	5.4
Per cluster SF std [dB]	6.67	3

2.6 Conclusions

Propagation modelling for any telecommunications system requires a detailed characterisation of the key properties of the environment along with the relevant antenna characteristics. Obstructions as well as the dynamic nature of the propagating environment lead to sometimes significant fluctuations in ray and channel parameters, thus dictating the need for accurate channel models. This becomes increasingly important in mmWave systems where the variability of the system greatly increases even with minor spatial or temporal disturbances.

This chapter presents an overview of the basic concepts of wireless channel modelling. Wireless propagation and antenna design concepts were described as the foundations that underpin every modern channel model. Wireless channel characteristics such as path loss, fading and multipath propagation effects that cause dispersion on the channel were presented. Following this, antenna far-field radiation pattern and polarisation, directivity, efficiency, antenna patterns and gain, as well as phased antenna array configurations were described and discussed in detail in this chapter. The effects of antenna polarisation are also briefly explored within the context of throughput performance.

Multiple approaches are being used to characterise the channel including measurements, modelling as well as hybrid/combinatorial methods. An accurate channel model would help in the design, behaviour characterisation and performance optimisation of the constituents of a communication system. Deterministic and GSCMs are two of the most employed methods used to define the channel characteristics. Stochastic channel models are currently widely deployed due to their intrinsic low complexity. However, even though SCMs only require a low computational expense, only a part of the channel features is retained, a high variability between results is observed and the analysis in a 3D domain is quite restricted. Stochastic channel models have been extensively studied by groups such as 3GPP, mmMAGIC, NYU and METIS and provide a relatively accurate representation of the mmWave channels.

Ray-tracing based (i.e. deterministic) radio wave propagation prediction models manage to reduce this variability and include a greater amount of the channel features with only a slight increase in the computational load. Moreover, the accuracy of deterministic models is much higher when compared to stochastic models as the physical characteristics are all retained. As mentioned, this work is based in ray-tracing based modelling. The specific models used to describe the interactions within the channel are presented in the following chapter

CHAPTER 3

EXPERIMENTAL METHODS AND ASSUMPTIONS

Beamforming (BF) techniques constitute one of the most important factors to investigate when considering mmWave vehicular communications as they enhance throughput, increase spatial reuse, mitigate interference and most importantly increase the coverage range. This is important specifically in vehicular networks as it reduces infrastructure costs, meaning sparser and more efficient placement of AP throughout the environment.

Modelling techniques in mmWave communications need to accurately describe the channel while considering trade-offs regarding the accuracy and simulation speed of the model. Increased resolution of the environment characteristics along with low simulation times will allow BF schemes to be analysed in detail before field tests and deployments.

3.1 Introduction

Adaptive BF techniques have been under long-term development in order to provide enhanced communication quality. Regarding mmWave BF, several works focus on BF based on estimated channel state information (CSI) [53], i.e. finding the optimal weight vector for both the transmitter and receiver. However, some trade-offs, such as beamwidth and beamforming gain, have to be considered. By increasing the directivity of the beam (i.e. making it narrower), we effectively see an increase in the transmit gain and thus in range and transmission rate.

As presented in Chapter 2, channel models need two main elements in order to be formulated; the antenna and the propagation model. Ray-tracing allows antennas and RF propagation to be studied cost effectively and in detail in all types of 3D virtual environments. ProPhecy ray-tracing tool allows both urban and rural propagation modelling by employing a Radar Cross Section (RCS) algorithm that was developed in-house over a 15-year period. Within this framework, traditional

Single Input Single Output (SISO) or MIMO antenna systems can be located anywhere in the virtual world [22]. Apart from ProPhecy, multiple well documented and validated ray tracers (RTs) were identified in literature such as:

- Karlsruhe University RT - Raster-based, semi-stochastic for mobility
- Brunswick University RT - Vector and raster-based modelling, no mobility functions)
- Aalto University RT - Indoor ray tracing tool
- UC Louvaine RT - Outdoor vector-based tool but not fine-tuned for 5G and beyond technologies
- Nanjing University RT - Ray studies up to 28GHz channels
- Samsung RT
- 3DScat (University of Bologna)

Apart from the availability of the source code and the in-house design/validation, ProPhecy was picked out of these academic/commercial products due to the capability to study both raster and vector-based environments in multiple available real-life locations. Moreover, the ability to selectively study environments by using digitally rendered 3D architectures and the modularity of the ray tracing and simulation solutions allow us to fine-tune the parameters of the experiment, while performing less computationally expensive operations.

The aim of this chapter is to introduce the building blocks and the underlying technologies that were used throughout this work to model the physical characteristics of the channel and describe its performance. Understanding the reasoning and methodology behind the work is imperative as it demystifies the process and accounts for the decisions taken and the process that was followed. Specifically, in this chapter each part of our model, from generating the antenna and using ray-tracing to characterise the environment, to the formulation of codebooks and application of beamforming is presented.

In general, our modelling process follows these steps:

- Initially the propagating environment is specified in the form of raster or vector databases.
- The propagation mechanisms that define the behaviour of the multipath components throughout this environment are specified and defined in the ray tracer.
- Measurement of a single antenna element that will be used as the basis for our antenna array is provided.
- Generation of the planar array is achieved by superposition of multiple elements in defined spacing.

- Application of 802.15.3c codebooks using phase shifts and rotation matrices to rotate the synthesized beam in the desired locations. The proposed codebook is a result of an angular, and temporal analysis of the environment surrounding the target antenna in each general use scenario.

- System-level simulations using a Physical Abstraction Method to achieve SNR, spread and throughput metrics of the channel.

- Generated data are then used for relevant case studies, to compare performance of different schemes.

This process is illustrated in Figure 3.1. All the assumptions and available models at each stage are compared and discussed in detail in terms of mmWave-specific parameters and the most appropriate ones are in terms of vehicular analysis are presented in the following sections.

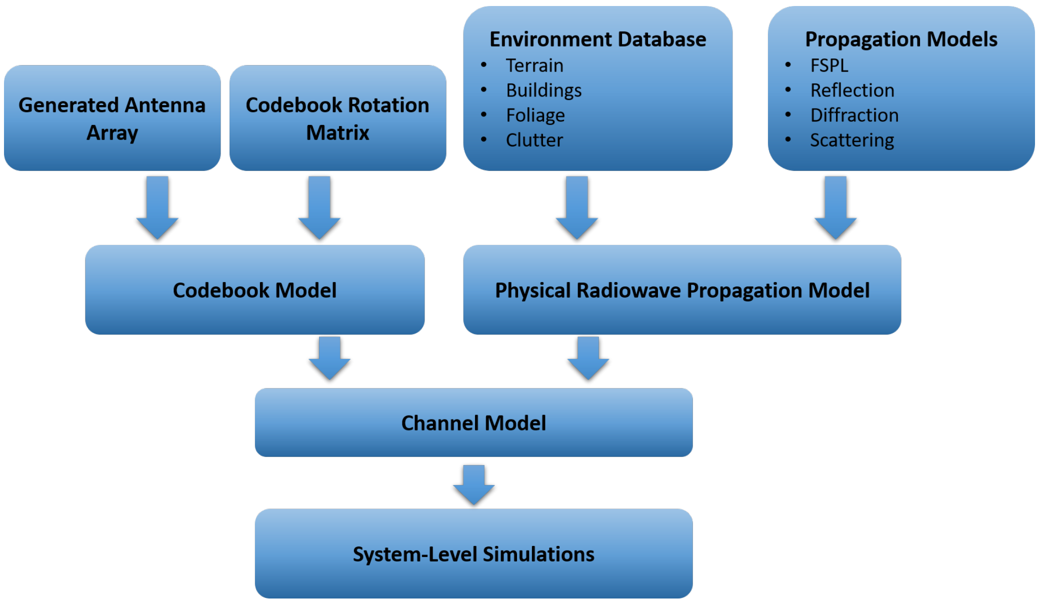

FIGURE 3.1. Schematic representation of the modelling process

The rest of the chapter is organised as follows. Section 3.2 will introduce the the ray tracer and the formulation of the environment as seen by the eyes of ray-tracing. Updates proposed for the ray-tracer that were introduced throughout this PhD are discussed as well. Following this the propagation mechanisms as well as relevant models for each are shown and discussed in detail considering mmWave vehicular infrastructure. The properties of antennas in relation to their design and propagation environment are presented in Section 3.3. Measurement, rotation techniques and codebook beam generation is presented as well. Section 3.4 introduces the physical layer abstraction simulator that will be used throughout the later stages of the analysis. Finally, section 3.5 introduces beamforming as defined in the antenna and discusses beamforming techniques as employed by the 802.11ad and 802.15.3c standards. Section 3.6 concludes the chapter.

3.2 3D Ray-Tracing Model

3.2.1 Database Formulation

In order to run a simulation, a 'field' (a landscape and its buildings if any) must be fully described. Typically this 'field' is described by data in text files, and the user must inform the simulator about the location of these files and their format.

The digital recreation of the propagation environment using simple approximations is a really important aspect of deterministic channel modelling as formerly discussed. In the ProPhecy ray tracer, a number of databases as parts of the complete 'field' are defined and described as per the sections below.

3.2.1.1 Terrain Database

The **terrain database** included in ProPhecy is formed by making simple geometric approximations using continuously updated LiDAR data. A simple rasterization technique with different resolutions for urban (1m, 2m, 5m, 10m) and rural (50m) areas is used to form the digital terrain map as in more dense areas physical features of the environment change at much smaller spatial intervals. To form the model for those series of plane scattering pixels or surfaces, the characterisation algorithm identifies the position of the 4 border and the centre pixel in 3D space. Hence the raw terrain characteristics are mostly retained. This technique is explained in more detail in [22, 23, 25].

3.2.1.2 Building Database

The rasterization concept described above is also translated into forming the **building database**. The building area is divided into cells in the desired resolution and the building turns into a vector representation. The different vectors that represent each boundary of a building are then grouped together to form a polygon and for every raster square a coverage check is performed. If the amount of the cell that is covered by the polygon exceeds 50% then the whole cell assumes the role of a building and thus inherits the characteristics of the specific building (e.g. height).

Clearly, there is an accuracy loss by using the rasterization process which essentially depends on the resolution used during the building area division to cells. Furthermore, there is the possibility that some buildings with ubiquitous structures to be totally missed or blockage to be created due to low resolution during this process. In ProPhecy, the resolution that is being used for the raster database is the same as the terrain database;i.e. 1m to 10m.

There is an obvious trade-off between raster model accuracy and computational time of a ray-tracing experiment. As expected, the execution times decrease (almost exponentially) as the terrain resolution is reduced. The prediction with the combination of the three terrain resolutions gives the second lowest computation time but does not differ appreciably from the prediction with 50m terrain resolution [25]. Considering mmWave research, any database with resolution less than 10m reduces the accuracy of the model considerably and should not be used.

3.2.1.3 Foliage Database

Another database that is featured in the ProPhecy tool is a foliage database that gives the approximate size and shape of the vegetation in the raster cell. This however is only an approximation as vegetation tends to change at a quite rapid rate. The outlines of the canopy shape are used to form a 2D vector defined polygon associated with a specific height, while the vegetation is modelled as a 3D estimate of its outline. The attenuation of those elements however is not deterministic. The best way to model foliage are empirical models and especially the ITU-Recommendation which gives the signal attenuation at millimetric and microwave frequencies [23]. ITU-R models signal attenuation as a function of propagation depth and wavelength [25]. The equation below describes the loss in the empirical model

$$Loss = (0.2f)^{0.3} * d^{0.6} dB \tag{3.1}$$

where f and d are respectively the frequency (in MHz) and the distance (in meters) travelled within the foliage.

3.2.1.4 Clutter Database

Apart from the geometry of the building or the terrain, two other important features that signal scattering depends on are the electrical and physical properties of the reflector/scatterer. Thus there is a need to distinguish between many different scenarios that could severely affect propagation. Currently the model covers 10 different clutter classes that use the same raster model on the respective terrain resolution. The classes are listed below:

- Dry Ground
- Farmland
- Field/Grassland
- Bush/Heath
- Dense Forest
- Fresh Water

- Sea Water
- Concrete Pavement
- Buildings up to 6m high
- Buildings over 6m high

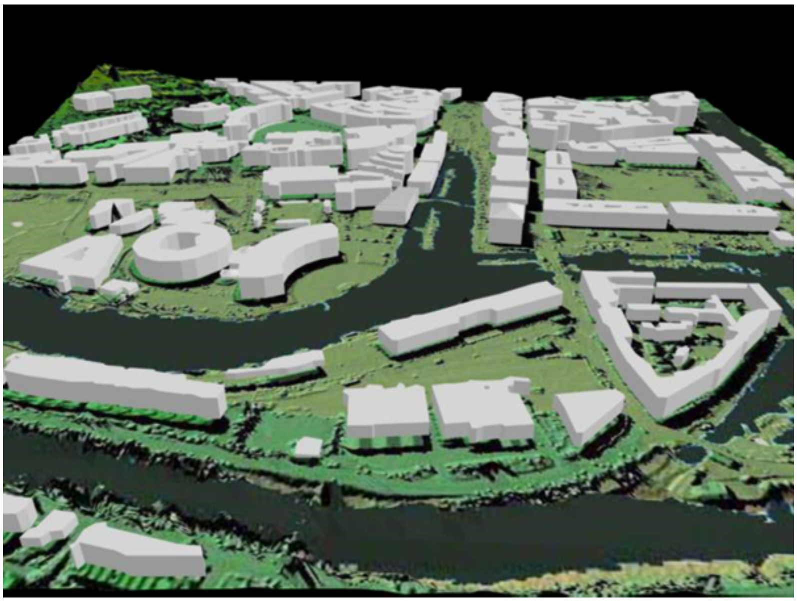

FIGURE 3.2. Digital 3D representation of Bristol's harbourside area

3.2.2 The Vector Ray-Tracing Solution

The need for update in the database is imperative in a constantly changing environment. When the physical characteristics of the propagating environment change, e.g. a new or destroyed building or a block or in higher frequencies, even urban clutter could totally change the propagating multipaths. Advancements however in air photography detail and machine learning techniques, could reduce to this a pretty trivial process.

A repeating discussion throughout this document is database resolution. Resolution plays a really important role in the accuracy of the produced channel model.

This section is about the feasibility and the practicalities of extending the ray tracing tool to be capable of performing operations in environments consisting of significantly more general meshes. At the time of writing the raytracing engine evaluates point-to-point (transmitter/receiver antenna pair) electromagnetic and raytracing problems in urban settings using either:

1. a raster-type model of terrain and buildings (supplemented by a raster-type model of foliage/vegetation), or

2. a quad-subdivision field model, providing variable-resolution pseudo-raster type representations of buildings

The above raster-type models are limited in that they tightly constrain the allowable geometries of terrain and buildings. In both of the above cases buildings are cuboidal structures whose walls are aligned to the principal compass directions north/south/east/west (a discrete set of possible directions).

A number of ray tracing tools avoid using rasterization processes and instead form the model by using the high resolution vector-type data. Vector modelling approaches increase accuracy but at the same time significantly increase the amount of data and thus the computational expense of the model. For microcells and generally medium-size areas (in the order of km), such a process would not pose a serious problem, but as the size increases to reach macrocell modelling, this technique would produce an extremely high amount of data. For picocells and very small cell sizes however (in the order of hundreds of meters at most), it would considerably increase the accuracy of the model. Picocells would normally employ higher frequency technologies, thus as discussed above even small blockage in the Fresnel zone might even cause loss of the free space scenario. Thus for such scenarios vector-type models might increase the accuracy of the model.

'Vector raytracing' features are capabilities that would enable the engine to process urban models not subject to these raster-type restrictions, including models for which there is no requirement that the normals of walls should point in the principal compass directions. These capabilities apply to the modelling of foliage/vegetation also. In a vector raytracing environment buildings and regions of foliage/vegetation may express highly variable shapes, areas, volumes, and orientations, and buildings need not be cuboidal in nature.

Example vector and raster databases employing all those features can be seen in Figures 3.3 and 3.4.

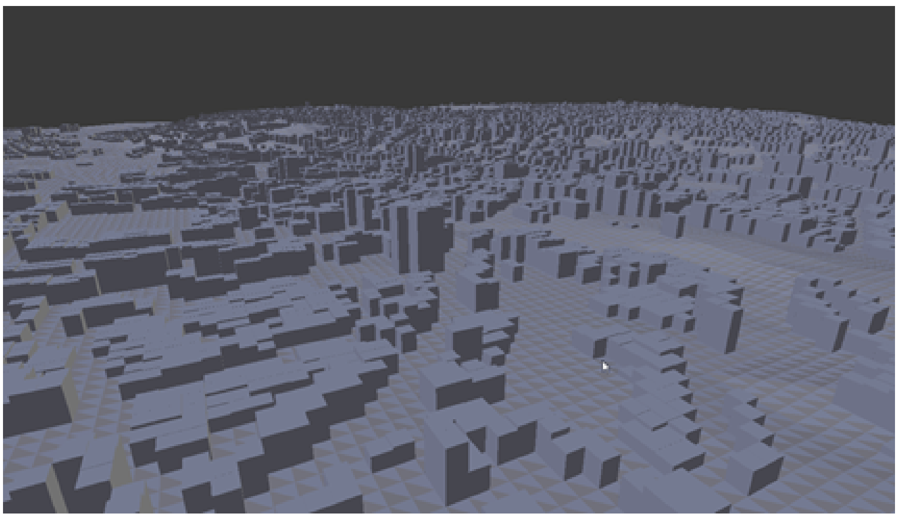

FIGURE 3.3. Example Raster Building Database

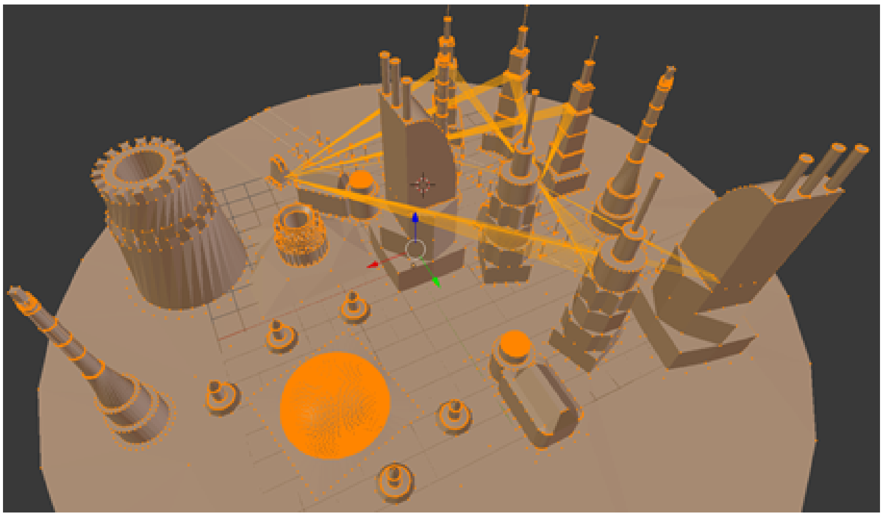

FIGURE 3.4. Example Vector Database

The ability to admit such highly variable buildings and geometries allows modelling of highly specific environments that the ray-tracer was not able to resolve previously. Abstractions and parts of larger environments are now able to be modelled using vector ray-tracing solutions. With the emergence of open source 3D modelling tools, complex and specific environments can be dynamically developed to research specific interactions with increased detail. These are the same tools that are used by professionals and authorities to generate realistic models of cities to research or plan future expansion. Some example programs are Blender, AutoDESK software, MeshLab, etc. Specifically, Blender was used to create a test database for the study of high resolution urban environments in Chapter 6.

A method to allow us to directly import real life data was also developed during the early stages of the project. By importing OpenStreetMaps raw data into 3D design programs and then by performing filtering and reconstruction for highly specific surfaces and building roofs the data was processed to display real life scenarios. However, this was only a temporary solution as the ray-tracer has moved to more sophisticated and efficient integrated methods to import and interpret real-life maps making this work obsolete.

In relation to the ray-tracing and studies performed throughout this thesis, the vector-based ray tracer was exlusively used in Chapter 6, while in Chapter 4 and 5 the raster solution was chosen. Apart from the need of increased resolution databases for complex city geometries, the choice of raster for rail scenarios has to do with the update timeline of the vector solution, as during the start of the PhD there was no working solution for vector ray-tracing embedded in the program.

It has to be noted that the updated ray tracer was rebuilt for this purpose by a third-party company, using models and processes derived from the raster-based ProPhecy. The author's contribution to the update process mainly entailed sensitivity analyses, consulting work for functionality and features as well as work on integrating and configuring 3D databases using open source solutions.

3.2.3 Propagation Mechanisms

This section focuses on the techniques currently employed in the ray tracer to approximate and mathematically model the propagation mechanisms. The techniques used to form the deterministic 3D propagation model and thus predict the channel coefficients and parameters such as power, time, angle of arrival and also provide fading information will be also presented.

Each process or propagation mechanism is assigned a processor that is essentially a sub-module that simulates that specific effect. All these processors are integrated in the ray-tracing tool and can dynamically be included or omitted using a simple xml file, to isolate the effects of specific geometries. In this work a composite processor will be provided. This composite processor will supplement conventional losses (eg. due to vertical plane diffraction and surface scattering) with foliage losses by first computing the distance travelled by rays inside of vegetation and then by delegating to a foliage attenuation algorithm (eg. COST) to compute the overall foliage loss factor.

3.2.3.1 Free Space Propagation

As seen previously on chapter 3 free space propagation is the simplest form of propagation scenarios. Even though the term free space propagation refers to an idealised open, empty and unlimited space, it can be extended with some approximation to real environments. In theory [19], the emitted energy originating from an omnidirectional antenna was seen in previous sections to be distributed over a sphere with radius d. Thus the power at a distance d from the emitting source will also be given by the following equation:

$$P_R = P_T G_T G_R \left(\frac{\lambda}{4\pi d}\right)^2 \tag{3.2}$$

To analyse the power flow between the transmitting and receiving terminal the Fresnel zone is introduced. Named after the physicist Augustin-Jean Fresnel this zone consists of a series of ellipsoids that alternate in a propagating wave's strength volumes resulting from constructive and destructive summation of the refracted and diffracted MPCs [54].

The Fresnel zone can be easily calculated using the equation below:

$$F_n = \sqrt{\frac{n\lambda d_1 d_2}{d_1 + d_2}} \tag{3.3}$$

Where F_n represents the n^{th} Fresnel Zone radius, d_1 the distance of P from one end, d_2 is the distance of P from the other end and λ is the wavelength of the transmitted signal. P refers on a plane perpendicular to the line joining points A and B passing through point C in Figure 3.5

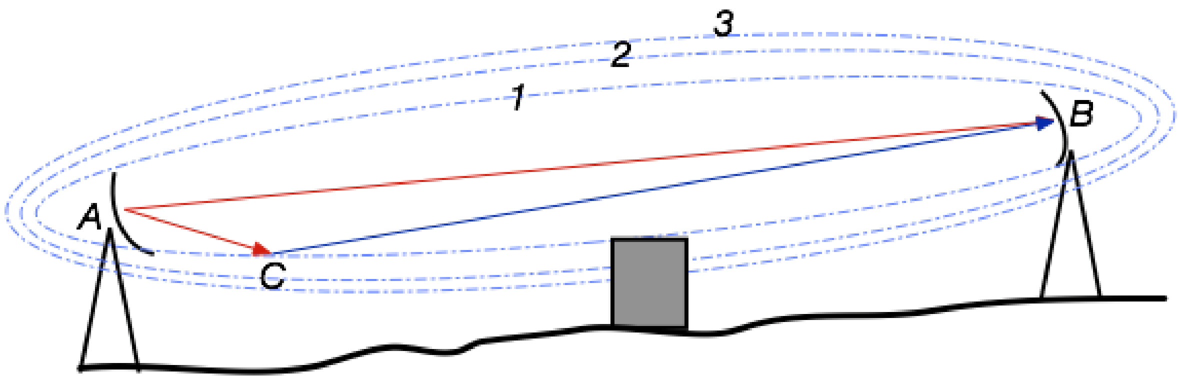

FIGURE 3.5. The Fresnel zone

Frequency effects play an important role on determining the Fresnel zone and thus the LoS propagating zone. To put it simply, the higher we move into the frequency spectrum the narrower the cone becomes, thus even small objects have a large possibility of violating the 60% criterion defined above.

TABLE 3.1. Fresnel Zone Size per Frequency

Frequency	100kHz	10MHz	100MHz	1GHz	10GHz
R_1	316m	100m	32m	10m	3m
R_2	447m	141m	45m	14m	4m

To allow for free space propagation, first of all a LoS needs to be determined first. The first ellipsoid as in Figure 17 below represents the first Fresnel zone most of which needs to be kept clear of obstructions (at least the 60%) such that free space propagation to be achieved.

3.2.3.2 Propagation by Reflection

The second and equally important mechanism of propagation is reflection. Reflection occurs at the boundary areas between two different media leading in a change of direction in the wavefront. In the case that the reflecting media is a surface of large dimensions while having not many irregularities, specular reflection is observed. To put it simply, the smoothness of the reflecting surface is the ultimate measure used to determine if a specular reflection occurs. However, the smoothness perceivable at each case is wavelength dependent, i.e. the resolution of the reflecting surface varies according to frequency. A building wall for example, might be perceived as a smooth surface in a model operating at 900MHz but probably electromagnetically rough for a wave in the mmWave range.

In the case the surface is perceived as smooth, then Snell's laws take over and specular reflection is observed; i.e. the reflected ray angle normal towards the surface equals the angle of the incident ray. When the surface is characterised as rough compared to the wavelength, the signal scatters everywhere. How the signal propagates in this case however will be studied in following sections.

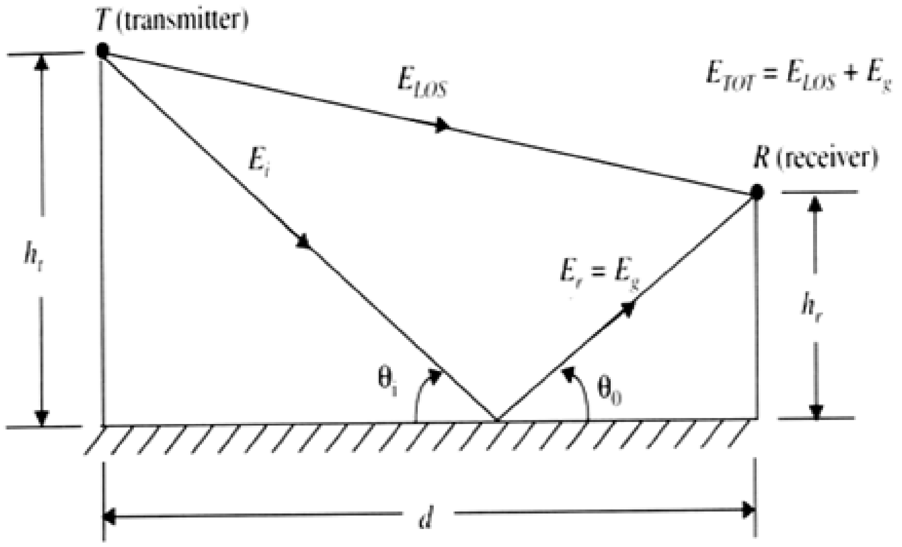

FIGURE 3.6. The two-ray model

In a mobile radio channel a single link between the transmitting and receiving terminals is rarely observed rendering the free space model inaccurate on its own. In many cases a two ray ground reflection model that considers both the free space (LoS) scenario and the reflected path is used as seen in Figure 3.6. Such a model is mainly useful in large cells that spread over several miles thus having the transmitter way above building height. The two ray model might be quite useful when considering mmWave frequencies as not many MPCs will be considered due to the directive nature of the beam. Though further research and measurements are needed to quantify the effect it will have in high frequency channels.

3.2.3.3 Propagation by Diffraction

Free space propagation and propagation by reflection are two main use cases of geometrical optics. However, physical optics would predict a zero field in the shadow regions around an obstacle. This portion of radiation is commonly refered to as a diffracted wave. Diffraction models describe conduction and displacement currents that appear on the suface when an obstacle is encountered, thus, preserving the electric field [55]. Those currents consequently create secondary radiation that extends to all space. Signal spreading is caused in different amounts in accordance with the physical dimensions of the edge and the wavelength propagating wave.

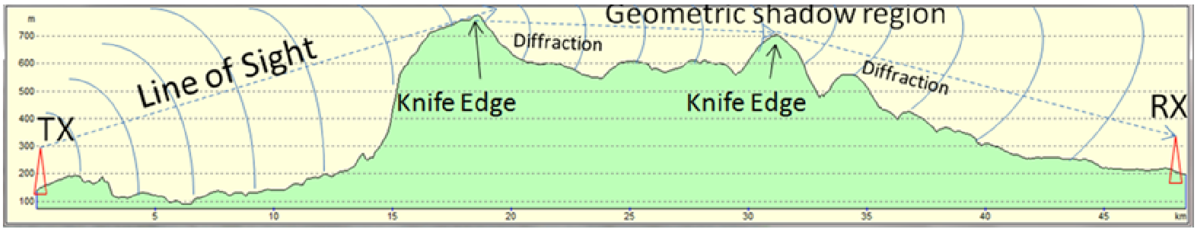

FIGURE 3.7. Geometric approximations for diffraction

Tthe diffraction of a wave is essentially a boundary problem. However, as most of the obstructions that a wave may come across do not have an ordinary shape, appropriate abstractions need to be defined such that modelling becomes easier and less computationally expensive. Thus the problem is usually reduced to modelling the complex object as a combination of simpler geometries for which detailed diffraction measurements and models exist, e.g. spheres, cylinders or ridges such as wedges or knife-edges. An illustration of all the above mentioned can be seen in Figure 3.7.

When only a single obstruction is blocking the path of the ray, modelling can be simply performed by using an equivalent knife edge. The knife-edge approximation is one of the most popular and widespread models in use for diffraction modelling as the mathematical analysis involved is fairly straightforward and easy to implement. However, many important electromagnetic characteristics (electrical properties, the lateral profile and local surface roughness effects) are omitted from the analysis.

When multiple obstructions are in the path of the ray, more intricate analysis is needed. Multiple approaches are described in literature, but only the most prevailing ones will be presented here. Bullington (Figure 3.8) describes in his approach an equivalent knife edge that would be formed at the intersection of the horizon paths of the transmitter and receiver to replace all knife-edges with a single one [56, 57]. Epstein and Peterson treats every edge that is illuminated by the transmitter or by a diffracted wave as a source. Each of the edges is assessed individually and then the effects are summed up all together to calculate the diffraction losses [56, 58]. Picquenard's approach [56] models the diffraction for the transmitter and the receiver independently as well and then superpositions them. The first edge is then treated as a source to calculate the attenuation and thus diffraction loss at the receiver.

An alternative theory in diffraction modelling, uses wedges as a replacement to the knife edge described previously. The Uniform Geometrical Theory of Diffraction (UTD) is an improved version of Keller's geometrical theory of diffraction. UTD appears to be able to present results with higher accuracy in the expense of computationally more demanding subroutines compared to knife edge theory. This is nonetheless insignificant in many cases as UTD is able to retain information on wave and diffracting surface properties such as polarisation, local roughness and electric properties of the wedge.

It is still not clear though if diffraction would need to be modelled in higher frequencies. Measurements taken at the university of Bristol with a Keysight M8190A arbitrary waveform generator (ARB) show that without beam steering to exploit the strongest possible MPC the signal strength drop is really large [44, 59, 60]. Results mention an approximate 30dB drop once the user has moved just 20-50cm into the shadow region for distances of 0.5m to 2m from the corner. By moving further away from the wall the shadow region seems to persist with the signal power although not almost instantly dropping. At a distance of 10m from the corner, the user needed to move about 1.2m into the shadow region in order for the same drop of 30dB to be observed again [59].

Both knife edge and UTD modelling is implemented in the developed ray tracing model to allow for comparison in many different cases, especially in multiple edge modelling. UTD was found to perform better in most scenarios compared to knife edge models [24]. The smallest difference in results being observed in modelling a single diffraction edge in ranges around 600-800m by particularly using the Epstein-Peterson model.

Further comparison of the results obtained in the mmWave channel measurements with Knife Edge Diffraction theory, perfect agreement of results is noticed at 60 GHz while comparisons with

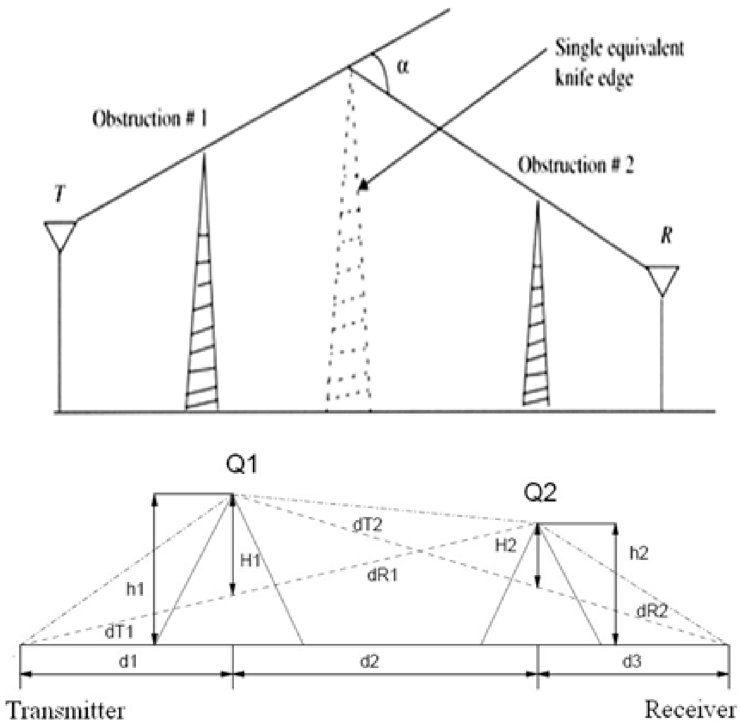

FIGURE 3.8. Approaches to multiple knife edge modelling: (a) Bullington, (b) Epstein and Peterson

UTD are still in progress. Thus careful consideration is needed and many more measurements in indoor and especially outdoor environments to consider how it affects propagation. In this work, Epstein-Peterson algorithms are used for the majority of the ray-traced routes.

3.2.3.4 Propagation by Scatter

As mentioned in section 3.1.2.2, when a surface is electromagnetically rough, the signal would bounce off in all possible directions due to the microscopic irregularities of the material. Models however need a dynamic threshold that could be used to determine if the surface is rough and also resolve the degree of roughness to decide the model to be used to represent scattering.

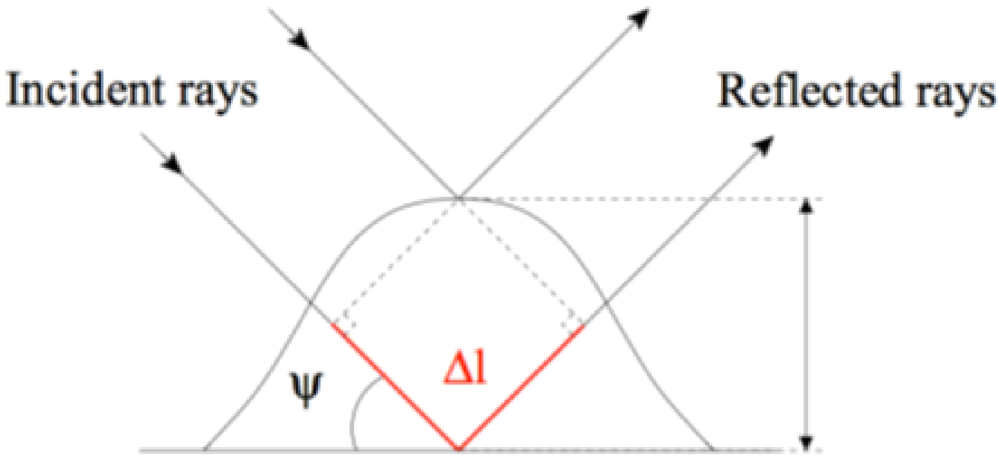

FIGURE 3.9. Derivation of Rayleigh Criterion

To mathematically define and thus translate this into the model, the Rayleigh criterion is defined. The Rayleigh criterion [61] states that if the phase difference $\Delta\phi$ between two reflected waves is less than $\pi/2$ radians, then the surface may be considered as smooth, and is defined by

$$\Delta h < \frac{\lambda}{8\sin\psi} \tag{3.4}$$

Where Δh is the height difference between two rays as seen in Figure 3.9.

To classify surfaces according to their roughness, two measures are taken into consideration; the standard deviation of the distribution and the correlation distance (L). The second measure is devised as it is possible to have surfaces with the same standard deviation but irregularities could be either densely packed or smoothly spread in the surface area. Two such surfaces would scatter the electromagnetic wave in a completely different fashion hence distinction of such differences is vital. Thus the correlation distance as the distance for which the correlation between the surface height deviations from the mean level at two different points on the surface drops to $e^{(-1)}$ [62].

Disregarding the challenges that signal scattering poses in modelling the propagation environments, this effect could have benefits for future technologies as the received signal is often stronger than that predicted by simple reflection/diffraction models. The EM wave incident upon a rough or complex surface is scattered in many directions and provides more energy at a receiver energy that would have been absorbed is instead reflected to the receiver [63]. When studying a smooth surface, the energy measured after the reflection can be related to the incident energy by terms of the reflection coefficient R_o of the surface. R_o is ultimately the ratio of the reflected over the incident field of the surface. To account for rough surfaces as well, the ProPhecy tool defines a scattering factor that is used to calculate the effective reflection in such cases. The effective reflection is given by the following equation

$$R_{eff} = \rho R_o, \quad \text{with } 0 < \rho < 1 \tag{3.5}$$

The scattering coefficient (ρ) is calculated by processes such as Lambertian, Kirchoff and Small Perturbation scattering. The main use of this coefficient is to take into consideration the energy loss due to the irregularities in the reflecting surface.

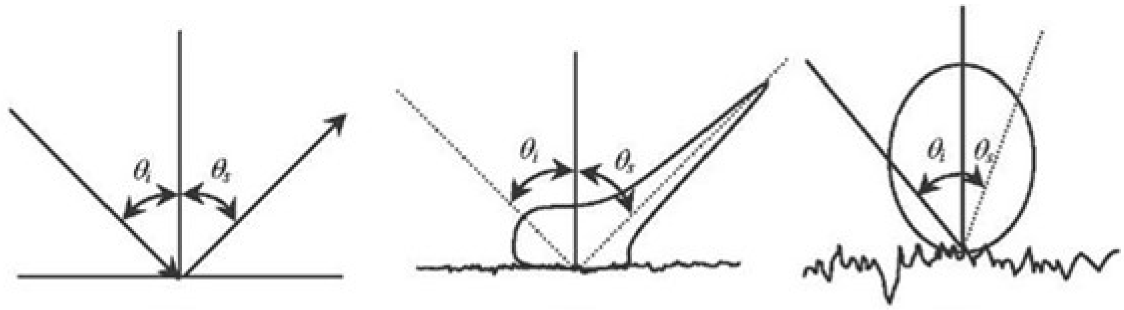

FIGURE 3.10. The effect of surface roughness in reflection or scattering

Lambertian reflectance is the property that defines a surface which apparent brightness is perceived to be the same for an observer regardless of his angle of view [64]. To put it on technical terms, a Lambertian surface's luminance tends to be isotropic. This specific property, makes Lambertian reflectance a valuable tool into modelling surfaces whose roughness is high, as the emission of a Lambertian radiator does not depend upon the amount of incident radiation, but rather from radiation originating in the emitting body itself [63].

The second model that is used in rough surface modelling is the Small Perturbation Model (SPM). SPM accuracy was studied to increase when modelling surfaces of medium roughness or applications employing long wavelengths. In SPM the surface under analysis is first decomposed into its Fourier spectral components [64]. Each of these spectral components is then related with a sinusoidal surface and by resonating each with the respective wavelength and angle of incidence it causes scattering.

Finally, the Kirchoff model for scattering has been shown in multiple occasions to be used to model an elementary interaction of an electromagnetic wave. “The Kirchhoff assumption is that the field present at a particular point on a scattering surface can be approximated by the field on the plane tangential to the surface at the point” according to [65]. This model has an advantage in terms of ray-tracing as it is a dererministic physical model, meaning that it can be applied by simply supplying the required parameters and choosing the frequency.

3.2.3.5 Propagation by Transmission

As discussed previously, blockage in the Fresnel zone causes severe attenuation in the signal that is caused by signal absorption from different materials. However, at lower frequencies that are able to penetrate materials, propagation by transmission is a really important mechanism as the signal is able to penetrate the materials and connect terminals separated by a wall. For example this would find practical application if the transmitter and receiver are located in either a different room or if the signal from the basestation propagates through the building wall from outdoor environment into the building. Indoor ray tracing a modelling is out of the scope of this project however, thus it will not be investigated.

3.2.4 mmWave Specific Considerations

The main mechanisms that apply in mmWave research are building and ground reflections/scatter and diffraction. Due to the placement of APs in urban scenarios being low compared to other technologies, rooftop diffraction does not affect the link significantly. Even though the main sources of diffraction are lateral in the examined technologies, both sources of diffraction are considered in ProPhecy to account for low buildings or clutter in the ray-traced environment.

A reccurring discussion throughout this document is that propagation is very dependent of the buildings’ shape, location and composition. Reflections, diffractions and free space propagation normally lead to ducting increasing the range and multipath richness of the link allowing extended cells to be formed. As antennas are usually located quite low and below the height of urban clutter and obstructions, it is vital to correctly model the environment as these factors significantly decrease the possibility of a LoS channel. Even though extended cells are formed, mmWave presents a significantly more confined architecture. For this reason along with the reduced number of considerable reflections, links display lower time dispersion with a high LoS probability as the antennas are placed in locations that maximise these LoS effects.

In some experiments, scattering sites may be evaluated for transmitter/receiver antenna pairs situated in such a way that the geometry of the scattering problem includes an incident or a scattering angle of zero radians to the surface normal - ie. the direction of the incoming ray is antiparallel to the surface normal or the direction of the scattered ray is parallel to it. This condition may arise especially in batch experiments for which grid samples of the entire terrain field are required. It is possible to devise and use scattering cross section models that have the property that the scattering cross section multiplier depends on the limit of the angle phi as theta tends to zero from above. Measurement campaigns considering the effects of scatter in mmWave environments discover that the reflected power from all types of surfaces display a considerable drop after the incident angle was increased [66]. Thus, reflection and scattering is only considered an angular range between 35° and 70° from the reflecting surface.

Moreover, recent research on millimetre wave has uncovered significant results regarding some pretty common misconceptions about LoS and NLoS propagation in urban environments. Some pretty common misconceptions in mmWave systems considered only the LoS components to be resolvable. Researchers in [67], after measurements performed in New York City, have discovered that links between the transmitter and receiver were quite common in angles where the receiver terminal was pointed at least 50° (off-boresight) away from the unobstructed LOS direction to the transmitter.

At mmWave frequencies even surfaces previously regarded as smooth become electromagnetically rough leading into the signal being scattered rather than reflected into the environment. As the frequency increases, the effects of a specific roughness surface seem to increase resolution of the surface increases and what was viewed as homogenous surface in a lower frequency wave could induce scattering in high frequencies. Thus, accurate modelling of these components are necessary for the planning of The largest issue with reflections however is the discrepancy of the transmitted and received polarisation. Scattering polarises components in unexpected ways thus leading to a need of more complex baseband for Rx antennas, which significantly incurs larger costs. For the majority of this research, the Kirchoff model will be applied for scattering in the ray-tracer either during ray-tracing itself or in post-processing.

3.3 Antenna Array and Codebook Generation

Millimeter wave technologies may have introduced a plethora of challenges that need to be solved before complete, integratable solutions are developed but have also introduced some advantages in antenna design. Due to the inherent small wavelengths of this technology, high packing density of elements (i.e. small form factor) can be achieved in mmWave APs and devices. This is important in this case as phased array transmit/receive architectures employing high-gain and high-resolution beamforming solutions need to be applied [68]. Such solutions include uniform linear arrays (ULAs), uniform planar arrays (UPAs) or even uniform circular arrays (UCAs)[26]. For simple solutions, such as backhauling or infrastructure-to-infrastructure (I2I) configurations, ULAs have been widely proposed and studied [69–77]. However, UPAs have been gaining traction due to higher space efficiency and the implicit interference mitigation due to 3D beamfoming [78].

3.3.1 Measured Antenna Patterns

The first step of the antenna performance assessment methodology is to determine the far-field radiation patterns. In the context of this thesis, 3D far-field radiation patterns with full magnitude, phase and polarisation information are measured [1] in University of Bristol's 8 m (long) by 5 m (wide) by 4 m (high) anechoic chamber designed by Emerson and Cuming and fully lined with pyramidal carbon-loaded cones. The antenna test facilities use a wideband horn antenna that will separately transmit two orthogonal polarisations and is connected to one port of an Anritsu 37397C Vector Network Analyser (VNA) [28]. The Antenna Under Test (AUT) is placed at a specific distance from the reference antenna and is manually rotated to all directions by the use of motors. The AUT is connected to the other port of the VNA and thus, radiation pattern measurements for these two polarisations, at every realisable LoS angle are measured.

A (θ,ϕ) spherical coordinate system was used in the measurements. The raw data from the measurements is a data file for each antenna element that represents the complex electric field levels for ranges θ (-180° to 180°) and ϕ (-90° to 90°) and for the two orthogonal polarisation components E^{θ} and E^{ϕ}. This data includes all cabling and path loss within the measurement environment, and hence it is normalised by relating all levels to the maximum received signal level. The total power radiation pattern (irrespective of polarisation) is also computed and gives an indication of the coverage angle of an antenna. As explained in Chapter 2, the maximum directivity of the two orthogonal polarisation pattern components and of the total power radiation pattern can be calculated from this.

Considering mmWave architectures, measuring an antenna poses more challenges. Using a novel Over-The-Air test method based on ellipsoid reflectors, a set of elliptical cylinder reflectors and a set of discrete reflectors distributed in a part-ellipsoid structure authors in [79, 80] realised methods for measuring the far field pattern of mmWave directional antennas using a similar configuration as the one described in the above paragraphs. The measured pattern of an antenna array measured using these methods is shown in Figure 3.11(a).

Due to the the low profile and ease of fabrication of the patch and the reduced resolution of the measurements for the full antenna array (no higher than 10°), the patch antenna element was chosen instead as a basis for the array configurations to be presented. Moreover, the fact that the measured antenna was measured in a predefined 64x64 configuration, without specifying the element phases or spacing (to the authors best knowledge) would complicate the defined antenna generation and rotation techniques. The initial radiation pattern of both the antenna patch and the measured antenna array is shown in Figure 3.11.

It has to be noted that with this configuration, the lobes on the back side of the antenna are not measured.

[1] The antenna measurements and evaluation methodology presented in this chapter has been initially developed by Dr. Evangelos Mellios at the Communication Systems and Networks Group, University of Bristol, United Kingdom

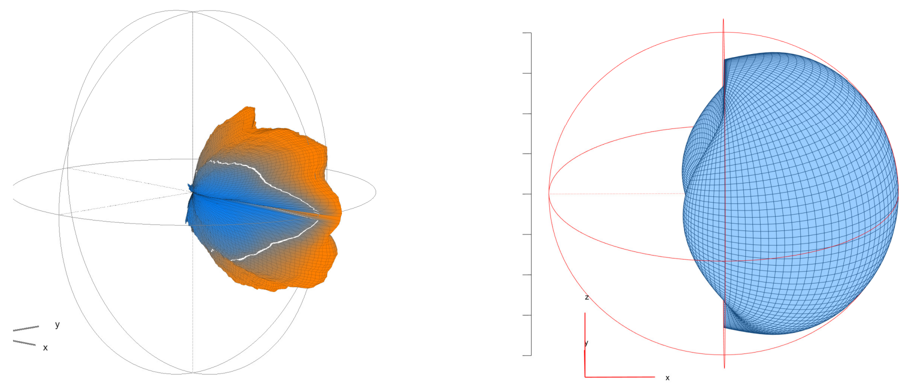

(a) AnokiWave Antenna (b) Single Element Patch

FIGURE 3.11. Power Radiation Patterns

3.3.2 Antenna Rotation

As briefly mentioned Section 1.2.1, rotation of the antenna beams in analog beamforming systems is achieved by changing the phase of each element in the planar array. In this subsection, we demonstrate how this rotation is achieved in Cartesian coordinate systems by using R; a 3×3 rotation matrix as described in [29]. R is defined as:

$$R = R_x * R_y * R_z \tag{3.6}$$

$$R = \begin{bmatrix} 1 & 0 & 0 \\ 0 & \cos\omega_x & \sin\omega_x \\ 0 & -\sin\omega_x & \cos\omega_x \end{bmatrix} \begin{bmatrix} \cos\omega_y & 0 & -\sin\omega_y \\ 0 & 1 & 0 \\ \sin\omega_y & 0 & \cos\omega_y \end{bmatrix} \begin{bmatrix} \cos\omega_z & \sin\omega_z & 0 \\ -\sin\omega_z & \cos\omega_z & 0 \\ 0 & 0 & 1 \end{bmatrix} \tag{3.7}$$

where ω_x, ω_y and ω_z correspond to the right-hand-rule rotation angles against each of the principle directions x, y, z respectively.

Next, the direction vector for an angle specified as (θ, ϕ), is calculated relative to the coordinate system specified at the antenna. The direction vector is specified as:

$$\begin{bmatrix} x \\ y \\ z \end{bmatrix} = \begin{bmatrix} \cos\phi * \sin\theta \\ \sin\phi * \sin\theta \\ \cos\theta \end{bmatrix} \tag{3.8}$$

So far only the rotation of the vector has been specified in the same coordinate system of the antenna. To calculate the rotation with respect to the global coordinate system we multiply the direction vector with R.

$$\begin{bmatrix} x' \\ y' \\ z' \end{bmatrix} = \mathrm{R} \begin{bmatrix} x \\ y \\ z \end{bmatrix} \tag{3.9}$$

and then convert the values to spherical coordinates as such:

$$\begin{gathered} \theta' = \tan^{-1}\left(\frac{\sqrt{x'^2+y'^2}}{z'^2}\right) \\ \phi' = \tan^{-1}\left(\frac{y'}{x'}\right) \end{gathered} \tag{3.10}$$

Next angle α that defines the polarisation is calculated. The polarisation vectors p'^{θ}, p'^{ϕ} corresponding to the local systems are defined as:

$$p'^{\theta} = \begin{bmatrix} \cos\theta' \cos\phi\prime \\ \cos\theta' \sin\phi' \\ -\sin\theta' \end{bmatrix} \tag{3.11}$$

$$p'^{\phi} = \begin{bmatrix} -\sin\phi^{AoA'} \\ \cos\phi^{AoA'} \\ 0 \end{bmatrix} \tag{3.12}$$

The polarisation vectors of rotated angles are shown as well.

$$Rp^{\theta} = \mathrm{R} \begin{bmatrix} \cos\theta \cos\phi \\ \cos\theta \sin\phi \\ -\sin\theta \end{bmatrix} \tag{3.13}$$

$$Rp^{\phi} = \mathrm{R} \begin{bmatrix} -\sin\phi \\ \cos\phi \\ 0 \end{bmatrix} \tag{3.14}$$

These vectors exist on the same plane but are shown to be out of alignment by an angle α:

$$\alpha = \cos^{-1}\left(p'^{\theta} \cdot Rp^{\theta}\right) = \cos^{-1}\left(p'\phi \cdot Rp^{\phi}\right) \tag{3.15}$$

Having calculated α it is not difficut to calculate the far field radiation pattern of the antenna at an angle of (θ, ϕ),

$$\begin{bmatrix} E^{\theta} \\ E^{\phi} \end{bmatrix} = \begin{bmatrix} \cos\alpha & -\sin\alpha \\ \sin\alpha & \cos\alpha \end{bmatrix} \begin{bmatrix} E^{\theta}(\theta', \phi') \\ E^{\phi}(\theta', \phi') \end{bmatrix} \tag{3.16}$$

It needs to be noted however, that the angular intervals have a specific resolution due to measurement techniques struggling to achieve good resolutions, especially in mmWave architectures.

3.3.3 Codebook Generation and Beam Selection

Standardised codebook designs such as IEEE 802.15.3c (hereinafter referred to as “3c codebook design”) have been employed since the emergence of MIMO communication to select the optimum code vectors betweeen the two sides of the link. The majority of the work in 3c codebook design assumes ideal omni-directional antenna pattern, neglecting the impact of physical parameters in the antenna pattern. In this thesis however, instead of a theoretical and standardised codebook, a synthesised antenna based on the measured patch described above was used as a base for the 2D codebook presented following the principles defined in the standard [7].

1. The codebooks are designed for a phased antenna array, each column of a codebook matrix specify the phase shift of each antenna element.
2. The codebooks are designed symmetrically spanning the 360° around devices.
3. The codebooks support a multitude of antenna configurations and it is also available for different numbers of antenna elements.
4. For a 2D antenna array, separate codebooks are associated with each dimension as well as for transmit and receive.
5. For a complex beamforming antenna array, the weights can be adjusted in both phase and amplitude.

The rotation method that was described above is used as a basis for this operation. In the previous section the single element calculation was performed, however, it can be scaled to any number of elements placed on the antenna plane allowing linear, planar and even circular configurations to be generated by simply using a zero reference point. Multiple antenna arrays can then be accounted for by using a fixed reference point and assign a relative phase of $e^{j\mathbf{kr}}$ to subsequent elements according to wavelength and distance, as defined in the point expansion technique [34] and shown in the equation below.

$$\mathbf{kr} = \frac{2\pi}{\lambda}\left(x^0 \sin\theta\cos\varphi + y^0 \sin\theta\sin\varphi + z^0\cos\theta\right) \tag{3.17}$$

where $\mathbf{k}$ denotes the wave vector, $\mathbf{k}$ the relative position from the zero-phase reference point, λ the wavelength, while ϕ and θ the local polar coordinates of the system.

This method allows rotation of the generated beam in any angle both in elevation and on azimuth. Following these principles our codebooks are initially designed by employing beam patterns uniformly spread around the azimuth plane of the AP and are normalised based on the highest gain beam. In later studies the codebooks will not be confined in just the azimuth plane but will also expand in the elevation domain. The value of uniform sectors will be discussed considering the trade-off between beamwidth, processing power and sector sweep overhead. Future studies will aim on quantifying this value for a multitude of environments, antennas and arrays.

3.4 Physical Abstraction Method (RBIR)

To complete the analysis of the end-to-end links between two antennas, system-level metrics and performance needs to be calculated. Bit-accurate PHY simulations is an ideal method that provide link level analyses for a multitude of devices and configurations. Such tools have the ability to consider different devices, orientations, modulation and coding scheme (MCS) modes as well as antenna deployments throughout the propagating environment. System-level metrics such as SNR, throughput, K-factor and all the different spreads can be derived with such techniques. Computationally, however, bit-level simulations are prohibitive the more the network and resolution scale. Thus, approximations through a 802.11n PHY layer Received Bit Mutual Information Rate (RBIR) abstraction method are used to compute performance in an efficient manner [2]. The RBIR simulator is based on an Effective SNR Mapping (ESM) technique and is extensively described and validated in [30, 81–83]. The proposed RBIR abstraction method in these works allows exponential reduction in the calculation of Packet Error Rates (PER) and throughput for a single channel. The operation of the ESM mapping is briefly analysed below.

ESM techniques allow the large SNR variations observed accross the subcarriers of an OFDM system due to frequency selectivity from the inherent multipath to be compressed into a single value; a single effective-SNR(ESNR). In the simulator this value is descibed as per the following equation [81].

$$ESNR = \Phi_m^{-1}\left\{\frac{1}{N \cdot N_{SS}} \sum_{n=1}^{N} \sum_{k=1}^{N_{SS}} \Phi(SNR_{n,k})\right\} \tag{1}$$

, where $SNR_{n,k}$ is the SNR observed in the n^{th} subcarrier and especially in the k^{th} spatial stream. N is the number of subcarriers, NSS is the number of spatial streams, while m is the modulation order. $\Phi(\cdot)$ is defined as the defined as the Symbol Information (SI) following a mutual information ESM approach [29], where SI is defined as:

$$SI(\gamma, m) = E_{XY}\left\{\log_2 \frac{P(Y \mid X, \gamma)}{\sum_X P(X) P(Y \mid X, \gamma)}\right\} \tag{3.18}$$

where Y is the symbol with SNR equal to γ while $P(Y \mid X, \gamma)$ denotes the AWGN channel transition probability. Using those two equations the instantaneous PER is calculated from the ESNR and a look-up table for each MCS mode

[2]The description of the PHY layer Received Bit Mutual Information Rate (RBIR) abstraction method has been provided by Dr David Halls at the Communication Systems and Networks Group, University of Bristol, United Kingdom.

In this work, the following assumptions are made. In the simulator, for each location, 1000 packets were sent over a single carrier. The suitable Modulation and Coding Scheme (MCS) mode was then chosen by the link adaptation algorithm to maximise the throughput for the link in every scenario. All MCS modes (1-12) are supported in the simulator. Finally, statistics are generated based on the MCS modes and data throughputs of every generated point-to-point link. Any MAC overheads or TCP/IP retransmissions which can cause additional throughput reduction as in real WLAN implementations are not covered in this work.

3.5 Model Validation

Validation of the specific parts such as the diffraction, scattering and foliage models defined within the ray-tracer was already performed in [22–25, 28, 29] even in mmWave frequencies. The complete ray tracing solution along with antenna pattern integration is presented and validated against MIMO measurement data in [84], where good agreement in the prediction of wideband and MIMO characteristics. Specifically, an average path-loss error of 2 dB and a normalized capacity error of 1.5 b/s/Hz is shown. Any further validation, is outside of the scope of this thesis, and as far as this work is considered, discussions relevant to the choice of the model for each of the propagation mechanisms is relevant and was already covered within this chapter.

The validity of the ray-tracing process was also benchmarked against Friis' Free Space Path Loss (FSPL) model to assure validity of the study. As seen in Figure 4.2, where the received power vs the distance from the transmitter is plotted, the simulated output shows similar performance to Friss' FSPL values. Both raster and vector databases in both HST and urban environments are validated as seen in the same figure.

Moreover, validation of the RBIR simulator presented in the previous section is not presented within this work as there are no changes apart from angular coordinate translation. The simulator has aleady been extensively reported and validated in [30, 82, 85–87]. A comparison between the RBIR abstraction technique and IEEE 802.11ad bit-level simulator in LoS channel using ray-traced data from multiple locations in Bristol,UK is shown in Figure 3.13.

3.6 Beamforming in mmWave

The purpose of beamforming is to select the optimal beam pattern pairs, in other words, define the best weight vectors for the transmitter and the receiver antennas with high antenna gains [88]. Those weight vectors are then optimised by measuring the link quality and applying a cost function that follows a certain criterion. In our case this criterion is Signal to Noise Ratio (SNR) but it can generally include function that follows a certain criterion such as Signal to Interference plus Noise (SINR), capacity, etc [89].

Fully digital precoding has been proven to be the most accurate method to achieve beam alignment by employing one radio frequency (RF) chain per antenna element. Such methods

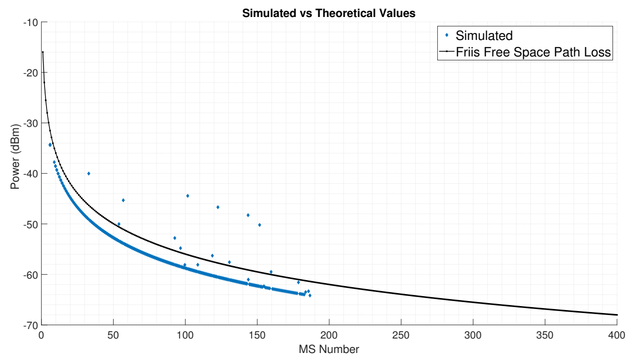

(a) Simulated vs Theoretical Path Loss Cars (Vector Database)

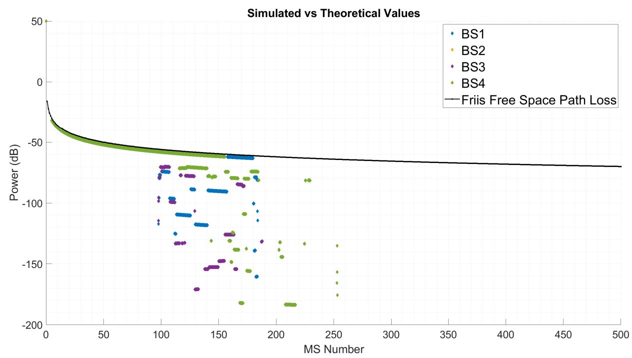

(b) Simulated vs Theoretical Path Loss Urban Scenarios

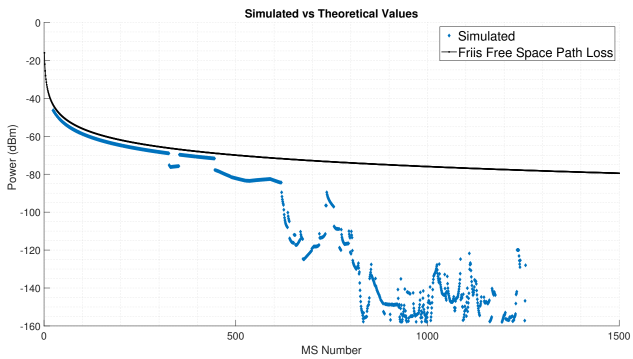

(c) Simulated vs Theoretical Path Loss Train Scenarios

FIGURE 3.12. Simulated vs Theoretical Path Loss Values

allow for better performance and higher spectral efficiency as multiple data streams can be easily precoded [69, 70, 72–74]. However, in mmWave systems such techniques are considered far from cost-effective due to the increased number of antenna elements required for the formulation high-gain and high-resolution beamforming solutions.

Analog beamforming achieves similar functionality by employing a single RF chain shared

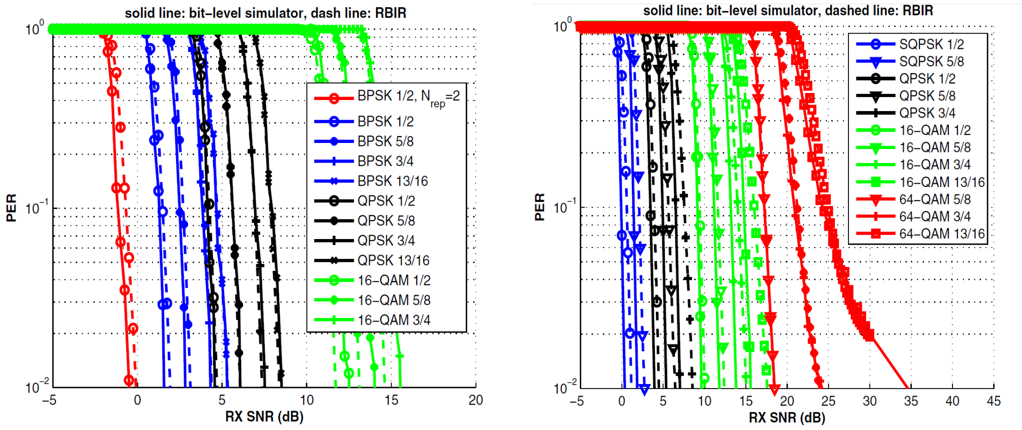

(a) SC-PHY

(b) OFDM-PHY

FIGURE 3.13. Comparison between RBIR abstraction technique vs. IEEE 802.11ad bit-level simulator in LoS channel

among the different elements of the array, achieving in this way similar performance with a fraction of the hardware cost and power consumption [70]. Performance suffers greatly however in such configurations as beamforming loss is observed due to the envelope constraints only a single data stream is realisable with this architecture.

Hybrid beamforming architectures are able to partly mitigate the disadvantages of both scenarios by combining features from both techniques to improve performance while still having low complexity [77, 90–93]. Multiple RF chains are used in this architecture, but not as many as the antenna elements combining into a mmWave massive MIMO system, as RF chains control groups of elements through sets of phase shifters [74–77]. An example hybrid architecture is presented in Figure 3.14.

In the code, a fully analog solution was developed due to the lower complexity required and

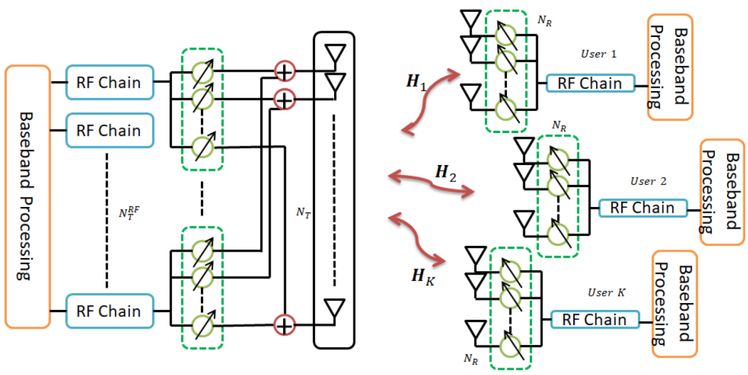

FIGURE 3.14. Hybrid Beamforming Architectures [94]

higher compatibility with the existing format of data. However, hybrid configurations are under development as well to discuss performance metrics in simulated and ray-traced data.

3.6.1 Beamforming Set-Up for Device Linking

To construct the transmit and receive beamformers the channel state information (CSI) matrix needs to be constructed at the transmitter side through the process of receiver feedback. However, estimating the CSI for weight vector calculation is a computationally expensive process that incurs high overheads. This is especially true in mmWave systems due to the increased number of resources that are required to train each antenna element [95, 96].

A codebook is a matrix where each column specifies a BF weight vector [97] and by extension an antenna pattern. Codebooks are the basis of every modern directional system, especially in mmWave and massive MIMO use cases. Codebooks are achieved by discrete phase shifts of the antenna elements in the array. On the simpler form, only the phase shifts without any explicit amplitude adjustment are defined [97, 98]. Codebooks allow beamforming to be achieved without the need of acquisition of accurate CSI matrices.

For the analysis and benchmarking of the beamforming performance the methods based on the processes proposed in the 802.11ad and 802.15.3c standards will be used. According to [98], IEEE 802.11ad and IEEE 802.15.3c perform exhaustive sector/beam search to setup a beamformed link between stations/devices in mmWave systems. Exhaustive search methods reduce the BF overhead significantly to CSI acquisition, but values are still high, especially when high resolution 3D systems are considered. Methods such as the ones in [97], define a number of stages in which two devices are linked to dynamically reduce the number of steps required in high-resolution configurations, again based on the above protocols. The number may differ research between different configurations but the same principles are applied.

To reduce beamforming overhead, [97] proposes the process to be divided into three stages for the system to calculate the optimal vectors (i.e. best transmit and receive beam pair):

1. Device-to-Device (DEV-to-DEV) linking
2. Sector-level searching (SLS)
3. Beam-level searching (BLS)
4. Beam-tracking (optional)

The methods are presented in detail in the following sections for the mandatory SLS phase and the number of steps required in the training process is calculated for both current BF algorithms of two standards and proposed methods as defined in [98]. The same principles unless explicitly stated apply for the rest of the stages as well. Timing in terms of frame length and time will be discussed in 3.5.3.

During the DEV-to-DEV stage of beamforming, the devices need to discover each other and establish an initial link between them. After this linking phase has been completed, and the two devices have been linked, the sector-level search is performed. Assuming the AP has N sectors and the MS has M sectors we calculate the required steps as follows.

3.6.1.1 802.11ad

To define the entities in an 802.11ad system, the devices are categorised as initiators (the access point that initiates the beamforming procedure) and responders. After these two device have been linked, each of the sectors of the initiator transmits a unique frame that is tracked by its unique sector ID. The SNR of each received frame is tracked by the responder during this phase. This concludes the first part of the SLS that is defined as Initiator Sector Sweep (ISS). A similar process is now applied in the responder side. Each of the responder sectors transmits a frame back to the initiator, but this time feedback information (FB) is attached to the frame. This phase is called Responder Sector Sweep (RSS). During both phases, the station that is receiving the frames is set to "listening" mode, i.e. employing quasi-omni patterns.

Last, the Sector Sweep Feedback (SSW-F) phase is performed. In this phase a frame from the initiator's highest SNR sector that was determined in the previous phase is sent as FB, containing the best sector of responder transmitter. An acknowledgement frame is then sent by the responder to complete the operation with the SSW Acknowledgement (SSW-ACK) phase.

The number of steps required for this operation is now calculated. For consistency, only SLS phase steps are considered. The initiator transmits N frames in ISS and the responder transmits M frames in RSS. Adding two frames for SSW-F and SSW-ACK, we have $N+M+2$ steps needed to train the transmit sectors of both stations.

$$S_{11ad} = AP_{sectors} + MS_{sectors} + 2 \tag{3.19}$$

3.6.1.2 802.15.3c

Although a different protocol is introduced in IEEE 802.15.3c, both standards define a multi-phase training process. The processes in 802.15.3c beamforming are based on superframe architectures [99], illustrated in Figure 3.15.

As shown in the figure, the superframe consists of three main parts:

1. A Beacon
2. A contention access period
3. A channel time allocation period (CTAP)

Each of the CTAPs consists of channel time allocations (CTAs) which are essentially Time Division Multiple Access (TDMA) slots granted by the network coordinator. CTAs is the structure

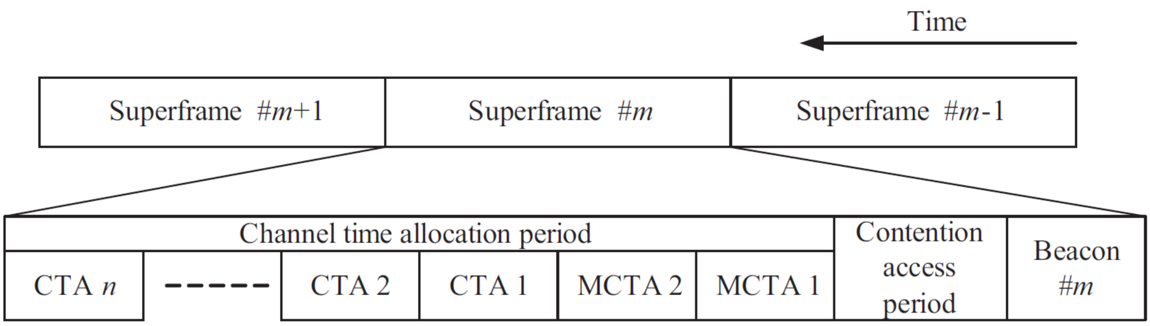

FIGURE 3.15. Superframe structure in WPAN piconets

inside which the beamforming process takes place. It should be noted that a CPA is allocated to each device, process or service in the network. Multiple devices are not explicitly considered in this work but will need to be analysed to measure the scalability of those systems in future analyses.

The following four sub-phases are defined in the architecture:

1. Sector training
2. Sector feedback
3. Sector to beam mapping
4. Acknowledgement

The sector training sub-phase is further subdivided to two parts: **DEV1 to DEV2** and **DEV2 to DEV1**. During the DEV1 to DEV2 phase, each sector transmits training sequences (TSs) each ending with a short inter-frame spacing (SIFS) to be received by different receive sectors of DEV2. The number of sequences that each sector produces has to equal the number of sectors at the receiver. This constitutes the main difference from 802.11ad and is defined as a "cycle" in the standard. Thus during this first stage of DEV1 to DEV2 linking, the number of cycles equals the number of transmitting sectors of DEV1. Similarly, at the DEV2 to DEV1 phase, the roles of transmitter and receiver are reversed and the same process is repeated. The process is shown in Figure 3.16.

At the end of sector training, both devices know each others' optimal sector. This information is then shared with each other at the next stage, the sector feedback stage. During that stage DEV1 transmits FB frames followed again by SIFS from each of the transmitting sectors. However, DEV2 only needs to send a unique frame from its best receiving sector. Feedback frames consist of Announce Commands followed by an acknowledgement command as seen in Figure 3.17.

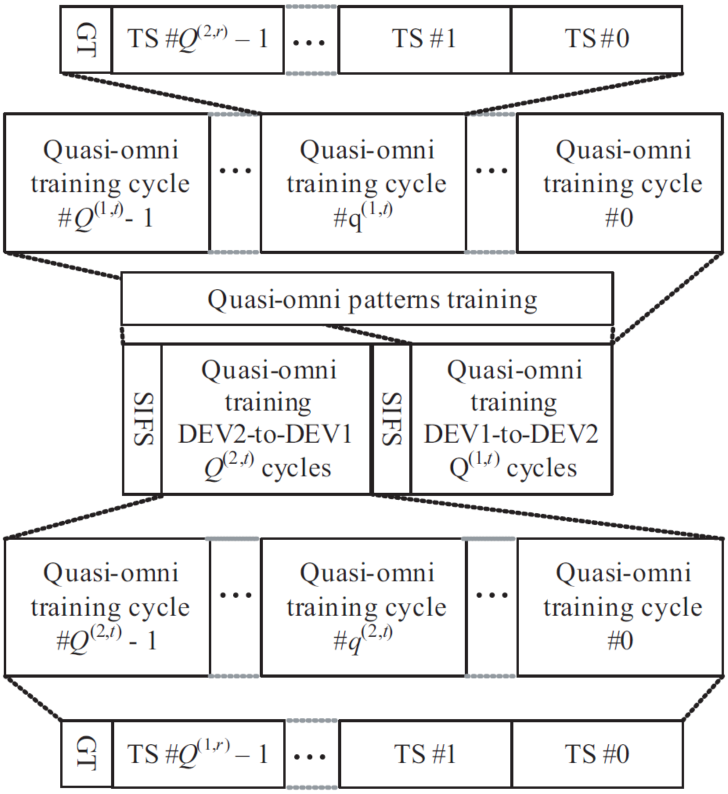

FIGURE 3.16. Quasi-omni pattern training period

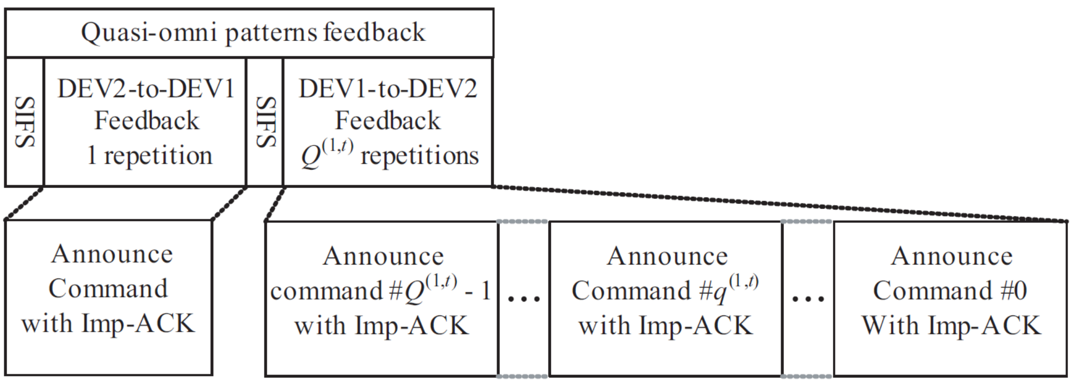

FIGURE 3.17. Quasi-omni pattern feedback period

This largely concludes the process as during the next stages (mapping and acknowledgement) the devices only send a series of acknowledgements; one each in the mapping stage and a single acknowledgement in the last stage. This is mathematically shown in the following equations.

During sector training, for the DEV1 to DEV2 part, there are N cycles for each transmit sector of DEV1. That counts $N \times M$ training sequences for DEV1 training. Similarly, $M \times N$ sequences are needed for DEV2 training. Adding the $N+1$ FB and three mapping, acknowledgement commands, sector training is completed in $N \times M \times 2 + N + 1 + 3$ steps [98]. This number might appear too high compared to the WLAN standard, but in this case instead of packets or frames, preambles are used as training sequences during the sector training stage hence, training time is relatively the same length.

$$S_{3c} = AP_{sectors} \times MS_{sectors} \times 2 + AP_{sectors} + 1 + 3 \tag{3.20}$$

Hence the time can be calculated as:

$$T_{3c} = (TS \times Q^{2,r} + GT) \times Q^{1,t} + (TS \times Q^{1,r} + GT) \times Q^{2,t} + (AC + I_{ACK}) \times \left(Q^{1,t} + 1\right) + 4 \times SIFS + AC + 2 \times I_{ACK} \tag{3.21}$$

where TS is the training sequence, GT the guard time, $SIFS$ the short inter-frame spacing, and $Q^{1,t}, Q^{2,t}, Q^{1,r}, Q^{2,r}$ the DEV1 and DEV2 transmitting and receiving sectors respectively.

Comparing the IEEE 802.11ad and the IEEE 802.15.3c BF algorithms, the most important difference is, while only transmit (or receive) sectors of both stations are beamformed at the end of the protocol in the former; in the latter, both DEVs are beamformed on their both receive and transmit sectors. It should also be emphasized that in IEEE 802.15.3c, BF is optional. On the other hand, it is mandatory in IEEE 802.11ad [98]. Example MAC parameters for such systems are presented in Table 3.2.

TABLE 3.2. MAC Related Simulation Parameters. Values based on [7, 97]

Maximum Superframe Period	65535 μs
PHY Preamble	3.259 μs
Beacon	15.81 μs
Training Sequence (T_s)	3.259 μs
PHY Header	1.581 μs
Feedback IE as payload	0.632 μs
Mapping IE as payload	0.751 μs
Association Request IE as payload	2.607 μs
Association Response IE as payload	3.277 μs
SIFS (T_{SIFS})	2.5 μs
ACK (T_{ACK})	7.212 μs
Guard Time (T_{GT})	0.0625 μs

To shorten the BF setup time, in this work the exhaustive BF process will be divided in three stages based on the previously presented method: **DEV-to-DEV linking**, **sector-level searching**, **beam-level searching** and an optional **beam-tracking stage** [97]. Through these stages, the proposed BF will find the best transmit and receive beam pair.

The process for finding the optimal beams for each stage is similar. The only difference between the different stages is seen from the second stage onwards, where the feedback stages of both directions have only one repetition of feedback.

3.7 Conclusions

As mentioned in previous chapters, this work is based in ray-tracing based modelling. Deterministic methods are able to model the environment not only in increased detail compared to stochastic models, but also allow an extension of the model in 3D while stochastic models tend to struggle in that domain.

Within this chapter the building blocks and the underlying technologies required for the description of a deterministic ray tracing model are discussed. Abstraction methods for the surrounding environment, antenna generation techniques as well as definition and benchmarking of propagation mechanisms that define the behaviour of the multipath components are described specifically in the context of mmWave communications. Methods used and proposals made to extend the use of this tool to accommodate the upcoming use of these higher frequency bands, smaller cell sizes, and smart MIMO antenna systems were also described. Within this framework, the intrinsic increased accuracy accompanying vector raytracing databases is presented and shown

In order to generate the MIMO channel matrix suitable for system-level simulations, the propagation model needs to be combined with an appropriate antenna model. Specifically, measured antenna elements are used for MIMO antenna array generation and by using phase shifts and rotation matrices within each element, 3D beams are described as a means to create high resolution codebooks for high mobility mmWave applications. Finally beamforming methods were presented along with some popular beamforming standards that will allow us to discuss the effects of set-up time in high-speed mmWave environments.

The following chapters will mainly focus on solidifying the channel modelling techniques, comparing the performance of the ray tracer against well established stochastic models and using them to accurately address mmWave challenges present in high mobility environments. This work will help in integrating the outputs of the ray-based double-directional model with system-level simulators to perform research on Key Performance Indicators (KPI) for selected mmWave applications and scenarios.

CHAPTER 4

Propagation Channel Characteristics and Impact of Antenna Properties in Vehicular Environments

User mobility introduces several challenges in mmWave communication systems as it incurs significant changes of the channel state. As users move throughout the environment, the distance between the transmitter (TX) and the receiver (RX) varies, leading to channel state fluctuations. To design systems that provide seamless connectivity to vehicles the propagating channel needs to be characterised properly. To adequately formulate BF schemes for such vertical applications, accurate models of the physical environment and antenna are required along with specific use case considerations. In the case of mmWave implementations in HSTs and cars, rail track/urban design as well as phased array design is important as it influences the system design decisions for such use cases. A propely characterised system - both the environment and the active components - will allow efficient application of adaptive beamforming methods, optimal antenna spacing and placement, which in turn significantly influence cost and viability.

4.1 Introduction

Connected and autonomous vehicles will play a pivotal role in future Intelligent Transportation Systems (ITS) for “vertical” industries such as smart cities and High-Speed-Railways. Such architectures would support both operational (backhaul) and end-user services. High data rate and low-latency links will allow safety and support information to be communicated from the relevant authorities while cloud solutions will be used as well to transfer data between multiple vehicles to achieve higher traffic efficiency by minimising traffic problems. However, these applications require high capacity and low-latency systems to allow seamless and constant connectivity.

Regarding high mobility vehicular environments, research has shown that mmWave solutions can provide many improvements compared to current infrastructure, such as increased spectral efficiency and data rates (up to several Gbps in some cases). Many argue, however, that the Doppler spread can be too high due to the small wavelength. Research suggests however, that this is true only for omnidirectional communication, showing that in vehicular channels, "the coherence time increases at least proportional to the inverse of the beamwidth" [100], thus there is an optimum operating beamwidth that results in a large coherence time. Hence, when the beam coherence time is larger than the channel coherence time, a reduction in the beam alignment overhead can be observed [101].

As seen in Chapter 2, as the frequency increases, the wavelength of the propagating wave decreases; thus, surfaces that were previously considered smooth in sub-6GHz frequencies are now electrically rough and diffusely scatter the incident radiation. Authors in [66] have shown that increased roughness in the reflecting surface directly affects the received power and the diffuse power to specular power ratio scattered from that reflecting surface. Those high attenuation properties encountered at mmWave frequencies [3] require appropriate characterisation and consideration to achieve optimal performance, especially in time-varying channels.

In this context, seamless broadband internet connectivity in high mobility scenarios constitutes a great challenge, even more so in train scenarios where speeds in many cases can even surpass a few hundreds of kilometres per hour. As wireless vehicular access currently lacks the ability to serve high-throughput and high-capacity links, research into various technologies harmonisation (i.e. LTE, mmWave and optical networks) as well as accurate synchronisation among mobile stations (MS), Access Points (APs) and the core network is a necessity. A complete infrastructure solution is thus required to support a converged transport network and flexible access. Work on this thesis concentrates around the mmWave enabling technologies of the vehicular framework. Synchronisation and harmonisation as well as packet core design for such technologies is not on the scope of this study. An overview of propagation and signal processing techniques for 5G can be found in [12, 13] as well as in Chapter 2, where the basic concepts that define the wireless propagation channel were presented.

Channel modelling is a crucial and indispensable tool in the design and optimisation of communication systems. Stochastic channel models (SCMs) are currently widely deployed due to their low intrinsic complexity. However, even though SCMs only require a low computational expense, only a part of the channel features is retained, high variability between results is observed, and the analysis in a 3D domain is quite restricted. Deterministic techniques such as ray-tracing based radio wave propagation prediction models manage to reduce this variability and include a greater amount of the channel features with only a slight increase in the computational load. Also, ray-tracing can be more flexible due to its ability to model both indoor and outdoor scenarios.

Ray tracing approaches were used in [102, 103] to study mmWave solutions for vehicular networks, but no analysis on the physical characteristics of the channel is performed. Also, although [104] presents a temporal analysis of LoS links (RMS delay spread), it does not include any other spatial characteristics of the channel. In the majority of the literature, ray-tracing studies are largely focused on stationary practical environments [3, 22, 23, 105]. Fewer ray-tracing studies have been performed on dynamic environments due to the need of a constant update of the channel parameters which is computationally expensive in high resolution realistic environments, thus many of them are based on either stochastic or empirical models [106–109]. It is important to treat mobility properly in a ray based propagation model, as in dynamic environments the scene consistently changes both in the eyes of the mobile station and from a high-level perspective.

In this chapter, ray tracing is used to investigate both LoS and NLoS propagation in the wireless environment of both frequencies described above (26,60GHz)[1]. A spatial throughput performance evaluation assessing the effects of BF, frequency and BS range in mmWave railway infrastructure is introduced throughout this chapter as well. With the aid of the ray-tracing tool to obtain predictions of the mmWave channels and the IEEE 802.11ad mmWave Matlab simulator, to model the system and acquire the throughput performance, we investigate the channel response and evolution of parameters using beamforming in mmWave scenarios.

The main objective is to characterise the mmWave channel in terms of its temporal evolution of the parameters and effects of steerable, directional antennas. Within the following chapters we will leverage the angular analysis of the multipath profiles to propose robust antenna design and use those parameters to form efficient beamformers. Moreover, a ray-tracing analysis is performed to derive the channel parameters in two vehicular situations, with the objective to discuss the recommendations and current limitations of the widely deployed models. Finally, a performance evaluation of a train scenario is performed in terms of Base Station range, and the effects of Maximum Ray Beamforming are presented[2] to discuss how directional communication affects system performance as well.

The rest of the chapter is organised as follows. In section 4.2, the temporal and angular statistics of the propagation channel are derived and compared with the nominal 3GPP and mmMagic values. An analysis is performed to discuss the evolution of the spatial characteristics of the link and metrics for angular rate of change are derived. The effects of the application of antennas and beamforming to the same parameters derived in the same section is discussed as well. Directional antennas are placed on either or both sides of the link and the same temporal and angular statistics are produced. In section 4.3 the system model, network structure and

[1]The evaluation methodology presented for the temporal and angular analysis in this chapter has been initially developed by Dr. Angelos Goulianos at the Communication Systems and Networks Group, University of Bristol, United Kingdom. Results from this work were produced as a contribution for the 3GPP mmWAVE technical discussions, in June 2017

[2]The study of the train environment performed in this chapter has been a collaborative effort with Dr. Vaia Kalokidou at the Communication Systems and Networks Group, University of Bristol, United Kingdom as part of the 5GPicture project

physical layer design for the rail based simulations is shown. A performance analysis regarding received power, throughput and beamforming gain directional antennas on both sides of the link is performed for two frequencies. Finally, section 4.4 concludes the chapter.

4.2 mmWave Angular and Temporal Statistics

Mobile objects can cause Doppler shifts which has significant consequences in throughput and coverage performance, if for example intercarrier spacing is not properly treated. Moreover, multiple mobile objects normally causing blockage traverse the environment at the same time, thus, dynamically changing the environment. Thus, proper antenna height and placement is vital to avoid such artefacts. For example, an antenna placed at a height of 10m will avoid any blockages by surrounding vehicles for a distance of 255m even considering high-rise vehicles (3m height) and a MS at 300m away from the AP. Theses values can be calculated using the following set of equations.

Assuming the AP is mounted at a height y_1 and the vehicle is at a distance x_1 from the antenna (start of axis to simplify analysis), a right angle triangle of height y_1 and length x_1 is formed. The point that a vehicle of height 3m disrupts the LoS criterion can be calculated as x' and is at the point where $y' = 3$. The equation for x' is calculated as follows.

The line passing through $(x_1, 0)$ and $(0, y_1)$ is of the form $y = ax + b$. If $x = 0$ then $b = y_1$ and if $y = 0$ then $a = -\frac{y_1}{x_1}$. Therefore,

$$y = -\frac{y_1}{x_1}x + y_1 \tag{4.1}$$

Now for a point (x', y') where y' is known to be on the line described by the equation above, equation 4.2 must be satisfied.

$$y' = -\frac{y_1}{x_1}x' + y_1 \Leftrightarrow x' = x_1\frac{y_1 - y'}{y_1} \tag{4.2}$$

To communicate between vehicles and infrastructure, both LoS and NLoS channels are used. The feasibility of NLoS mmWave communication was demonstrated in [103]. Work based on measurements, like [110], clearly gives some insight into the mmWave channel, from which useful conclusions can be made. However it is difficult to focus exclusively on an individual propagation mechanism using traditional measurements, and in that sense, the insight they can provide is limited.

In this section, the evolution of static channel characteristics is studied in both rail and urban environments. The power of the individual paths or rays, the number of signals with independent AoA, the angular separation of signals and the spatial dynamics due to movement are being studied to characterise the channel around both the transmitting and the receiving antenna.

Moreover, parameters defined in static environments are also studied to compare the ray-traced mmWave parameters with the ones specified in the 3GPP and mmMagic models.

Two vehicular environments are being considered for this study; first an urban vehicular scenario at the center of Bristol, UK and second, an urban rail environment starting from Temple Meads train station in Bristol, UK as well. For the first environment, four Base Stations (BS) were placed at the roadside as shown in Figure 4.1(a) in the city centre of Bristol, UK, at the height of 5m (Scenario 1) and 10m (Scenario 2) above ground. The transmit power at BSs was set to 0 dBm and the operation frequency was 60 GHz. Two scenarios are modelled in the urban vehicular environment using different mobile station resolution and transmitter height. A 500m-long route was modelled every 1 cm intervals in scenario 1 and scenario 2 respectively. The mobile station (MS) (or RX) height was set 1.5 m above ground level. A more in-depth analysis regarding the height choices for the Base Stations and the mobile stations in urban environments will be presented in Chapter 6.

Regarding the second environment (Scenario 3), the route was modelled every 1m from the beginning of a 1400m-long rail track, as shown in Figure 4.1(b). Base Station (or Access Point) height was set to 5m and the mobile station height to 2.5m above ground level

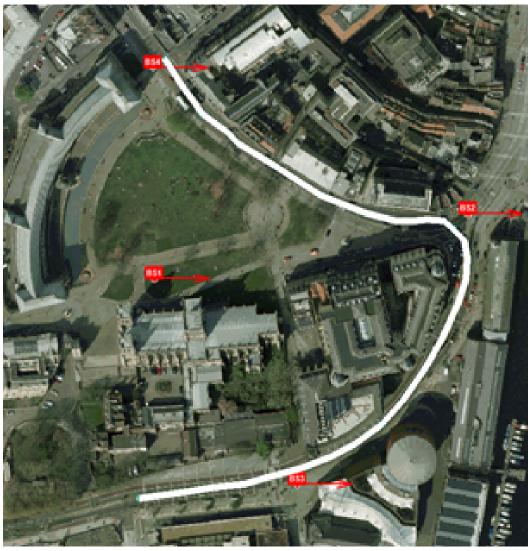

(a) Urban Vehicular Scenario

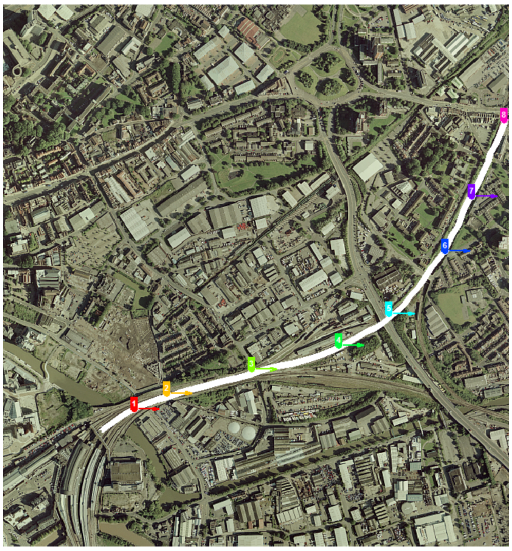

(b) High Speed Train Scenario

FIGURE 4.1. Test Scenarios

Table 4.1 summarises the most important modelling parameters used in the simulations. It should be noted that the environment considered here is a relatively irregular urban environment.

In scenario 1, for each BS 50000 links were simulated therefore channel statistics are given for in total 200000 links. When rays are superimposed from 4 BSs, the channel statistics were given for 50000 links. In scenario 2, for each BS 5000 links were simulated thus the results were given for 20000 links. When rays are superimposed from 4 BSs, the channel statistics were given

TABLE 4.1. Simulation parameters for route scenarios

Parameters	Scenario 1	Scenario 2	Scenario 3
Frequency	60 GHz	60 GHz	26/60 GHz
Database Resolution	5 m	5 m	1 m
Tx height	5 m	10 m	5 m
RX height	1.5 m	1.5 m	2.5 m
Ray tracing interval	0.01 m	0.1 m	1 m
Number of points per route	50000	5000	1400
Route length	500 m	500 m	1410 m
Tx power	0 dBm	0 dBm	0 dBm

for 5000 links. In scenario 3, the number of BSs doubles therefore channel statistics are given for a total of 11280 links (or 1410 when superimposed).

In scenario 2, the simulation parameters (assumptions) are similar to the ones specified in the 3GPP and mmMAGIC model parameters, and hence the results for omni antenna type configurations are comparable. In addition, different TX heights and antenna patterns (10° HPBW directional antenna) were considered at the TX and RX and the parameters were provided for these implementations. Rays were discarded if their powers were below a threshold of 25 dB (unless otherwise stated) relative to the strongest ray as any paths lower than that value are usually non-resolvable and mostly irrelevant to the link.

4.2.1 Angular Characteristics of the Propagation Channel

Characterisation of the angular parameters of the radio channel is extremely important in mmWave environments and especially ones that are predisposed of high mobility. Angular analysis allows us to describe the spread of the multipath environment in all principal directions, allowing better insights on the design parameters of antennas and beamforming properties. In this section, the channel parameters (and especially the angular characteristics) of the environments descibed above are plotted and the nominal values are compared against the proposed ones from the 3GPP and mmMagic standards.

According to the simulations a significant deviation from the standards' update distance values is seen as the LoS ray state is observed to be lasting on average 200 meters in regular environments; a value 4 times larger than the update distance proposed by 3GPP. Severe degradation to this value might be observed if the geometry is really assymetrical or if the placement of the antenna is much lower than the recommended values.

Line of Sight links dominate the mmWave environment. From the total number of links present in all 3 environments, more than 90% of the links presented a LoS component. A lower number of 169340 LoS links were found in the urban evironment (about 84.67% of the total number), when the basestation was placed at a 5m height. However, the increased number of NLoS links is expected, as the placement of the BSs in the urban environment is yet to be

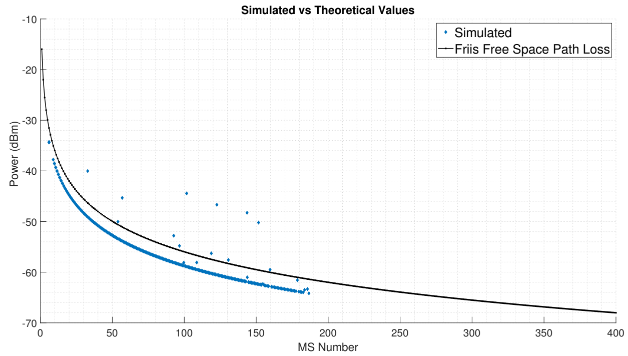

(a) Simulated vs Theoretical Path Loss Cars (Vector Database)

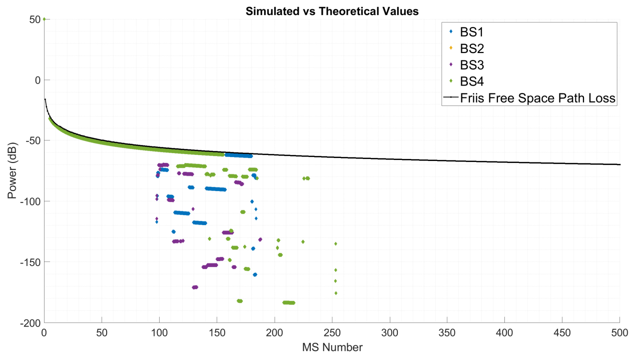

(b) Simulated vs Theoretical Path Loss Urban Scenarios

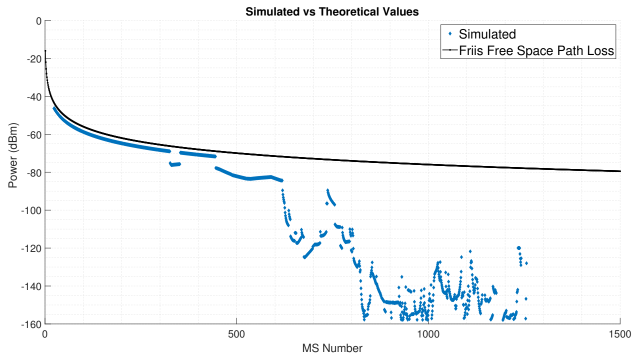

(c) Simulated vs Theoretical Path Loss Train Scenarios

FIGURE 4.2. Simulated vs Theoretical Path Loss Values

optimised and increased blockage from buildings, street furniture and foliage naturally occurs. Figure 4.2 shows the predicted power versus the distance from the basestation compared to the theoretical FSPL (Friis path loss) in the case where the AP is placed at 5m. The differentiation of LoS and NLoS components is apparent in the plot along with the increased number of NLoS links. The effects of antenna placement in link parameters and channel performance will be discussed in detail throughout Chapter 6 of this thesis.

To calculate the angular spread the following method is applied based on 3GPP calculations. First, the LoS angle is set as reference to 0°

$$\phi_1^{[1]} = 0 \tag{4.3}$$

and

$$\phi_{2...L}^{[1]} \sim \mathcal{N}\left(0, \sigma_\phi^2\right) \tag{4.4}$$

Then, the so obtained angles need to be mapped to the interval $[-\phi,\phi]$. This is done by a modulo-2 operation which wraps the angles around the unit circle.

$$\phi_l^{[2]} = \left(\phi_l^{[1]} + \pi \bmod 2\pi\right) - \pi \tag{4.5}$$

The mean power weighted angle $\bar{\varphi}$ estimated as described in Equation 4.4 to calculate the spread:

$$\bar{\varphi} = \frac{\sum_{l=1}^{L} P\left(\varphi_i\right)\varphi_i}{\sum_{l=1}^{L} P\left(\varphi_i\right)} \tag{4.6}$$

Angle wrapping is applied again on the normalized angles $\phi_l^{[2]}$ and $\bar{\varphi}$, thus

$$\phi_l^{[*]} = \left(\phi_l^{[2]} - \bar{\phi} + \pi \quad \bmod 2\pi\right) - \pi \tag{4.7}$$

and

$$\sigma_\varphi = \frac{\sqrt{\sum_{l=1}^{L} P_l \cdot \left(\phi_l^{[*]}\right)^2 - \left(\sum_{l=1}^{L} P_l \cdot \phi_l^{[*]}\right)^2}}{\sum_{l=1}^{L} P\left(\varphi_l\right)} \tag{4.8}$$

It should be noted that this study was conducted with the downlink in mind so angles of departure are the angles for the BS and angles of arrival are the angles for the mobile station. However, this does not affect the modelling parameters as they are still valid for the uplink due to channel reciprocity.

The angular dispersion in urban LoS environments is studied in Figure 4.3. Using the above method as described in 3GPP models, we plot the distribution of angles and spreads in mmWave urban environments. A one sided-Laplacian distribution is observed in the elevation domain,

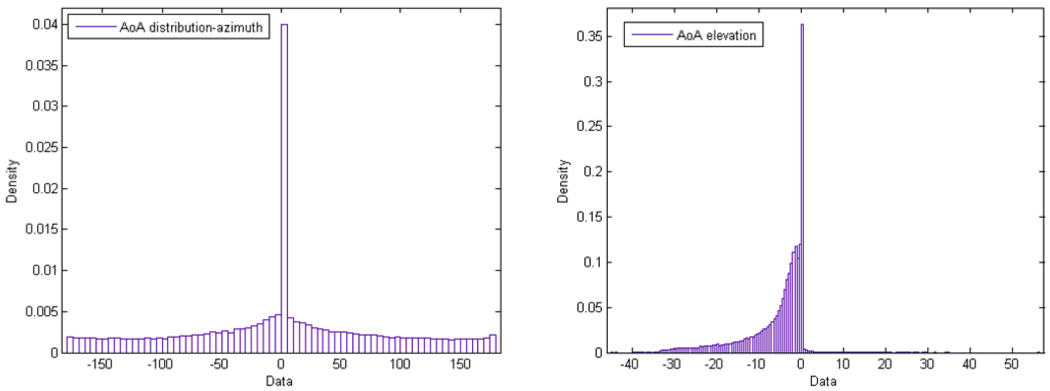

(a) AoA Azimuth Distribution (b) AoA Elevation Distribution

FIGURE 4.3. Distribution of AoA Angles in Scenarios 1 and 2

while in the azimuth domain a wrapped Gaussian Distribution is seen. Similarly, a Laplacian distribution is observed if the method defined in mmMagic standards is observed.

Comparing the AoA spread at azimuth and elevation planes, the results indicate lower values than 3GPP for all route scenarios. (i.e. almost half the spread proposed by 3GPP). AoA spreads were generated in this analysis but by symmetry, the same principles apply to the AoD spreads. No distance dependency is observed in the azimuth spread, however, an exponential dependency on the elevation spread is seen in Figure 4.4.

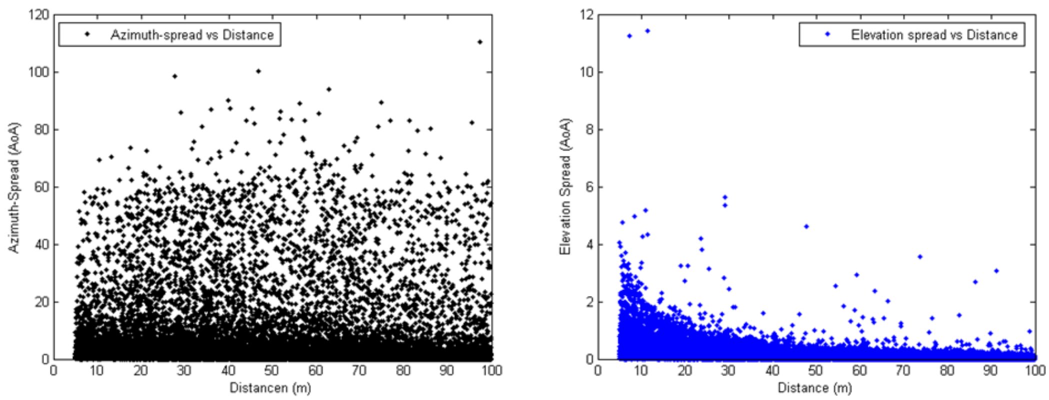

(a) Azimuth Spread Vs Distance (b) Elevation Spread Vs Distance

FIGURE 4.4. Angular Spreads

Delay spread, K-factor and Angle of Departure (AoD) are similar to 3GPP in both urban route scenarios. A larger discrepancy is observed in the delay spreads in rail scenarios where a larger value (almost quadruple) is observed in both LoS and NLoS cases. Even larger difference is seen in the standard deviation in this parameter. Finally, no dependency on distance can be observed throughout the whole route for all environments and scenarios. In general, the standard deviation of all parameters is much higher than 3GPP for both route scenarios for both TX heights (5 m and 10 m). Comparing TX heights of 5 m and 10 m in route scenario, only elevation AoA spread increases slightly as TX height increases. For the rest of the parameters the differences are almost negligible. A detailed view of these values can be seen in Table 4.2 and Table 4.3.

A much smaller number of multipath components (MPCs) than the ones proposed by 3GPP is seen in urban environments. Over all simulations (275000 links for the route), the maximum number of MPCs observed was no more than 18 in the urban vehicular scenario. This is due to the sparse nature of the ray tracing, which under predicts the scattering paths when compared to the measured profiles. This is clearly illustrated in Figure 4.5 which is in agreement to similar studies that highlight the sparseness of the environment at mmWave frequencies.

It should be noted, however, that the number of clusters and MPCs per cluster that the ray-tracer identifies depends on the resolution of the database. A raster database with a resolution of 5m was used to generate the urban dataset, while a 1m resolution was used for the train scenario. A 5m resolution means that in a point to point link the ray-tracer will identify only one reflection (i.e. one MPC) from a 5x5m building. We can see an increase to the number of MPCs in the 1m database which should be totally expected as a higher database resolution means there are more reflecting surfaces (as they exponentially increase), thus leading to a more accurate model of the environment. However, even in the case of higher resolution, the number is still much smaller than the proposed value. In the real world, this link would probably consist of a cluster of MPCs as a result of the local environment, which cannot be represented in the ray-tracer due to its limitations at the point this study was performed. In order to have a more accurate insight into the number of clusters and MPCs per cluster we will need a much more detailed resolution of the database and the effect of diffuse scattering properly incorporated in the model.

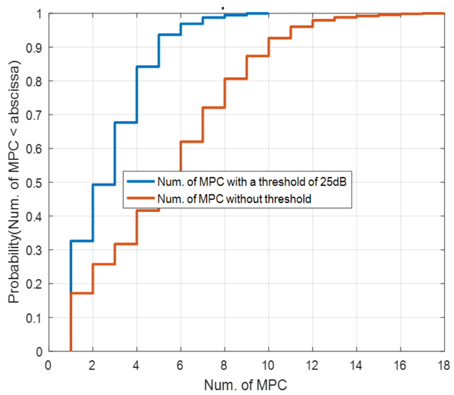

(a) Number of MPC Scenario 1

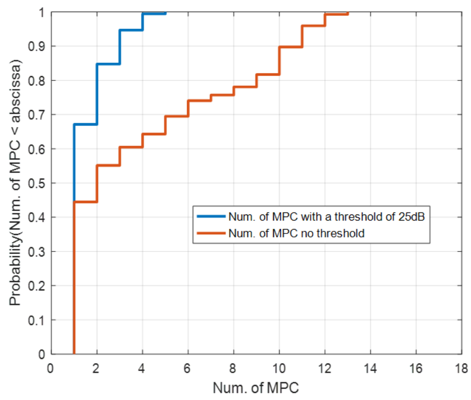

(b) Number of MPC Scenario 2

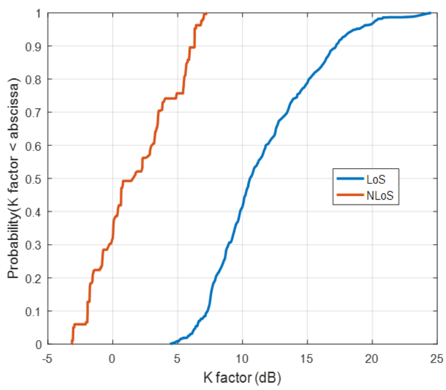

(c) K-factor Scenario 1

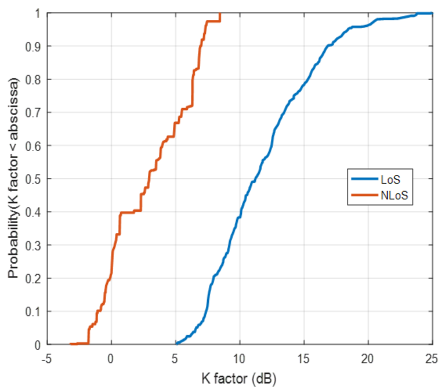

(d) K-factor Scenario 2

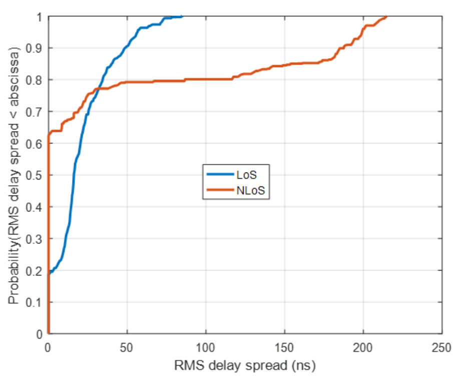

(e) RMS delay spread Scenario 1

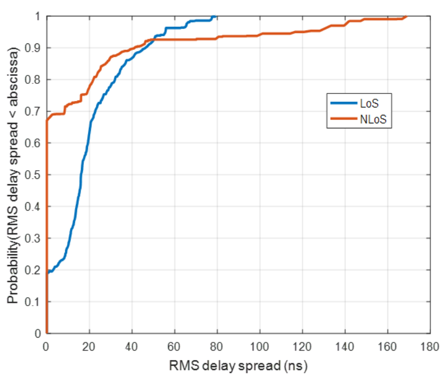

(f) RMS delay spread Scenario 2

FIGURE 4.5. Channel statistics for Omni antennas at TX and RX

Table 4.2: 3GPP, mmMAGIC and Ray tracing parameters comparison at 60 GHz - Urban Environment

Scenario		60 GHz mm-Wave Results (Omni)							
		LOS (3GPP)	NLOS (3GPP)	mm-MAGIC (LoS)	mm-MAGIC (NLoS)	UoB (Scenario 1)(LoS)	UoB (Scenario 1)(LoS)	UoB (Scenario 2)(LoS)	UoB (Scenario 1)(NLoS)
Delay spread -nsecs	m_{mlgDS}	27.5	56.23	20.4	63.2	32.3	65.3	19.72	15.1
	s_{lgDS}	2.39	3.7	0.28	1.8	31.6	66.4	17.34	34.3
AoD spread $lgASD = \log_{10}(ASD/1°)$	m_{lgASD}	13.8	13.18	25.7	7.58	15.9	31.12	11.96	7.96
	s_{lgASD}	2.57	3.36	1.9	1.9	15.2	24.9	9.85	17.18
AoA spread $lgASA = \log_{10}(ASA/1°)$	m_{lgASA}	38.2	45.4	21.1	27.5	16.62	28.1	10	12.73
	s_{lgASA}	2.1	3.36	1.7	1.9	15.3	25.9	8.58	23.02
ZoA spread $lgZSA = \log_{10}(ZSA/1°)$	m_{lgZSA}	3.63	6.19	4.46	5	0.84	0.64	0.65	0.094
	s_{lgZSA}	1.86	1.94	1.72	1.87	1	0.97	0.82	0.22
Number of paths (per cluster)	N	240	380	40	78	4	5	4	2
K-factor (K) [dB]	m_K	9	N/A	4.6	N/A	10.85	N/A	11.74	N/A
	s_k	5	N/A	5.9	N/A	8.67	N/A	3.88	N/A

Table 4.3: 3GPP, mmMAGIC and Ray tracing parameters comparison at 60 GHz - Train Environment

Scenario		60 GHz mm-Wave Results (Omni)					
		LOS (3GPP)	NLOS (3GPP)	mm-MAGIC (LoS)	mm-MAGIC (NLoS)	Train LoS	Train NLoS
Delay spread -nsecs	m_{mlgDS}	27.5	56.23	20.4	63.2	97.12	225.46
	s_{lgDS}	2.39	3.7	0.28	1.8	145.01	162.77
AoD spread $lgASD = \log_{10}(ASD/1°)$	m_{lgASD}	13.8	13.18	25.7	7.58	18.44	28.8
	s_{lgASD}	2.57	3.36	1.9	1.9	23.28	25.14
AoA spread $lgASA = \log_{10}(ASA/1°)$	m_{lgASA}	38.2	45.4	21.1	27.5	10.9	44.6
	s_{lgASA}	2.1	3.36	1.7	1.9	13.22	31.32
ZoA spread $lgZSA = \log_{10}(ZSA/1°)$	m_{lgZSA}	3.63	6.19	4.46	5	1.72	3
	s_{lgZSA}	1.86	1.94	1.72	1.87	1.894	2.4962
Number of paths (per cluster)	N	240	380	40	78	162	130
K-factor (K) [dB]	m_K	9	N/A	4.6	N/A	12.65	N/A
	s_k	5	N/A	5.9	N/A	8.28	N/A

4.2.1.1 Spatial evolution of MPC

Regarding the spatial evolution of MPCs, this section is focused on characterising the rate of change of AoA and AoD in both azimuth and elevation planes as a vehicle traverses through the environment. The analysis performed is based on both LoS and NLoS links as well as on mixed LoS and NLoS links. The figures below depict the evolution of the azimuth and elevation AoD and AoA angles for BS1. As seen in the Figure 4.7, the 2 columns of subplots contain the LoS and

NLoS angles. Apart from the traditional separation of the parameters in LoS and NLoS links, in this part we include the first reflection as well to discuss scattering effects in the channel. Figure 4.6 contains the 1st order reflections for all BS1 links.

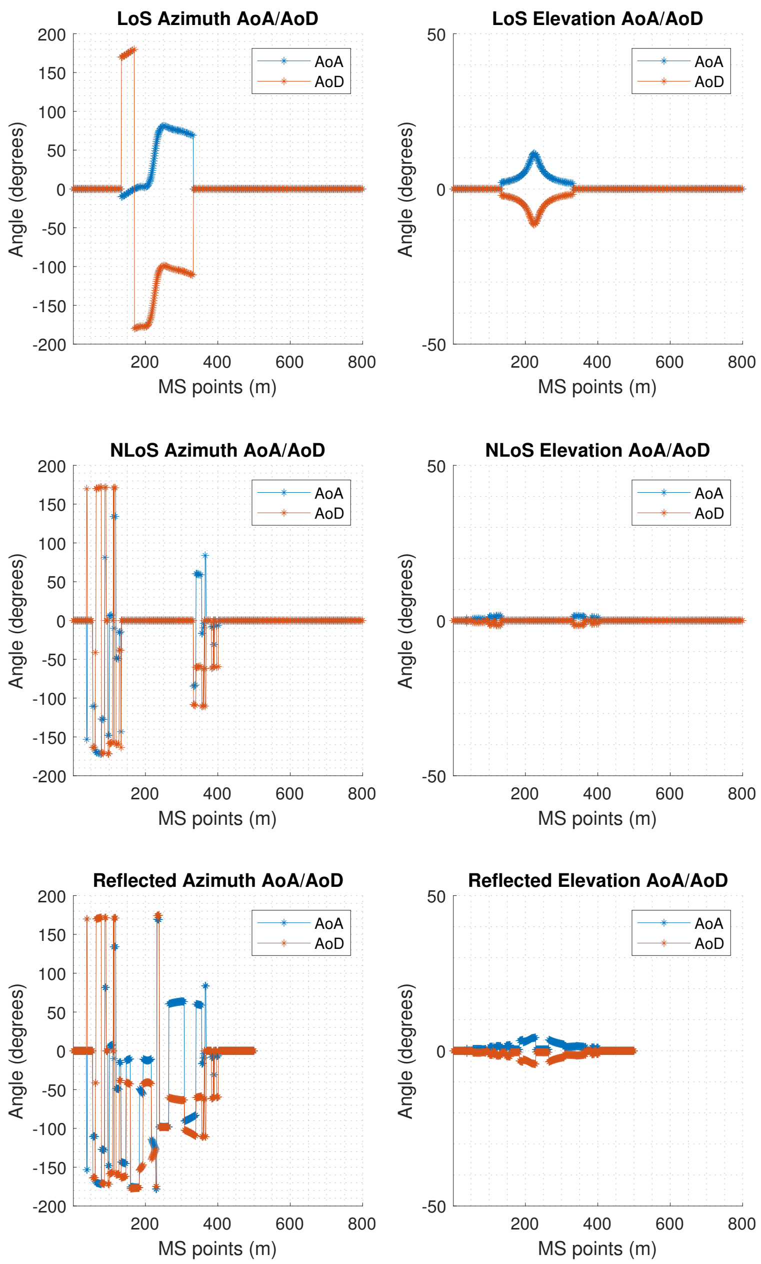

FIGURE 4.6. Azimuth and Elevation AoD/AoA vs distance for LoS and NLoS links (BS1)

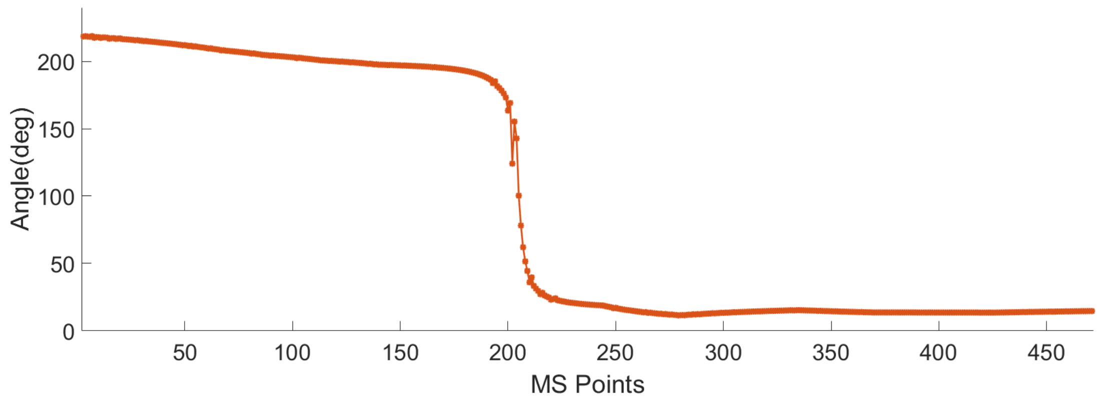

FIGURE 4.7. Azimuth AoD/AoA vs distance for in Rail Environments (BS2)

In the NLos and reflected cases, small spread of angles can be observed, while an increased angular range can be seen in the LoS case as expected, due to the MS being close to the BS. Regarding the azimuth plane, the LoS links display the expected behavior, while irregular observations are seen in the NLoS and reflected rays. Thus the LoS links do not only display higher power due to reduced interactions with the environment, but will always display more predictable angles allowing more straightforward design choices to be made for beamforming. In this case, the angular range does not even exceed 200 degrees even with random BS placement.

Furthermore, to be able to provide a metric regarding the rate of change of the above parameters, beamwidths of 8, 10, 15, 50 and 90 degrees were considered to investigate when (according to the profiles seen above) the MS and the BS have to perform a search for a new beam. In the tables below, we can see the travelled distance required in each case for every BS and each scenario before a new search takes place.

TABLE 4.4. Rate of Change of Angles - Urban Vehicular

	8 deg	10 deg	15 deg	50 deg	90 deg
LOS (m)	26.3	31.3	32.7	59.4	74.2
NLOS (m)	4.8	4.58	5.17	5	7.64
1st order reflection (m)	8	6.38	7.02	6.3	10

TABLE 4.5. Rate of Change of Angles - Urban Rail

	8 deg	10 deg	15 deg	50 deg	90 deg
LOS (m)	23.667	28.396	37.979	58.16	76.5
NLOS (m)	6.2323	7.91875	8.079	16.25	8.5
1st order reflection (m)	6.6098	8.69	9.34	7.3	13.5

Thus, regarding spatial consistency, results indicate that NLoS ray parameters should be updated more frequently than LoS parameters (i.e. 6 meters intervals, whereas 3GPP proposes 12 meters).

4.2.2 Impact of Antenna and Beamforming to Channel Characteristics

The 3D ray model provides accurate space-time characteristics of the propagation channel, allowing beamforming (BF) to be applied in post-processing to model the steerable antenna arrays [111].

Considering our antenna model, an array with a main lobe of Gaussian form in linear scale and constant level of side lobes was generated. Maximum power ray BF algorithm that selects the best steering direction depending on the ray with the highest received power was implemented. This beamforming algorithm essentially assumes an infinite resolution codebook, meaning that the antenna can steer the beam towards the angles of the maximum received ray, whichever that may be. The effects of beamforming and antenna patterns to the propagation channel were plotted and statistics were derived to characterise and compare with already existing models. These parameters are shown in Tables 4.3 and 4.6.

Multiple antenna and beamforming datasets were simulated and the effects of directional and omnidirectional configurations were studied. Initially, as in the previous section, omni antenna parameters are drawn. We then apply directional antennas through beamforming on one side of the link, i.e. either on the transmitter or the receiver side. In both cases, all spreads are reduced along with the number of MPC, although the degree of reduction slightly varies depending which side the beamforming is applied. When beamforming is applied on both sides of the link, all spreads (delay, AoD azimuth, AoA elevation and azimuth) and the number of MPCs are radically reduced to fractions of the omnidirectional values, whereas K factor is increasing as expected.

Finally, when all the rays are superimposed from 4 BSs, all spreads (delay, AoD azimuth, AoA elevation and azimuth) and the number of MPCs are increasing whereas K factor is decreasing. The superposition of the rays is important in this research as it allows us to discuss system performance and eliminate the effect of any outliers that might occur in specific areas of the route. This increased spread is totally expected as there is no consistent method of placement of the antennas on roadside, while an assymetrical topology is observed throughout the urban environment.

Measurement results performed as part of an analysis in [66] indicate a similar behaviour to ray tracing simulations, with respect to both number of clusters and number of rays within the profile when beam-forming was applied to one end of the link. In the measurement studies, results for LoS and NLoS locations are taken from real measurements at 60 GHz, at multiple locations in the University of Bristol campus. In these studies, one end of the link consists of a directional transmitter with 20 dBi of gain, whereas the receiving end is a synthetic isotropic receiver. Measurements indicate no more than 3 spatial clusters are present when LoS propagation is considered and no more than 2 spatial clusters for NLoS links. The temporal processing of

TABLE 4.6. Ray tracing parameters at 60 GHz with omni and directional antennas at the TX and RX

Scenario		60 GHz mm-Wave Results - Beam forming							
		TX: Omni/ RX: Omni (LoS)	TX: Omni/ RX: Omni (NLoS)	TX: Omni/ RX: Directional (LoS)	TX: Omni/ RX: Directional (NLoS)	TX: Directional/ RX: Omni (LoS)	TX: Directional/ RX: Omni (NLoS)	TX: Directional/ RX: Directional (LoS)	TX: Directional/ RX: Directional (NLoS)
Delay spread -nsecs	m_{mlgDS}	20.79	39.54	3.71	4.1	4.46	2.65	$3.9e^{-4}$	0.0158
	s_{lgDS}	18.12	71.3	8.08	18.46	11.64	10.45	0.008	1.13
AoD spread $lgASD = \log_{10}(ASD/1°)$	m_{lgASD}	11.84	14.74	4.08	2.7	0.15	0.12	$4.2e^{-4}$	0.0032
	s_{lgASD}	9.87	24.5	8.34	10.74	0.31	0.34	0.0087	0.0379
AoA spread $lgASA = \log_{10}(ASA/1°)$	m_{lgASA}	10.75	13.91	0.12	0.084	3.15	12.73	0.0017	0.02
	s_{lgASA}	8.75	22.31	0.27	0.39	7.04	0.0064	0.032	0.2
ZoA spread $lgZSA = \log_{10}(ZSA/1°)$	m_{lgZSA}	0.29	0.081	0.031	0.005	0.014	0.64	$7.7e^{-7}$	$5e^{-6}$
	s_{lgZSA}	0.38	0.14	0.078	0.034	0.036	0.021	$1.5e^{-5}$	$2.9e^{-4}$
Number of paths (per cluster)	N	4	2	2	2	2	2	2	2
K-factor (K) [dB]	m_K	11.55	1.82	16.37	9.69	16.82	6.42	24.462	14.08
	s_k	3.94	3.07	3.44	4.14	3.93	4.42	0.2778	2.17

TABLE 4.7. Ray tracing parameters at 60 GHz with omni and directional antennas at the TX and RX. Beam forming is applied to the isotropic data. Rays from 4 BSs were superimposed

Scenario		60 GHz mm-Wave Results (Omni)					
		LOS (3GPP)	mm-MAGIC (LoS)	TX: Omni/ RX: Omni (LoS)	TX: Omni/ RX: Directional (LoS)	TX: Directional/ RX: Omni (LoS)	TX: Directional/ RX: Directional (LoS)
Delay spread -nsecs	m_{mlgDS}	27.5	20.4	43.26	31.15	30.28	28.73
	s_{lgDS}	2.39	0.28	28.29	28.46	30.66	29.91
AoD spread $lgASD = \log_{10}(ASD/1°)$	m_{lgASD}	13.8	25.7	27.46	22.42	19.21	19.02
	s_{lgASD}	2.57	1.9	23.45	25.71	26.75	26.64
AoA spread $lgASA = \log_{10}(ASA/1°)$	m_{lgASA}	38.2	21.1	25.68	19.17	19.49	19.16
	s_{lgASA}	2.1	1.7	23.99	26.68	26.82	26.75
ZoA spread $lgZSA = \log_{10}(ZSA/1°)$	m_{lgZSA}	3.63	4.46	0.56	0.34	0.31	0.30
	s_{lgZSA}	1.86	1.72	0.5	0.4	0.42	0.42
Number of paths (per cluster)	N	240	40	5	3	3	2
K-factor (K) [dB]	m_K	9	4.6	9.45	13.3	12.87	13.14
	s_k	5	5.9	5.2	6.69	7.21	7.27

those results shows explicit similarity to the ray-traced simulated scenarios with directional transmitter and omnidirectional receiver, as no more than 10 spatio-temporal paths were observed for all measurement profiles. This analysis show significant disagreement to 3GPP parameters, where 12 and 19 clusters are proposed for LoS and NLoS locations respectively. Furthermore, the number of paths proposed are 20 per cluster whereas the simulation and measured results presented here show not more than 18 paths in total. However, this is representative of a picocell rather than a longer range vehicular scenario, where clusters might increase due to the increase of reflectiong surfaces.

4.2.3 Ray Birth/Death Statistics

In this section, birth and death position of each scatter component and LoS components along the route was identified for the four BSs in the urban vehicular scenario. This was done by post-processing the ray tracing data shown in Section 1.1.1.

The birth and death of a ray describes when a ray appears and disappears and more importantly the distance or length it has been visible for. This is used an indicator to know how frequently (or fast) an antenna needs to switch to track the strongest ray as part of its beamforming. It should be noted that only first and second order reflections are used in this study, as further reflections are non-resolvable in mmWave environments.

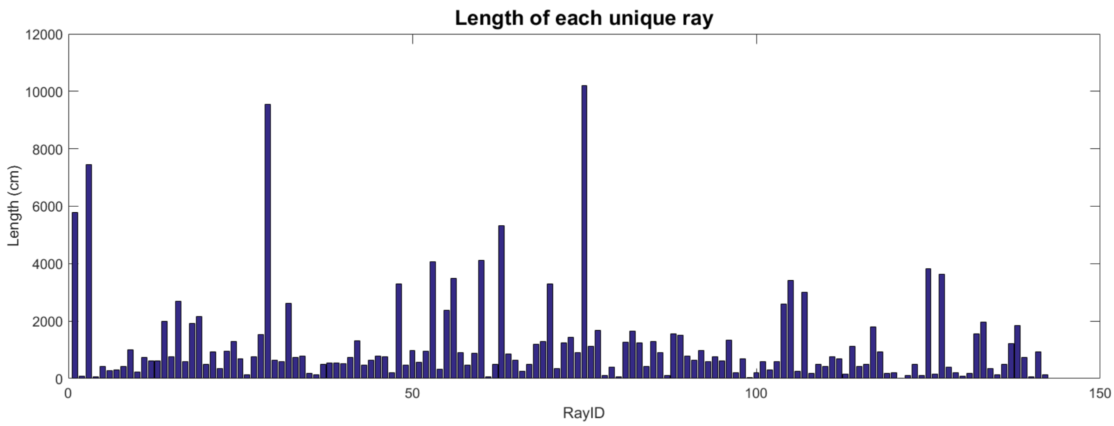

FIGURE 4.8. Length of Each Ray Component in the Environment (Birth/Death of the Ray)

Birth and death was investigated by using ray tracking data obtained from the ray-tracer for scenarios 1 and 2. The following steps outline the procedure used to derive those values.

1. Each ray modelled in the ray-tracer was given a unique identification (ID). This was done by defining any ray reflected from the same surface or wall as the same ray (hence same ray ID). As for second order reflections (a ray reflecting off two surfaces sequentially), any ray reflecting from the same two surfaces in the same order (i.e. reflect off wall 1 then wall 2) was considered as the same ray, hence same ray ID.

2. All rays with same ray ID were grouped together.

3. Each unique ray was then tracked at every point and the length of each unique LoS and NLoS rays were then calculated.

The bar chart shows that there were 142 distinguishable rays. Only three rays lasted for a length of more than 6,000 cm while the majority of rays are below 2,000cm. This is displayed better in Figure 4.9 where the CDF plot of the ray length is presented. It is shown that 80% of the rays have a length of 2,000 cm or less while the other 20% have lengths that range from 2,000 - 10,000 cm. The mean ray length was calculated to be 1,170 cm having a standard deviation of 1,580 cm. The maximum ray length from these results was 10,200 cm. These values confirm the results presented in the previous sections, showing comparable results on the distance each beam is used before a new search has to be initiated.

The ray length data include all the rays from all the four BSs. It is shown that LoS rays last significantly longer than NLoS rays. For the 500 m route, the median length is 200 m for LoS rays and 6 m for NLoS rays. It should be noted that there is much less samples for LoS rays as there are maximum 2 unique LoS rays per BS. In average there is only 126 unique NLoS rays along the route. The results show that the spatial consistency parameters for NLoS links should be updated more frequently than LoS link. This further supports the validity of the results shown for the angular rate of change, where in all cases the rate of change for NLoS rays was significantly larger compared to the LoS ones.

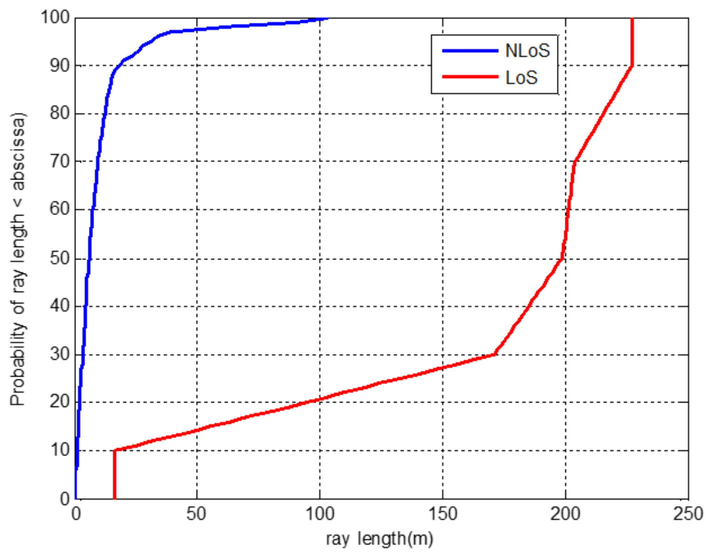

FIGURE 4.9. CDF of Ray Length

4.3 Performance Evaluation of mmWave and Beamforming in 5G Communications

As stated above, user mobility poses several challenges in mmWave vehicular systems, as the channel state is constantly changing. Channel capacity, throughput and coverage are greatly affected by the design of such environments. Specifically, in [112] it was shown that channel capacity varies with the distance significantly. Due to the restricted coverage of such architectures, user mobility will cause significant and rapid signal fluctuations in each BS [113]. This is especially true in High-Speed Train environments, where the speed is considerably larger than urban applications. Thus, mobile station linking and handovers between multiple APs play an important role in the performance of mmWave systems to allow seamless connectivity and optimised load balancing.

Handover performance can be improved if more information about the link is available, such as velocity or direction of travel. Information like this, can easily be transmitted through mmWave systems. Thus, even with all these limiting factors, mmWave systems are a great candidate for vehicular communications due to the inherent low latencies and high data rates allowing such information to be passed through the system. This is especially true in rail architectures where the route and velocities used by the train are more or less predefined, allowing smoother transition between the basestations.

As mentioned above, high throughput is expected in rail terrains, where sometimes optical fiber is difficult to be installed, and therefore the employment of mmWave APs, since mmWave provide very high throughput, along the track side is one of the main solutions considered for both fronthaul (FH) and backhaul (BH) networks. However, many argue that in high mobility vehicular environments, the doppler spread can be too high, due to the small wavelength. Authors in [106] suggest that this is true only for omnidirectional communication, showing that in vehicular channels “the coherence time increases at least proportional to the inverse of the beamwidth” [106].

Regarding high mobility vehicular environments, mmWave solutions seem to provide many improvements compared to current infrastructure such as increased spectral efficiency and data rates (up to several Gbps in some cases). Also, as the beam coherence time is larger than the channel coherence time a reduction in the beam alignment overhead can be observed [101].

Considering mmWave HST communications, beamforming is one of the most important factors to investigate, since it can provide huge data rates. There are several trade-offs that need to be considered though. For instance, the narrower the beam is, the higher the transmission rate gets, providing however additional alignment overhead [114]. Therefore, the choice of beamforming (i.e. fixed, adaptive, location-aided, etc.) should be based on the environment feature and requirements in each case. When the APs are placed close to rail track, it would be beneficial to use wide beams, whereas when there is a greater distance to the track, narrower beams can be used, though

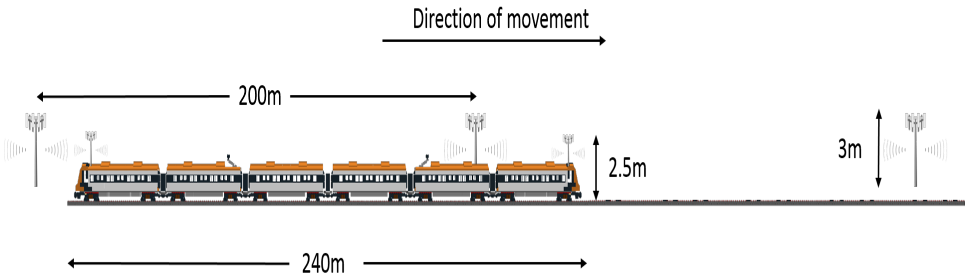

FIGURE 4.10. Network Configuration

reducing rate and coverage. In [106], authors compare three beamforming schemes for HST communication, denoting the importance of a solid wireless FH/BH between BSs on the ground and APs on the train. With the use of directional antennas, they propose three schemes:

1. adaptive beamforming at transmitter (TX) and receiver (RX),
2. fixed beamforming at TX and RX, and
3. fixed beamforming at TX and adaptive beamforming at RX.

The authors conclude that adaptive beamforming provides the highest SINR, with the fixed beamforming achieving similar performance in many cases. Location-aided beamforming is also considered as a solution to robust high data rate communication to HSTs since the route is predetermined in contrast to vehicular communications to cars. However, this beam training method, which exploits spatial information to focus the beam search in specific areas, thus reducing the overhead [106], results in increased noise and degraded beam alignment performance. In [109], authors resolve this issue based on the Bayesian team decision problem.

4.3.1 Railway Application

Our focus in this section is the 5G railway vertical, considering HSTs in mmWave frequencies to demonstrate seamless service provisioning and mobility management support. Therefore, a major aspect of the above would be the wireless solutions for such an environment, resulting in the performance evaluation of the rail environment, in terms of throughput and coverage.

Two different urban rail environments have been considered for this study; the previously presented 1.4 km rail route close to Temple Meads railway station in Bristol, UK (previously scenario 3), and a rail route of equivalent length leading to Paddington train station in London, UK, depicted in Figure 4.11(a) 1. In both environments, mmWave APs are placed alongside of the track with a minimum separation of 2-5m between the AP and the MS. The ray-tracing algorithm was applied on a point-to-point basis at a spatial resolution of 1m along both routes. This configuration is chosen to model a typical scenario of antennas mounted on already existent infrastructure to reduce cost and minimise interference as seen in Figure 4.10. Omnidirectional dipoles that illuminate a circular area around the BS were used in both scenarios for the APs. Modelling and simulations were performed at two different transmit frequencies (26, 60GHz) with a transmit power of 22dBm. Receiver antenna sensitivity was set to -120dB to disregard any low power rays and channel snapshots were taken every 1m throughout the whole route.

The data obtained from the ray tracer were then processed by a Matlab System Level Simulator (developed in the University of Bristol), where an actual train configuration was considered. Maximum ray selection beamforming (MRBF) is applied to each link. As for the train, we consider a train with a total length of 240m (assuming 8 carriages of 30m length) equipped with two antennas, one placed at the front, and one at the rear of the train to achieve receive diversity. The notion of distributed antennas on the train (for instance two per carriage), has been introduced in [115, 116]. With proper AP spacing, distributed directional antennas within the concept of elongated cells, would allow the HST to be connected to multiple cells simultaneously, this increasing performance. The complete network configuration is shown in Figure 4.10.

(a) Paddington Route

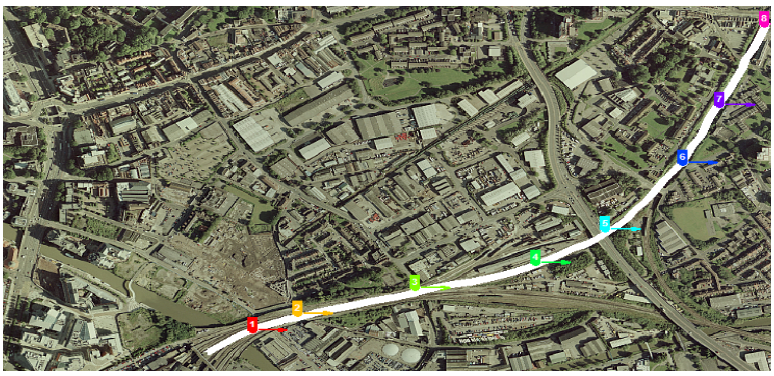

(b) Temple Meads Route

FIGURE 4.11. Train Route Scenarios

Our research focuses on how the distance between the APs, the frequency, and the application of beamforming affect the throughput performance. Most results will be presented based on our simulations for the Temple Meads rail track, however a comparison between the Temple Meads and Paddington routes will be also presented. Considering two antennas are mounted on the train (front and rear) to achieve receive diversity, for all our simulations, we choose the antenna with the highest throughput.

4.3.2 Distance between the APs

The communications links' performance is highly dependent on the amount and density of the deployed Access Points on the side of the rail track. Deploying and maintaining APs in a large scale network application such as national rail can be costly. It is crucial to deploy a number of APs in the most suitable locations, to improve the overall network performance. Given the variety of urban environments, it is necessary to find the optimal spacing of antenna arrays. In this section we discuss how distance between the APs affects the system's performance. Beamforming is applied to both sides of the link and the performance is discussed in environments where the link is dominated by LoS components.

The main metrics we used to evaluate our system performance are capacity and coverage. Coverage is one of most important parameters to discuss when implementing wireless V2I communication systems. Systems may differ in terms of center frequency, modulation, transmission power, cell size, network structure, but adequate coverage must be ensured to avoid any loss of service and severe degradation of QoS metrics. Downlink capacity is another important aspect of wireless networks, as vehicular systems would need to be able to transfer large amounts of data. Scaling of capacity with number of users in the system and the number and complexity of the offered services are really important parameters to be considered but they will not be considered in this study. Instead only a spatial analysis of the environment is performed.

Considering the Temple Meads route, the impact of the distance in which APs are placed as well as the employment of beamforming is investigated. Figs. 4.12 and 4.13 depict the throughput for the journey of the train on the designated track, with no beamforming considered, for distances of 200, 400, 600 and 800m between the APs, for 26GHz and 60GHz respectively. One can observe that the throughput, when APs are placed 200m and 400m apart reaches 4.7Gbps, slightly dropping at 2.8-3 Gbps along the route. When APs are placed further apart (600m), the throughput ranges from 2.5-4.7Gbps, which is still a good result considering that in practice this would allow 400m radius mmWave cells. Moreover, in the case of 800m, the connection drops completely between points 800-1170, which could be optimised if APs were placed in a better spot along the trackside. In addition, similar results were obtained for the case of employing maximum ray selection beamforming, as depicted in Figs. 4.14 and 4.15. The throughput reaches 4.7Gbps, dropping to even 0 at the end of the track for 600m and 800m at 26GHz, and 800m at 60GHz.

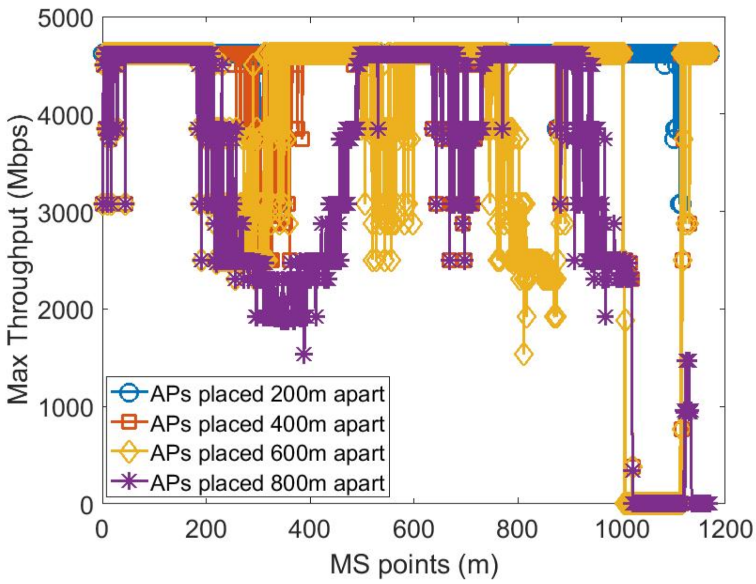

FIGURE 4.12. Max. throughput at 60GHz for various distances between APs (no beamforming)

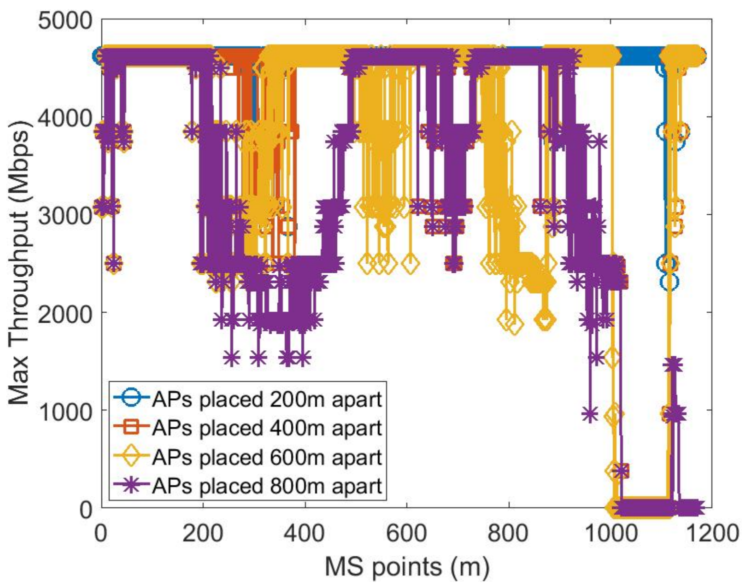

FIGURE 4.13. Max. throughput at 26GHz for various distances between APs (no beamforming)

4.3.3 Frequency Comparisons

Furthermore, a comparison on the performance difference between 60GHz and 26GHz with the application of beamforming was carried out for the Temple Meads rail track, for various

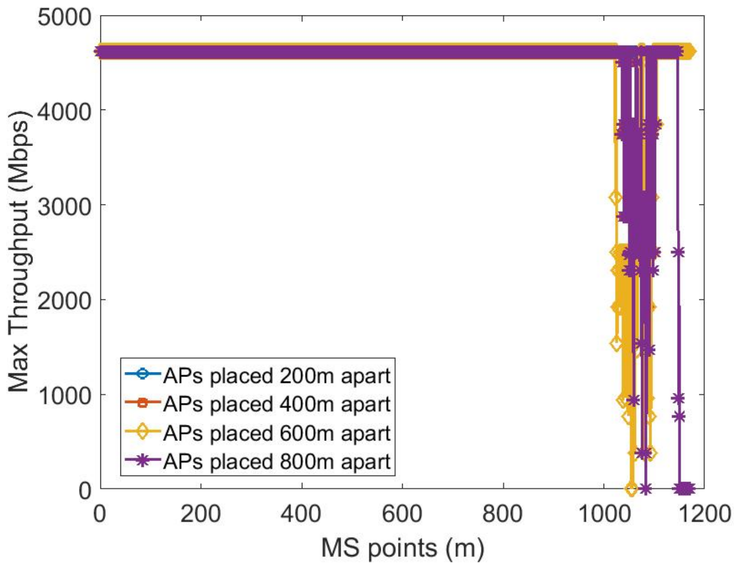

FIGURE 4.14. Max. throughput at 60GHz for various distances between APs (with maximum ray selection beamforming)

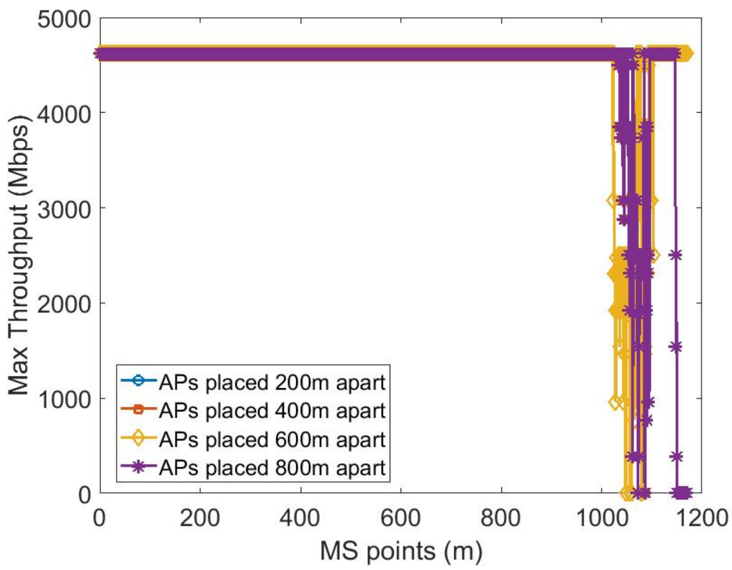

FIGURE 4.15. Max. throughput at 26GHz for various distances between APs (with maximum ray selection beamforming).

distances between the mmWave APs. The employment of beamforming (maximum ray selection) considerably improves the performance, resulting in maximum throughput of 4.7Gbps in all cases. An anomaly is observed in the case of APs placed at 600m apart, throughput ranges between 0-4.5Gbps, along points 1100-1170, as Figure 4.16 suggests, probably due to a misalignment of the eighth (last) mmWave AP. Finally, overall throughput performance at both frequencies follows the same trend, and as the distance between the APs increases the maximum throughput reduces, reaching however acceptable levels even in the case that APs are placed at 800m distance.

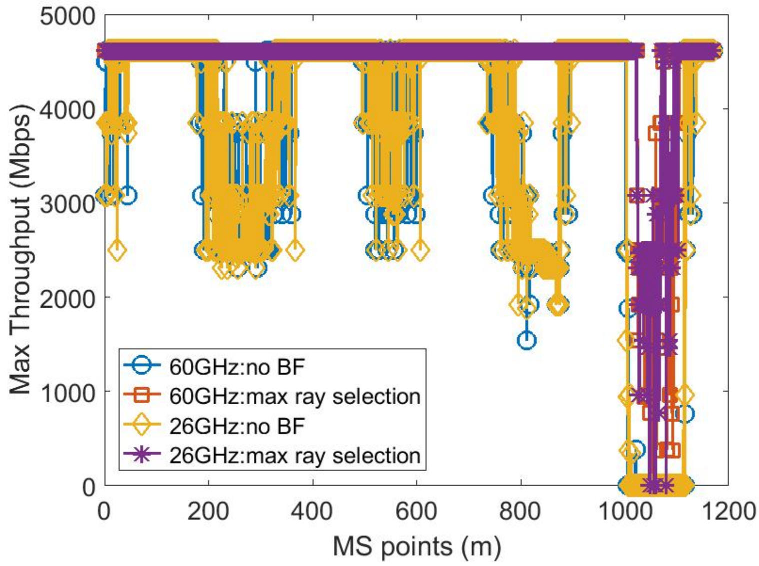

FIGURE 4.16. Max. throughput - 600m distance between APs (60,26GHz)

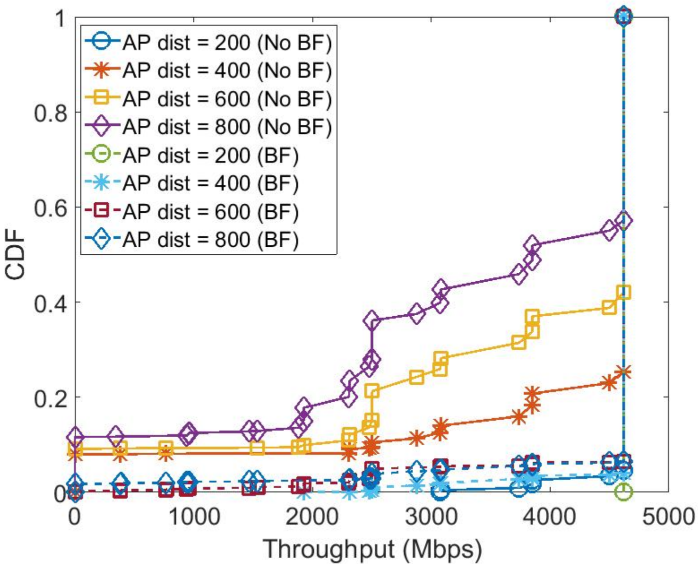

FIGURE 4.17. CDF of Max. Throughput at 60GHz

Moreover, a comparison was made between results obtained for Temple Meads and Paddington. For the case that APs are placed at 400m apart, Figures 4.12 and 4.13 show the maximum

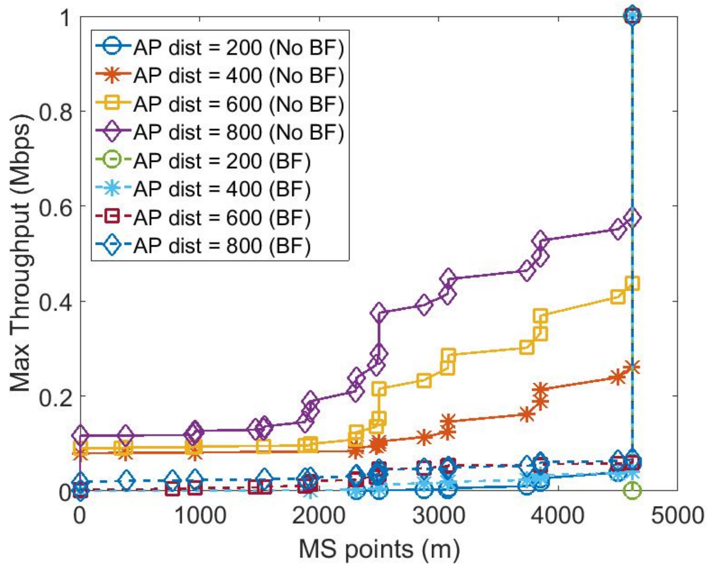

FIGURE 4.18. CDF of Max. Throughput at 26GHz

throughput achieved, by the best antenna on the train, for the cases of no beamforming and beamforming respectively. Without beamforming, results obtained from the Paddington route give lower throughput compared to the Temple Meads scenario. This is by no means unexpected, since we are comparing two different rail environments. Figures 4.14 and 4.15 depicts the throughput in the case of beamforming, resulting in a throughput of 4.7Gbps, for both environments, apart from the case of Temple Meads that the throughput decreases along around 70m at the end of the route. Overall, the trend is similar, although for the case of the Paddington route, there is a more distinctive difference in the throughput performance between 26GHz and 60GHz, with the former resulting in lower values

Even though slightly better performance is observed in an ideal scenario, in the following chapters a frequency of 26GHz will be used due to lower atmospheric absorption, better range performance and lower rain attenuation as these parameters have significantly larger values in 60GHz links.

4.4 Conclusions

In this chapter the angular and temporal characteristics of the wireless channel considering 2 urban environments were studied and compared against well established models for outdoor environments. Azimuth and elevation spreads were shown to largely coincide with the values proposed by 3GPP and mmMagic models, while the number of multipaths vastly differs. The spatial evolution of the multipath components was also studied and a metric for the angular rate of change in terms of beamwidth was derived.

By studying the impact of the antenna parameters and beamforming we can see that most of the channel parameters were affected, with the channel being compressed with the use of beamforming and the relevant parameters were shown. Ray birth and death statistics were drawn to discuss the length of specific rays throughout the environment and to discuss the frequency of beamforming.

Deterministic ray-tracing approaches predict a lower number of clusters and multipaths meaning that in realistic urban environments we can expect less hotspots of of NLOS rays and thus we can focus the beam design to adaptively use the LoS rays. NLoS links are important in vehicular environment as they enrich the wireless media as possible candidates for transmission. However, as birth death statistics and cluster/multipath comparisons with well defined models have shown, LoS rays dominate the links and NLoS links are not as uniformly arranged throughout the environment. This helps when designing beamforming options as NLoS links are only considered as secondary priority and are considered as redundant in many cases except where severe blockage of the main LoS ray. Blockage can be largely mitigated however by correct network planning and design maximising the LoS links to ensure good coverage as it will be shown in Chapter 5 and 6.

The effects of beamforming on throughput performance and antenna spacing were also discussed considering a realistic HST scenario. Considering a train, mounted with two antennas (front, rear) traveling along a real train track (Temple Meads, Paddington), and several mmWave APs placed at the trackside, we have shown that seamless connectivity can be achieved even when APs on the trackside are placed 800m apart. Additionally, the application of maximum ray selection beamforming has considerably improved the throughput performance. The maximum achievable throughput was simulated at around 4.7 Gbps.

The results presented in this section suggest that, in a well-designed track, seamless service, with high data rates, can be achieved with mmWave APs placed along the track every 800m. Moreover, the importance of applying beamforming is clearly shown with regards to throughput improvement. In addition, our system investigation at both 26 and 60 GHz and two rail tracks, shows similar results following the same trend. However, these results are achieved using optimal beamformers, which are computationally expensive and unrealistic in real life deployments. Realistic beamformers based on codebook generation are studied in more detail in the next chapter while compared to those ideal beamformers, while optimisation of such methods is discussed in more detail.

Chapter 5

Impact of Beamforming, Antenna and Codebook Design Upon Performance in High-Speed Train Environments

Beamforming is essential, specifically in HST networks, as it reduces infrastructure costs, meaning fewer APs required for a set route. Adaptive BF techniques have been under long-term development to provide enhanced communication quality. By increasing the directivity of the beam (i.e. making it narrower), we effectively see an increase in the transmit gain and thus in range and transmission rate but require more tightly packed beams and larger antenna arrays. Unlike cellular communications scenarios where users follow random paths and request access from random locations, an HST travels along a predictable path. That makes mobile stations' positions more or less predictable compared to some chaotic vehicular urban environments. Knowing the mobile station's general position and direction of travel allows us to use the limited angular profile to develop more efficient techniques of providing seamless service. By pointing the codebook's beams at specific angular directions, and selecting the best available beam, a good mmWave signal coverage can be achieved around the terminal without the need for spherical coverage.

5.1 Introduction

Previous work presented in Chapter 4 and published in [27] shows that in a realistic railway scenario, even when APs on the trackside are placed 800m apart, the coverage is almost seamless, and throughput is stable whilst using a 15° beam in the transmitter and a 20° in the receiving antenna. However, this performance was calculated using ideal beamforming architectures (Maximum Ray BF) paired with theoretically generated antennas.

Regarding mmWave BF, several works focus on BF based on estimated channel state information (CSI) [53], i.e. finding the optimal weight vector for both the transmitter and receiver. Even though this physical layer solution may provide higher received signal power, acquisition of the entire CSI matrices is time costly and incurs high overhead [117]. Adding up to that the high-power consumption of radio frequency (RF) band electrical elements in order to generate the weight matrices with exact phase shifts and exact amplitudes, optimal physical layer BF may become infeasible for mmWave systems.

As a solution to this increased complexity and overhead, codebook-based BF mechanisms were proposed in many standardised systems, such as IEEE 802.16e [89] and 3GPP LTE [118, 119]. However, the codebooks in [89] and [119] are designed for baseband signal processing, that is, precode or post-code matrix for multiple-input multiple-output (MIMO) systems [120]. In mmWave scenarios this becomes impractical as multiple RF chains are needed, leading to increased power consumption and cost. Moreover, in contrast to MIMO, mmWave wireless networks focus on improved spatial efficiency rather than coding or multiplicity [120] thus favoring the use of codebook-based media access control (MAC) layer solutions.

In Chapter 3, a ray-based double-directional channel modelling approach was introduced, which combines the antennas of a communication system with the radiowave propagation. A system-level simulator was then described to model the achievable throughput and system parameters. This chapter follows the aforementioned channel modelling technique to highlight the significant effect of antennas and propagation on the system-level performance of digital wireless communication systems in High-Speed Train (HST) environments. Antenna arrays digitally synthesised from a single measured patch are used in this analysis to see the effects actual antennas in the channel.

Specifically, this chapter introduces a spatial throughput performance evaluation, assessing the effects of BF and codebook design of HSTs in mmWave infrastructure. The main objective within this chapter lies in the use of the previously derived channel parameters to perform a performance evaluation of different beamforming schemes, and propose a "lighter" codebook, ideal for ultra-high mobility scenarios based on both analytical and simulated data.

Using the approach described in Chapter 3 to model the system and acquire the throughput performance, we investigate the performance of a codebook based approach using a measured antenna. The selected codebook scheme is then compared to the initial omnidirectional scenario, a fixed beam Access Point (AP) configuration and a maximum ray selection beamforming scheme as seen in [27]. A mathematical solution is then derived to provide the angular characteristics that will allow us to maximise range while reducing the number of sectors needed. Using the aforementioned analysis, we will provide a sensitivity analysis to benchmark different codebook mechanisms. Finally, a non-uniform codebook solution and a spatial throughput performance evaluation assessing the effects of codebook design and BF setup time of HSTs in mmWave infrastructure will be presented in terms of both link-level and system-level parameters.

The rest of the chapter is organised as follows. In section 5.2, we describe the system model,

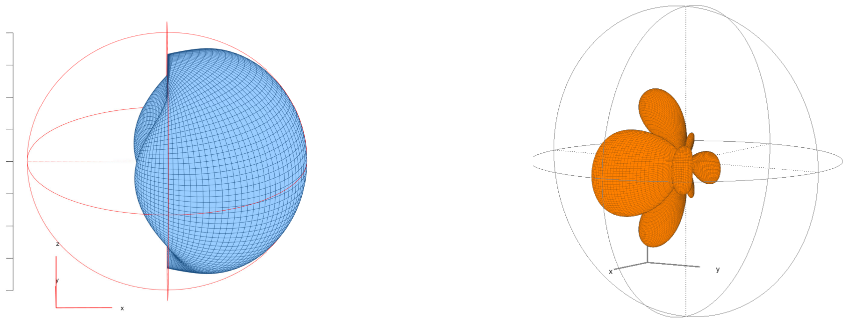

(a) Single Element Antenna (b) Planar Array

FIGURE 5.1. Power Radiation Patterns

network structure and physical layer design. A beam radiation pattern and the resulting uniform codebooks are presented in the same section. The performance of these codebooks is then benchmarked against the ideal Max Ray BF scheme. Following this analysis, we introduce the mathematical model that will allow us to optimise our parameters for any railway configuration and apply them in the generation of non-uniform codebooks. The generated non-uniform codebooks are then generated and analysed to provide the optimal parameter values. Section 5.3 will include a performance analysis regarding received power, throughput and beamforming gain using the proposed schemes. The effects of the codebook parameters in beamforming setup overhead and DEV-to-DEV link time are discussed in Section 5.3. Section 5.4 concludes the chapter.

5.2 Codebook Design in mmWave Train Communications

5.2.1 Uniform Codebook Design

5.2.1.1 Antenna Array Design

As mentioned in Chapters 2-4, a reduction in the antenna's beamwidth results in a higher antenna gain, thus (along with correct planning) allowing us to design the beam to cover a more significant portion of the railway track even though the beamwidth is small. One of our goals with this analysis is to reduce deployment and processing costs for the antennas deployed as APs [27]. Hence, the patch antenna element presented in Chapter 3 was chosen due to the low profile and ease of fabrication. The single element patch was measured in the previously described anechoic chamber to provide the initial radiation pattern with parameters explicitly shown in Table 5.1 and Figure 5.1(a).

As previously presented, as the number of antenna elements increases, the beam gets narrower; thus, the main lobe's width decreases along with side lobes' width. The elements of the array are arranged uniformly along the 2D grid in the xy-plane, with an element spacing d_x in the x-direction and an element spacing d_y in the y-direction based on the operating frequency of the antenna. Hence, the beamwidths in each of the principal directions are determined by a linear array along the corresponding direction.

To ensure the validity of this study, it is vital to correctly model the antenna systems, especially in mmWave and high mobility scenarios where even minor artefacts can severely harm the study of channel and system parameters. Thus, three planar arrays based on the patch antenna element described in Chapter 3 have been modelled for both the Access Point and the Mobile Station antennas and have been chosen to suitably represent the antenna structures employed by such antenna systems in reality. The first array is formed by 12 elements horizontally in parallel (x-axis) and seven elements oriented perpendicular (y-axis) to the direction of flight. The second one is formed by nine elements horizontally in the x-axis and seven elements perpendicularly in the y axis. In comparison, the third uses seven elements horizontally and seven elements perpendicularly. The elements in these configurations are separated by half a wavelength ($\lambda/2$) in both directions. The arrays can achieve 8°, 10° and 15° central lobe azimuth HPBW and a 15° elevation HPBW with the directivities (i.e. gain assuming 100% efficiency) being 24.17 dBi, 23.11 dBi and 22.06 dBi respectively. Figure 5.1(b) shows the total power radiation pattern of one of those arrays with its parameters shown in Table 5.1.

The measured single element patch has 100% of the total radiated power in the horizontal polarisation component of the pattern and 0% in the vertical component. The same is true for the generated arrays as the initial configurations point their main beam towards a plane perpendicular to the ground plane (x-y plane) with no rotation. Hence, an Access Point (AP) employing this type of antenna configuration is expected to affect only horizontally polarised Mobile Stations (MS).

5.2.1.2 Codebook Generation and Parameter Sensitivity

As discussed in Chapter 3, optimum BF incurs a high overhead. The 3c codebook design principles that were defined in Chapter 3 will be used to generate the desired configurations using the above-synthesised antenna array by phase modulation of the array's elements. Moreover, general asymmetric antenna systems (AAS) are considered in this work for the following reasons:

TABLE 5.1. Patch Antenna Parameters

Parameter	Single element Antenna
Azimuth HPBW (deg)	90
Elevation HPBW (deg)	121
Gain (dB)	6.8

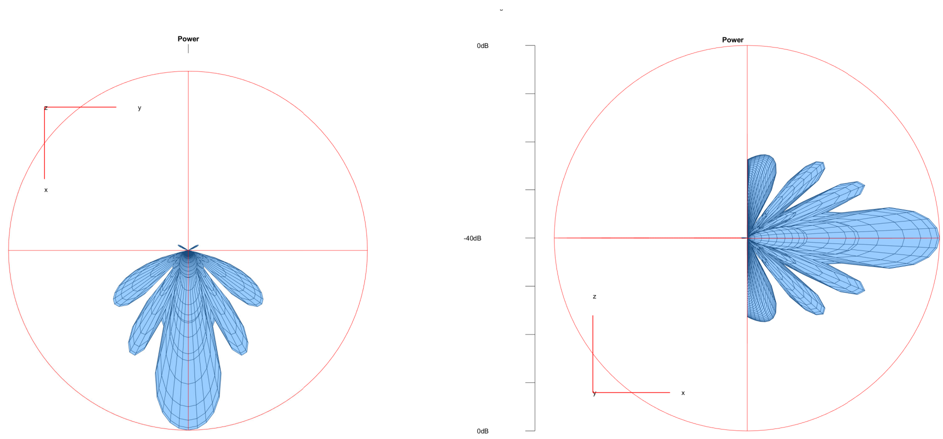

(a) Antenna Top View (b) Antenna Side View

FIGURE 5.2. Top and Side view of the array pattern

1. Different antenna array configurations are used in the transmitter and receiver side.

2. Element subsets the antenna array may be used for transmission or reception to generate different beamwidths or beam patterns.

3. Reciprocity of both communication directions is not guaranteed in a fast-moving vehicle scenario and different paths may arrive at the two ends of communications links

Following these principles, several codebooks were initially designed by employing 8, 16, 32 and 64 beam patterns, uniformly spread around the AP and MS azimuth plane. These values were chosen to study the trade-offs between beamwidth, processing power and sector sweep overhead that would still achieve good coverage. It should be noted that rotation of the antenna in the azimuth plane does not affect its polarisation characteristics (as is the case with rotation in elevation); instead, it only changes the direction of the pattern beams and nulls.

The performance of those codebooks was then investigated using 8°, 10° and 15° half-power beams. Preliminary analysis showed that for an eight beam pattern, the most robust configuration was employing 15° beamwidths as any higher gain beams would leave large areas of nulls in the azimuth domain. For the same reasons, the 16 beam configuration was paired with 10° beams and the 32 and 64 beam codebooks with 8° beams. Configuring our codebooks this way ensured coverage through the whole azimuth domain while at the same time radiating at the highest gain possible.

In Chapter 4, two real-world HST scenarios were modelled using the University of Bristol's outdoor 3D ray-tracing software tool to provide some analysis on channel parameters, frequency, application of beamforming and network infrastructure. The same two propagation environments in London and Bristol's city centres will be used in this chapter to provide an analysis on the

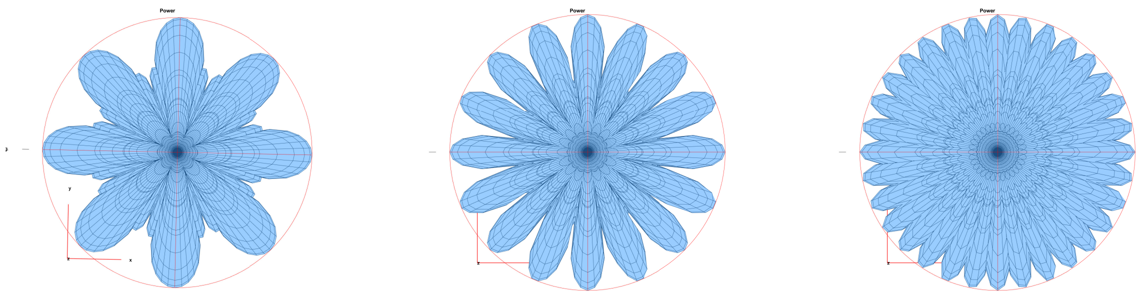

(a) 8 Beam Resolution (b) 16 Beam Resolution (c) 32 Beam Resolution

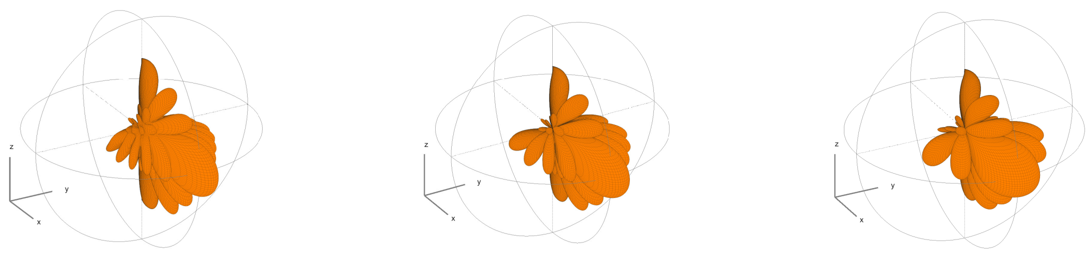

(d) 8° HPBW (e) 10° HPBW (f) 15° HPBW

FIGURE 5.3. Antenna and Codebook Radiation Patterns

effects of Codebook approaches to beamforming. These two scenarios are the ones presented in Section 4.2.

The effect of the different resolution uniform schemes is investigated. The scenario is presented in Figure 4.11(b), with APs deployed at locations separated by 800m. The received signal power at every point in the route is plotted versus its HST location. Figure 5.4 shows a clear improvement on the SNR of the channel over the whole route as the codebook beams increase. Due to the experiment setup dictating that the higher the resolution, the narrower the beams that are employed, the 64×64 case provides the highest SNR with the least amount of fluctuations, due to tight beam packing. In the 32×32 case, we can observe a similar pattern but with some variation in the SNR levels throughout the route, while in lower resolutions, a considerable drop in the received signal strength and an increase in the channel fluctuations are observed. However, 64-Beam AP and MP incur very high overhead during the setup time and reduced resolution codebooks such as the 32-Beam configuration might be more viable in a realistic configuration. Thus, for the rest of the analysis, the 32 beam pattern configuration will be used as the selected uniform scheme, as it provides a good trade-off in SNR and link time.

Further analysis was performed to capture the effects of using different resolution codebooks in the AP and MS. However, no effects of SINR improvements were observed in cases of assymetrical AP and MS configurations; i.e. different number of AP and MS beams.

The main concern with HST and generally any vehicular scenario is seamless connectivity. With the high speeds observed in these scenarios, antenna misalignment due to slow update speed reduces the achievable performance and might cause loss of service. Thus, minimising the device setup and beam selection time between AP and MS is important as it reduces channel aging artifacts (these will be studied in more detail in Chapter 6).

Several APs need to be placed periodically to achieve constant connectivity throughout a rail route. Scaling this to a national rail network or even just large network sections, would incur considerable deployment costs to the provider. Range and distance between the APs were two critical factors for the analysis discussed in Chapter 4. However, apart from the total number of antennas to be used, the cost of each antenna array, depending on its physical characteristics and processing complexity, is a vital parameter in the cost equation. Thus, the most simplistic configuration needs to be examined and compared against beamforming techniques to find the ideal trade-off between performance, setup time and cost.

A preliminary examination of the ray-traced AoA and AoD using omnidirectional antennas gives us some insight into the best beamwidth configurations to be chosen for each specific scenario. As seen in Figure 5.5(a) where the highest power angles per MS point are plotted for one AP, there is no substantial variation in the transmitted and received angles for the majority of the route. This pattern can be observed in the area around one of the APs of the Bristol route, but similar observations can be drawn for every AP in the route on every scenario in Line-of-Sight (LoS) links. At distances larger than 30m from the AP, a connection can be maintained with beamwidths of 20° in the azimuth domain. A further increase to 30° allows the AP to serve the MS up to a distance of 10m without a change in the beam pattern.

Considering the angular profiles shown in Figure 5.5, another planar array based on the same patch antenna element, has been theoretically modelled to cater for another simulation scenario to be evaluated; a fixed beam AP configuration. In the fixed beam scenario, the antenna is

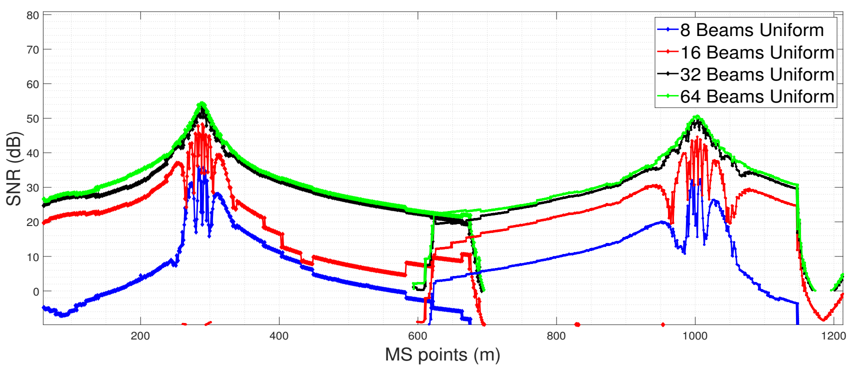

FIGURE 5.4. SNR per MS point for AP_2 and AP_6

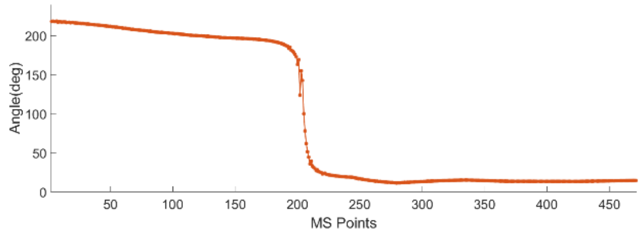

(a) Evolution of AoA through the route

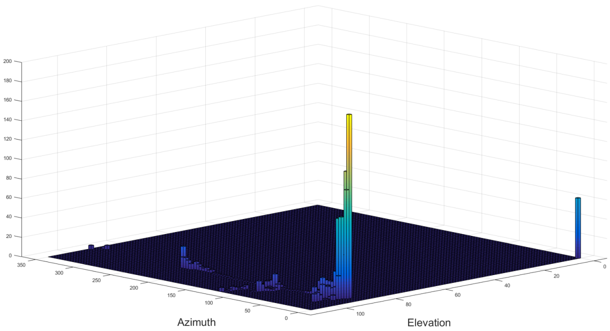

(b) Histogram of the most common angles (degrees)

FIGURE 5.5. Angular Profile of the Temple Meads route in degrees

TABLE 5.2. Antenna Array Parameters

Parameter	**Codebook**	**Fixed AP**
Array azimuth HPBW (deg)	14	30
Array elevation HPBW (deg)	20	17
Array Gain (dB)	21	18

generated and then for each AP manually rotated to face the most common AoD angle. According to the angular profiles, an AP with a beamwidth of 30° in the azimuth and 17° in the elevation plane. Figure 5.2 shows the 7×5 configuration required to produce such Half-Power-Beam-Width (HPBW) at 26GHz with a separation of half a wavelength ($\lambda/2$) between the elements. The resulting gain and HPBW values are shown in Table 5.2 in comparison to the chosen codebook array configuration.

5.2.1.3 Throughput and Coverage Performance of Uniform Codebooks

The rest of this section will focus on how the application of a uniform codebook-based BF approach affects the system performance and minimum distance between the APs in multiple frequency bands. Initially, results from both rail environments will be presented, despite no significant difference, to allow for comparison. As we proceed further with the analysis, only the Temple Meads case will be shown, and the conclusions drawn are equally applicable to the other case.

First, the effect of the various beamforming schemes is investigated. The scenario in Temple Meads is presented in Figure 5.6, with APs deployed at locations separated 400m between each other. The received signal power at every point in the route is plotted versus HST location showing a clear improvement on the SNR of the channel when any BF scheme is applied with maximum power ray BF having the best performance of all the schemes. Similar behaviour was observed in the London scenario on both frequencies as well.

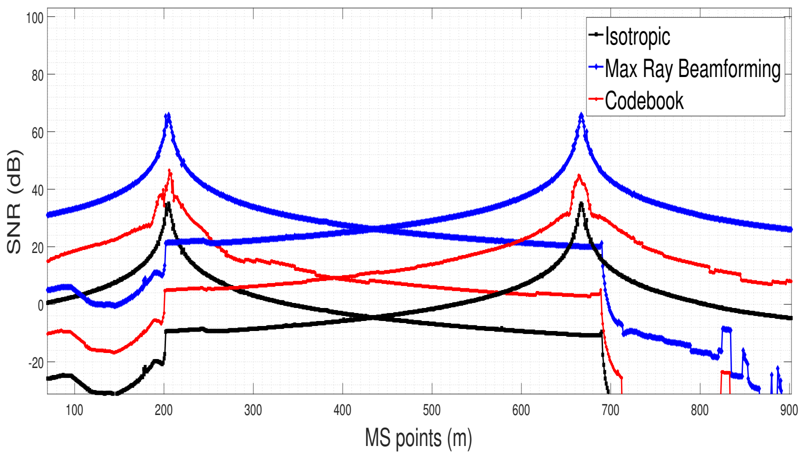

FIGURE 5.6. SNR per MS point for AP_2 and AP_4

Figure 5.8(a) depicts the throughput for the route of the train on the designated track, with no beamforming (isotropic antenna), for separations of 400m (i.e. 4 APs), 600m (3 APs) and 800m (2 APs). The line showing results for the initial 400m separation is not easily distinguishable as the 600m and 800m spacings overlay the line. However, with a closer inspection, we can see that it holds the highest value between the 600 and 800 lines. One can observe that the throughput when APs are placed 400m and 600m apart reaches 4.7Gbps in some cases but with significant variations. When APs are placed further apart (600m), the throughput ranges from 4.7Gbps, dropping down to even 0 Gbps in some places along the route. Moreover, in the case of 800m AP spacing, the connection drops entirely between points 350-700. This loss of service could be avoided if APs were placed in better locations along the trackside but clearly shows that isotropic solutions without a high gain can perform poorly in rail scenarios.

Figure 5.8(b) considers the case where the fixed antenna was employed in the AP side, while

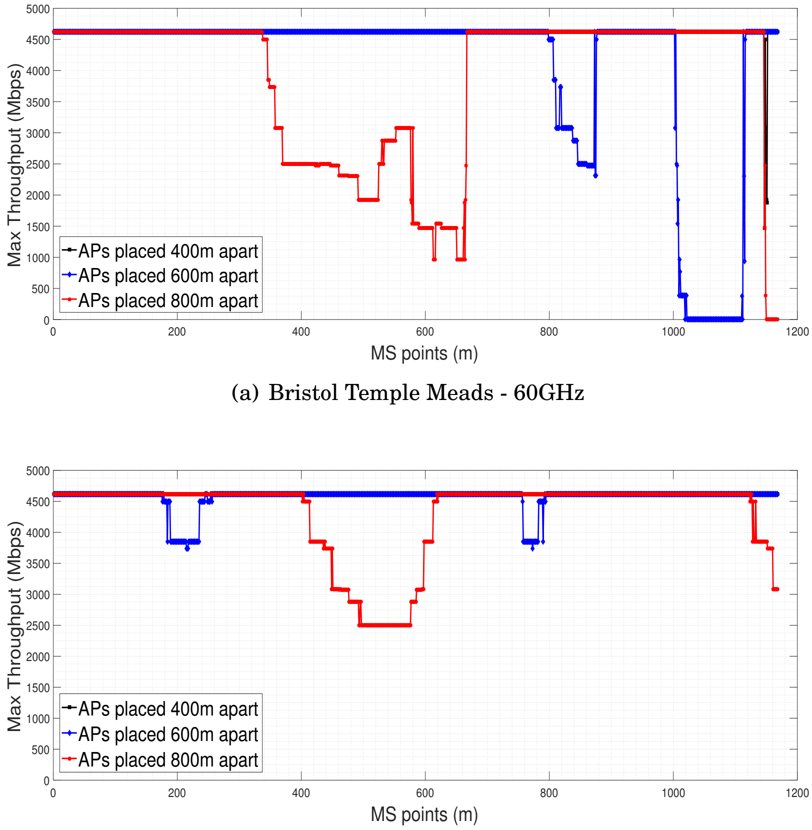

(a) Bristol Temple Meads - 60GHz

(b) London Paddington - 60GHz

FIGURE 5.7. Codebook (CB) throughput per MS point

the APs were placed 400, 600 and 800m apart. If APs are placed 400m apart, the network can provide connectivity to the train for the majority of the route. While the APs are moved further and further away, data rates and coverage severely deteriorate, and significant drops in throughput are observed throughout the route.

Results for the case of employing maximum ray selection BF are depicted in Figure 5.8(c). In this figure, a clear improvement over the whole scenario is observed. Maximum ray selection seems to provide full coverage in the scenario where APs are spaced 400m apart. A slight drop to 0 Gbps is observed around the edge of the track. That, however, occurs due to blockage caused by an overhead crossing present in that area of the track. This loss of service is a direct result of the ray tracer's lack of tunnel models, especially when in mmWave frequencies LoS dominate the links. This is confirmed by comparing to the London scenario, where no such loss of service is observed throughout the route, as seen in Figure 5.7(b). In Figure 5.7(a) where the codebook scenario is plotted, we can see a similar pattern to the optimal beamformer but with some variation in the throughput levels throughout the route.

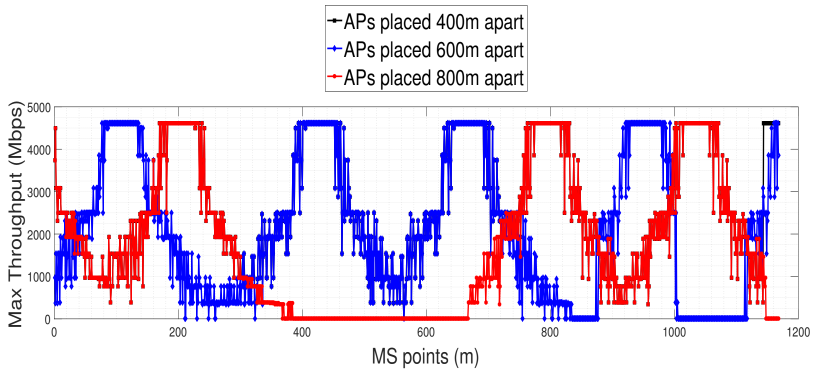

(a) Isotropic

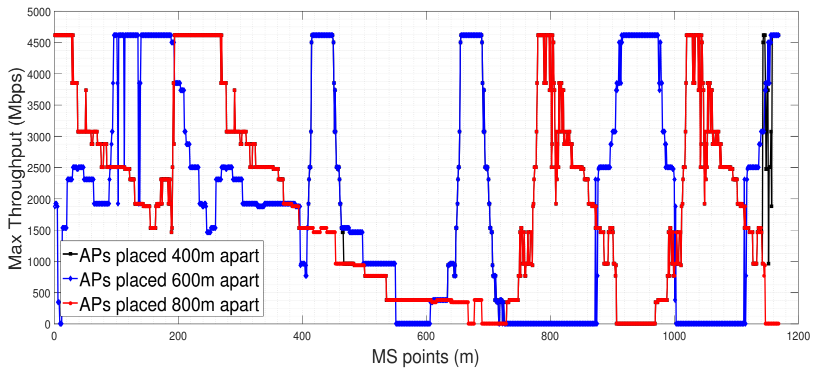

(b) Fixed AP

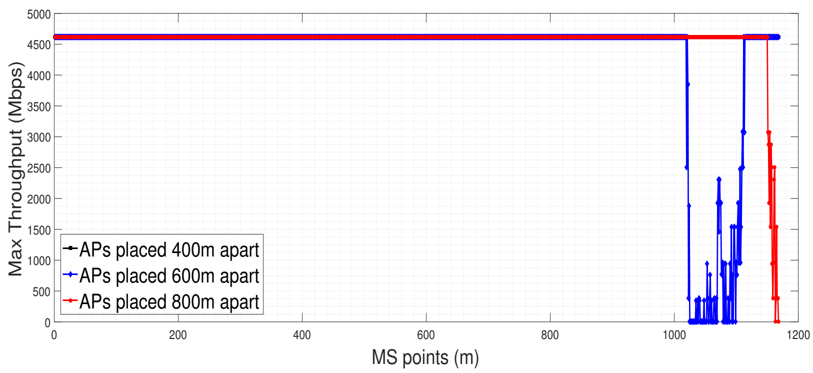

(c) Maximum Ray BF

FIGURE 5.8. Throughput Performance in 3 Different Isotropic, Fixed AP Beam and Beamforming Architectures

Furthermore, the Cumulative Distribution Functions (CDFs) of the maximum throughput is shown in Figure 5.9(a) and Figure 5.9(b). In both figures, we can observe that with the application of beamforming, there is less than 10% probability to achieve less than 4.7Gbps throughput for all different distances between APs. Moreover, when the fixed AP is applied, we can see a more distinct difference in the results we get for different distances between the APs. For instance, there is a 25% probability to achieve a throughput of 4.7 Gbps with a 600m distance between the APs placed along the trackside, and 50% to achieve a throughput greater than 2 Gbps. The differences between the fixed beam and both maximum ray and codebook-based BF can be seen in both figures. Codebooks can also approximate maximum ray BF performance as there is a 70% probability to achieve 4.7 Gbps at 800m AP separation.

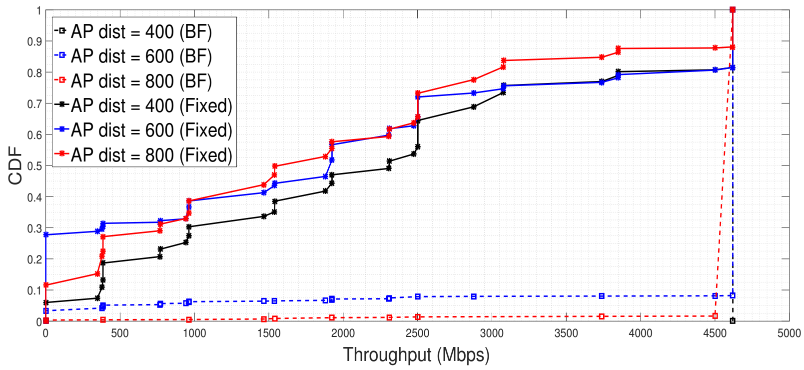

(a) Fixed AP vs Max Ray BF

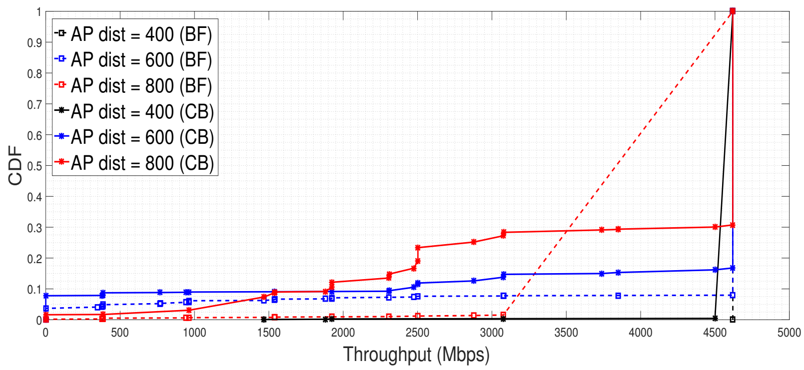

(b) Codebook vs Max Ray BF

FIGURE 5.9. CDF of Throughput

The average throughput and percentage of total outage (i.e. throughput of 0 Mbps) averaged over all frequencies and routes is presented in Table 5.6. The fixed AP configuration provides lower data rates with more significant outage percentages in most scenarios. On the other side, maximum ray beam selection provides high data rates and coverage even in cases of 800m AP separation. As expected, codebooks seem to provide a reasonable improvement to the fixed AP scenario but slightly reduced performance compared to the maximum ray scenario. We can see almost identical mean throughput between codebook spacing and max ray at 400m spacing, but an increase in outage levels is observed as it increases. One might notice an increased outage percentage in the 600m spacing due to the previously discussed overhead crossing in the Bristol route, as in a route with no blockage (e.g. London), it stays at values less than 1%.

TABLE 5.3. Coverage and Throughput per Distance

Mean tput (Gbps) Outage (%)	**AP Spacing**		
	400	**600**	**800**
Isotropic	2.7, 0.14	2.1, 9.05	1.7, 17.8
Fixed 1 sector AP	2.4, 5.3	1.8, 20.6	1.7, 23.4
Codebook in AP,MS	4.6, 0.0073	4.3, 3.5	4, 0.8
Maximum ray BF	4.6, 0.0073	4.5, 0.6	4.6, 0.1

Concluding, directional transmission based on either fixed beam, codebook or antenna array beamforming (BF) configurations with high gain and resolution is widely favoured over other systems. Fixed beam configurations can provide good throughput and coverage only in specific scenarios where the angle spread is small and AP spacing is significantly lower compared to BF architectures. These configurations seem to be sub-optimal, however, in areas that require a more significant angular spread to be served [121]. Maximum ray BF has been shown to yield the highest and most stable throughput from any other scheme providing perfect coverage even in the case where the APs were placed 800m apart [27], at the expense of high beam-alignment overhead. Codebook solutions provide the best performance compromise between data rates, outage percentage and AP separation, allowing constant connectivity between terminals though with a more considerable variation in throughput levels [121]. However, as codebook beamforming is a finite resolution version of a maximum ray BF algorithm, it still has a considerable overhead depending on its resolution.

However, the benefits offered by beamforming-based systems are predicated on the availability of accurate CSI at both the transmitter and the receiver. This property may not always hold due to various physical impairments such as pilot contamination, channel estimation errors, and channel aging [122, 123]. This discrepancy between the channel coefficients being used for beamforming/data detection and the actual channel values leads to degraded system performance. The effect of channel aging on the achievable rates of sub-6GHz systems has been analysed in [124]. Channel aging can severely affect the link quality, especially in rapidly time-varying channels such as HST; thus, any impairing factors, such as BF overhead introduced by high-resolution configurations, should be minimised.

5.2.2 Rail Track Design

There are multiple methods in literature regarding reducing BF overhead. A straightforward solution to minimise setup times would include using reduced resolution uniform codebooks. However, sparsely populated codebooks have the downside of introducing reduced gain configurations and hence impairing transmission range. Reduced range leads to an increased amount of APs required, thus increasing deployment cost considerably. At the same time, if a narrow beamwidth is maintained to avoid reduced gain in these low-resolution schemes, antenna nulls increase as the beam narrows, thus leading to inconsistent coverage, and as such, impaired QoS. The method that is proposed in this work is leveraging design considerations of HST rail tracks to position the APs in certain positions that will allow high-resolution and high-gain BF schemes to be employed while reducing the BF overhead.

5.2.3 Track Geometry

This is where the design of railways helps us with some design considerations. Rail engineering normally dictates three types of solutions when designing high-speed tracks [125].

1. Tangent track (straight line).
2. Curved track.
3. Transition curve.

From a telecommunications aspect, a straight track configuration can also be approximated as a curved track with a radius close to infinity that would require an even smaller angular spread to be served according to the following analysis. The minimum horizontal radius of a single high-speed railway line should ensure that "when the superelevation is set to ultrahigh maximum, the unbalanced centrifugal acceleration does not exceed the allowable value's kinetic characteristics" [126]. For high-speed railway wherein high-speed and medium-speed train services run on the same line, the curve radius should also be set to ensure that when either one of them passes along the line, the unbalanced superelevation is not out of gauge. Table 5.4 shows the horizontal curve parameters as proposed by multiple rail operators [126]. This limit value is based on an equilibrium cant of 290 mm, while the recommendation radius is based on an equilibrium cant of 170 mm, i.e. 100 mm of cant and 70 mm of cant deficiency [125, 126]. It should be noted that the angular values throughout the whole chapter are dynamically adjusted using these values to consider the effects of cant and cant deficiency in the AoA/AoD and ZoA/ZoD profiles.

TABLE 5.4. Railway Curve Parameters

	200 (km/h)	250 (km/h)	300 (km/h)	350 (km/h)
Recommended radius (m)	2776	4338	6247	8503
Limit radius [m]	1628	2543	3662	4984

Arc analysis is the primary tool used in our analysis for the set up of the codebook in the AP. If the AP is placed on the outside of the curve, the AP can serve all the MS points in the route using only one side of the quasi-omni pattern and thus we can significantly reduce the setup time

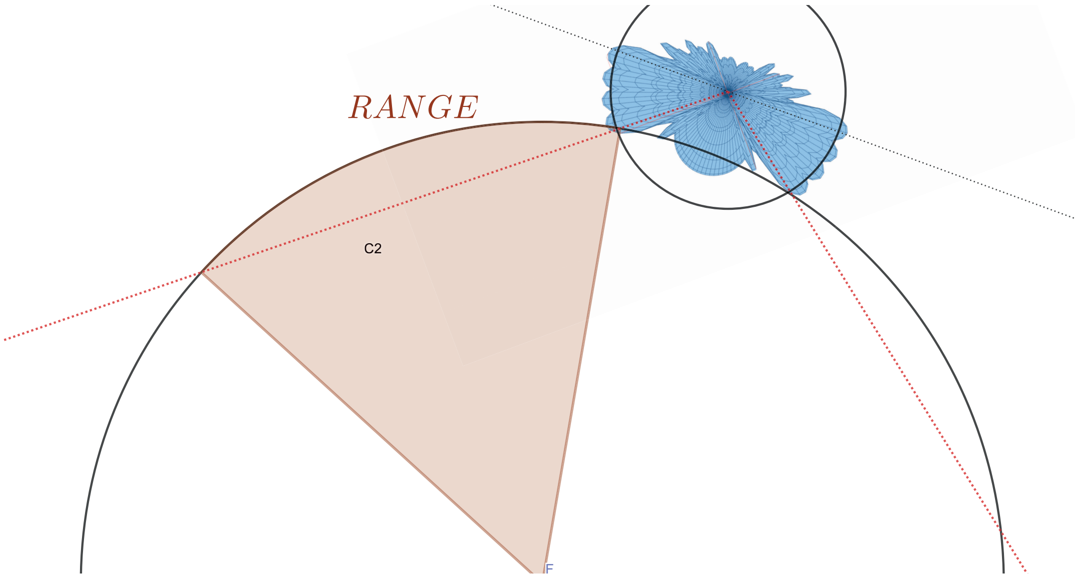

FIGURE 5.10. Proposed Codebook Scheme

for such operations. In other words, we can drastically reduce the number of angles that need to be examined to find the optimal beam as the search area is reduced to less than 180° as long the curvature and/or the direction track does not change drastically.

By employing codebooks that are characterised with higher resolution and gain in the sides, where the majority of the rail track lies compared to the antenna, and much lower resolution to serve the area right in front of the AP, we can further reduce the beamforming overhead by reducing the codebook resolution (and unavoidably the gain) where the train is close to the AP.

An inspection of the ray-traced Angles of Arrival and Departure (AoA/AoD) in the same Bristol rail route (Figure 4.11(b)) gives us some insight into the best beamwidth configurations to be chosen for each specific scenario. In Figure 5.5(a), where the evolution of highest power angles per MS point is plotted for one AP, no substantial variation in the transmitted and received angles is observed, with the majority of the received and transmitted angles of the strongest rays being tightly packed. Similar observations can be drawn for every AP in the route on every scenario dominated by Line-of-Sight (LoS) links. Further analysis shows that when a uniform codebook was applied to both the AP and MS antennas, only about 50% out of all the employed sectors in the codebook were used. This percentage drops further down to about 10% if we only consider the beams used for a considerable part of the track.

This chapter only focuses on HST as an initial analysis of a more defined environment. Chapter 6 will quantify these value for complex environments with high variability, such as city-wide scenarios populated with a multitude of vehicle types. As seen in Figure 5.5(a), at distances larger than 40m from the AP, a connection can be maintained with beamwidths of 25° leaving an 80m area with a significant angular rate of change. A further increase to 30° allows the AP to serve the MS up to a distance of 20m. The area next to the AP, where the rapid change in angles occurs, will be serviced by a reduced gain beam of the codebook. Tracking the beam through that stage only provides us with increased overhead, thus introducing CSI mismatch artefacts due to channel aging. The rest of the codebook (i.e. the side areas) will remain at a high resolution/high gain configuration to avoid any range impairment.

5.2.4 Calculation of maximum train arc size

The purpose of the following analysis is to mathematically describe the aforementioned high-gain side and low-gain middle areas for every possible combination of AP separation from the track, any railway track curvature and any proposed "dead zone" distance. The general solution will provide us with the optimal angle (θ) and maximum range for the sides that need to be populated with high-resolution narrow beams in relation to the distance of the AP from the track (d_1), the radius of the railway curve (r_2) and the distance that we want to cover with the reduced gain wider middle beam (r_1). The resulting values will then be compared with simulation data acquired for multiple non-uniform configurations to find the optimal angle for our scenarios and see if the mathematical analysis is reproducible in a realistic deployment.

Assuming the start of the axis is the point that the AP would be placed (and hence the centre of circle C_1) and $y_L = r_2 + d_1$ the centre of C_2 we get:

$$C_1 : x^2 + y^2 = r_1^2 \tag{5.1}$$

$$C_2 : x^2 + (y - y_L)^2 = r_2^2 \tag{5.2}$$

$$x^2 = r_1^2 - y^2 \Rightarrow x_A = \pm\sqrt{r_1^2 - y_A^2} \tag{5.3}$$

$$\begin{gathered} C_2 : r_1^2 - y_A^2 + (y_A - y_L)^2 = r_2^2 \Leftrightarrow \\ r_1^2 - y_A^2 + y_A^2 - 2y_A y_L + y_L^2 = r_2^2 \Leftrightarrow \\ 2y_A y_L = r_1^2 - r_2^2 + y_L^2 \Leftrightarrow \\ y_A = \frac{1}{2y_L}(r_1^2 - r_2^2 + y_L^2) \end{gathered}$$

We take the negative solution but the answer can symmetrically translate to the positive one as well thus,

$$x_A = -\sqrt{r_1^2 - y_A^2} = -\frac{\sqrt{2y_L r_1^2 - r_1^2 + r_2^2 - y_L^2}}{2y_L} \tag{5.4}$$

Hence we calculate point (x_A, y_A) which is the point in the circle that has distance r_1 from (x_1, y_1). Then all we need is to calculate the equation for the line that passes through these 2 points and find in which other place it intersects the circle, i.e. to . So to calculate (x_B, y_B) we need to find line α.

$$\left.\begin{array}{l} y = \beta x \\ \beta = \frac{y_A}{x_A} \end{array}\right\} \Leftrightarrow y = \frac{\frac{r_1^2 - r_2^2 + y_L^2}{2y_L}}{-\sqrt{\frac{2y_L r_1^2 - r_1^2 + r_2^2 - y_L^2}{2y_L}}} x$$

To find the common points of line α and circle C_2

$$(2) \Leftrightarrow x^2 + (y - y_L)^2 = r_2^2 \Leftrightarrow x^2 + (\beta x - y_L)^2 = r_2^2 \Leftrightarrow$$
$$(\beta^2 + 1)x^2 - 2\beta y_L x + y_L^2 + r_2^2 = 0 \Leftrightarrow$$
$$x_A, B = \frac{2\beta y_L \pm \sqrt{4y_L^2\beta^2 - 4(\beta^2 + 1)(y_L^2 - r_2^2)}}{2(\beta^2 + 1)}$$

We take the negative solution for x_B as $x_B < x_A$ and we have already calculated x_A. Thus,

$$x_B = \frac{2\beta y_L - 2\sqrt{y_L^2\beta^2 - (\beta^2 + 1)(y_L^2 - r_2^2)}}{2(\beta^2 + 1)} \Leftrightarrow$$
$$x_B = \frac{\beta y_L - \sqrt{y_L^2\beta^2 - (\beta^2 + 1)(y_L^2 - r_2^2)}}{\beta^2 + 1}$$

Also,

$$y_B = \beta x_B \tag{5.5}$$

So now that we calculated $A = (x_A, y_A)$ and $B = (x_B, y_B)$ that our line and circle coincide, we need to calculate chord $|AB|$ so that we can get the distance of B from $(0,0)$ which is our centre point and centre of circle C_1.

Hence,

$$\left.\begin{array}{l} |AB| = \sqrt{(x_A - x_B)^2 + (y_A - y_B)^2} \\ y_A = \beta x_A \\ y_B = \beta x_B \end{array}\right\} \Rightarrow |AB| = \sqrt{(x_A - x_B)^2 + \beta(x_A - x_B)^2} = \sqrt{(\beta^2 + 1)(x_A - x_B)^2}$$

Also,

$$x_A - x_B = \frac{2\sqrt{\beta^2 {y_L}^2 - (\beta^2 + 1)(y_L^2 - r_2^2)}}{\beta^2 + 1}$$
$$= \frac{4(\beta^2 {y_L}^2 - (\beta^2 + 1)(y_L^2 - r_2^2))}{\beta^2 + 1}$$

Hence,

$$|AB| = \sqrt{\frac{4(\beta^2 {y_L}^2 - (\beta^2+1)(y_L^2 - r_2^2))}{\beta^2+1}} \tag{5.6}$$

Simplifying β^2+1, as $\beta = \frac{y_A}{x_A}$

$$\begin{aligned}\beta^2+1 = (\frac{y_A}{x_A})^2+1 = (\frac{y_A}{r_1^2-y_A^2})^2+1 = \frac{y_A^2+r_1^2-y_A^2}{r_1^2-y_A^2} = \frac{r_1^2}{r_1^2-y_A^2} = \frac{r_1^2}{x_A^2}\\ = \frac{2y_L {r_1}^2}{2y_L {r_1}^2 - r_1^2 + r_2^2 - y_L^2}\end{aligned}$$

Hence,

$$\begin{aligned}(6) \Rightarrow |AB| &= 2\sqrt{\frac{\beta^2 {y_L}^2 - (\beta^2+1)y_L^2 + (\beta^2+1)(r_2^2)}{\beta^2+1}}\\ &= 2\sqrt{\frac{y_L^2}{\beta^2+1} r_2^2}\end{aligned}$$

By substituting the simplified β^2+1,

$$\begin{aligned}|AB| &= 2\sqrt{r_2^2 - \frac{y_L^2(2y_L {r_1}^2 - r_1^2 + r_2^2 - y_L^2)}{2y_L {r_1}^2}}\\ &= 2\sqrt{\frac{2r_1^2 {r_2}^2 - 2y_L^2 r_1 + y_L {r_1}^2 - y_L {r_2}^2 + y_L^2}{2r_1^2}}\end{aligned}$$

To evaluate this analysis, a Monte Carlo simulation was performed with d_1, r_1, r_2 being a number in the range of [1,10], [20,50], [2000,5000] to get a randomised set of possible combinations. Looking at the minimum values of the chord and angle, we saw that the minimum distance we can serve as long as the curvature does not change is about 4.6km (with a probability of the chord being > 6000 being about 93%) which is much larger than the range of an AP. Meanwhile, the minimum and maximum angles to achieve those numbers are ranged from $\theta_1 = 1.4°$ and $\theta_2 = 30.3°$.

From Table 5.4, we can conclude that larger radii are required to ensure safety and speed optimisation as the HST speed increases. From the derived equations above, we can conclude that the larger the curve's radius, the smaller the angle θ becomes, leading to a smaller angular spread which we need to cover with high-resolution side-sectors.

5.2.5 Non-Uniform Codebook configurations

Optimised, high resolution, non-uniform codebooks could considerably reduce the setup time and introduce less complex processing leading to simpler configurations and reduced power consumption and BF overhead. To design these non-uniform codebooks, the optimal number of beams and beamwidth of each beam is needed to achieve coverage in the majority of the track while maintaining a considerably faster setup time.

There are already standardised codebook designs in literature, such as IEEE 802.15.3c. Again, instead of a theoretical codebook, a synthesised antenna from a measured patch is used as a base for the 2D codebook presented, following, however, the design principles defined in the standard [7]. Uniform codebooks were designed by employing 8, 16, 32, and 64 beam patterns homogenously spread around the AP using the multiple antenna beamwidths discussed in Section 1.1.1. These values were chosen to discuss the effects of beamwidth, processing power and sector sweep overhead as well as any trade-offs between them.

The non-uniform case, however, needs some special considerations in terms of design and optimisation.

1. Side-beam number.
2. Side-beam Half-Power-Beam-Width (HPBW).
3. Mid-beam HPBW.

These configurations mainly affect the antennas in the multiple APs scattered throughout the environment. Due to the larger range of angles that have to be present in the moving train's side, the receiver side retains a uniform codebook with a set resolution.

5.3 Performance Evaluation of mmWave codebooks in Train Communications

As discussed in the previous sections, defining a high and low-resolution area around the transmitting antenna is vital if we want to reduce the codebooks' size. The mathematical analysis has provided insight into the angular values expected in each scenario. However, before we can provide a meaningful suggestion on the codebook values, the performance of different beamwidths and different configurations needs to be benchmarked.

The effects this has on the antenna design were initially presented in Chapter 2 and 3, discussing the gain and power delivery in the antenna and its effects on the radiated power, respectively.

The following section will include a sensitivity analysis to determine the most appropriate rail communications parameters regarding AP and MS codebook design. Beams with different -3dB points, along with multiple configurations for the low and high-resolution areas and beams, will be generated and discussed mainly based on their SINR and size. We will also discuss performance in terms of gain, directivity, number of beams and the existence of a low-resolution middle beam.

5.3.1 Codebook Parameters Sensitivity Analysis

Using the three arrays derived in the previous sections, we investigate the performance of different configurations of the main parameters of these codebooks in realistic scenarios.

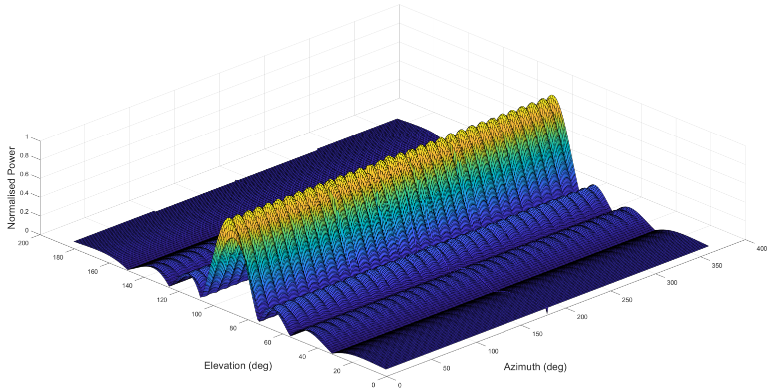

FIGURE 5.11. Receiver (or Mobile Station) Codebook

The antenna array's initial physical orientation is not relevant in this analysis, as the antenna system will later be placed on the side of the track, with the middle beam facing the point on the track closest to the AP. The following analysis will be performed on the principle that the antenna is rotated at 0 degrees around the y-axis and x-axis. The APs are placed on already existing infrastructure at a height of 5m, while the MS placed at a 2.5m height over the ground, with the minimum distance betweeen the MS and the AP being about 5-10m. Thus, the lowest zenith angle we can expect is -12° from the reference plane assuming there is no radical change in elevation in the track.

Moreover, by installing two antennas in the HST, we do not only achieve receiver diversity. Given the train's size, even if the antenna further from the AP transitions outside of the angular range of the beam or incurs blockage from the surrounding environment (infrastructure, dense foliage or another train), the other antenna would most probably still be within the range of the AP's beam.

However, when compared to the AP configurations, MS arrays have to cover a larger azimuth angular range. The main reason for this is that they have to cater for antennas placed on both sides of the track or for trains that are moving both sides. For this reason, a high resolution uniform codebook is required in the MS to allow seamless connectivity.

To be able to generate non-uniform codebooks, our hardware needs the ability to generate multiple beamwidths using subsets of the same array. As repeatedly mentioned in this document, the more antenna elements exist in a direction, the narrower the beam becomes in that same plane. Thus, using subsets of the initial high gain antenna array as shown in equation 5.7

a lower gain beam occurs. This is achieved by phase and amplitude modulation of the array elements/radiators.

$$\begin{pmatrix} e_{1,1} & e_{1,2} & \cdots & & & e_{1,361} \\ e_{2,1} & e_{2,2} & & & & \\ \vdots & & \ddots & & & \\ & & & \begin{bmatrix} e_{i,j} & \cdots & e_{i,j+k} \\ \vdots & \ddots & \\ e_{i+h,j} & & e_{i+h,j+k} \end{bmatrix} & & \\ & & & & \ddots & \\ e_{181,1} & & & & & e_{181,361} \end{pmatrix} \tag{5.7}$$

High gain beams on the codebook's side allow us to service the majority of the track in range. So, depending on the beamwidth of the side beams, i.e. 8°, 10° or 15° main lobe azimuth HPBW, antenna arrays with 12×7, 9×7 or 7×7 elements are initially generated. In Section 1.1.2 it was shown that the larger the track design speed is, a larger resulting curve radius occurs, leading to reduced angular range in the sides. Thus, the proposed beam has to be able to achieve high-gain to allow for the extended range and the number and resolution of beams has to be adequate not to inhibit the performance of the system. This affects the width of the middle beam as a consequence as well. The middle and low gain beam would thus range from a 50° to a 90° beamwidth, thus only using 2×7 to 3×7 elements in the principal directions depending on the angular range of the side beam area that needs to be covered.

In the following section, a sensitivity analysis on those values to determine the most highly performing configuration in an urban railway scenario was performed. The previously discussed route starting in Temple Meads station in Bristol, UK, is again ray-traced and simulated using the methods previously described. The codebooks are applied over the 0 dB gain, and 0dBi transmit power omnidirectional pattern and the beam providing us with the highest power is identified. In section 5.1.1, the study concluded that the most viable scheme for uniform configurations consists of 32 beam patterns equally spaced around the azimuth plane. The same principle is applied for the following analysis unless stated otherwise. Thus, the beam patterns on the high gain areas of the codebook will be spaced at an angular difference of 11.25°. The most generated codebook radiation patterns are shown in Figure B.1 as a surface displacement plot derived from the total E values for a 50° middle beam HPBW. A complete account of the codebooks' angular parameters can be seen in Table 5.5 and the rest of the diagrams are presented in Appendix B.

The mathematical analysis in the previous section showed that the angular range required to achieve all of the possible configurations range from $\theta_1 = 1.4°$ and $\theta_2 = 30.3°$. In Table 5.5, we can see the total angular range achieved on the high-resolution/high-gain areas of the codebook in each configuration. Correlating those numbers with the maximum possible angular range to be

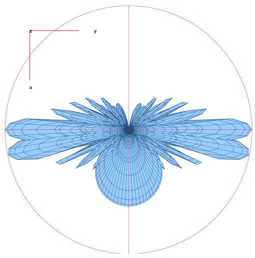

(a) 4 Side Beam Configuration, 8° Side Beam HPBW

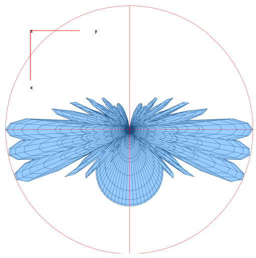

(b) 6 Side Beam Configuration, 8° Side Beam HPBW

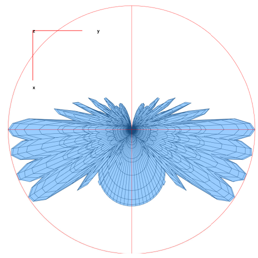

(c) 8 Side Beam Configuration, 8° Side Beam HPBW

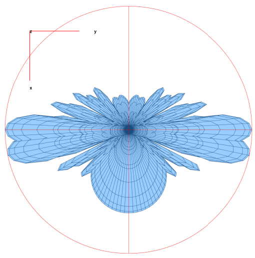

(d) 4 Side Beam Configuration, 10° Side Beam HPBW

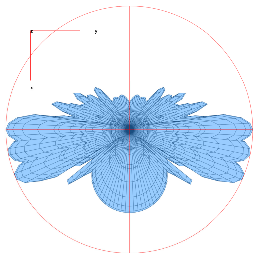

(e) 6 Side Beam Configuration, 10° Side Beam HPBW

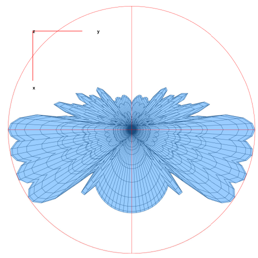

(f) 8 Side Beam Configuration, 10° Side Beam HPBW

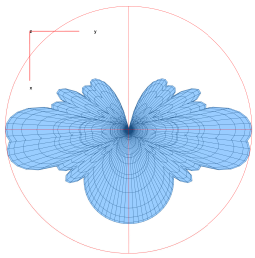

(g) 4 Side Beam Configuration, 15° Side Beam HPBW

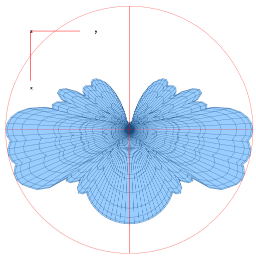

(h) 6 Side Beam Configuration, 15° Side Beam HPBW

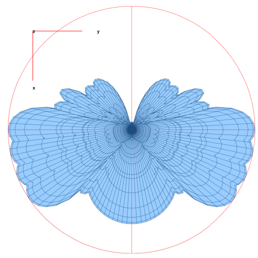

(i) 8 Side Beam Configuration, 15° Side Beam HPBW

FIGURE 5.12. Access Point Codebook Radiation Patterns

TABLE 5.5. Total Angular Range of Codebook Side Beams per Configuration

-		**8° HPBW**	**10° HPBW**	**15° HPBW**
16 Beam Resolution	5-Beam CB	30.5	32.5	37.5
	7-Beam CB	53	55	60
	9-Beam CB	75.5	77.5	82.5
32 Beam Resolution	5-Beam CB	19.25	21.25	26.25
	7-Beam CB	30.5	32.5	37.5
	9-Beam CB	41.75	43.75	48.75
64 Beam Resolution	5-Beam CB	12.625	15.625	20.625
	7-Beam CB	19.25	21.25	26.25
	9-Beam CB	24.875	26.875	31.875

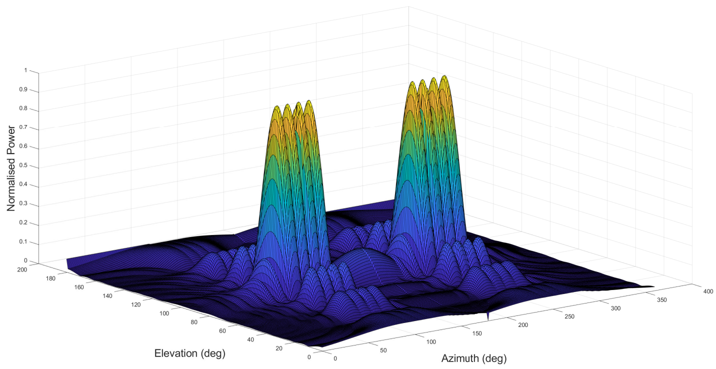

(a) 8 Side Beam Configuration, 8° Side Beam HPBW

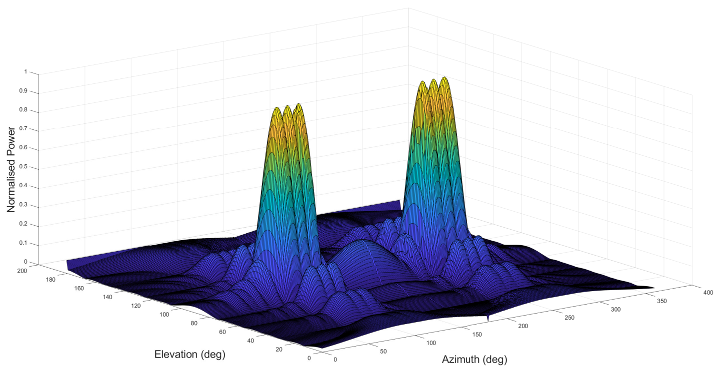

(b) 6 Side Beam Configuration, 10° Side Beam HPBW

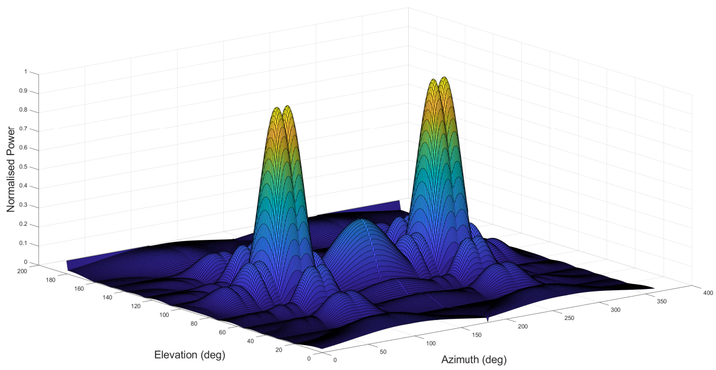

(c) 4 Side Beam Configuration, 15° Side Beam HPBW

FIGURE 5.13. Access Point Highest Radiation Per Point

covered (30.3°), we can observe two configurations able to achieve this number while maintaining the highest possible gain; a 7-beam codebook with 11.25° spacing, and a 9-beam codebook with

5.625° spacing between the 10° HPBW beams. The 10° HPBW 9-beam codebook with 5.625° spacing also achieves that number, but it makes no sense to use a 5.625° separation of beams that have a comparatively larger aperture.

Initially, the effects of the parameters that populate the side areas of the codebook beams are studied. Figure 5.14 demonstrates the received signal strength at the selected user locations for three different side-beam configurations assuming 8°, 10° and 15° HPBW while maintaining a 32 beam resolution on the high-gain areas of the AP. The number of side beams in the AP is also discussed when 4,6,8 total beams are deployed (i.e. 2,3,4 symmetrical on each side). A 32-beam resolution is assumed throughout the MS as well for symmetry.

By examining the power graphs, an apparent increase in the overall power is observed as the gain of the beam increases as expected. Furthermore, an increase in the number of side sectors seems to further affect the system's performance further away from the AP remarkably, especially in the cases of 10° and 15° HPBW. Sudden drops in received power are also observed in the area close to the AP in configurations with four side beams (i.e. only two patterns on each side).

In the case of an 8° HPBW, the performance appears mostly the same for most side configurations, even when only two beams are employed on each side. This further reinforces the mathematical study as it shows that in the track leaving Temple Meads station, where tracks are designed for medium speed and acceleration/deceleration purposes, the angular range does not surpass 20° in total. Hence, the track case being studied entails a railway curve with a considerable radius.

The best performance, however, is achieved with the highest number of side beams for any side-beam configuration. Thus, a scheme employing four beam patterns on each high-gain side, i.e. a 9-beam codebook with an 8° HPBW, would be the most versatile option for railways of a multitude of specifications.

Having decided on the parameters for the high gain areas, a discussion on the necessity and the middle beam parameters is essential. Figure 5.16(a) shows the evolution of the received signal power from the MS around the areas next to AP_2 and AP_6. The assumption that there is no need for a middle beam can be made as there is no loss of service and no significant fluctuations were observed when the middle beam was removed. However, this is predicated two antennas placed on top of the train.

Figure 5.16(a) considers the case where the middle and low gain beam is omitted from the codebook (i.e. only side beams are used). As can be seen, there is a drop in the SNR around the area that the specific beam should have serviced. Even without that beam, no loss in connectivity is observed, as the area is still covered by the side lobes of other codebook sectors. This could cause a considerable drop in throughput when only one antenna in the train is available. Blockage and interference from other trains or equipment might cause one of the train mounted antennas to become unusable. As seen in the Cumulative Distribution Function (CDF) of the maximum throughput in Figure 5.15, there is less than 5% probability of achieving less than 3Gbps

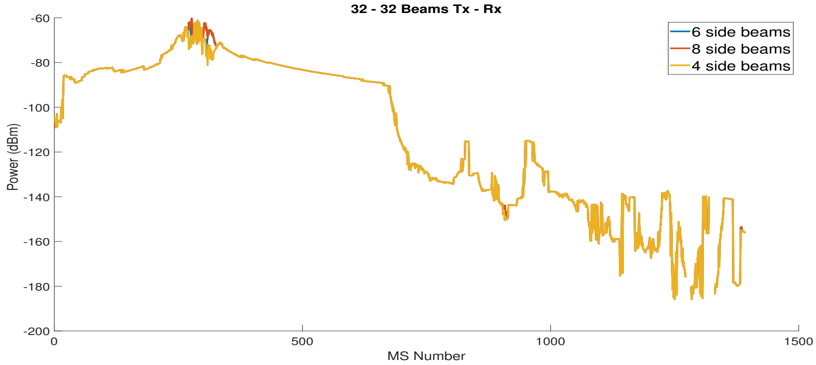

(a) 8° Half-Power Beamwidth

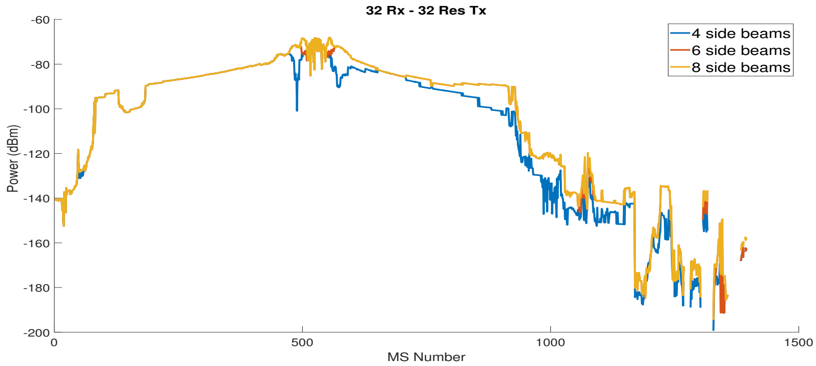

(b) 10° Half-Power Beamwidth

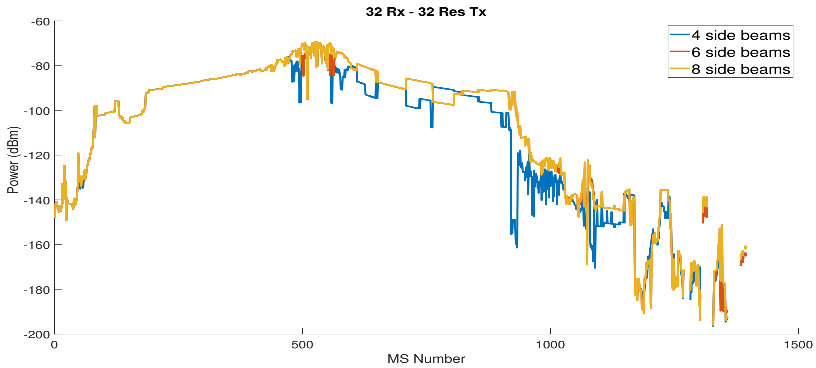

(c) 15° Half-Power Beamwidth

FIGURE 5.14. Side Beam Number vs Beamwidth Received Power

throughput when both antennas are available. When only one happens to be available, the codebook without a mid beam has above 20% probability to have less than 3Gbps throughput, thus quantifying the need for a lower gain/middle sector in realistic deployments. Hence, we can see an evident loss in performance once the middle beam is omitted. Moreover, a beam in the

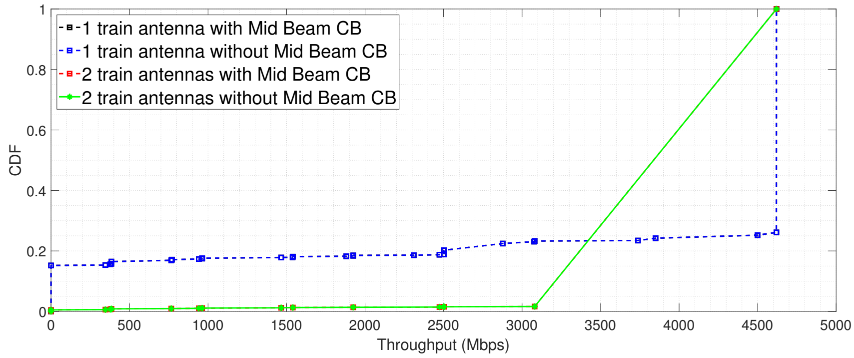

FIGURE 5.15. Throughput CDF

centre of the APs codebook can ensure that there is the possibility of linking to at least one of the trains antennas in the case of accidental blockage.

In Figure 5.16(b), we can see the effects of beamwidth in the aforementioned beam pattern. A 90° beamwidth might provide us with slightly lower received power but offers a more uniform coverage leading to fewer signal fluctuations in the area next to the AP. Finally, Figure 5.16(c) provides us with the power profile for the four different configurations that proved to be more viable through this analysis. Similar performance can be observed in all four, with insignificant differences found around the AP area. Thus all those four designs can be used interchangeably in rail scenarios on a per-case basis.

Finally, the effect of the codebook resolution on the MS is discussed. With Figure 5.16, we complete our analysis on the transmitter side of the system. Even though the MS antenna array might differ per manufacturers, it is necessary to provide suggestions for the antennas mounted on trains. 16, 32 and 64 beam resolution codebooks with a 10° beamwidth are employed in the Mobile Station to study the effects in the received signal power throughout the route. Figure 5.17 demonstrates the interfering received signal strength for the route of the train on the designated track around AP_4 for those three indicative codebook configurations. In each of the sub-figures, the effects of different resolutions in the Access Point's side beams are shown. As expected, the 64 beam resolution in the mobile station with 32 beam resolution on the sides of the AP achieves the best overall performance, even though it is by a minimal amount. Only a small drop is observed in the received signal strength due to the lower gain beams in lower resolution MS configurations. Hence, to reduce the set-up time while still achieving seamless connectivity, a 32 beam scheme is proposed for the receiver side.

In previous analyses, we showed that with uniformly spaced codebooks, we could maintain connectivity with data rates reaching 4.7Gbps while at the same time reducing the outage probability down to < 10% even in the case where the APs were 800m apart [121]. This section focuses on how non-uniform schemes compare with this performance and how heuristically adapting the parameters of these Codebooks affects overall system performance.

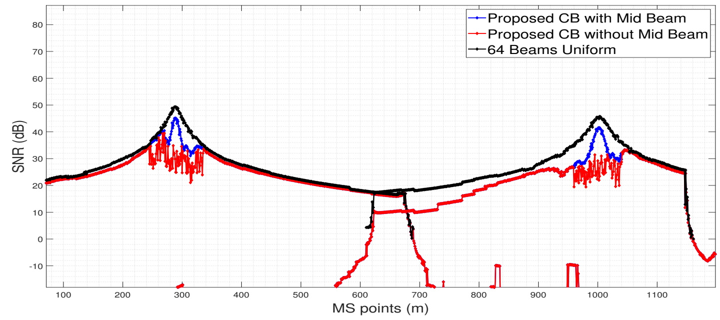

(a) Mid-Beam vs No Mid-Beam SNR

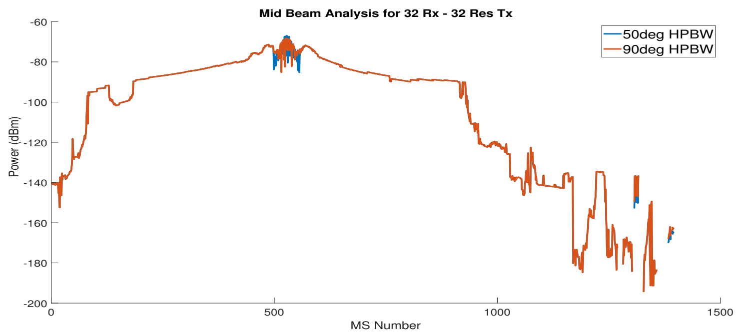

(b) Comparison with Uniform 64 × 64

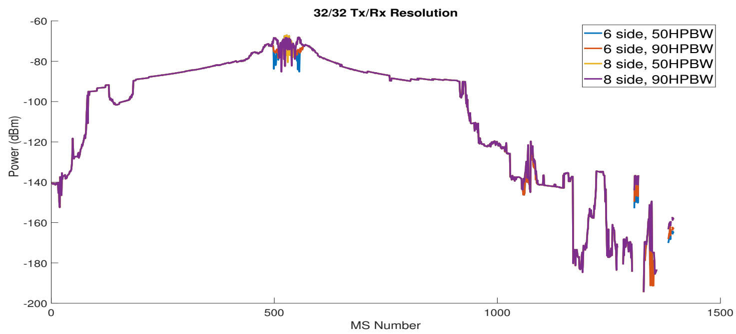

(c) Existence of middle beam effects

FIGURE 5.16. Middle Beam Beamwidth Effects in Performance

Figure 5.18 allows us to study the effects that the previously discussed parameters have on system performance.In this figure, the SNR throughout the designated track for 5-, 7- and 9-sector codebooks while comparing them to the 64 × 64 Uniform case is presented. The 7- and 9-sector cases show almost identical performance with the high-resolution uniform codebook. However, the seven sector codebook shows signal degradation further away from the antenna due to less gain in the main-lobe.

Finally, the performance of the proposed schemes is compared to an oversampled uniform

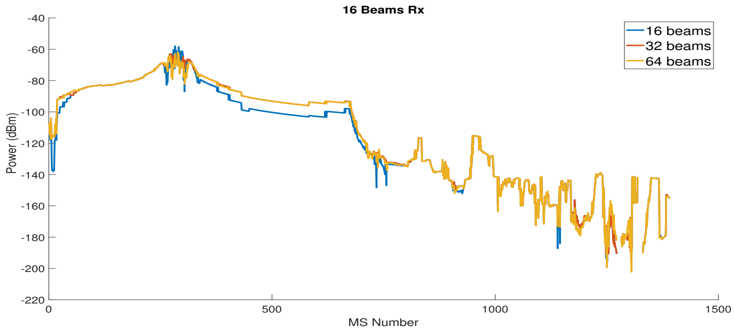

(a) 16 Beam Resolution MS

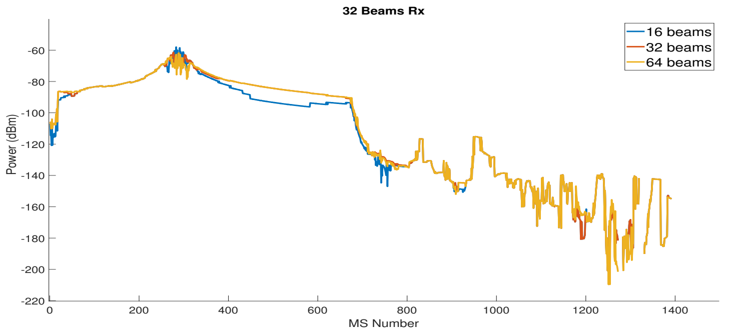

(b) 32 Beam Resolution MS

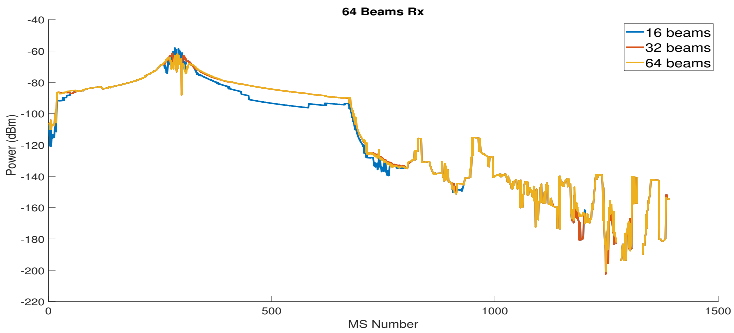

(c) 64 Beam Resolution MS

FIGURE 5.17. Effects of Receiver Resolution on Performance

scheme. In Figure 5.18 the SNR of three schemes differing on the side beams number while employing a 10° side beam and a 50° middle beam HPBW. The figure clearly shows almost non-discernible differences in link quality and performance, thus proving the selected schemes can effectively replace large and high-resolution codebooks to reduce set-up time in rail scenarios drastically.

To extract some practical information from all this data in terms of network deployment and design, the averaged percentage of total outage (i.e. throughput of 0 Mbps) was derived. As

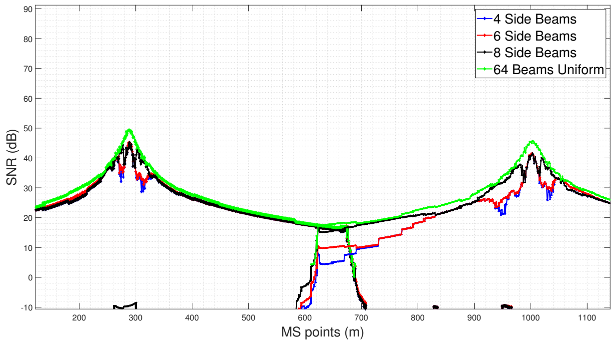

FIGURE 5.18. SNR of Throughput

expected, the two proposed codebook configurations seem to be performing to the same standard as the 64 × 64 uniform configuration with a near-negligible 0.1% outage percentage difference. Precisely the same throughput performance, with a considerable reduction in the number of steps needed for BF setup, is observed as well. A complete analysis on the number of steps and beamforming setup time is provided in the next Chapter. Considerable degradation can be seen only in the case where only one train antenna is available, and no mid-beam is employed in the codebook, with lower data rates (3.4Gbps) and more significant outage percentages (15.2%).

TABLE 5.6. Coverage and Throughput per Distance

	600m AP Spacing	
	Mean tput (Gbps)	**Outage (%)**
Max Ray BF	4.3	3.5
Uniform Codebook in AP,MS	2.1	9.05
Non-Uniform Codebook in AP	3.5	0.1
Non-Uniform Codebook in AP (without Middle Beam)	3.4	15.2

The driving force behind that chapter was a method that can allow faster search of the optimal beamforming vectors by reducing the sectors and thus the number of required steps and time to achieve them. However, this analysis will be provided at the end of Chapter 6 in order to include results from every vehicular scenario discussed throughout this thesis.

5.4 Conclusions

In this chapter, we studied enabling mmWave BF technologies to meet the increasing data demand for HST communications. Throughout the chapter, a fixed beam and two BF schemes based on a synthesised beam pattern were introduced and investigated in two different environments at both 26 and 60 GHz. Considering a train, mounted with two antennas travelling along a train track, a simulation has been conducted to show the three BF scenarios' performance in different AP separations to draw conclusions regarding throughput and outage.

Our aim in this chapter is to provide a comprehensive study that will optimise the network in HST scenarios by considering deployment density, complexity, and performance. Fixed beam configurations can provide good throughput and coverage only in specific scenarios where the angle spread is small. These configurations are sub-optimal in areas that require a larger angular spread for the AP. Even by employing a wider beam and hence more densely deployed APs, the train still loses connectivity when passing through the antenna nulls. Almost twice the number of APs will be needed to achieve the same performance with the discussed BF schemes. However, by providing a less complex solution with no processing in the AP, they describe a more cost efficient solution on a per-unit basis. Service providers will have to seriously consider this parameter while performing the network deployment cost analyses.

On the other hand, maximum ray BF has shown to yield the highest and most stable throughput from any other scheme providing perfect coverage even in the case where the APs were placed 800m apart, at the expense, however, of high beam-alignment overhead. Concluding, codebook solutions provide the best performance compromise between data rates, outage percentage and AP separation, allowing constant connectivity between terminals though with a larger variation on throughput.

However, spherical coverage that is highly desirable for uniform 802.15.3c codebooks is computationally complex and hence even more time consuming. Thus, a mathematical solution is derived to provide the angular characteristics that will allow us to maximise range while reducing the number of sectors needed. Angular analysis allows us to propose dynamic and non-uniform resolution codebooks according to the frequency a speciffic sector is used. HST analysis is a great stepping stone as the paths in such cases are pretty much defined with little to no variability. In Chapter 6, similar analysis is provided for more complex and dynamic urban vehicular environments. The values for beamforming steps and time will be provided for both train and urban architectures.

CHAPTER 6

Network Design and Performance Evaluation in High Speed Environments with High Variability

In Chapter 5, an analysis of the effects of codebook design was performed to assess mmWave infrastructure in High-Speed-Train environments. Rail geometries, even though they provide the basis of vehicular design concepts, are not representative of more complex and dynamic environments. Unlike HST communications scenarios where users follow predefined paths with little variability and request access from specific locations, urban vehicular environments appear to be more complex. In a wider sense, although predefined routes still exist, the lack of physical tracks means that the vehicle's vector and positions cannot be accurately defined thereby, highlighting the need for technologies to consider/respect these additional parameters in the design phases. Moreover, the predefined and less obstructed rail track environment allows for a more stringent set of design rules whereas, urban environments tend to be more variable within sectors of the same area.

6.1 Introduction

Next-generation Intelligent Transportation Systems (ITSs) will require Vehicle-to-Infrastructure (V2I) wireless connectivity to enhance road safety and efficiency in urban vehicular environments [127]. Current solutions mainly include sub-6GHz picocell systems with Access Points placed on top of buildings in urban environments [3]. Although reliable, these systems do not seem to allow for the increased rates and capacity required by ITS applications, such as Machine-to-Machine communications for self driving cars. M2M communications required for autonomous vehicles is predicted to generate as much as 40 terabytes of data an hour from cameras, radar, and other sensors [2, 128]. The introduction of mmWave systems for these vehicular environments has been proven to significantly improve the performance in small-cell access networks [3] through its inherent low latency and resulting gigabit-per-second data rates [129, 130]. There is an opportunity for future 5G networks operators to exploit the existing urban architecture to deliver substantial data rates with huge spectral efficiencies.

In Chapter 4, each AP's radius and the distance between consecutive APs were examined in both HST and urban scenarios. Several works have focused on deriving algorithms to optimise the placement of the AP throughout the environment [3, 127, 131]. As mmWave APs are costly to deploy and maintain, the design of such systems needs to maximise coverage while minimising design complexity. Placement of road-side units is essential to achieve seamless transmission as well as allow efficient and accurate localisation.

Previous studies have deployed agile techniques which utilize ray-tracing or link estimation methods to determine the optimal placement of APs [129]. However, these studies focus on minimising the number of APs needed for a set number of city blocks assuming perfect transmission [130, 131] without explicitly studying factors that deteriorate the quality of the link in mmWave frequencies. These factors include foliage loss, environment scattering, vehicle and urban clutter blockage and low-gain antenna radiation patterns. Other studies might consider blockage effects [108]; however, they only utilise a simplistic two-ray model for the propagation environment, compared to the analytical ray-tracing model described in Chapter 3.

Throughout this thesis it was shown that in the urban environment, the mmWave links are dominated by LoS rays. Thus, the sectors with the highest antenna gains should be focused around the majority of the LOS ray directions. These properties might be limiting for legacy sub-6GHz systems but inversely make mmWave systems a great candidate for next-generation vehicular applications as they can easily fulfil the rigid bitrate and latency Quality-of-Service (QoS) constraints [129]. Proposed algorithms aim to find the sector covering the LOS ray in fewer steps by ignoring several sectors and reducing the resolution of others, and employing multi-step search algorithms.

In this chapter, we study the unique road and building layout of urban environments as defined by road design manuals provided by US and UK authorities as well as the strict QoS constraints of vehicular applications in such environments. Multiple road-side deployment infrastructures are considered, and their effect in the propagating environment is assessed. Specifically, Infrastructure-to-Vehicle (I2V) solutions such as dedicated antenna masts, street furniture or buildings are modelled and compared against each other using a vectorised ray tracing approach. Highway and urban systems, where vehicles receive high data rate streams transmitted by mmWave APs, are also discussed. With the aid of the IEEE 802.11ad RBIR engine, we model the system, acquire the throughput performance and investigate the performance of multiple codebook-based approaches and AP placements using again a measured antenna. The spatial throughput performance evaluation of these non-uniform, reduced-resolution codebooks is then correlated to BF setup time by comparing the resulting number of steps using two well-defined beam searching algorithms defined in [119].

The rest of the chapter is organised as follows. In Section 6.2, we present a short analysis of how Access Point positioning may affect the propagation environment. We discuss three placement positions and rank them based on performance, feasibility, cost and complexity of the resulting codebooks. In Section 6.3, we describe the system model, network structure and physical layer design for an urban route application. The beam radiation patterns and the proposed codebooks will also be presented in this section and their performance will be discussed. Non-uniform codebooks are then modelled and analysed to provide the optimal parameter values. Section 6.4 will include a performance analysis regarding received power, throughput and beamforming gain using the proposed schemes. The effects of the codebook parameters in beamforming setup overhead and DEV-to-DEV link time are discussed in Section 6.5. Resulting link-time values are discussed for a multitude of scenarios, both train and urban, based on geometry and speed. Section 6.6 concludes the chapter.

6.2 Access Point Positioning

Chapter 5 discussed configurations that allowed us to take advantage of the reduced angular range present in HST communications utilising placement on specific locations in rail environments. For such configurations, the candidate mounting locations are quite specific; either furniture on the side of the track or specially built antenna masts. The analysis previously presented was only possible due to the small variations present in the route that the train has to follow. To apply a similar analysis to urban vehicular scenarios, we first need to define the AP's positioning, and the inherent spatial redundancies in the vehicle's angular profile served by said AP.

Unlike HST communications, users in urban environments follow random paths and request access from random locations. However, in vehicular cases, even though there is no physical track for the vehicles to travel on, road safety and vehicle rules are in place as defined in the highway code. Thus, a similar behaviour to railway configurations is observed as mobile stations' positions are more or less predictable. A greater degree of variability is observed in the route as the standard deviation of the vehicles' distance from the theoretically defined position is significant. This factor will have to be considered when discussing the frequency of beamforming and beam parameters as it may induce increased artefacts due to channel aging and misalignment.

Moreover, in urban vehicular scenarios, radical changes in the elevation profile might be observed as the vertical design of roads is heavily defined by the natural environment within the city. For example, for a 20% grade slope, the vertical distance or else "rise" would be about 80m in a horizontal distance of 400m which denotes our AP's range in LoS conditions. From the AP's perspective, a 20% grade slope translates to more than 10° angle of elevation. These values have to be considered when discussing AP placement or beam and codebook design.

The complexity of the environment is another factor that needs careful assessment. There are no clear universal standards on the design of urban environments, as cities were built and developed with different standards at different eras, thus showing significant variability in design. For ease of analysis, the terminology "regular" will be used for environments that allow for symmetric environments such as Manhattan grid-type configurations. "Irregular" will be used for less symmetric and more complex environments, showing increased variability throughout, such as Bristol or London. An example of regular geometries can be seen in Figure 6.4, while irregular have already been shown in Figures 4.11(b) and 4.1.

City complexity plays quite an important role when designing the network. Buildings are the primary source of blockage in outdoor urban environments; thus, real-life deployments have to be able to exploit any geographical advantages that may occur. It also highlights the need for accurate blockage modelling techniques due to the high sensitivity of throughput performance and coverage estimates in link quality. This is mainly due to the notable difference in path loss for LoS and non-Line-of-Sight (NLoS) links in mmWave frequencies, thus showing the need for accurate modelling for correct deployment planning.

Existing blockage models are largely inadequate when studying track coverage in mmWave compared to empirical or ray-traced solutions, as proved in [132]. Thus, in this study, ray-tracing using real-life and digitally modelled building locations will be performed to capture these trends better.

Apart from blockage modelling, the complexity of the urban environment predominantly affects the density of AP deployment, as previously seen in Chapter 4. High-density schemes are needed in mmWave networks as they have proven to improve the cell edge rates, as demonstrated by system simulations in [133] and analytical studies in [134, 135]. However, the cost of such deployments needs to be considered and the optimal trade-off between density and deployment feasibility needs to be quantified. However, this will not be covered in the course of this thesis. However, we need to consider the cost of such deployments and find the trade-off between density and deployment feasibility.

6.2.1 Highway Scenarios

This Chapter's primary focus is to quantify and evaluate the parameters needed for well-defined codebooks to be employed in APs in cities and high speed roads. The first environment category to be studied is a typical highway or an avenue scenario surrounded by either low rise buildings or no buildings.

In Chapter 5, three types of geometries were defined for the design of high-speed tracks [125]. Highway environments are in many ways similar to rail track environments. The same design principles are applied to highways and urban avenue configurations, with the only difference being that instead of a single track, vehicles now move in a multiple lane environment. As such, highways can be abstracted as the superposition of multiple tracks, displaced in a direction

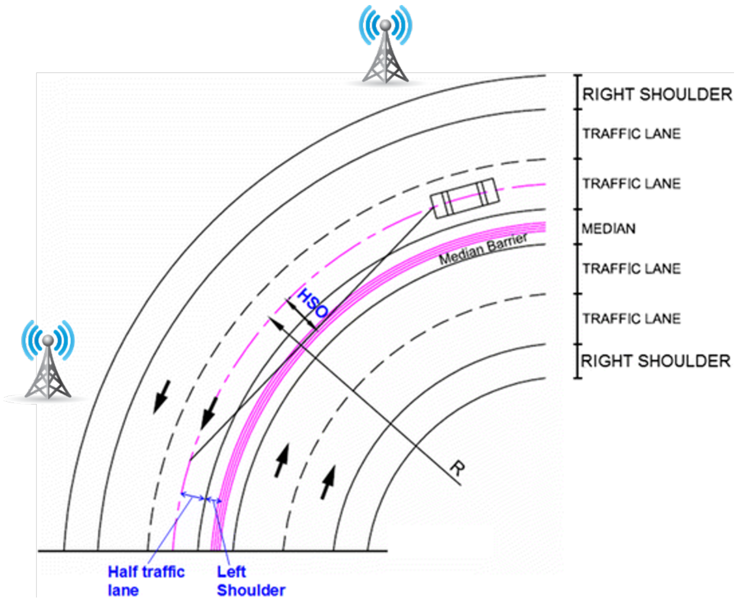

FIGURE 6.1. Typical Highway Route

such that they never coincide. Multiple tracks still exist in rail environments as well, but in a comparatively smaller scale compared to highways. In context to the mathematical analysis demonstrated in Chapter 5, the AP's distance (d_1) from the lane in question increases with each displacement. This can be seen in the schematic shown in Figure 6.1. Thus, the same analysis performed in Chapter 5 still applies in typical highway scenarios, with a need, however, of updated parameters.

One of the main differences in highway scenarios compared to rail tracks is the AP and MS height. Street furniture and vehicles are designed at a different specification compared to High-Speed-Trains. Lighting in highway environments is provided by high-masts, i.e. tall poles with lighting attached to the top pointing towards the ground reaching up to even 30 m. APs can be placed on those already raised masts in any desirable height in its range. Typical values in most UK and European countries for Urban Traffic Routes, Main Distributor Roads are set to a 10 m mounting height for the LED luminaires.

All street and highway lighting follow the BS 5489-1:2020 , Code of Practice for the design of road lighting [136]. This set of rules specifies the height and distance of the lighting masts from the highway. A minimum of 0.8 metres from the kerb edge to the column's face is specified, with no surrounding obstructions or foliage permitted. Unless specific considerations occur, the masts can be placed even further away from the kerb edge as long as they are situated within the area of the estate which it is proposed will be adopted as highway, and they do not obstruct footpaths or vehicular access [136].

In a typical highway scenario, lanes are about 3.5 meters wide, thus for a 3-lane dual carriageway (or a divided highway), the distance between the edges of the highway is about 18 meters (including safety lanes and the divider). Thus the minimum distance of a mobile station from the access point would range between 3-15m.

Antenna height at the MS differs as well compared to the HST cases. For sub-6GHz systems, authors in [105, 137] have discussed the most efficient antenna placement to maximise gain and reduce blockage from the vehicle. A variety of positions were measured and the most uniform radiation patterns were shown to be radiated when the antenna was placed over the car's ceiling. As vehicle size and height massively differ between manufacturers and different vehicle types (e.g. cars, busses and lorries), the antenna on the vehicle side positioned on a height range of 1.2 to 2.5 meters.

This analysis assumes an 8-meter AP mounted on those columns/masts to reduce blockage from higher vehicles in areas further away from the AP. A typical highway scenario of 800 m length is considered to allow comparison with the same length of track described in Chapter 5.

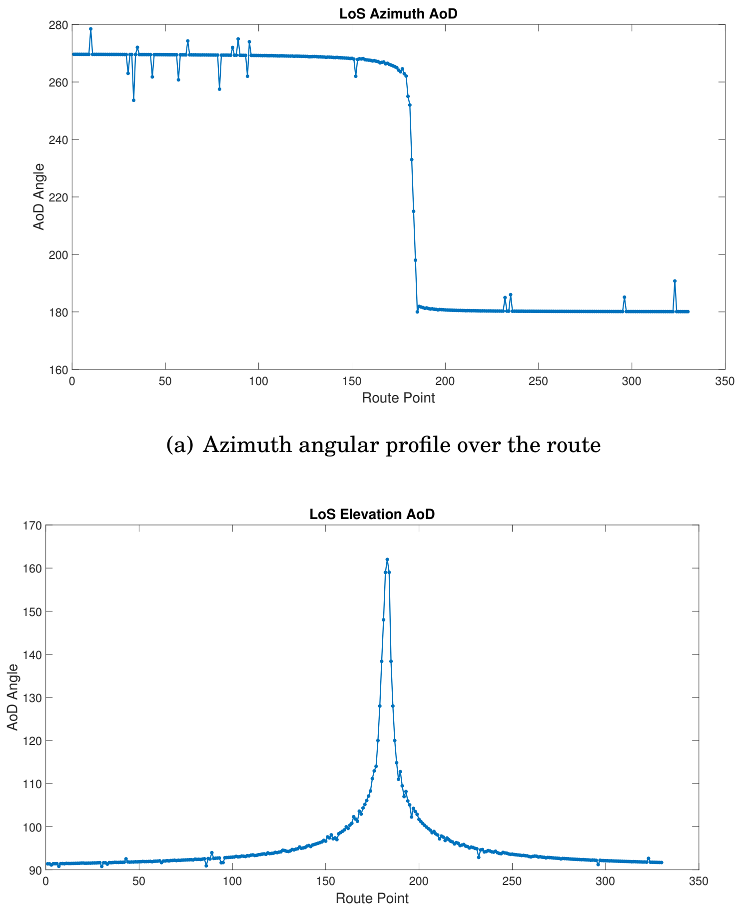

(a) Azimuth angular profile over the route

(b) Zenith (or elevation) angular profile over the route

FIGURE 6.2. Effects of codebook parameters

The ray-traced AoA and AoD in both elevation and azimuth using omnidirectional antennas are presented in Figure 6.2, where the highest power angles per MS point in the vicinity of the AP are plotted for the highway scenario shown in Figure 6.1. Similar patterns emerge in the evolution of the azimuth angles of arrival at the MS and departure from the AP compared to the HST scenario, thus the same non-uniform configuration can be used. In the elevation domain, however, a larger deviation is observed in those angles. Specifically, in the highway scenario, we see an increased angular range and spread in areas close to the AP.

To address the increased angular range stemming from the higher AP placement, beam tilting in the elevation domain or increased elevation HPBW is necessary to reduce antenna nulls and provide seamless throughput performance and coverage. As previously explained, increasing the beamwidth will reduce the antenna gain while tilting the beam increases the vertical polarisation component, thus reducing the effective range of the access point and demanding denser configurations. A beam tilt of 5° and an increased elevation beamwidth in the middle low-gain beam is adequate to avoid any nulls and maintain similar performance in this architecture

6.2.2 Urban Scenarios

Compared to train and highway environments that are dominated by large open areas with a limited amount of blockage, urban vehicular environments are much more complex and irregular. In dense urban environments, sensitivity to blockages creates the need for more sophisticated network planning [138].

Authors in [129, 138] have proposed an agile strategy for deploying road-side nodes in dense city scenarios. This method is based on the Geometric Dilution of Precision (GDOP) metric to evaluate the accuracy provided by Road-Side Unit (RSU) placements, which is in more detail described in [139]. These studies have shown that in mmWave urban environments, high throughput data transfer is predicated on the existence of a LoS channel component.

To reduce the amount of APs needed while still deploying a dense network, authors in [107] discuss direct delivery and multi-hop relaying techniques. A vehicle in transmission range and LoS of the access point will, for the largest part, achieve direct delivery of results while multi-hop is used to improve performance and add a safety mechanism when the MS in the vehicle appears to be out of range.

Access points in urban environments are usually deployed either in already existent infrastructure or specially designed antenna masts, where the APs are mounted. Three mounting scenarios will be discussed during this study:

- Traffic Light mounts
- Building mounts
- Antenna masts placed at the middle of roundabouts

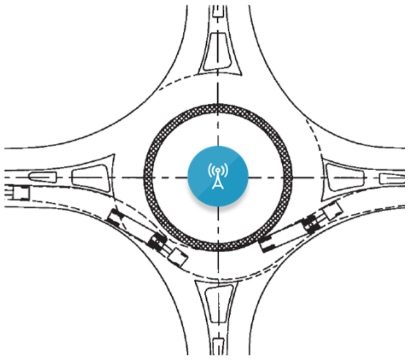

(a) Middle Island Configuration

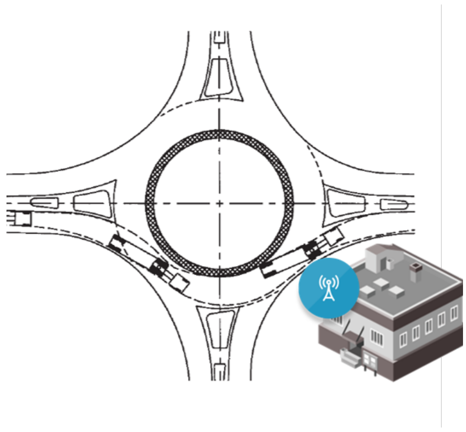

(b) Building side mount

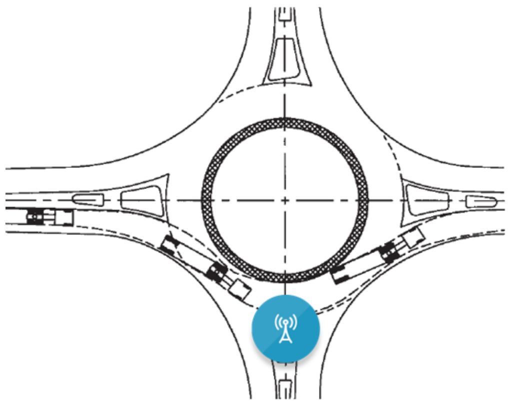

(c) Traffic lights mount

FIGURE 6.3. Schematic of Mount Scenarios

It is crucial to deploy the APs in the most suitable locations to improve overall network performance. The unique road and building layout of an urban environment will need to be considered as well when we are placing APs. Tools such as the simulator developed as a process for [138] are used for a preliminary examination of the environment to allow planning of AP placement to maximise coverage while at the same time providing the optimal densification of the system. Placing antennas on the side or the rooftops of buildings has been a solution since wireless communication were first perceived. In an ideal scenario, buildings would provide the most cost-efficient mounting option as there is no shortage in any scenario. However, buildings might be privately owned within a city, away from the road or blocked by vegetation, thus increasing the difficulty of access for deployment or maintenance and accentuating the high loss effects of mmWave frequencies in many cases.

As we have mentioned already, street furniture is already a good prospective candidate for

AP placement in highway environments. This property translates quite well in urban vehicular environments, as street furniture design is well defined. Moreover, such structures are already present in the large majority of roads that will need the introduction of mmWave APs for V2I applications. Compared to highway configurations, in urban and rural scenarios, street lights typically range between 5 - 12m with Industrial Estate, Local Distributor and Access Roads generally using 8-10 meter mounting height columns, while Residential Roads, Access Roads and Footpaths values in the range of 5-6 meters. Lighting poles are viable mounting locations but would only make sense in either long stretches of roads or as cheap offloading APs with minimal processing and simplistic configurations. The street furniture of choice for this scenario will include traffic lights as they are usually placed at road intersections and are specifically designed to have an extended line of sight for safety reasons. The minimum height for traffic lights is defined as 5 meters. Our study will be performed with that number to provide a performance analysis at the edge case.

Placement of uniform linear and circular mmWave arrays on the side of buildings and in street furniture has already been extensively studied in [26] to study short-range and line of sight "massive multiple-input massive multiple-output" (MMIMMO) propagation channels with the intent of employing backhaul solutions in urban scenarios based on block discrete Fourier transform [1]. However, only V2I scenarios will be presented in this thesis.

In several countries, crossroads are heavily realised by the use of roundabouts instead of conventional traffic light controlled crossings. Roundabouts are a point of symmetry for the surrounding environment. APs more centrally located on the road can largely avoid wall and rooftop blockages [140]. Even in irregular city geometries where crossroads are not symmetrical and orthogonal, the point at the middle of the roundabout provides us with the maximum visibility in all directions, thus maximising the LoS components of the channel. Thus, antennas can be strategically placed in the middle of such structures to maximise coverage. However, the absence of street furniture in the middle of the roundabout islands demands antenna masts to be raised instead of the AP being fitted in already existing infrastructure.

When intermediate vehicles cause an obstruction, V2I and V2V communications need to operate in NLoS conditions. A mathematical expression to calculate at which point a vehicle of specific height will introduce blockage in the LoS link has already been derived in Chapter 4. In such cases the rays diffracted on the road's surface and on other vehicles on the road are the ones reaching the MS. However, these NLoS links display considerable signal attenuation due to scatter from the aforementioned surfaces, thus significantly affecting throughput and coverage performance of the link.

This is mostly mitigated by increasing the height of the mounted AP, by efficient antenna placement both within the environment and on the vehicle as well as by utilising multi-hop

[1]For this collaboration, ray-tracing and simulation results were produced using a multitude of predefined scenarios by the author, with the help of Dr. Di Kong in CSN, Bristol, United Kingdom

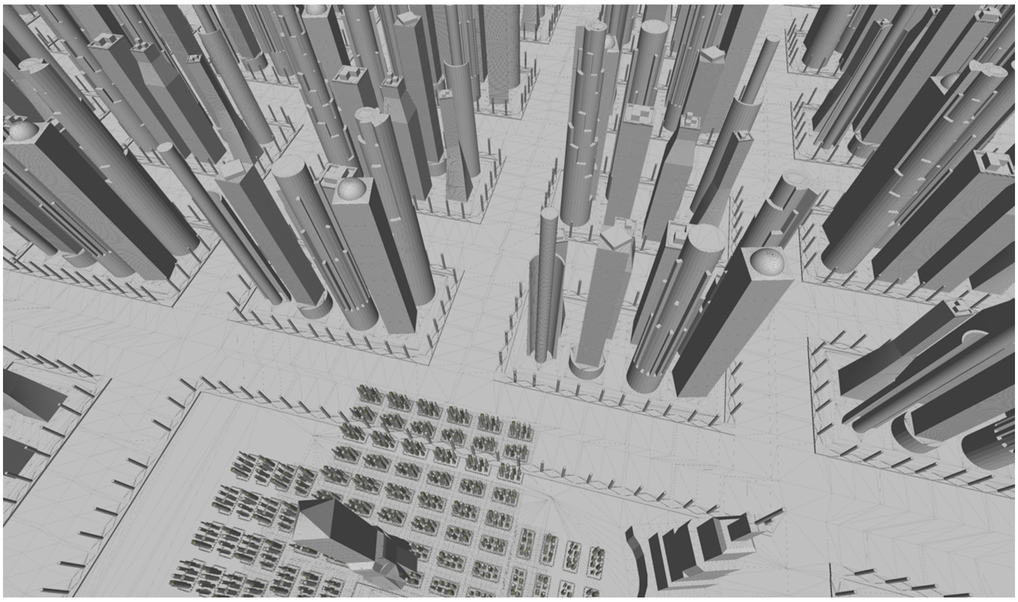

FIGURE 6.4. Manhattan Grid Type 3D Model

networks. However, multi-hop techniques and configurations are outside the scope of this project and will not be studied in this thesis.

To come up with efficient codebook solutions for an urban environment, the effect of the different mounting schemes on the propagation environment is investigated. The scenario is presented in Figure 6.4, with a single AP deployed in three locations at a road crossing scenario. This database is digitally created using Blender [2] by superimposing multiple types of buildings, as seen in Figure 6.5. The database is specified as a vector field with > 1.5 million facets to capture the channel effects of mmWave propagation. These are clearly depicted in subfigures Figure 6.5(a), Figure 6.5(b) and Figure 6.5(c).

The three different mounting options - middle of the roundabout island, side of the building and top of traffic light mast - are presented in Figure 6.3. The received signal power at 0.1m intervals inside a 500×500 meter grid around the antenna is plotted versus its location to assess the effects of blockage of power spread in urban geometries. During this ray-tracing activity, only first order surface scattering is considered as mmWave links severely deteriorate after the second interaction with a surface mainly due to scattering and polarisation effects.

The predicted power of all three mounting options is shown in Figure 6.7. As expected, the propagation statistics significantly depend on the AP mounting option.

Roads with immediate LoS conditions show similar channel characteristics with high signal strength and a high percentage of LoS links as expected. In adjacent and parallel roads, we observe more power dispersed in the case of the building mounted APs. Thus when the AP is is mounted on the side of a building, we see increased power dispersion throughout the grid

[2]https://docs.blender.org/manual/en/latest/

compared to the two other scenarios. In the scenarios where the AP is placed in structures in the middle of the road, we notice a more focused type of power profile.

This is probably because of strong reflections on the wall on which the AP is mounted and the more considerable amount of realisable incident angles for reflection and scattering. Placing the AP in the middle of the road increases the average incident angle, which, according to [66], has a detrimental effect on the first-order reflection's received signal power.

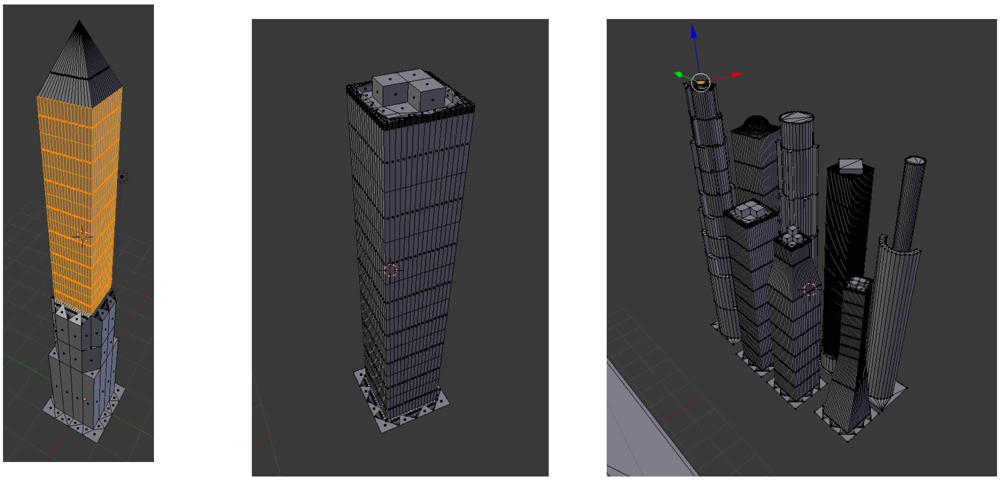

(a) High-rise building

(b) Medium-rise building

(c) Cluster of buildings forming a block

FIGURE 6.5. Building Types

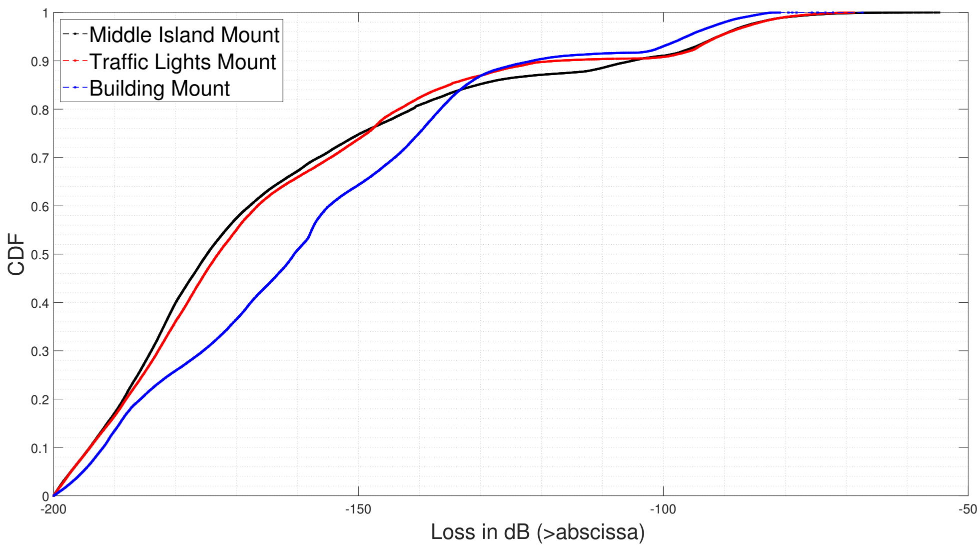

FIGURE 6.6. CDF of Received Signal Strength

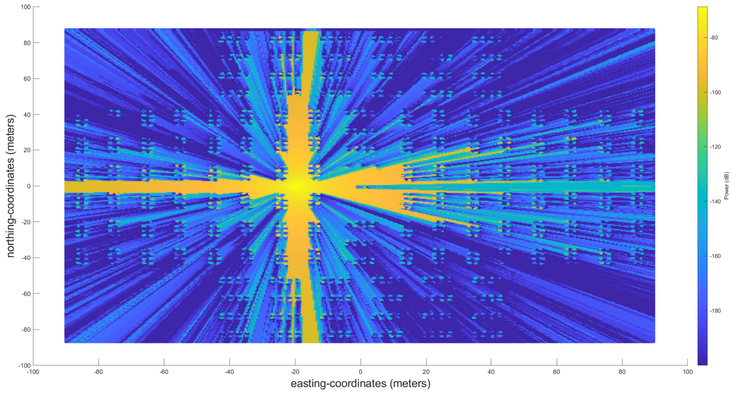

(a) Middle Island Mounted AP

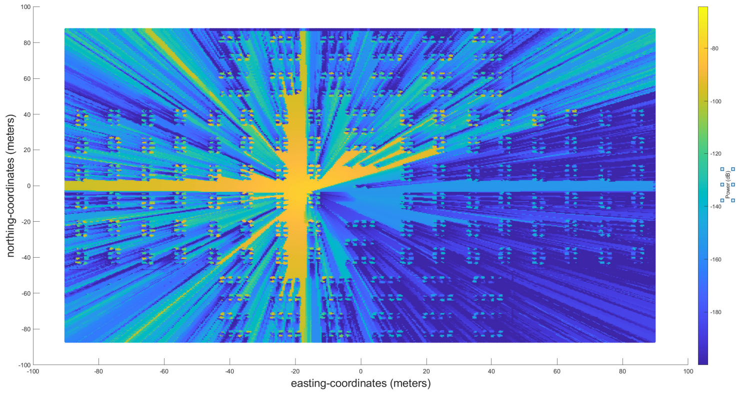

(b) Building Mounted AP

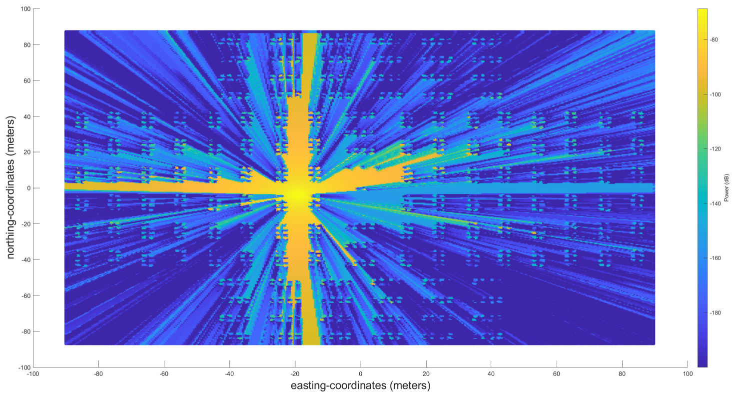

(c) Traffic Lights Mounted AP

FIGURE 6.7. Grid Power Profile

The average power drop observed throughout the environment is similar in all these cases with a value of about -160 dBi with observable variations in the distribution of power. For the case of the middle island AP, we observe marginally higher average power throughout the environment (-157 dBi), but with a significantly larger standard deviation (31.85). The standard deviation is high in the traffic light mounting option (29.36) compared to building scenarios (22.1), but still slightly lower than the middle of the roundabout case.

An increased RSSI of about 5dB for the NLOS links is observed in the building scenario, as more angles are within the 35° to 70° angular range that is expected of mmWave links as specified in the ray-tracing parameters. The CDF of the received power for each mounting option can be seen in Figure 6.6. Similar performance can be seen in all three scenarios. However, for the building mount case a lower percentage of links displayed loss higher than 130 dBi. This loss range should contain mainly NLoS links, thus the proposition that higher power is observed in such links on the building scenario is shown here. Performance of the link in the LoS areas seems almost identical in all three mounting schemes.

As cities are complex environments with a great degree of variability in intra- or inter-city geometries, consistent placement of the AP cannot be guaranteed. That is why we rank AP placement by priority in terms of design and deployment costs and simplicity. If we want to prioritise performance, the following placement priority should be followed:

1. Middle of Roundabout.
2. Traffic Lights.
3. Street Lamps.
4. Mounted on Building Side.

If we want to prioritise ease of deployment and costs the traffic light scenario mounts should be chosen as only a small reduction in power and small dispersion of rays is observed comparatively to the middle of the island roundabout. The building mounts should be the last option for both performance and deployment cost mainly due to their inconsistent placement in urban environments and reduced ease of access. Building mounts are also not ideal if a reduced resolution codebook scheme is to be introduced not only the performance further deteriorates in irregular geometries but also reduces the ease of standardisation of such techniques. This will be discussed in more detail in the following sections.

6.3 Access Point Design

Throughout Chapter 5, it was shown that for transition areas, i.e. areas that the angular profile of the MS changes considerably faster compared to the rest of the route, coverage can be realised by using low gain and low-resolution configurations. These areas are usually populated with a low number of users, due to the limited time the MS spends there. These areas are usually located around the AP, thus narrow and high-resolution codebook beams will only impair the link due to channel aging and misalignment as the rate of angular change in these areas is significantly higher compared to the rest of the route. For the rest of the route, high-gain configurations allow us to cover a significant portion of the route even though the beamwidth is small as the angular range further away from the antenna is low.

6.3.1 Array Generation and Codebook Configuration

In rail scenarios, by merely placing the AP on the outside of a curve, we achieve at least a 50% reduction in the number of angles we needed to search to find the optimum beam. In urban geometries, however, this property will severely underperform due to the environment's irregular nature and the need for a 360° coverage in the azimuth domain. In these environments, the only possible redundancies that can be considered are direct blockages from buildings. However, these blocks are instrumental in reflection and scattering as a secondary ray; thus, removing propagation towards these sites will reduce performance in NLoS cases.

Access Point placement has been extensively discussed in previous sections. Due to the larger height difference between the AP and the MS and the fact that the APs are placed practically next to the road, we see an increased effective angular range in the elevation domain compared to train scenarios.

Another type of redundancy needs to be applied in these scenarios to achieve high throughput in areas further away from the AP while maintaining low beamforming set-up times.

It is vital to correctly model the antenna systems, especially in mmWave and high mobility scenarios where even minor artefacts can severely harm the study of channel and system parameters.

To suitably represent the antenna structures employed by such antenna systems the 12×7 planar array that described in detail in Chapter 5 was used. The total power radiation pattern of that array is shown in Figure 5.1(b) and a complete account of the array parameters can be seen in Table 5.1.

By placing an Access Point in the middle of the roundabout, we investigate the channel characteristics of a MS placed on the roof of a moving vehicle as it travels through a roundabout or a crossing. Three scenarios for a vehicle traversing a roundabout in an urban environment that are considered for this study are illustrated in Figure 6.8. The position of the mobile station is randomised around the line the vehicle is supposed to be following, to examine realistic situations. The analysis is applied for the middle of the roundabout AP placement, but we keep in mind the traffic light scenario requirements in designing our codebooks as a universal codebook needs to be designed, able to perform in most mount configurations.

Following the principles discussed in Chapter 5 to allow the ability to generate multiple beamwidths from the same array, a planar array based on the patch antenna element described

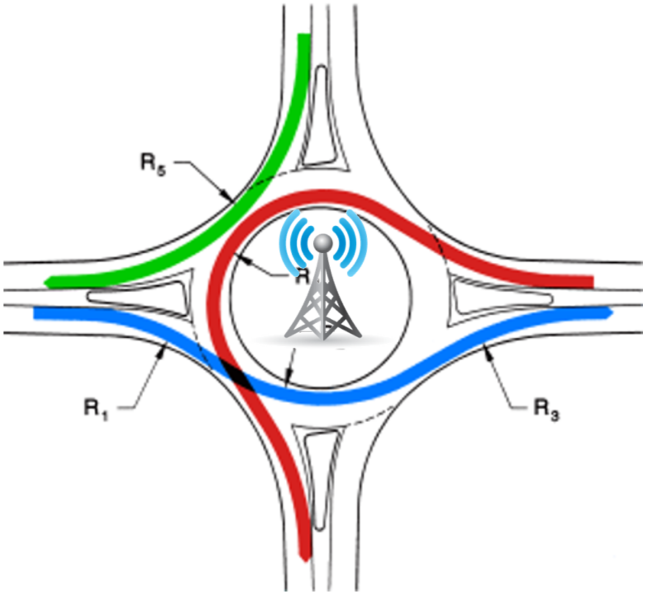

FIGURE 6.8. Roundabout Scenarios

in Chapter 3 has been theoretically modelled for both the Access Point and the Mobile Station antennas and has been chosen to suitably represent the antenna structures employed by such antenna systems in reality. Using omnidirectional dipoles to illuminate the area around the BS, the initial channel parameters are obtained. An overview of the ray-tracing parameters used to produce this data can be seen in Table 6.1.

6.3.2 Codebook Optimisation

To optimise the codebook configuration, an angular analysis of the ray-traced AoA and AoD is performed. In Figure 6.9, the highest power angles per MS point are plotted for the scenario where the vehicle performs a left turn after entering the roundabout (seen with colour green in the figure). As expected, no substantial variation in the transmitted and received angles is observed for areas further away from the AP. Similar observations can be drawn in the route on every scenario in Line-of-Sight (LoS) links. At distances larger than 15m from the AP, i.e. when the vehicle is approaching or leaving the roundabout, a connection can be maintained with beamwidths of 20° in the azimuth domain. The same principle applies in the elevation domain as well. However, as the vehicle starts the entry to the roundabout, a considerable variation in the angular profile is observed. Even though a similar behaviour with the HST scenarios is observed in the azimuth profile, a significant increase in the LoS spread is seen in the elevation angular profile. As shown in Figure 6.9(b) the change in elevation reaches even 50° in areas that are close to the AP.

Calculating the maximum elevation angular range value is relatively straightforward if the

TABLE 6.1. Ray Tracing Specification

Parameter	Value
Database	Vector, digitally modelled
Number of reflection facets	1.7 million
Reflection orders considered	Up to 1st order
Scattering model	Kirchoff
Diffraction model	Epstein-Peterson
Maximum backscatter angle	0.3926 rad
Incident angular range	30-75deg Incident Angle
Ray tracing interval (resolution)	1 m
Route length	400m
Antenna model	Isotropic
Tx power (ray-tracing)	0 dBm
Tx power (simulator)	22 dBm
Number of APs	1
Height of AP	5 m
Height of MS	1.5 m
Width of lane	2
Length of vehicle	3 m

roundabout's design characteristics, such as the rated speed, number of lanes, and positioning of the antenna on the moving vehicle, are available. Using the Pythagorean theorem, the elevation angular range can be calculated. The following shows the theorem in n-dimentions

$$d = \sqrt{\left(a_1{}^2 + a_2{}^2 + \ldots + a_n{}^2\right)} \tag{6.1}$$

For the smallest realisable configuration of a roundabout, a 4-meter central island diameter is specified. Allowing 1 meter extra for safety, this translates to a range of 0°-60° in the elevation domain if we assume a 5 meter high AP.

A 60° angular range cannot be realistically realised with a 2D codebook if high gain and

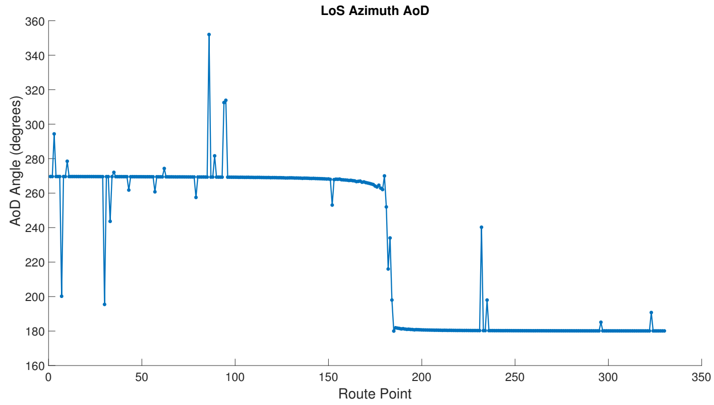

(a) Azimuth Anglular Profile

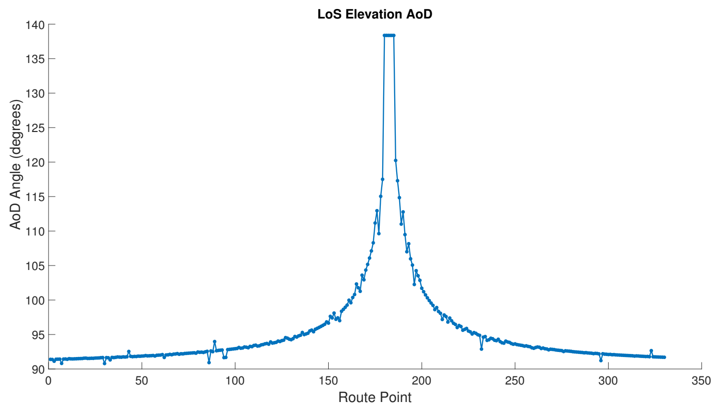

(b) Elevation Anglular Profile

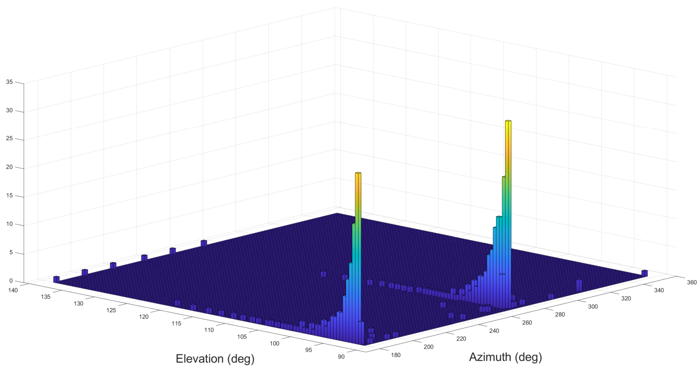

(c) Histogram of the distribution of angles (in degrees)

FIGURE 6.9. Urban angular profile

increased range need to be retained. Moreover, higher placement of the AP can significantly increase that value. In addition to that, if we are to take into consideration a traffic light mount in our design, the elevation angular range reaches its maximum value, covering the whole bottom hemisphere. Thus a design that caters for beams in the elevation domain is needed.

A building mounted antenna has a somewhat reduced azimuth angular range compared to the latter cases, mainly due to the increased distance from the road and due to the fact that there is no need of transmitting towards the building. However, the surrounding geometry dictates the need for more high-resolution sectors than in the cases of traffic lights or the middle roundabout one. In a regular urban environment with a high degree of symmetry, four sectors would suffice to determine the initial direction of transmission. Issues arise however when irregular geometries are considered, which consist the majority of urban scenarios. As discussed before, building mounted antennas display reduced LoS range, but increased scatter components. Hence, such configurations will need high gain beams pointed towards those locations, which are harder to predict or model due to the dynamic nature of the environment. This would significantly increase complexity in design and planning from a standardisation perspective.

The angular profile for each mount case is as below:

- Middle of Roundabout island: 360° Azimuth, and 60° Elevation
- Building: 270° Azimuth, and up to 60° Elevation
- Traffic Lights: 360° Azimuth, 90° Elevation (Scheme can also be applied in crossroads)

Mainly LoS rays are taken into consideration as walls are not consistent (material wise) in cities, and scattering greatly reduces power. First and second-order reflections from walls reach the receiver always with less power than that of the LOS ray, due to the increased distance in the NLOS environment and the scattered power from rough surfaces [98]. Relying on the fact that mmWave communication is efficient mostly for LOS environments [98] and assuming, the proposed method suggests reducing the gain and resolution of the beams highlighting the areas that are close to the antenna. NLoS rays will be considered in the design as well, not as a priority but more like a failsafe mechanism in cases of blockage.

By employing codebooks that are characterised with higher resolution and gain where the majority of the route lies compared to the antenna and much lower resolution in the areas around the AP, we can reduce the beamforming overhead by reducing the codebook resolution (and unavoidably the gain). In a uniform scenario, 3D codebooks with multiple elevation orders, each with a specific beam resolution and beam width. In the proposed scheme, we define the codebook in multiple elevation orders, each with its own resolution and gain characteristics. The first order lies at an elevation of -5°, second order at -25° and finally the third one at an angle of -60°. As we move higher through the order, the beam's elevation decreases, the resolution of the codebook decreases and wider, lower gain beams are used. Increasing the number of the order increments in the codebook allows higher granularity in the elevation domain and allows narrower and higher gain beams to be used. As the resolution in the elevation domain increases, the codebook size increases making them impractical for high-speed configurations. An example of the generated codebook can be seen in Figure 6.10.

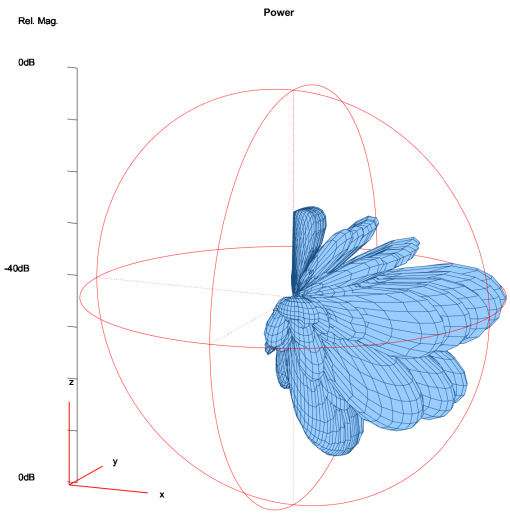

FIGURE 6.10. 3D Codebook Power Plot

A height of 5 meters for the AP and 1.5 meters for the MS are considered for this study to feature realistic passenger car scenarios. Assuming the previously discussed case of the smallest roundabout, an operating codebook can be realised even by two elevation orders. However, to maintain high-resolution beams in areas closer to the antenna, we design our codebook with three elevation orders decreasing the beams' resolution and array gain the lower the elevation they are pointed at. The design parameters will be described in one of the next sections shown in detail in Table 6.2.

Even though using high-gain and high-resolution beams in selective areas of the codebook reduces the link time, the computational and beamforming set-up load is still considerable due to the three-dimensional properties of such codebooks. In [98] and [97], the authors discuss using 2- or 3-step beamforming processes. In this work the search process is split into the DEV to DEV, sector and beam level search stages as described in [97]. When compared to exhaustive search mechanisms, this technique can achieve more than 95% reduction in setup time. The process and the time of each phase and sub-phase have already been presented in detail in Chapter 3. Using these equations, the time spent on each stage and the total link time in different scenarios will be derived and discussed in detail in Section 6.4.

The complexity and irregularity of roads in urban environments also has an effect in codebook design. Conceptually, roundabouts and crossings have three or more legs to divert traffic to, each with unique design characteristics affecting the size of the roundabout, entry speeds, width and number of lanes. Figure 6.11 shows examples of three generic roundabout configurations. To cater for such geometry we design our codebook such that roads emanating diagonally from the roundabout can still receive high gain LoS beams.

Adequate coverage can be achieved even with a four sector configuration during the second beamforming stage. However, to achieve better accuracy in the sector linking stage of the algorithm a higher number of sectors needs to be employed to provide good performance even for all the above described irregular geometries. An 8-sector configuration is thus proposed as it can provide more uniform coverage during that stage in urban configurations.

When the sector-to-sector mapping is complete, linking procedes the beam tracking phase. This is where we design and propose changes to the existing codebook techniques. Instead of the usual uniform 3-dimensional codebook, the above described non-uniform configuration is used. By dividing our transmit space to 8 sectors, we allocate a 45° range to each of them. If a 32 beam resolution is deployed (i.e. a beam every 11.25°), each sector would allow for three

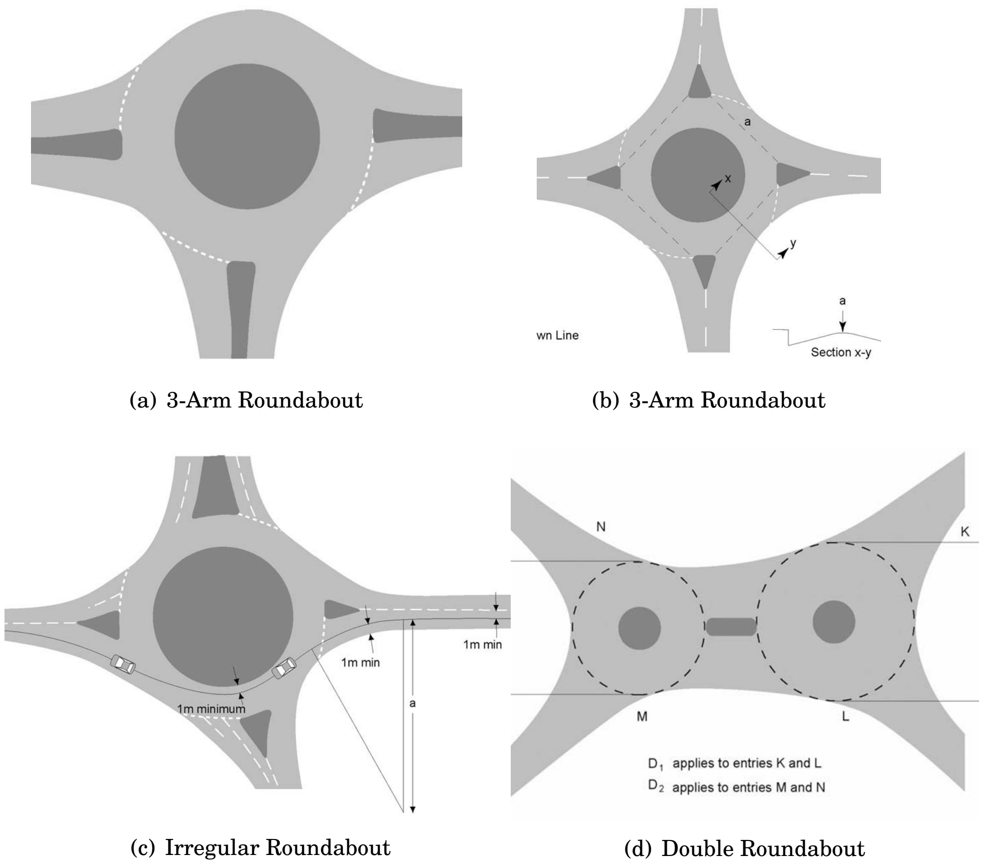

(a) 3-Arm Roundabout

(b) 3-Arm Roundabout

(c) Irregular Roundabout

(d) Double Roundabout

FIGURE 6.11. Roundabout Design

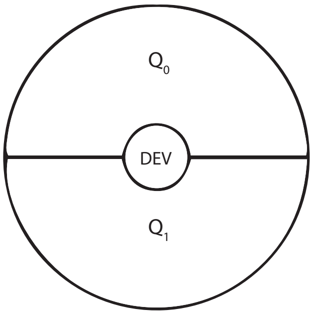

(a) Quasi-omni Pattern

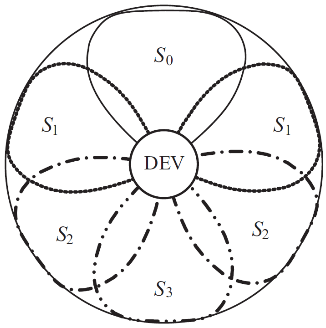

(b) 8 sector antenna

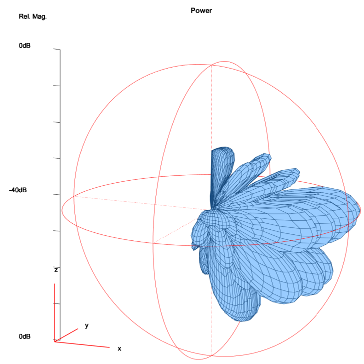

(c) Non-Uniform Codebook

FIGURE 6.12. 3-Stage Beamforming

beams. However, for the first order of the codebook we want to employ the highest resolution to allow higher granularity in areas further away from the codebook. Using a 64 beam resolution, we increase the number of beams per sector to 5 in the first order of elevation while using 10° beamwidths. This reaches to an angular range of 40° in the azimuth domain. For the second order, we achieve the same range with 3 beams using 15° beamwidths in a 32 beam resolution. Finally the third order uses just 1 beam with a HPBW of 45°.

The first order of the codebook uses a 15° HPBW in the elevation domain, while the second and third 23° and 30° respectively. Looking at the elevation AoD profiles throughout the route we can decide on the downtilt of each order of beams. Up to 25 meters away from the AP, while the antenna is still on the road approaching the roundabout, the angle changes only slightly. Finally at 25 meters away, it gets outside the range of the first elevation order at around -10° angle. While the codebook gets in the entry of the roundabout, the angular rate of change increases and after another 20 meters at an angle of -40° the beam is outside the range of the beam. For the rest of the angular range we use one beam, thus a 30° HPBW in the elevation domain is used for

TABLE 6.2. AP Codebook Parameters for Urban Vehicular Environments

	Azimuth HPBW	Elevation HPBW	Spacing	Gain (dB)	Elements Used	Number of Beams	Elevation Tilt
1st Elevation Order	8°	15°	5.625°	24.17	7×12	5	-5°
2nd Elevation Order	14°	23°	11.25°	23.09	6×9	3	-30°
3rd Elevation Order	45°	30°	-	15.32	3×5	1	-75°

the last beam to reach the 60° required in the worst case scenario. If this codebook is to be used for a traffic light configuration, the elevation HPBW of that last order in elevation would need to stretch up to 50 HPBW losing a significant amount of gain. These parameters can be seen in detail in Table 6.2, while a visual representation of the codebook used for the beam tracking phase for both the AP and the MS is shown in Figure 6.12.

6.4 Throughput Performance Evaluation of Codebook Parameters

Coverage and throughput are two of the most important metrics when studying the performance of V2I wireless systems. Systems in this space will most probably vary in frequency, transmission power, cell size, and network structure, but it is vital they are properly parametrised to achieve uniform coverage and high data rates throughout the environment. In this section, we analyze the coverage and throughput performance of the proposed codebook configuration and the necessary parameterization to achieve these requirements.

The proposed multi-stage scheme reduces the BF setup time significantly at an insignificant increase on the bit error rate (BER) in some cases. Different parameters affect the SNR and as a result BER as well so a sensitivity analysis is provided to discuss the effects of multiple codebook design choices. The main parameters that we will be discussing in the following analysis are beamwidth and number of beams per elevation order of the codebook.

Initially the beams for the first order of elevation are studied. As discussed in section 6.2, first order beams focus the power on areas further from the AP. To compare with the 5-beam configuration, a 3-beam configuration with the same 64 beam resolution (5.625° spacing) was generated. Even though the SNR was identical for the two cases in the specific environment,

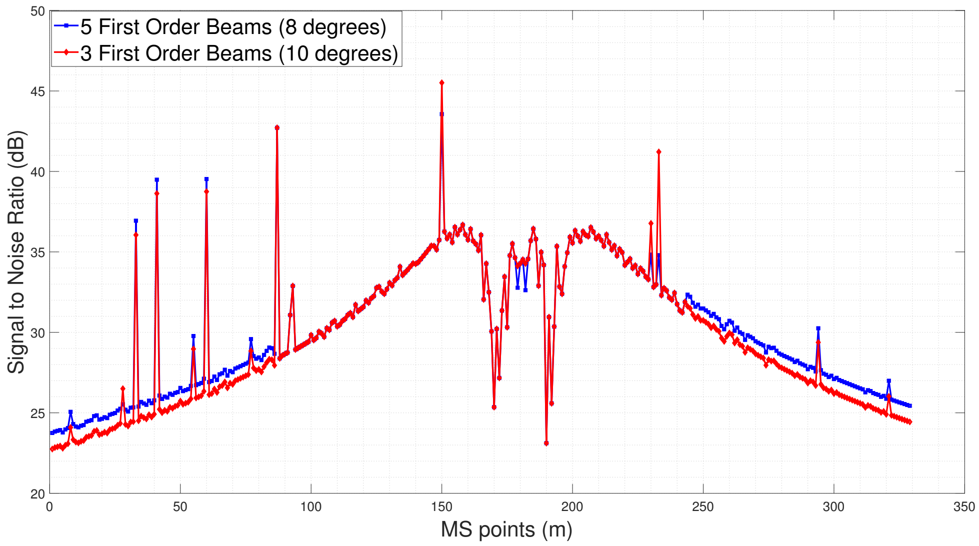

FIGURE 6.13. Effect of the number of beams in for the 1st elevation order of the codebook

differences might appear in irregular geometries when the LoS ray's AoD might exist at a higher off-boresight angle than the ones covered by the codebook beams By reducing the resolution and the beamwidth of the first order beams to match the second order parameters (10° HPBW with 11.25° spacing) we can overcome this issue. As shown in Figure 6.13 slightly lower SNR is observed areas further away (>30 m) from the AP, while no difference is seen for those closer to the AP. Thus, even though results are comparable in regular geometries, 5-beam configurations with a 64 resolution will be chosen for this elevation order to allow for a higher range and accuracy in areas further away from the AP.

Following that, the effects of the number of elevation orders in presented in Figure 6.14. Reducing the codebook to 2 orders instead of 3 has no significant impact in areas further away from the AP. Areas close or within the roundabout however, see an increased signal variation. Especially when the vehicle is inside the roundabout an increased number of nulls and poor service is observed. These effects are further amplified when increased height or another mounting solution is chosen.

As we have established that a third order is required in the codebook we discuss the effects of the design of that beam. Inreasing and reducing the width of that beam affects performance as it is shown in Figure 6.15. Initially a 20° beamwidth in the azimuth domain was used to achieve higher gain in areas close to the AP. However, fluctuations as the vehicle traverses through the roundabout are observed, especially in the areas on the side of the third order beam. A wider HPBW (45°) configuration allows higher angular coverage inside the roundabout and slightly

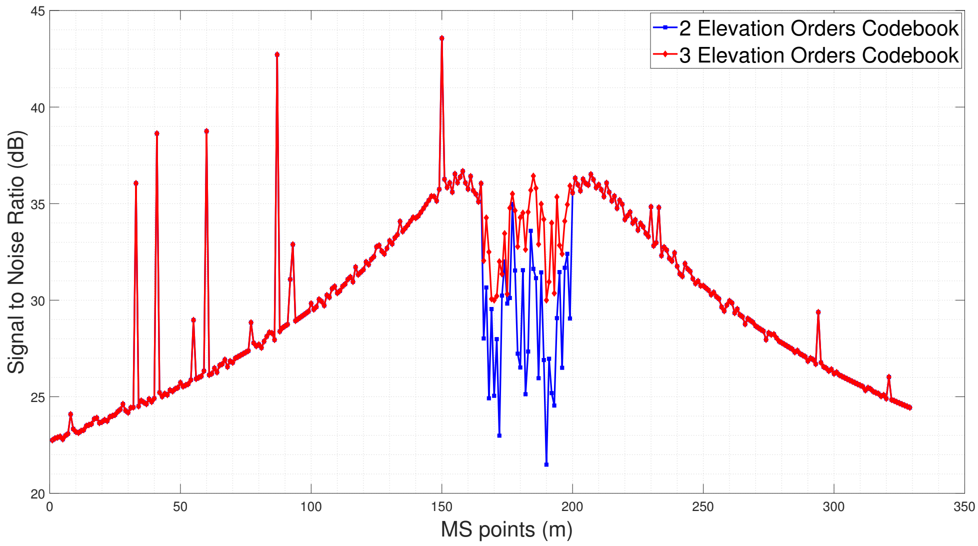

FIGURE 6.14. 2 order vs 3 order AP

mitigates that issue but at the expense of reduced gain. The introduction of a wide beam reduces variation and the number of nulls, without however, eliminating them completely.

Finally, the effects of the receiver side codebook parameters are discussed. A 2D codebook scheme, same as the one employed on top of the moving train, provides coverage in the az-

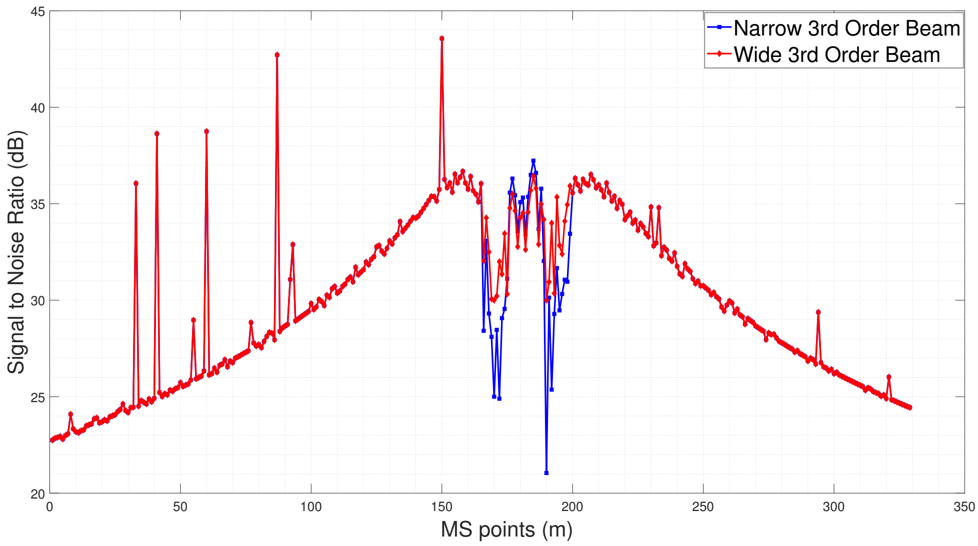

FIGURE 6.15. Effects of HPBW in the 3rd elevation order of the codebook

imuth domain. However, due to the increased angular spread in the elevation domain, beam misalignment is seen in areas closer to the AP. We clearly see these effects in Figure 6.16 where a comparison of the SNR of uniform 2D and 3D schemes is plotted. Increased power is observed in the areas closer to the AP when the 3D MS codebook is applied due to better alignment of the beams. It should be noted that in this 3D scheme, 2 elevation orders are only needed to account for the increased spread, thus in total 64 beams are employed in the MS.

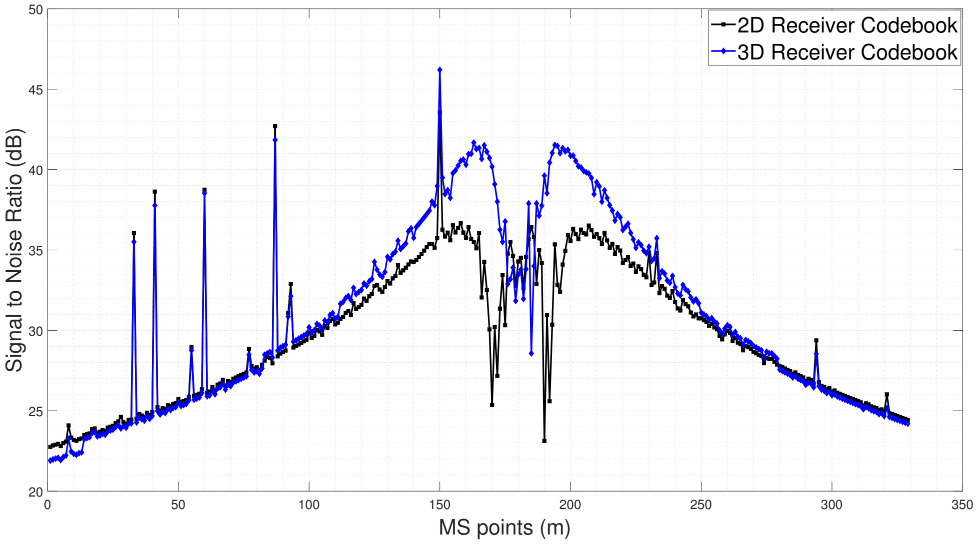

FIGURE 6.16. Effects 3-dimensional receiver codebook

The resulting codebooks are shown in Figure 6.17.

The analysis provided above, was based on the left turn scenario that was previously described. In Figure 6.18, we see the SNR performance of the codebooks discussed above. Even though variation in the signal levels is observed close to the AP, no nulls are seen, and thus high throughput and no outage is achieved using the proposed codebooks.

6.5 Channel Aging for Multi-step Adaptive Codebooks in Urban and Highway Scenarios

Up to this point, we showed that the deployed non-Uniform codebooks have comparable throughput performance with high-resolution uniform codebooks. To be able to extract some practical information from all this data in terms of network and codebook deployment and design, the total number of steps needed for AP to MS linking is presented in Table 6.3 for comparison. The respective times needed for the setup of those links are calculated and presented in Table 6.4.

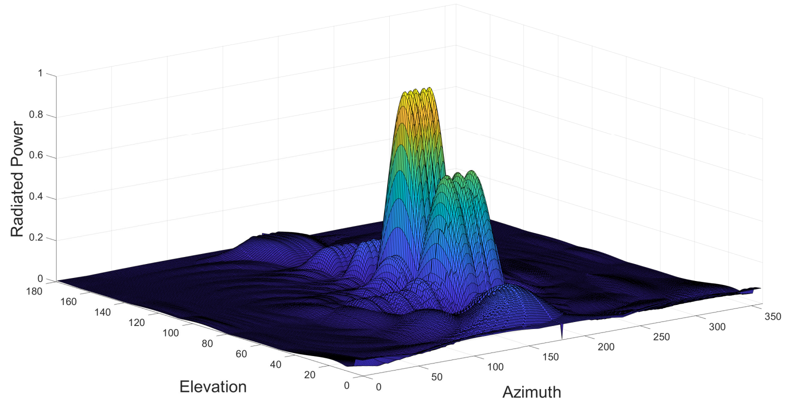

(a) AP Codebook

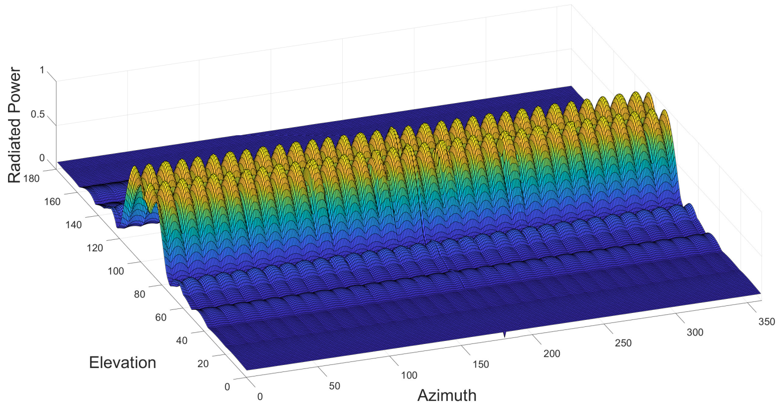

(b) MS Codebook

FIGURE 6.17. Codebook Power Profile

In Chapter 3 the beamforming process was discussed in detail and the times for every sequence or block were defined. The equations for the steps required for the linking process of two devices according to the 802.11ad and 802.15.3c standards were derived. In the context of 802.15.3c, the equation for the time required for linking those same devices was presented with the timings within the frame.

As defined in Section 6.3, the receiving device (i.e. the MS) is populated with 64 beams while the transmitter by a 9-beam codebook every 45°, thus 72 beams in total. In the 3-stage algorithm, both the AP and MS configurations are separated into 8 sectors with 9 and 8 beams respectively. We assume that a quasi-omni pattern is able to cover 2 sectors (due to the initial patch parameters), that is, in total we have 4 quasi-omni patterns. Finally, in this analysis, equal AP and MS codebook sizes are used for the uniform cases, while for the non-uniform cases, the proposed codebooks are used in the AP paired with a 32 or 64 beam configuration MS according

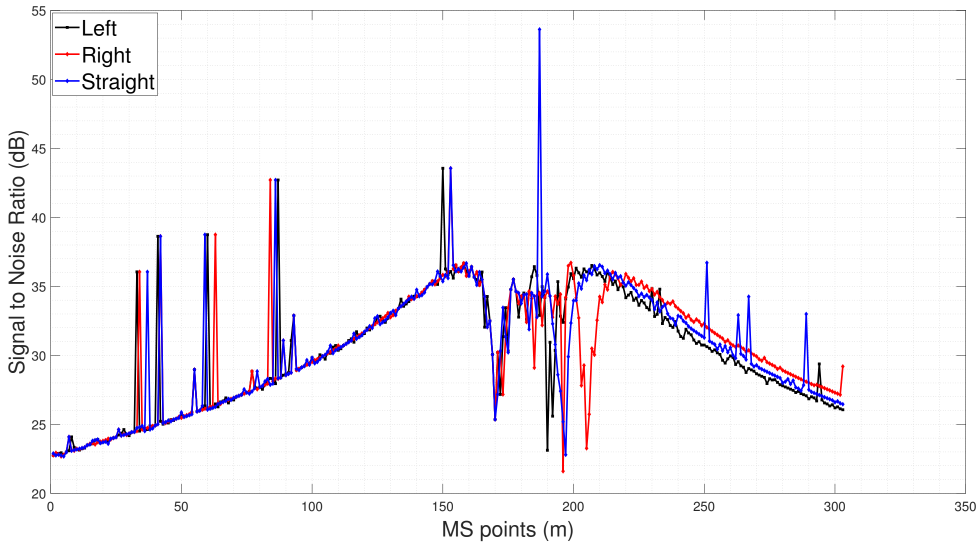

FIGURE 6.18. SNR For 3 Roundabout Scenarios (Left, Straight and Right Turn)

to the environment under study.

6.5.1 Set-Up Time and DEV-to-DEV Linking

The uniform, and non-uniform configurations derived for both car and train scenarios throught the course of the last two chapters are discussed in terms of their size, step count and setup times. The uniform cases show a linear increase of steps in the case of 802.11ad and an exponential increase in 802.15.3c. As expected, the non-uniform train schemes manage to keep the number of steps considerably lower, even with a high side-beam resolution. For example, the largest codebook that includes 8 side- and one middle beam needs almost half the steps while using 802.11ad algorithms and only a quarter of the steps included in 802.15.3 when compared to a 32×32 uniform case.

In the tables, “uniform” refers to 2D or 3D codebooks with 8,16,32 and 64 beams employed uniformly in the azimuth domain with the same number of beams in both the AP and the MS. “Non-Uniform” 5,7 and 9 configurations represent the generated AP codebooks for the train scenarios described in Chapter 5,employing 2,3 and 4 beams on each side respectively. In these cases a 32-beam codebook is assumed for the MS. Uniform and non-uniform “car” codebooks refer to the codebooks generated in this chapter, while in total 72 beam patterns are assumed for the non-uniform and 96 beams for the uniform AP (3 elevation orders), while 64 beam patterns for the MS (2 elevation orders).

Even without employing multi-stage beamforming techniques, BF overheads are kept low in the HST scenarios even when the resolution and size increases in the side-beam areas. A 9-beam

TABLE 6.3. Number of steps per BF method

Azimuth HPBW(degrees)	Steps in 802.11ad	Steps in 802.15.3c	Search Method
Uniform 8	18	140	Exhaustive
Uniform 16	34	532	Exhaustive
Uniform 32	66	2084	Exhaustive
Uniform 64	130	8260	Exhaustive
Non-Uniform 5 (Trains/Chapter 5)	12	329	Exhaustive
Non-Uniform 7 (Trains/Chapter 5)	16	459	Exhaustive
Non-Uniform 9 (Trains/Chapter 5)	20	589	Exhaustive
Uniform Car 3D	162	12388	Exhaustive
Non-Uniform Car 3D	138	9292	Exhaustive
Non-Uniform Car 3D	43	310	Multi-stage

non-uniform configuration requires only a quarter of the steps needed for the equivalent uniform configuration, and directly compares with the performance of a 16x16 uniform codebook.

The number of steps required for DEV to DEV linking is directly connected to the setup time. For this analysis, an 802.15.3c based method is used to calculate the total time required from the arrival of the first allocated CTA. Different devices in different vehicles are linked in multiple Channel Allocation Periods as defined in the MAC frame format. For this analysis we use a network of two devices. When the exhaustive search method is used, which tries all beam pair combinations and finally finds the best pair for transmit and receive, the set-up time is around 31.57ms, even in an ideal channel with PER=0. Using the proposed codebook and the 3-stage scheme, more than a 97% decrease in the number of steps and hence setup time is observed. In Chapter 3 a complete review on the timing of beamforming was performed based on a superframe model. Using the derived parameters, the link times required for every configuration was calculated using Equation 3.21 and are shown in Table 6.4.

TABLE 6.4. Setup time per BF method

Codebook Configuration	BF time in μs	Search Method
Uniform 16	1885.4	Exhaustive
Uniform 32	7061	Exhaustive
Uniform 64	27424	Exhaustive
Non-Uniform 5 (Trains/Chapter 5)	1144.6	Exhaustive
Non-Uniform 7 (Trains/Chapter 5)	1582.8	Exhaustive
Non-Uniform 9 (Trains/Chapter 5)	2021.1	Exhaustive
Uniform Car 3D	41110	Exhaustive
Non-Uniform Car 3D	30846	Exhaustive
Non-Uniform Car 3D	1255	Multi-stage
Non-Uniform Car 3D	8279	Multi-stage (Only in AP side)

As we can see, the proposed car codebook achieved a 25% decrease in the beamforming time even with no multiple stage BF applied. Using 3-stage BF achieves a 96% reduction from the uniform codebook employing exhaustive search.

As the channel deteriorates and BER values increase, the BF setup time naturally increases by 13.2% compared to an ideal channel with no transmission errors due to the command retransmissions after a waiting time [97]. Moreover, since significant changes occur to the vehicular channel due to mobility, the directional communication link may be lost and the operation will need to be repeated. However, cases of retransmission or repeated BF will not be covered in this work.

6.5.2 Effects of Speed in System Performance

Design speeds ultimately refer to the maximum speed at which a corner can be travelled while keeping the vehicle on the road. The formula given in [141] ensures that this is achieved by balancing the centripetal/centrifugal forces experienced while cornering.

Train environments have recommended maximum design speeds according to the track characteristics and the train used. Steam trains, carriage trains, electric trains and Maglevs all have different recommended values. The focus in this analysis is in high-speed railway thus 320 km/h (200 mph) is chosen as the speed value for our study. As discussed throughout this thesis, mobility plays an important role in DEV to DEV linking. The 2 devices linked are not static and need to update the parameters and track the device on the moving vehicle in certain periods. These periods greatly vary in the different environments discussed throughout this study.

Similarly different road architectures specify different speeds in urban and highway environments. The more complex nature of urban environments dictates the need for more parameters to be considered while designing these architectures. In this analysis the design speed is considered instead of speed limit as those limits are normally defined by local or country authorities and considerably differ even within the same country. One important parameter is the recommended maximum entry design speed, which essentially defines the speed the vehicle will be traversing throughout different environments. In crossings these values are significantly smaller as the flow of traffic is slower and much more dynamic. The proposed values for different types of roundabouts are seen in Table A.2 in Appendix A. The focus of this work is urban environments, thus an average value of 50kph will be used in this analysis.

To be able to provide a metric regarding the rate of change of the angular parameters of the link, the analysis discussed in Chapter 4 is performed. In this case, beamwidths of 8, 10, 15, 50 and 90 degrees were considered to investigate when (according to the profiles seen above) the MS and the AP have to perform a search for a new beam. In Table 6.5, we can see the travelled distance in meters required in each case before a new search needs to take place in the roundabout scenario.

TABLE 6.5. Rate of Change of Angles

	8 deg	10 deg	15 deg	50 deg	90 deg
LOS (m)	26.3	31.3	32.7	59.4	74.2
NLOS (m)	4.8	4.58	5.17	5	7.64
1st order reflection (m)	8	6.38	7.02	6.3	10

The values for the train environments have already been presented in Chapter 4 and specifically in Table 4.5. These tables are really important in the design of beamforming as they provide an upper bound for the search period ($T = \frac{d}{s}$) such that seamless connectivity is achieved According to Table 6.4 in the case of 32x32 codebooks beamforming is finished in 7.06ms. Using a 10° HPBW antenna array measurements that beam searching needs to be applied every 31 m to achieve correct alignment and avoid any loss of service. Thus, for a train moving with a speed of 350kph (about 97 m/s), that means every 31/97=0.32s, while for a vehicle in urban environment, every 2.2 seconds.

As shown, 7.06ms are needed for the codebooks to link and thus 0.32-0.007=0.313 seconds are used for transmission of data. Thus, the effective data rate will be $0.313 \times C$ for every beamforming cycle or $0.313 \times C \times 3.3$ Mbps. For this case this means $\frac{0.313 \times C \times 3.12}{C} = 97\%$ of the maximum achievable rate. Similarly, the percentage for every scenario is calculated and presented in Table 6.6.

TABLE 6.6. Percentage of maximum data rate

Codebook Configuration	Percentage (%) of Maximum Data Rate Achieved
Uniform 16	100
Uniform 32	97
Uniform 64	91.28
Non-Uniform 5	100
Non-Uniform 7	100
Non-Uniform 9	100
Uniform Car 3D	98.14
Non-Uniform Car 3D	98.6
Non-Uniform Car 3D (3-stage BF)	100

Finally, the impact of channel aging in mmWave systems is investigated. Channel aging refers to "the mismatch between the CSI at the time instant when the channel is estimated and when it is used for data transmission and occurs due to the time-varying nature of the channel" [122]. This discrepancy between the channel coefficients being used for beamforming/data detection and the true channel values leads to degraded system performance. The effect of channel aging on the achievable rates of large MIMO systems has been analyzed in [88, 122, 125, 126].

Taking into consideration retransmissions due to the high loss channel in mmWave frequencies, we assume a 16x16 codebook can beamform every meter of the route (i.e. every 10 ms) while maintaining high data rates. Codebook systems with higher number of beams and hence larger number of setup steps will thus need to beamform on multiples of that 1 meter resolution.

Using the values previously presented in Table 6.3, we conclude that 3D uniform antennas

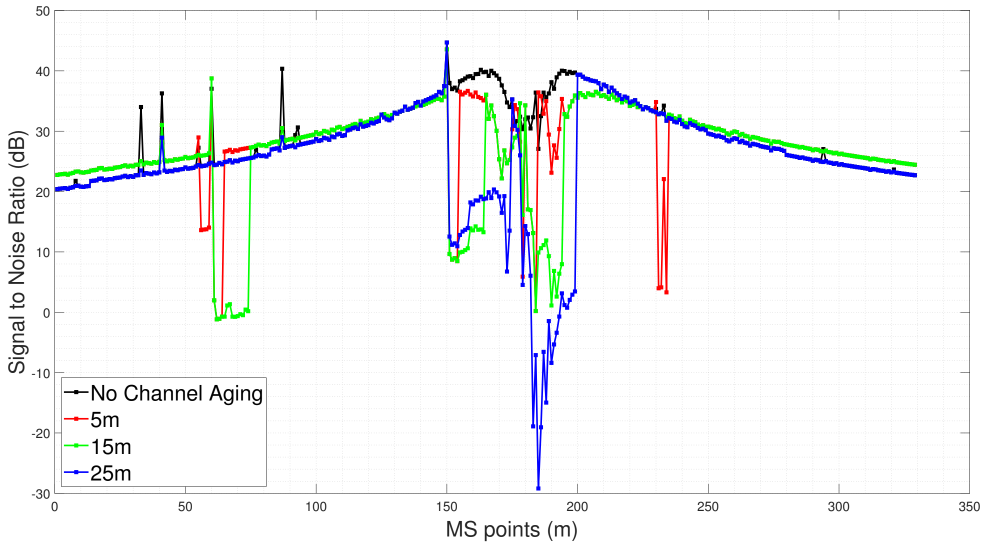

FIGURE 6.19. Channel Aging Effects

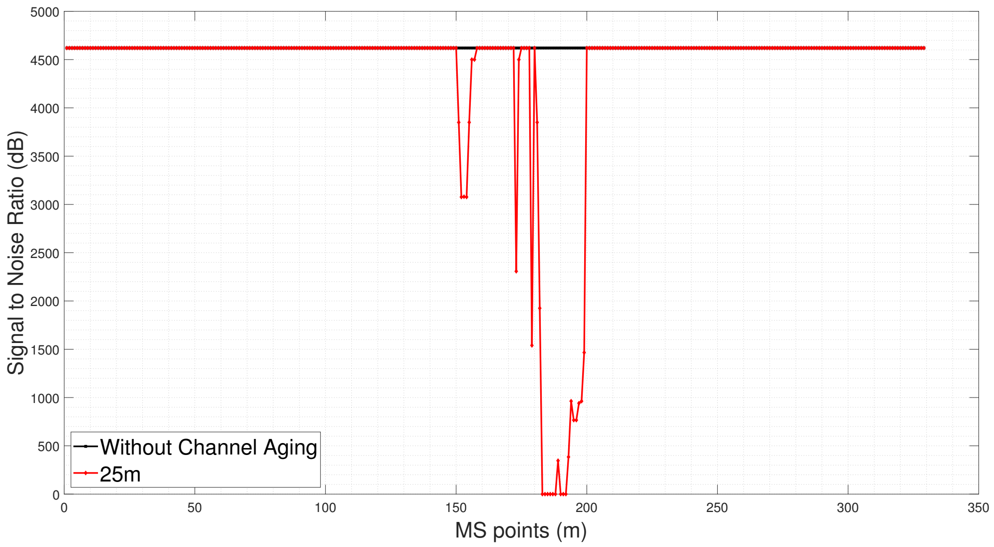

FIGURE 6.20. Channel Aging Effects

serving urban scenarios have the worst performance as the number of beams they employ is significantly higher than any other case. The number of steps needed to link a 96 by 64 codebook is 12388 which is about 25 times the steps of the 16x16 configuration. This means that they are only able to beamform every 25m.

The proposed 3-stage non-uniform codebook, however, has only 0.6 times the steps of the 16x16 scenario, which means we can beamform every meter throughout the route. In Figure 6.19 we show the predicted SINR for these three cases in both an urban and train environments. Throughput performance is plotted as well in Figure 6.20. Is is clear that the nulls seen in the SNR plots are quite severe, thus leading to significant drops in throughput performance in the areas next to the AP. The percentage of total outage in this case reaches slightly over 2.75% when larger codebooks that incur channel aging with an average throughput reduction of about 6%.

As expected the 16x16 and the proposed codebook completely coincide. The uniform case however shows significant signal degradation. The effects of channel aging due to increased beamforming time become apparent in this graph showing the conciseness of our design which performs the same as the optimal scenario.

6.6 Conclusions

This chapter concludes our research in vehicular environments. In this chapter enabling architectures for urban vehicular geometries were studied. Throughout the chapter, the mounting of antennas is discussed in terms of their position in urban geometries. Specifically the road and roadside furniture requirements are drawn and the optimum placement of the APs in highway and urban scenarios are drawn. To account for the large variability seen in city geometries, a ranking of AP placements based on performance in three mounting scenarios is discussed. To achieve that, grid ray tracing solutions were used to draw conclusions on how the power is diffused in the environment assuming only one order of reflection.

Mounting options that are in a point of symmetry in the road, i.e. the middle of a roundabout or a crossing displayed the highest performance. Mounting on traffic lights showed comparable performance for urban geometries, while building mounts were proposed to be avoided due to the increased maintenance costs and their unpredictable placement within urban geometries.

In previous analysis, we showed that LoS links dominate mmWave links thus, a solution that focuses on taking advantage of this property and ignoring the redundancies of the environment is designed. An access point codebook is introduced for roundabout and traffic light mounts and its parameters were optimised through route analysis. The codebook was then presented as a part of a 3-stage BF process. The proposed codebook managed to achieve similar throughput and coverage performance as uniform codebooks despite the reduction in resolution of the beams in the elevation domain. In HST communications, the codebook was designed to directly focus on the LoS rays. However, while urban vehicular scenarios try to maximise the effects of the LoS rays, it still achieves 360° coverage around the AP by varying beamwidth and resolution values. Thus, NLoS and reflected rays are also considered as potential alternatives in this design in cases of blockage or shadowing as discussed in [106] and in Chapter 4.

Finally, the effects of codebook size in beamforming setup were discussed. The number of steps required for two devices to link and the resulting times were calculated based on the processes defined in the 802.15.3c standard. These values were then linked to channel aging and degradation of performance considering a single vehicle acting as the mobile station in the environment. It was shown that the reduction of the azimuth resolution on every elevation step makes the search process require less steps and hence less time to setup. Moreover,the combination of the proposed codebook with 3-stage BF processes further reduce the setup time of high resolution codebooks to a trivial number, which reduces the effects of channel aging in mmWave environments.

Chapter 7

Conclusions and Future Work

7.1 Summary

This thesis presented a comprehensive physical layer analysis of communication systems integrating antennas and propagation modelling for complex and realistic vehicular environments. Overall, it was shown that the antennas, propagation environment and beamforming applications are of fundamental importance in a wireless channel, and therefore they need to be carefully and accurately considered to evaluate and optimise the system performance.

Chapter 2 began by introducing the basic concepts that define the wireless propagation channel, e.g. path loss, small and large scale fading, along with antenna properties that allow us to define the channel. Both the propagation model and the antenna model are essential to accurately describe the characteristics of the channel. Different wireless modelling techniques were described in this chapter. Stochastic models are widely deployed due to their low complexity and thus low computational expense. However, they are also characterised by a reduced capability to model the elevation domain, which is vital for higher frequencies. Commonly used models include 3GPP, mmMAGIC, NYU and METIS. These models have been briefly analysed and classified in terms of the modelling approach used. Deterministic channel models provide a more accurate solution to describe the channel with only a slight increase in the computational expenses while retaining all of the channel's characteristics. This is essential for higher frequencies that blockage and loss have to be determined in greater detail, meaning that any stochastic process (such as the clustering used) could result in considerable inaccuracies in the model's output.

The 3D ray model and antenna array assumptions were introduced in Chapter 3, and the method for creating the combined channel and antenna matrix was discussed in detail. The ray-based double-directional model is one of the most widely used methods to describe the channel, as it allows separation of the effects of the antennas and the effects of propagation. Database formulation and key processes of ray-tracing, as well as improvements in deterministic modelling techniques, were initially discussed in terms of the generation of the radiowave model. An antenna model that can be used in conjunction with physical radiowave propagation models to generate a ray-based double-directional channel suitable for system-level simulations was then described. The model can support any antenna radiation pattern orientation and arbitrary MIMO array configuration in 3D space. System-level simulations based on a classic physical layer abstraction technique known as the Received Bit Mutual Information Rate (RBIR) were introduced. The propagation mechanisms and relevant databases were described in terms of ray tracing, considering the effects of mmWave technology. The methods used for antenna array generation, along with the rotation of the antenna pattern throughout the environment to form 3D codebooks was also discussed. Finally, codebook-based beamforming processes were presented along with some popular beamforming standards that will allow us to discuss the effects of setup time in High-Speed mmWave environments. This work combines previously reviewed work to study Key Performance Indicators (KPI) for selected mmWave applications and scenarios.

In chapter 4 the angular characteristics of the wireless channel considering 2 urban environments were presented. It was shown that the azimuth and elevation spreads largely coincide with the values proposed by 3GPP and mmMagic models, while the number of multipaths vastly differs. The spatial evolution of the multipath components was also studied, and a metric for the angular rate of change in terms of beamwidth was derived. The impact of the antenna parameters and beamforming was also studied. It was shown that most of the channel parameters were affected, with the channel being "compressed" with the use of directional antennas. Ray birth and death statistics have shown that NLoS links are important in vehicular environment as they enrich the wireless media, but the majority of the links display a LoS component. The system level benefits (in particular the throughput gains) of the application of high gain antennas in HST environments were also discussed in this section along with frequency and antenna spacing discussions.

In chapter 5, we studied enabling mmWave BF technologies to meet the increasing data demand for HST communications. Throughout the chapter, a fixed beam and two BF schemes based on a synthesised beam pattern were introduced and investigated in two different environments at both 26 and 60 GHz. Considering a train, mounted with two antennas travelling along a train track, a simulation has been conducted to show the three BF scenarios' performance in different AP separations to draw conclusions regarding throughput and outage. Metrics that would allow service providers to optimise the network in HST scenarios by considering deployment density, complexity, and performance were provided. Fixed beam configurations can provide good throughput and coverage only in specific scenarios where the angle spread is small but underperform adaptive BF architectures in any metric apart from device cost. Non-uniform solutions that consider the track geometry to take advantage of azimuth angular redundancies due to network design were introduced. These configurations displayed similar performance with high-resolution uniform configurations while employed with a reduced number of beams, leading to faster BF setup times.

Finally, in chapter 6, architectures for urban vehicular geometries were studied. The mounting of antennas is discussed and ranked in terms of performance and deployment costs. Mounting requirements to decide on the optimum placement of the APs in highway and urban scenarios are also drawn. Mounting options in a point of symmetry in the road, i.e. the middle of a roundabout or a crossing, displayed the highest performance. Mounting on traffic lights showed comparable performance for urban geometries while building mounts were shown to be avoided due to increased deployment and maintenance costs Solutions that focus on the direction of the LoS ray were discussed, and a scenario where the AP was deployed in the middle of a roundabout was used to optimise the parameters of the proposed codebook. By reducing the beams' azimuth resolution in every elevation order, the proposed codebook managed to achieve almost identical results as 3D uniform codebooks. To conclude, a 3-stage BF beamforming algorithm and exhaustive search algorithms were applied to discuss BF setup time. The number of steps required for two devices to link and the resulting times are calculated based on the processes defined in the 802.15.3c standard and were then linked to channel aging and performance considering a single-vehicle acting as the mobile station in the environment.

7.2 Conclusions

The ultimate aim of this work was to develop and demonstrate a set of useful tools and methodologies that can be exploited in order to answer the difficult question of which antenna, or MIMO antenna array, will achieve the best performance in complex multipath propagation environments.

With the design process being completely modular, antenna/codebook relevant parameters at any stage of the simulation can be modified for any relevant use case consideration. Thus, with a streamlined process such as the one derived within this work, future systems can be studied up to really high frequencies giving fine control to the researcher/user to completely customise and fine-tune the experiment.

Using a deterministic ray-tracing approach, a detailed analysis of the physical channel characteristics shows that LoS rays dominate the link in mmWave architectures. Although the antenna and codebook design have to cater for NLoS links in the case of blockage (or sub-optimal placement), this is not a priority while designing solutions based on those results. Correct network planning, AP placement and design maximising the LoS links can ensure good coverage up to a point but it is definitely not enough on its own. Thus, antenna systems that can beamform towards both the LoS and NLoS components have to be designed, although with a reduced resolution on the NLoS directions.

Considering beamforming, maximum ray BF schemes have shown to yield the highest and most stable SNR and throughput compared to any other scheme, providing perfect coverage even when the APs were placed 800m apart, with the requirement, however, of accurate CSI at both ends of the link. Codebook solutions provide the best performance compromise between data rates, outage percentage and AP separation, allowing constant connectivity between terminals though with a larger variation on throughput. Specifically, codebook solutions present themselves as the only viable solution for any 5G application, especially high-frequency and high-mobility use cases due to both higher performance and the high configurability and adaptability they expose to the system architect.

Spherical and uniform codebook coverage was shown to work in cellular and more chaotic environments throughout literature, but in simplistic HST scenarios where beamforming time becomes important, they were shown to underperform especially in areas with high angular rate of change. Instead, non-uniform solutions that consider the track geometry to take advantage of angular redundancies due to network design, present similar performance with high-resolution uniform configurations while employing a reduced number of beams. Such configurations lead to faster BF setup times, reduced channel aging artefacts and even lower costs while at the same time maintaining the same throughput and outage performance throughout the route.

As previously mentioned, the positioning of such APs in urban and train environment seems to be largely affect the performance of the system, even though it has not been studied in detail in literature. AP mount analysis has shown that antennas placed over the road or in the middle of a roundabout using either specialised equipment or existing traffic signalling infrastructure yields the best results. Additionally building mounting should be avoided due to increased deployment and maintenance costs as well as their unpredictable placement within urban geometries.

In such architectures, it was shown that 3-stage BF processes combined with the reduced resolution codebooks reduce the setup time of high-resolution codebooks to an almost trivial number, thus minimising the effects of channel aging in mmWave environments. 3-stage BF processes are required specifically in these applications due to the chaotic nature of the urban environment requiring close to hemispherical coverage around the AP Non-uniform schemes that reduce the beams' azimuth resolution in every elevation order is studied as in areas close to the AP the angular rate of change significantly increases. In high-mobility scenarios and specifically in areas that the angular characteristics of the LoS beam at both the transmitting and receiving antenna rapidly change, schemes such have the ability to significantly improve performance. The proposed codebooks manage to achieve almost identical results as 3D uniform and spherical codebooks only using a fraction of the total beams.

7.3 Future Work

There are many areas that require update and characterisation in order to address the challenges introduced by high frequencies and mobility in vehicular scenarios introduced by 5G that will carry over the next generation 6G (6th Generation) communication technologies. Ray tracing solutions will need to be updated with advanced models that can cover any geometry such as tunnels. Methods to dynamically update urban databases based on open source LiDAR and vectorised data will need to be implemented. Finally, an integrated solution for indoor to outdoor (and vice-versa) models to cater for IoT applications will need to be added. Physical measurement campaigns to validate the simulated data and to discuss and model the effects of polarisation in performance in such environments need to be performed as well.

Apart from the resolution requirements for improved accuracy, higher frequency technologies further require more detailed database characterisation. The 10 classes defined previously in the clutter database might prove to be insufficient in higher frequency scenarios. Thus it is proposed that the database would include an increased number of scenarios to classify the land, as their effects are even more significant in higher frequency applications. On top of the clutter database update, a need for moisture absorption and rain attenuation database is vital. Atmospheric effects (e.g. rain, fog, and moisture) could greatly restrict the range in millimetre wave communications due to the additional attenuation in such frequencies. Ultimately, this work has highlighted the need for higher resolution modelling or more detailed studies on the effects of clutter/pedestrians/other vehicles and obstructions in a more dynamic environment.

In this thesis, equations that describe vehicular geometries, as well as placement and positioning of appropriate infrastructure, were derived. Machine Learning and AI techniques can be used to optimise these parameters using deep and reinforced learning techniques.

Moreover, the simulation framework needs to be updated to include any number of users dynamically. Integration of the Eclipse Simulator for Urban Mobility (SUMO) with the current simulator was discussed but was not implemented due to time restrictions. The framework from the SUMO side has already been developed as part of another project. Traffic Control Interface (TraCI) was used to create a bidirectional channel between Matlab and SUMO traffic generator to parse vehicles and pedestrian mobility traces as positioning data. However, integration with the simulator will mean that the ray-tracer and RBIR simulator have to be configured to apply temporal analysis in the models, as the current solutions are non-efficient, non-scalable and introduce complex post-processing methods. Time sampling in these models is crucial in vehicular communications as the travel speed of each user and the resolution of the database would impact the accuracy of the results; thus they need careful consideration.

Finally, integration with channel emulators or network simulators such as $ns-3$ is a possible part of such analyses as a part of a 2-stage process, including the SUMO framework, to research dynamic scenarios with appropriate characterisation.

APPENDIX A

APPENDIX A

A.1 Urban Geometries Design Parameters

Recommended speeds, are a function of multiple variables such as the anticipated volume of traffic, the anticipated operating speed, and the environments' geometric requirements. In Table A.3 the speed profiles for urban and rural roads are defined based on the expected use of the road.

Table A.1 the the physical design parameters of the central island and safety mechanisms are shown.

Table A.2 shows the speed profiles for different roundabout configurations in terms of their design parameters.

TABLE A.1. Roundabout Design Speeds

Central Island Diameter (i.e. a)(m)	Central Island radius (m) + Safety	Minimum Inscribed Circle Diameter (i.e. f) (m)
4	3	28
6	4	28.8
8	5	29.8
10	6	30.8
12	7	32
14	8	33.2
16	9	34.6
18	10	36

TABLE A.2. Roundabout Design Speeds

Site Category	Recommended Maximum Entry Design speed
Mini-Roundabout	25 km/h (15 mph)/(7 m/s)
Urban Compact	25 km/h (15 mph)/(7 m/s)
Urban Single Lane	35 km/h (20 mph)/(9.7 m/s)
Urban Double Lane	40 km/h (25 mph)/(11.1 m/s)
Rural Single Lane	40 km/h (25 mph)/(11.1 m/s)
Rural Double Lane	50 km/h (30 mph)/(13.9 m/s)

TABLE A.3. Road Design Speeds

	Site Category	Recommended Design Speed
Urban	Two lane Local	30 mph
	Two lane Collector	35-50 mph
	Multilane Arterial Divided	45-50 mph
	Multilane Arterial Univided	45-60 mph
	Freeway	60-70 mph
Rural	Two lane Local	30-40 mph
	Two lane Collector	35-60 mph
	Multilane Arterial Divided	50-60 mph
	Multilane Arterial Univided	50-60 mph
	Freeway	65-70 mph

TABLE A.4. Distance travelled during setup

Codebook Configuration	Distance in meters	
	350 kph speed	50 kph speed
Uniform 16	34	0.03
Uniform 32	66	0.1
Uniform 64	130	0.4
Non-Uniform 5	12	0.016
Non-Uniform 7	16	0.022
Non-Uniform 9	20	0.028
Uniform Car 3D	20	0.57
Non-Uniform Car 3D	20	0.43
Non-Uniform Car 3D (3-stage BF)	20	0.018

APPENDIX

B

APPENDIX B

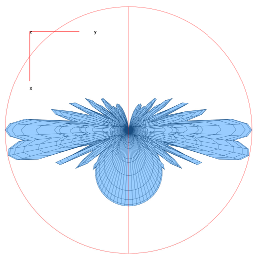

(a) 4 Side Beam Configuration, 8° Side Beam HPBW

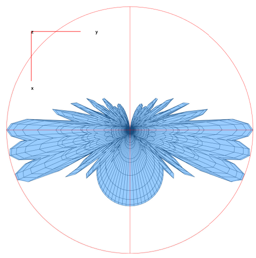

(b) 6 Side Beam Configuration, 8° Side Beam HPBW

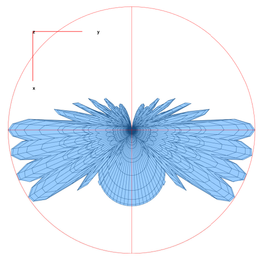

(c) 8 Side Beam Configuration, 8° Side Beam HPBW

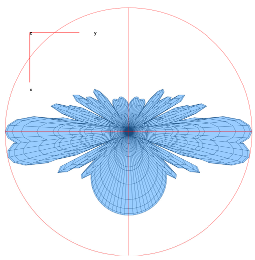

(d) 4 Side Beam Configuration, 10° Side Beam HPBW

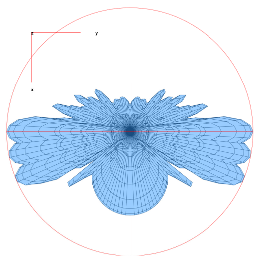

(e) 6 Side Beam Configuration, 10° Side Beam HPBW

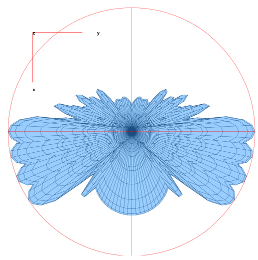

(f) 8 Side Beam Configuration, 10° Side Beam HPBW

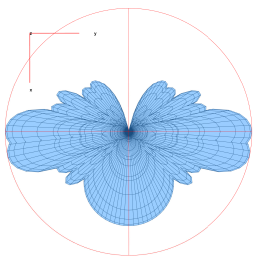

(g) 4 Side Beam Configuration, 15° Side Beam HPBW

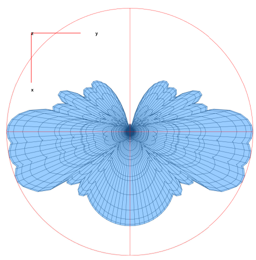

(h) 6 Side Beam Configuration, 15° Side Beam HPBW

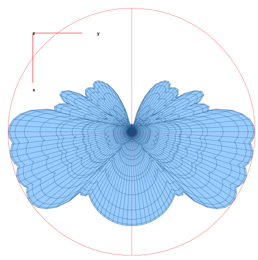

(i) 8 Side Beam Configuration, 15° Side Beam HPBW

FIGURE B.1. Access Point Codebook Radiation Patterns

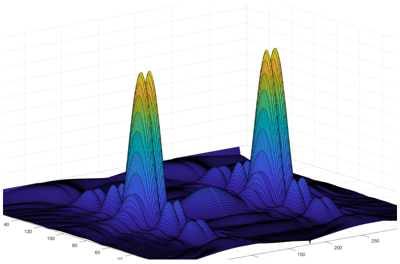

(a) 4 Side Beam Configuration, 8° Side Beam HPBW

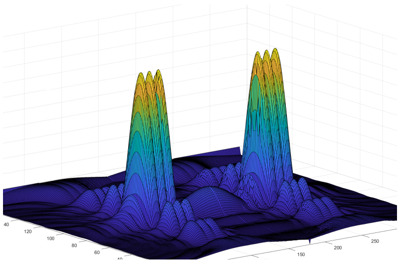

(b) 6 Side Beam Configuration, 8° Side Beam HPBW

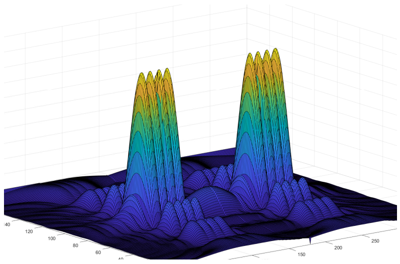

(c) 8 Side Beam Configuration, 8° Side Beam HPBW

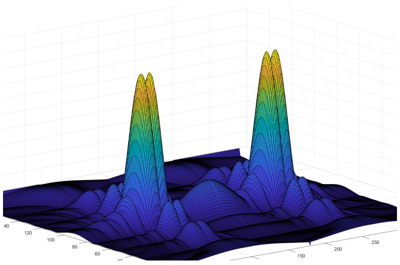

(d) 4 Side Beam Configuration, 10° Side Beam HPBW

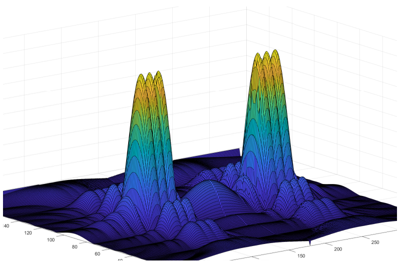

(e) 6 Side Beam Configuration, 10° Side Beam HPBW

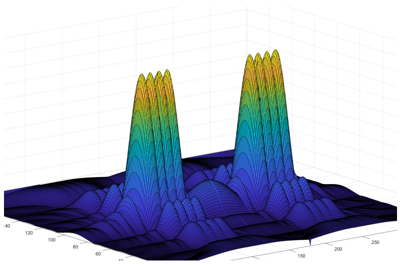

(f) 8 Side Beam Configuration, 10° Side Beam HPBW

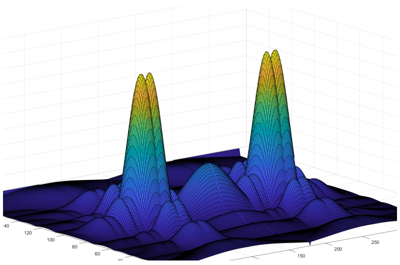

(g) 4 Side Beam Configuration, 15° Side Beam HPBW

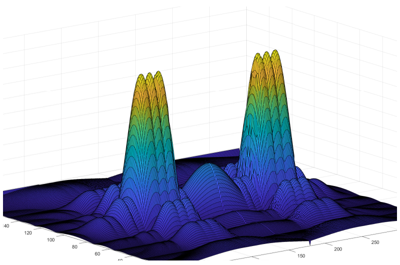

(h) 6 Side Beam Configuration, 15° Side Beam HPBW

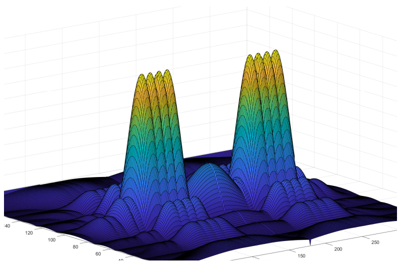

(i) 8 Side Beam Configuration, 15° Side Beam HPBW

FIGURE B.2. Access Point Highest Radiation Per Point

APPENDIX C

C.0.1 Comparison of 3GPP, mmMAGIC, NYU, and METIS models

3GPP TR38.901, mmMAGIC, NYU, and METIS channels models were compared at 28 GHz directly with the equations showed in each model for 3GPP and mmMAGIC models, whereas data of NYU was extracted from [142] , which developed a 3GPP like model for 28 GHz, and for METIS no calculation were needed since the model specifies a minimum and maximum values which are shown in the figures below.

The distribution of the cluster was first compared for LOS and NLOS scenarios. Figure C.1 can be read as: 3GPP has stated that for LOS scenarios at 28 GHz there exist 12 clusters, each one of those composed of 20 paths (rays). The characteristics within each cluster are RMS delay spread is around 5ns, the AOD spread Departure (ASD) must be in the order of 3 degrees, the AOA spread Arrival (ASA) is 17 degrees, the Zenith or elevation spread of departure (ZSD) has not been defined, and the ZSA is 7 degrees, and the cluster shadow fading(SF) is 3dB. NYU particularly defines a mean and a standard deviation and that is shown with the drawn white vertical error lines.

If the value is zero this means, that the parameter was not specified in the model, but for drawing purposes it was necessary to put them as zero. METIS does not specify the number of paths within the clusters.

Figure C.2 shows the cluster distribution for NLOs scenarios, and the values should be read as mentioned in the LOS scenario. As expected the number of clusters in this scenario is higher than in LOS for all models. MmMAGIC and NYU determined a smaller number of clusters 5 or 6 times less than 3GPP and the min value of METIS. The latter does not have a number of paths per cluster. There appears to be an agreement in ASD angles are around 8 to 10 degrees also for ASA in the order of 22 degrees, and for ZSA. ZSD has only been specified in METIS.

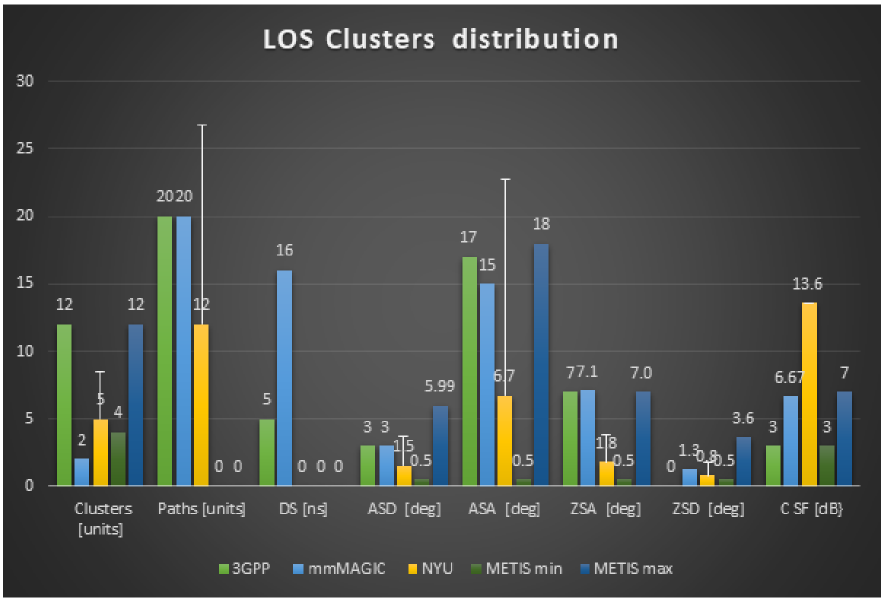

FIGURE C.1. Clusters Distribution in LoS

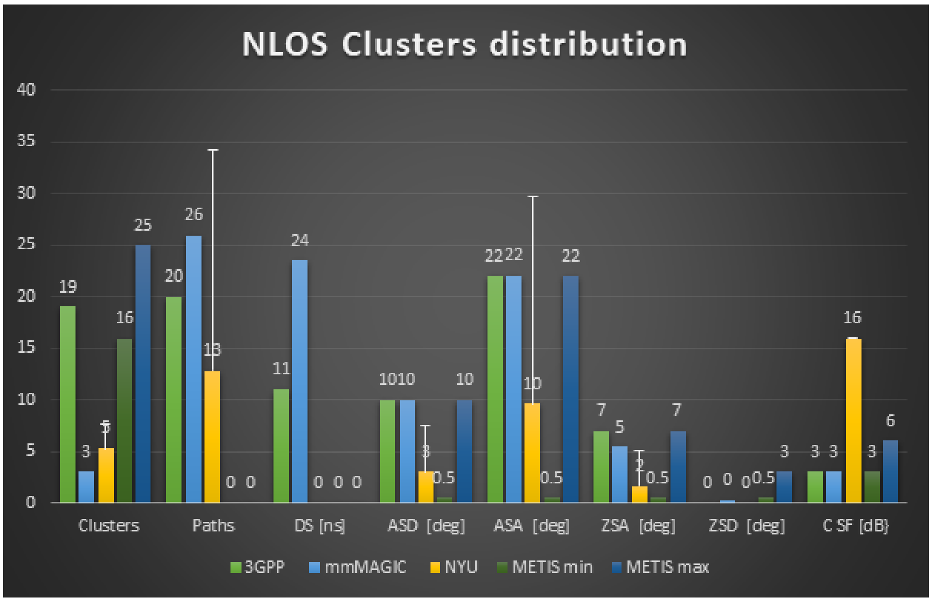

FIGURE C.2. Clusters Distribution in NLoS

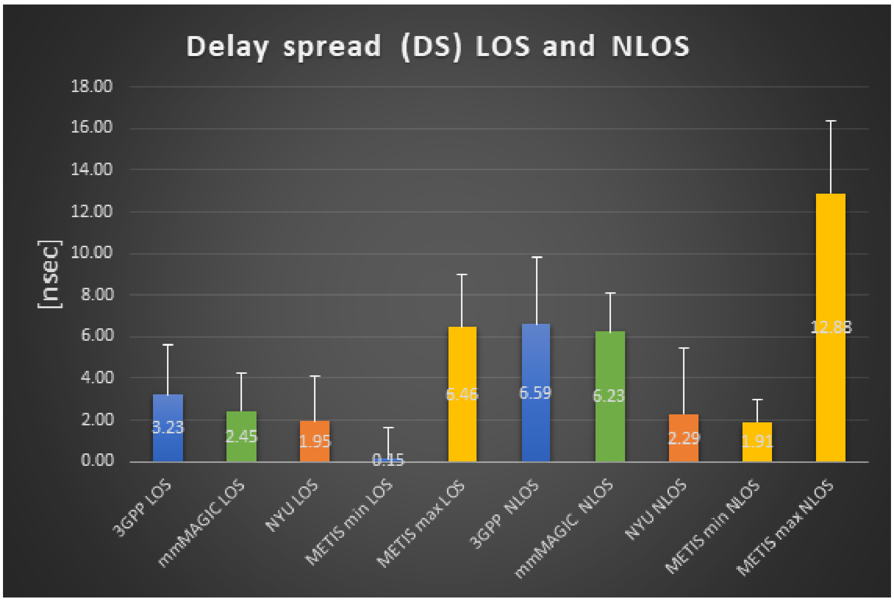

FIGURE C.3. Delay Spread in the models

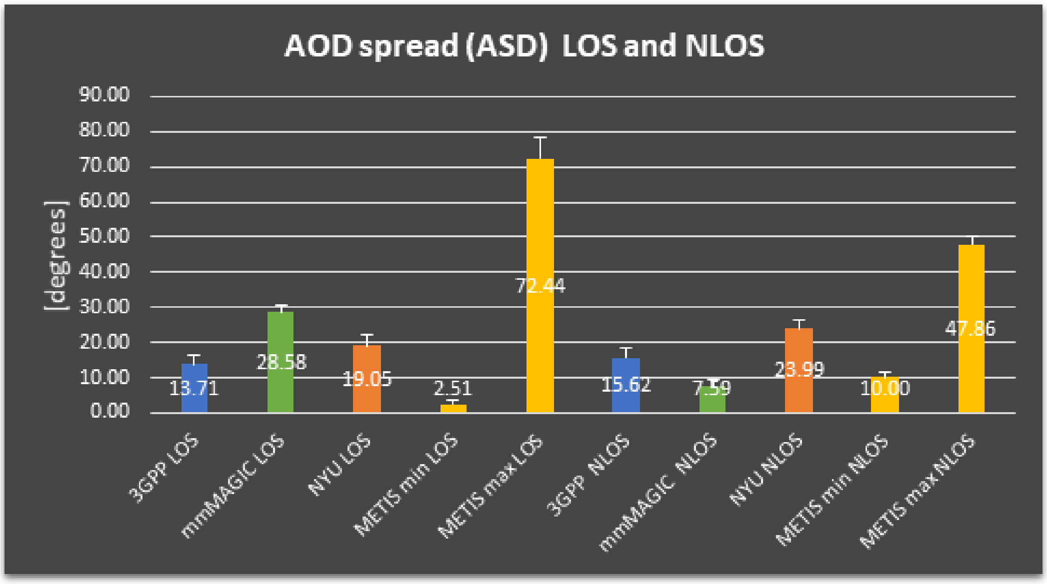

FIGURE C.4. Azimuth AoD Spread

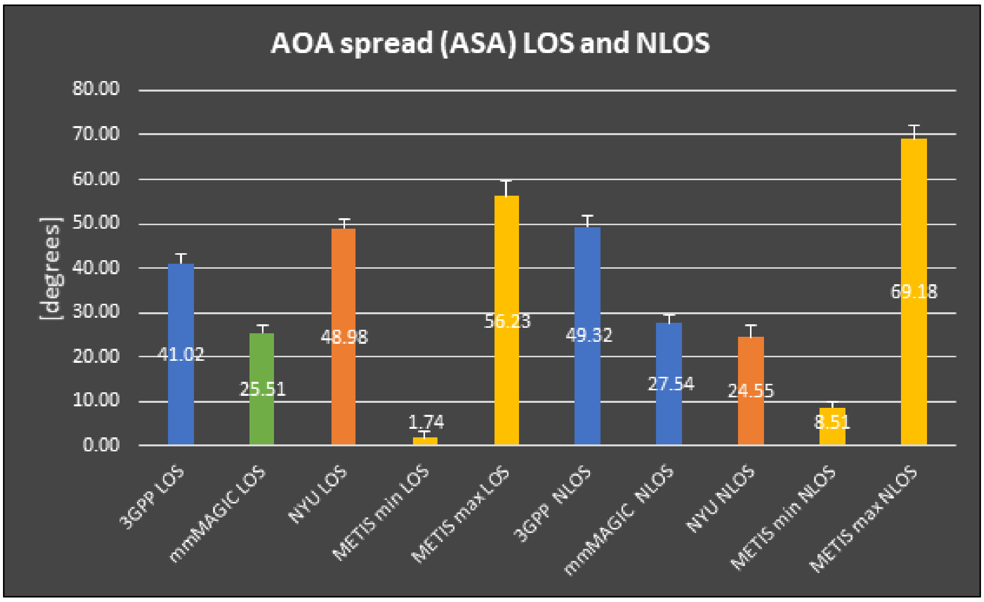

FIGURE C.5. Azimuth AoA Spread

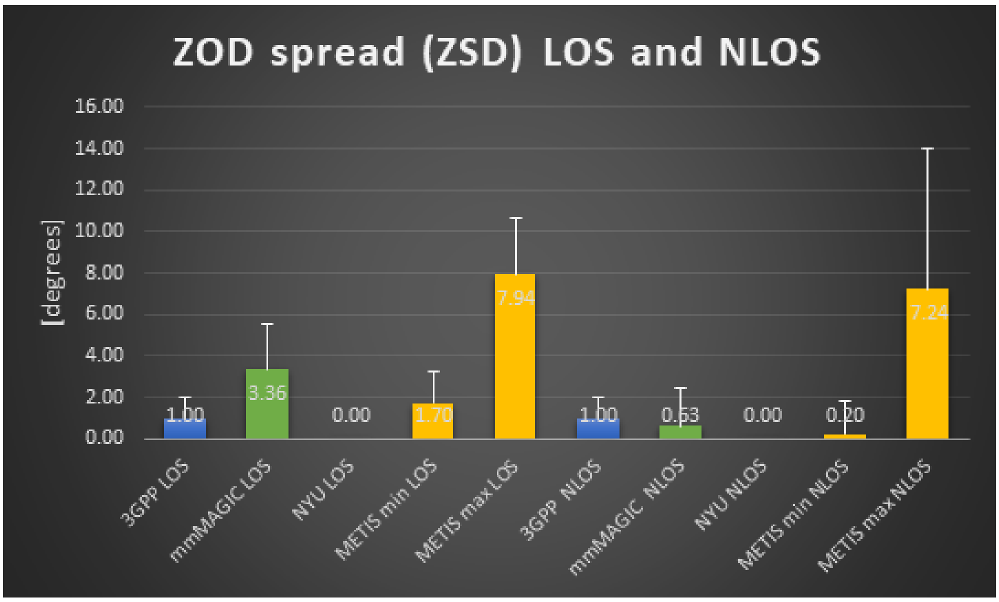

FIGURE C.6. Zenith (or elevation) AoD Spread

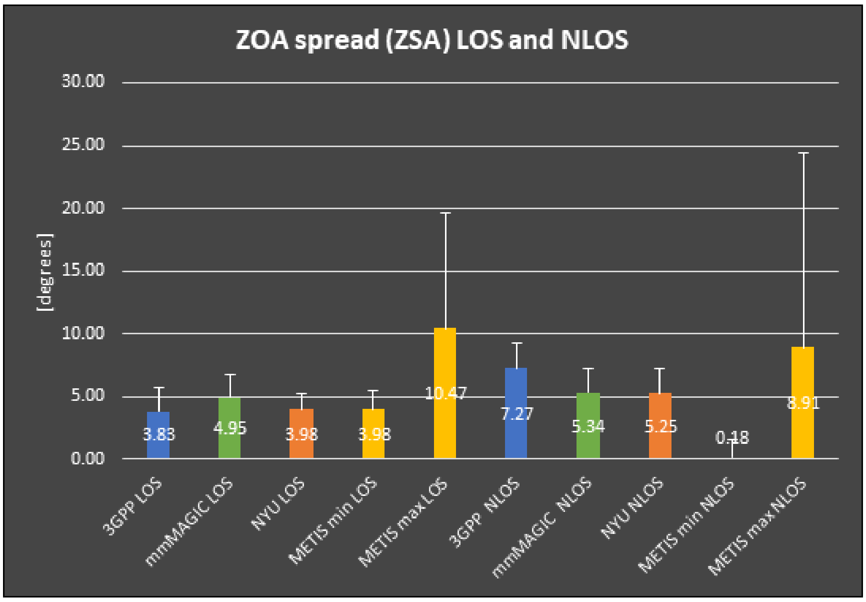

FIGURE C.7. Azimuth (or elevation) AoA Spread

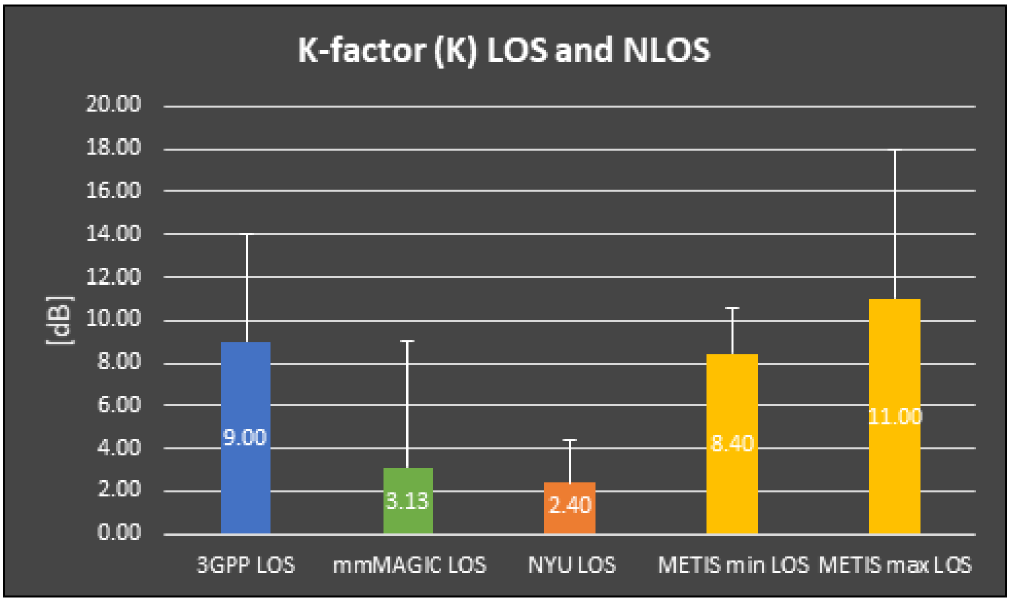

FIGURE C.8. K-Factor

BIBLIOGRAPHY

[1] CISCO, “Antenna patterns and their meaning,” *White Paper*, vol. 7, no. 16, 2007.

[2] Cisco, “Cisco visual networking index: Forecast and methodology: 2016-2021,” *White Paper*, Jun 2017.

[3] T. S. Rappaport, S. Sun, R. Mayzus, H. Zhao, Y. Azar, K. Wang, G. N. Wong, J. K. Schulz, M. Samimi, and F. Gutierrez, “Millimeter wave mobile communications for 5G cellular: It will work!,” *IEEE Access*, vol. 1, pp. 335–349, 2013.

[4] I. F. Akyildiz, D. M. Gutierrez-Estevez, R. Balakrishnan, and E. Chavarria-Reyes, “Lte-advanced and the evolution to beyond 4g (b4g) systems,” *Physical Communication*, vol. 10, pp. 31–60, 2014.

[5] M. Rumney *et al.*, *LTE and the evolution to 4G wireless: Design and measurement challenges*.
John Wiley & Sons, 2013.

[6] F. Khan and J. Pi, “Millimeter-wave mobile broadband: unleashing 3–300ghz spectrum in: Ieee wireless commun,” in *Netw. Conf*, 2011.

[7] “Iso/iec/ieee international standard - information technology – telecommunications and information exchange between systems – local and metropolitan area networks – specific requirements – part 15-3: High data rate wireless multi-media networks,” *ISO/IEC/IEEE 8802-15-3:2017(E)*, pp. 1–514, 2018.

[8] J. Mo, B. L. Ng, S. Chang, P. Huang, M. N. Kulkarni, A. AlAmmouri, J. C. Zhang, J. Lee, and W.-J. Choi, “Beam codebook design for 5g mmwave terminals,” *IEEE Access*, vol. 7, pp. 98387–98404, 2019.

[9] B. Luijten, R. Cohen, F. J. de Bruijn, H. A. Schmeitz, M. Mischi, Y. C. Eldar, and R. J. van Sloun, “Deep learning for fast adaptive beamforming,” in *ICASSP 2019 - 2019 IEEE International Conference on Acoustics, Speech and Signal Processing (ICASSP)*, pp. 1333–1337, 2019.

[10] A. J. Singh and M. Jayakumar, "Machine learning based digital beamforming for line-of-sight optimization in satcom on the move technology," in *2020 4th International Conference on Electronics, Communication and Aerospace Technology (ICECA)*, pp. 422–427, 2020.

[11] J. Chen, W. Feng, J. Xing, P. Yang, G. E. Sobelman, D. Lin, and S. Li, "Hybrid beamforming/combining for millimeter wave mimo: A machine learning approach," *IEEE Transactions on Vehicular Technology*, vol. 69, no. 10, pp. 11353–11368, 2020.

[12] T. S. Rappaport, Y. Xing, G. R. MacCartney, A. F. Molisch, E. Mellios, and J. Zhang, "Overview of millimeter wave communications for fifth-generation (5G) wireless networks,Äîwith a focus on propagation models," *IEEE Transactions on Antennas and Propagation*, vol. 65, pp. 6213–6230, Dec 2017.

[13] S. Kutty and D. Sen, "Beamforming for millimeter wave communications: An inclusive survey," *IEEE Communications Surveys Tutorials*, vol. 18, pp. 949–973, Secondquarter 2016.

[14] Y. Okumura, "Field strength and its variability in vhf and uhf land-mobile radio service," *Rev. Electr. Commun. Lab.*, vol. 16, pp. 825–873, 1968.

[15] M. Hata, "Empirical formula for propagation loss in land mobile radio services," *IEEE transactions on Vehicular Technology*, vol. 29, no. 3, pp. 317–325, 1980.

[16] R. Mardeni and T. S. Priya, "Optimised cost-231 hata models for wimax path loss prediction in suburban and open urban environments," *Modern Applied Science*, vol. 4, no. 9, p. 75, 2010.

[17] T. S. Rappaport *et al.*, *Wireless communications: principles and practice*, vol. 2. prentice hall PTR New Jersey, 1996.

[18] L. Li, G. S. Hilton, and D. L. Paul, "High efficiency lte band base station antenna array for mimo system evaluation," in *2010 Loughborough Antennas & Propagation Conference*, pp. 273–276, IEEE, 2010.

[19] M. A. Jensen and J. W. Wallace, "A review of antennas and propagation for mimo wireless communications," *IEEE Transactions on antennas and propagation*, vol. 52, no. 11, pp. 2810–2824, 2004.

[20] F. Bohagen, P. Orten, and G. E. Oien, "On spherical vs. plane wave modeling of line-of-sight mimo channels," *IEEE Transactions on Communications*, vol. 57, no. 3, pp. 841–849, 2009.

[21] W. L. Stutzman and G. A. Thiele, *Antenna theory and design*.
John Wiley & Sons, 2012.

[22] E. Tameh and A. Nix, “An integrated deterministic urban/rural propagation model,” 1998.

[23] E. K. Tameh and A. R. Nix, “A mixed-cell propagation model for interference prediction in a umts network,” in *IEEE VTS 53rd Vehicular Technology Conference, Spring 2001. Proceedings (Cat. No. 01CH37202)*, vol. 1, pp. 409–413, IEEE, 2001.

[24] E. K. Tameh and A. R. Nix, “The use of measurement data to analyse the performance of rooftop diffraction and foliage loss algorithms in a 3-d integrated urban/rural propagation model,” in *VTC ’98. 48th IEEE Vehicular Technology Conference. Pathway to Global Wireless Revolution (Cat. No.98CH36151)*, vol. 1, pp. 303–307 vol.1, May 1998.

[25] E. K. Tameh, A. R. Nix, and M. A. Beach, “A 3-d integrated macro and microcellular propagation model, based on the use of photogrammetric terrain and building data,” in *1997 IEEE 47th Vehicular Technology Conference. Technology in Motion*, vol. 3, pp. 1957–1961 vol.3, May 1997.

[26] D.-T. Phan-Huy, P. Ratajczak, R. D’Errico, J. Järveläinen, D. Kong, K. Haneda, B. Bulut, A. Karttunen, M. Beach, E. Mellios, *et al.*, “Massive multiple input massive multiple output for 5g wireless backhauling,” in *2017 IEEE Globecom Workshops (GC Wkshps)*, pp. 1–6, IEEE, 2017.

[27] V. Kalokidou, S. Typos, E. Mellios, A. Doufexi, and A. Nix, “Performance evaluation of mmWave in 5G train communications,” in *2018 IEEE 29th Annual International Symposium on Personal, Indoor and Mobile Radio Communications (PIMRC)*, pp. 391–395, Sep. 2018.

[28] E. Mellios, “Physical layer analysis of communication systems integrating antenna characteristics and propagation modelling for indoor and outdoor environments,” *Doctoral dissertation, University of Bristol, Bristol, UK*, vol. 1, no. 1, 2013.

[29] E. Mellios, *Physical layer analysis of communication systems integrating antenna characteristics and propagation modelling for indoor and outdoor environments*.
PhD thesis, University of Bristol, 2013.

[30] D. Kong, E. Mellios, D. Halls, A. Nix, and G. Hilton, “Closed-loop antenna selection for wireless lans with directional & omni-directional elements,” in *2011 IEEE Vehicular Technology Conference (VTC Fall)*, pp. 1–5, IEEE, 2011.

[31] V. Erceg, “Tgn channel models,” *802.11 document 03/940r4*, 2004.

[32] E. U. T. R. A. Network, “3rd generation partnership project; technical specification group radio access network; evolved universal terrestrial radio access network,” 2011.

[33] D. S. Baum, J. Hansen, J. Salo, G. Del Galdo, M. Milojevic, and P. Kyösti, “An interim channel model for beyond-3g systems: extending the 3gpp spatial channel model (scm),” in *2005 IEEE 61st Vehicular Technology Conference*, vol. 5, pp. 3132–3136, IEEE, 2005.

[34] R. Srinivasan, “Ieee 802.16 m evaluation methodology document (emd),” *IEEE 802.16 m-08/004r3*, 2008.

[35] J. Meinilä, P. Kyösti, T. Jämsä, and L. Hentilä, “Winner ii channel models,” *Radio Technologies and Concepts for IMT-Advanced*, pp. 39–92, 2009.

[36] J. Meinilä, P. Kyösti, *et al.*, “D5. 3: Winner+ final channel models v1. 0, jun. 2010 [j],” *Article (CrossRef Link)*, 2010.

[37] L. Liu, C. Oestges, J. Poutanen, K. Haneda, P. Vainikainen, F. Quitin, F. Tufvesson, and P. De Doncker, “The cost 2100 mimo channel model,” *IEEE Wireless Communications*, vol. 19, no. 6, pp. 92–99, 2012.

[38] A. A. Saleh and R. Valenzuela, “A statistical model for indoor multipath propagation,” *IEEE Journal on selected areas in communications*, vol. 5, no. 2, pp. 128–137, 1987.

[39] U. Ofcom, “Update on 5g spectrum in the uk,” 2017.

[40] F. C. Commission *et al.*, “Fcc takes steps to facilitate mobile broadband and next generation wireless technologies in spectrum above 24 ghz,” *press release, July*, vol. 14, 2016.

[41] J. GSA, “5g spectrum bands,” tech. rep., Tech. Report, Oct, 2017.

[42] 3GPP, “Study on channel model for frequencies from 0.5 to 100 ghz,” tech. rep., ETSI TR 138 901 V14.0.0, 2016.

[43] N. Docomo, “5g channel model for bands up to100 ghz,” tech. rep., Tech. Report, Oct, 2016.

[44] M. Peter, K. Haneda, S. Nguyen, A. Karttunen, and J. Järveläinen, “Measurement results and final mmmagic channel models,” *Deliverable D2*, vol. 2, p. 12, 2017.

[45] S. Sun, G. R. MacCartney, and T. S. Rappaport, “A novel millimeter-wave channel simulator and applications for 5g wireless communications,” in *2017 IEEE International Conference on Communications (ICC)*, pp. 1–7, IEEE, 2017.

[46] M. K. Samimi and T. S. Rappaport, “Characterization of the 28 ghz millimeter-wave dense urban channel for future 5g mobile cellular,” *NYU Wireless TR*, vol. 1, 2014.

[47] V. Nurmela, A. Karttunen, A. Roivainen, L. Raschkowski, V. Hovinen, J. Y. EB, N. Omaki, K. Kusume, A. Hekkala, R. Weiler, *et al.*, “Deliverable d1. 4 metis channel models,” in *Proc. Mobile Wireless Commun. Enablers Inf. Soc.(METIS)*, p. 1, 2015.

[48] R. Weiler, “Quasi-deterministic millimeter-wave channel models in miweba,” *EURASIP Journal on Wireless Communications and Networking*, vol. 1, 2016.

[49] N. Jaldén, P. Zetterberg, B. Ottersten, A. Hong, and R. Thoma, “Correlation properties of large scale fading based on indoor measurements,” in *2007 IEEE Wireless Communications and Networking Conference*, pp. 1894–1899, IEEE, 2007.

[50] M. K. Samimi and T. S. Rappaport, “3-d millimeter-wave statistical channel model for 5g wireless system design,” *IEEE Transactions on Microwave Theory and Techniques*, vol. 64, no. 7, pp. 2207–2225, 2016.

[51] D. Arthur and S. Vassilvitskii, “k-means++: The advantages of careful seeding,” tech. rep., Stanford, 2006.

[52] S. Wu, S. Hur, K. Whang, and M. Nekovee, “Intra-cluster characteristics of 28 ghz wireless channel in urban micro street canyon,” in *2016 IEEE Global Communications Conference (GLOBECOM)*, pp. 1–6, IEEE, 2016.

[53] G. Grosskopf, R. Eggemann, H. Ehlers, A. Kortke, B. Kuhlow, G. Przyrembel, D. Rohde, and S. Zinal, “Maximum directivity beam-former at 60 ghz with optical feeder,” *IEEE Transactions on Antennas and Propagation*, vol. 51, pp. 3040–3046, Nov 2003.

[54] J. Lindsey, “The fresnel zone and its interpetive significance,” *The Leading Edge*, vol. 8, no. 10, pp. 33–39, 1989.

[55] J. B. Keller, “Geometrical theory of diffraction,” *Josa*, vol. 52, no. 2, pp. 116–130, 1962.

[56] A. Picquenard, *Radio wave propagation*.
Macmillan International Higher Education, 1974.

[57] J. Deygout, “Multiple knife-edge diffraction of microwaves,” *IEEE Transactions on Antennas and Propagation*, vol. 14, no. 4, pp. 480–489, 1966.

[58] J. Epstein and D. W. Peterson, “An experimental study of wave propagation at 850 mc,” *Proceedings of the IRE*, vol. 41, no. 5, pp. 595–611, 1953.

[59] T. H. Barratt, E. Mellios, P. Cain, A. R. Nix, and M. A. Beach, “Measured and modelled corner diffraction at millimetre wave frequencies,” in *2016 IEEE 27th Annual International Symposium on Personal, Indoor, and Mobile Radio Communications (PIMRC)*, pp. 1–5, IEEE, 2016.

[60] M. Rumney, “Testing 5g: Time to throw away the cables,” *Microw. J.*, vol. 59, no. 11, 2016.

[61] J. W. S. B. Rayleigh, *The theory of sound*, vol. 2.
Macmillan, 1896.

[62] J. D. Parsons, *The mobile radio propagation channel*.
Wiley, 2000.

[63] C. A. Balanis, *Advanced engineering electromagnetics*.
John Wiley & Sons, 2012.

[64] F. T. Ulaby, R. K. Moore, and A. K. Fung, “Microwave remote sensing: Active and passive. volume 1-microwave remote sensing fundamentals and radiometry,” 1981.

[65] L. Sayer, A. L. Freire, E. Mellios, and A. Nix, “A kirchhoff scattering model for millimetre wavelength wireless links,” in *2018 12th European Conference on Antennas and Propagation (EUCAP 2018)*, 2018.

[66] A. A. Goulianos, A. L. Freire, T. Barratt, E. Mellios, P. Cain, M. Rumney, A. Nix, and M. Beach, “Measurements and characterisation of surface scattering at 60 ghz,” in *2017 IEEE 86th Vehicular Technology Conference (VTC-Fall)*, pp. 1–5, 2017.

[67] S. Sun, G. R. MacCartney, and T. S. Rappaport, “Millimeter-wave distance-dependent large-scale propagation measurements and path loss models for outdoor and indoor 5g systems,” in *2016 10th European Conference on Antennas and Propagation (EuCAP)*, pp. 1–5, IEEE, 2016.

[68] R. C. Hansen, *Phased array antennas*, vol. 213.
John Wiley & Sons, 2009.

[69] S. Hur, T. Kim, D. J. Love, J. V. Krogmeier, T. A. Thomas, and A. Ghosh, “Multilevel millimeter wave beamforming for wireless backhaul,” in *2011 Ieee Globecom Workshops (Gc Wkshps)*, pp. 253–257, IEEE, 2011.

[70] S. Hur, T. Kim, D. J. Love, J. V. Krogmeier, T. A. Thomas, and A. Ghosh, “Millimeter wave beamforming for wireless backhaul and access in small cell networks,” *IEEE transactions on communications*, vol. 61, no. 10, pp. 4391–4403, 2013.

[71] S. Hur, S. Baek, B. Kim, Y. Chang, A. F. Molisch, T. S. Rappaport, K. Haneda, and J. Park, “Proposal on millimeter-wave channel modeling for 5g cellular system,” *IEEE Journal of Selected Topics in Signal Processing*, vol. 10, no. 3, pp. 454–469, 2016.

[72] J. Song, J. Choi, S. G. Larew, D. J. Love, T. A. Thomas, and A. A. Ghosh, “Adaptive millimeter wave beam alignment for dual-polarized mimo systems,” *IEEE Transactions on Wireless Communications*, vol. 14, no. 11, pp. 6283–6296, 2015.

[73] J. Song, S. G. Larew, D. J. Love, T. A. Thomas, and A. Ghosh, "Millimeter wave beam-alignment for dual-polarized outdoor mimo systems," in *2013 IEEE Globecom Workshops (GC Wkshps)*, pp. 356–361, IEEE, 2013.

[74] S. Sun, T. S. Rappaport, R. W. Heath, A. Nix, and S. Rangan, "Mimo for millimeter-wave wireless communications: Beamforming, spatial multiplexing, or both?," *IEEE Communications Magazine*, vol. 52, no. 12, pp. 110–121, 2014.

[75] S. Noh, M. D. Zoltowski, and D. J. Love, "Multi-resolution codebook and adaptive beamforming sequence design for millimeter wave beam alignment," *IEEE Transactions on Wireless Communications*, vol. 16, no. 9, pp. 5689–5701, 2017.

[76] A. Alkhateeb, O. El Ayach, G. Leus, and R. W. Heath, "Channel estimation and hybrid precoding for millimeter wave cellular systems," *IEEE journal of selected topics in signal processing*, vol. 8, no. 5, pp. 831–846, 2014.

[77] O. El Ayach, S. Rajagopal, S. Abu-Surra, Z. Pi, and R. W. Heath, "Spatially sparse precoding in millimeter wave mimo systems," *IEEE transactions on wireless communications*, vol. 13, no. 3, pp. 1499–1513, 2014.

[78] Y.-H. Nam, B. L. Ng, K. Sayana, Y. Li, J. Zhang, Y. Kim, and J. Lee, "Full-dimension mimo (fd-mimo) for next generation cellular technology," *IEEE Communications Magazine*, vol. 51, no. 6, pp. 172–179, 2013.

[79] D. Reyes, M. Beach, E. Mellios, J. Haine, and M. Rumney, "Over-the-air test method for 5g mmwave devices with beamforming capabilities," in *2018 IEEE Globecom Workshops (GC Wkshps)*, pp. 1–6, IEEE, 2018.

[80] D. Reyes, M. Beach, M. Rumney, J. Haine, and E. Mellios, "Novel over-the-air test method for 5g millimetre wave devices, based on elliptical cylinder reflectors," in *2019 IEEE 90th Vehicular Technology Conference (VTC2019-Fall)*, pp. 1–6, IEEE, 2019.

[81] L. Wan, S. Tsai, and M. Almgren, "A fading-insensitive performance metric for a unified link quality model," in *IEEE Wireless Communications and Networking Conference, 2006. WCNC 2006.*, vol. 4, pp. 2110–2114, IEEE, 2006.

[82] D. Kong, E. Mellios, D. Halls, A. Nix, and G. Hilton, "Throughput sensitivity to antenna pattern and orientation in 802.11 n networks," in *2011 IEEE 22nd International Symposium on Personal, Indoor and Mobile Radio Communications*, pp. 809–813, IEEE, 2011.

[83] D. Kong, E. Mellios, G. Hilton, A. Doufexi, and A. Nix, "Enhancing in-home 802.11 performance: Mesh or mimo?," in *2013 IEEE 78th Vehicular Technology Conference (VTC Fall)*, pp. 1–5, IEEE, 2013.

[84] K. H. Ng, E. K. Tameh, A. Doufexi, M. Hunukumbure, and A. R. Nix, "Efficient multielement ray tracing with site-specific comparisons using measured mimo channel data," *IEEE Transactions on Vehicular Technology*, vol. 56, no. 3, pp. 1019–1032, 2007.

[85] M. Tran, D. Halls, A. Nix, A. Doufexi, and M. Beach, "Mobile wimax: Mimo performance analysis from a quality of service (qos) viewpoint," 04 2009.

[86] D. Halls, A. Nix, and M. Beach, "System level evaluation of ul and dl interference in ofdma mobile broadband networks," pp. 1271 – 1276, 05 2011.

[87] D. Halls, A. Nix, and M. Beach, "System level evaluation of interference in vehicular mobile broadband networks," pp. 1 – 5, 06 2011.

[88] W. Roh, J. Seol, J. Park, B. Lee, J. Lee, Y. Kim, J. Cho, K. Cheun, and F. Aryanfar, "Millimeter-wave beamforming as an enabling technology for 5G cellular communications: theoretical feasibility and prototype results," *IEEE Communications Magazine*, vol. 52, pp. 106–113, February 2014.

[89] "802.16e-2005, Part16: Air Interface for Fixed and Mobile Broadband Wireless Access systems," Feb 2006.

[90] F. Rusek, D. Persson, B. K. Lau, E. G. Larsson, T. L. Marzetta, O. Edfors, and F. Tufvesson, "Scaling up mimo: Opportunities and challenges with very large arrays," *IEEE signal processing magazine*, vol. 30, no. 1, pp. 40–60, 2012.

[91] A. Alkhateeb, O. El Ayach, G. Leus, and R. W. Heath, "Hybrid precoding for millimeter wave cellular systems with partial channel knowledge," in *2013 Information Theory and Applications Workshop (ITA)*, pp. 1–5, IEEE, 2013.

[92] A. Alkhateeb, G. Leus, and R. W. Heath, "Limited feedback hybrid precoding for multi-user millimeter wave systems," *IEEE transactions on wireless communications*, vol. 14, no. 11, pp. 6481–6494, 2015.

[93] Z. Wang, M. Li, Q. Liu, and A. L. Swindlehurst, "Hybrid precoder and combiner design with low-resolution phase shifters in mmwave mimo systems," *IEEE Journal of Selected Topics in Signal Processing*, vol. 12, no. 2, pp. 256–269, 2018.

[94] A. M. Elbir and A. K. Papazafeiropoulos, "Hybrid precoding for multiuser millimeter wave massive mimo systems: A deep learning approach," *IEEE Transactions on Vehicular Technology*, vol. 69, no. 1, pp. 552–563, 2019.

[95] B. Hassibi and B. M. Hochwald, "How much training is needed in multiple-antenna wireless links?," *IEEE Transactions on Information Theory*, vol. 49, no. 4, pp. 951–963, 2003.

[96] W. Santipach and M. L. Honig, "Optimization of training and feedback overhead for beamforming over block fading channels," *IEEE Transactions on Information Theory*, vol. 56, no. 12, pp. 6103–6115, 2010.

[97] J. Wang, Z. Lan, C.-W. Pyo, T. Baykas, C.-S. Sum, M. A. Rahman, J. Gao, R. Funada, F. Kojima, H. Harada, *et al.*, "Beam codebook based beamforming protocol for multi-gbps millimeter-wave wpan systems," *IEEE Journal on Selected Areas in Communications*, vol. 27, no. 8, pp. 1390–1399, 2009.

[98] Y. Yaman and P. Spasojevic, "Reducing the los ray beamforming setup time for ieee 802.11ad and ieee 802.15.3c," in *MILCOM 2016 - 2016 IEEE Military Communications Conference*, pp. 448–453, 2016.

[99] J. P. GILB, "Part 15.3: Wireless medium access control (mac) and physical layer (phy) specifications for high rate wireless personal area networks (wpans): Amendment 2: Millimeter-wave based alternative physical layer extension," *P802-15-3c-DF3_Draft_Amendment*.

[100] V. Va and R. W. Heath, "Basic relationship between channel coherence time and beamwidth in vehicular channels," in *2015 IEEE 82nd Vehicular Technology Conference (VTC2015-Fall)*, pp. 1–5, Sep. 2015.

[101] V. Va, J. Choi, and R. W. Heath, "The impact of beamwidth on temporal channel variation in vehicular channels and its implications," *IEEE Transactions on Vehicular Technology*, vol. 66, pp. 5014–5029, June 2017.

[102] J. Choi, V. Va, N. Gonzalez-Prelcic, R. Daniels, C. R. Bhat, and R. W. Heath, "Millimeter-wave vehicular communication to support massive automotive sensing," *IEEE Communications Magazine*, vol. 54, no. 12, pp. 160–167, 2016.

[103] T. Wada, M. Maeda, M. Okada, K. Tsukamoto, and S. Komaki, "Theoretical analysis of propagation characteristics in millimeter-wave intervehicle communication system," *Electronics and Communications in Japan (Part II: Electronics)*, vol. 83, no. 11, pp. 33–43, 2000.

[104] B. Antonescu, M. T. Moayyed, and S. Basagni, "mmwave channel propagation modeling for v2x communication systems," in *2017 IEEE 28th Annual International Symposium on Personal, Indoor, and Mobile Radio Communications (PIMRC)*, pp. 1–6, 2017.

[105] M. Schack, D. Kornek, E. Slottke, and T. Kürner, "Analysis of channel parameters for different antenna configurations in vehicular environments," in *2010 IEEE 72nd Vehicular Technology Conference-Fall*, pp. 1–5, IEEE, 2010.

[106] V. Va and R. W. Heath, “Basic relationship between channel coherence time and beamwidth in vehicular channels,” in *2015 IEEE 82nd Vehicular Technology Conference (VTC2015-Fall)*, pp. 1–5, IEEE, 2015.

[107] T.-J. Wu, W. Liao, and C.-J. Chang, “A cost-effective strategy for road-side unit placement in vehicular networks,” *IEEE Transactions on Communications*, vol. 60, no. 8, pp. 2295–2303, 2012.

[108] A. Yamamoto, K. Ogawa, T. Horimatsu, A. Kato, and M. Fujise, “Path-loss prediction models for intervehicle communication at 60 ghz,” *IEEE Transactions on Vehicular Technology*, vol. 57, no. 1, pp. 65–78, 2008.

[109] V. Va, J. Choi, and R. W. Heath, “The impact of beamwidth on temporal channel variation in vehicular channels and its implications,” *IEEE Transactions on Vehicular Technology*, vol. 66, no. 6, pp. 5014–5029, 2016.

[110] S. Rajagopal, S. Abu-Surra, and M. Malmirchegini, “Channel feasibility for outdoor non-line-of-sight mmwave mobile communication,” in *2012 IEEE vehicular technology conference (VTC Fall)*, pp. 1–6, IEEE, 2012.

[111] N. F. Abdullah, D. Berraki, A. Ameen, S. Armour, A. Doufexi, A. Nix, and M. Beach, “Channel parameters and throughput predictions for mmwave and lte-a networks in urban environments,” in *2015 IEEE 81st Vehicular Technology Conference (VTC Spring)*, pp. 1–5, IEEE, 2015.

[112] Y. Niu, Y. Li, D. Jin, L. Su, and A. V. Vasilakos, “A survey of millimeter wave communications (mmwave) for 5g: opportunities and challenges,” *Wireless networks*, vol. 21, no. 8, pp. 2657–2676, 2015.

[113] W. Nawrocki, *Measurement systems and sensors*.
Artech House, 2016.

[114] F. Maschietti, D. Gesbert, P. de Kerret, and H. Wymeersch, “Robust location-aided beam alignment in millimeter wave massive mimo,” in *GLOBECOM 2017-2017 IEEE Global Communications Conference*, pp. 1–6, IEEE, 2017.

[115] L. Tian, J. Li, Y. Huang, J. Shi, and J. Zhou, “Seamless dual-link handover scheme in broadband wireless communication systems for high-speed rail,” *IEEE Journal on Selected Areas in Communications*, vol. 30, no. 4, pp. 708–718, 2012.

[116] C. Yang, L. Lu, C. Di, and X. Fang, “An on-vehicle dual-antenna handover scheme for high-speed railway distributed antenna system,” in *2010 6th International Conference on Wireless Communications Networking and Mobile Computing (WiCOM)*, pp. 1–5, IEEE, 2010.

[117] F. Maschietti, D. Gesbert, P. de Kerret, and H. Wymeersch, "Robust location-aided beam alignment in millimeter wave massive MIMO," in *GLOBECOM 2017 - 2017 IEEE Global Communications Conference*, pp. 1–6, Dec 2017.

[118] Samsung Electronics, "Downlink mimo for EUTRA," *3GPP TSG RAN WG1 44/R1-060335*, Feb 2006.

[119] "3GPP TR 25.814: Physical layer aspect for evolved universal terrestrical radio access (release 7)," June 2006.

[120] J. Wang, Z. Lan, C. Sum, C. Pyo, J. Gao, T. Baykas, A. Rahman, R. Funada, F. Kojima, I. Lakkis, H. Harada, and S. Kato, "Beamforming codebook design and performance evaluation for 60ghz wideband wpans," in *2009 IEEE 70th Vehicular Technology Conference Fall*, pp. 1–6, Sep. 2009.

[121] S. Typos, V. Kalokidou, S. Armour, A. Doufexi, E. Mellios, and A. Nix, "Codebook performance evaluation of mmwave in train communications," in *2020 IEEE 91st Vehicular Technology Conference (VTC2020-Spring)*, pp. 1–6, 2020.

[122] K. T. Truong and R. W. Heath, "Effects of channel aging in massive mimo systems," *Journal of Communications and Networks*, vol. 15, no. 4, pp. 338–351, 2013.

[123] J. Jose, A. Ashikhmin, T. L. Marzetta, and S. Vishwanath, "Pilot contamination and precoding in multi-cell tdd systems," *IEEE Transactions on Wireless Communications*, vol. 10, no. 8, pp. 2640–2651, 2011.

[124] R. Chopra, C. R. Murthy, and H. A. Suraweera, "On the throughput of large mimo beamforming systems with channel aging," *IEEE Signal Processing Letters*, vol. 23, no. 11, pp. 1523–1527, 2016.

[125] T. F. Brustad and R. Dalmo, "Railway transition curves: A review of the state-of-the-art and future research," *Infrastructures*, vol. 5, no. 5, p. 43, 2020.

[126] M. Lindahl, "Track geometry for high-speed railways," *TRITA-FKT Report*, vol. 54, 2001.

[127] P. Belanovic, D. Valerio, A. Paier, T. Zemen, F. Ricciato, and C. F. Mecklenbrauker, "On wireless links for vehicle-to-infrastructure communications," *IEEE Transactions on Vehicular Technology*, vol. 59, no. 1, pp. 269–282, 2010.

[128] C. Bloom, J. Tan, J. Ramjohn, and L. Bauer, "Self-driving cars and data collection: Privacy perceptions of networked autonomous vehicles," in *Thirteenth Symposium on Usable Privacy and Security (SOUPS 2017)*, (Santa Clara, CA), pp. 357–375, USENIX Association, July 2017.

[129] I. Mavromatis, A. Tassi, R. J. Piechocki, and A. Nix, "mmwave system for future its: A mac-layer approach for v2x beam steering," in *2017 IEEE 86th Vehicular Technology Conference (VTC-Fall)*, pp. 1–6, 2017.

[130] A. Tassi, M. Egan, R. J. Piechocki, and A. Nix, "Modeling and design of millimeter-wave networks for highway vehicular communication," *IEEE Transactions on Vehicular Technology*, vol. 66, no. 12, pp. 10676–10691, 2017.

[131] I. Mavromatis, A. Tassi, R. J. Piechocki, and A. Nix, "Efficient millimeter-wave infrastructure placement for city-scale its," in *2019 IEEE 89th Vehicular Technology Conference (VTC2019-Spring)*, pp. 1–5, 2019.

[132] M. N. Kulkarni, S. Singh, and J. G. Andrews, "Coverage and rate trends in dense urban mmwave cellular networks," in *2014 IEEE Global Communications Conference*, pp. 3809–3814, 2014.

[133] A. Ghosh, T. A. Thomas, M. C. Cudak, R. Ratasuk, P. Moorut, F. W. Vook, T. S. Rappaport, G. R. MacCartney, S. Sun, and S. Nie, "Millimeter-wave enhanced local area systems: A high-data-rate approach for future wireless networks," *IEEE Journal on Selected Areas in Communications*, vol. 32, no. 6, pp. 1152–1163, 2014.

[134] T. Bai and R. W. Heath, "Coverage and rate analysis for millimeter-wave cellular networks," *IEEE Transactions on Wireless Communications*, vol. 14, no. 2, pp. 1100–1114, 2014.

[135] S. Singh, M. N. Kulkarni, A. Ghosh, and J. G. Andrews, "Tractable model for rate in self-backhauled millimeter wave cellular networks," *IEEE Journal on Selected Areas in Communications*, vol. 33, no. 10, pp. 2196–2211, 2015.

[136] T. B. S. Institution, "Design of road lighting. lighting of roads and public amenity areas. code of practice?," vol. BS 5489-1:2020, 2020.

[137] H. Schumacher, H. Tchouankem, J. Nuckelt, T. Kürner, T. Zinchenko, A. Leschke, and L. Wolf, "Vehicle-to-vehicle ieee 802.11 p performance measurements at urban intersections," in *2012 IEEE International Conference on Communications (ICC)*, pp. 7131–7135, IEEE, 2012.

[138] I. Mavromatis, A. Tassi, R. J. Piechocki, and A. Nix, "Efficient millimeter-wave infrastructure placement for city-scale its," in *2019 IEEE 89th Vehicular Technology Conference (VTC2019-Spring)*, pp. 1–5, IEEE, 2019.

[139] R. Zhang, F. Yan, W. Xia, S. Xing, Y. Wu, and L. Shen, "An optimal roadside unit placement method for vanet localization," in *GLOBECOM 2017-2017 IEEE Global Communications Conference*, pp. 1–6, IEEE, 2017.

[140] S. Friedner and R. House, “5g infrastructure requirements in the uk,” *LS telcom UK, Tech. Rep*, 2016.

[141] H. Agency, *Design manual for roads and bridges*.
HM Stationery Office, 1994.

[142] M. K. Samimi and T. S. Rappaport, “Local multipath model parameters for generating 5g millimeter-wave 3gpp-like channel impulse response,” in *2016 10th European Conference on Antennas and Propagation (EuCAP)*, pp. 1–5, IEEE, 2016.